Ultrasound Assisted Synthesis and Characterization of Polymethyl Methacrylate (PMMA) Nanocomposites

A
Thesis
Submitted in
Partial Fulfillment of the
Requirements for the Degree of

DOCTOR OF PHILOSOPHY

Maneesh Kumar Poddar

Department of Chemical Engineering
Indian Institute of Technology Guwahati
Guwahati – 781039, Assam, India

March 2017

Dedicated

To

Almighty, My Guide and My Family Members for

Their Constant Support and Encouragement

Throughout My Research Work

Certificate

It is certified that the work contained in thesis entitled **" ULTRASOUND ASSISTED SYNTHESIS AND CHARACTERIZATION OF POLYMETHYL METHACRYLATE NANOCOMPOSITES "**, by Maneesh Kumar Poddar (Roll No. 136107036), has been carried out under my supervision and that this work has not been submitted elsewhere for a degree.

Date: 17.03.2017

Prof. V. S. Moholkar **CEng, MIChemE, FRSC, MAIChE (Sr)**
Department of Chemical Engineering
Indian Institute of Technology Guwahati
Guwahati – 781039, Assam, India

CONTENTS

LIST OF TABLES

Chapter 5

Chapter 6:

LIST OF FIGURES

CHAPTER 1

GENERAL INTRODUCTION

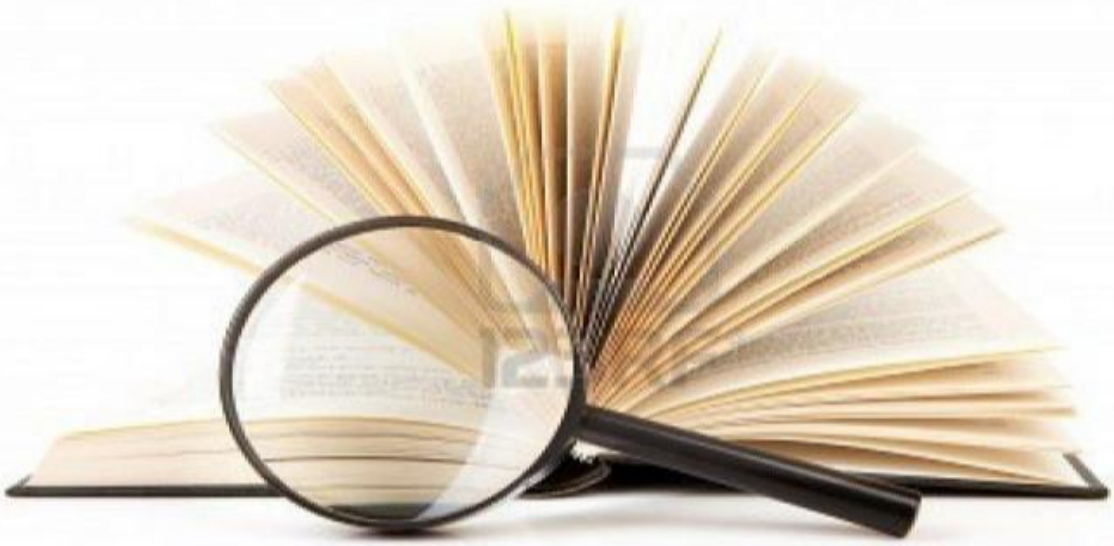

CHAPTER 1

General Introduction

1.1 Introduction

Polymer nanocomposites have emerged as new class of materials with distinct physical and chemical properties. Polymer nanocomposites comprise of a polymer matrix with dispersion of nanoscale inorganic or organic filler material in it. Addition of various filler materials such as inorganic clay, semiconductor metal oxide, transition metal oxide, carbon nanotubes and graphene based material with nanoscale morphology has been widely attempted for the enhancement of thermal, mechanical, electrical and optical properties of the pristine polymer. The development of this new class of materials with unique physical and chemical properties will circumvent use of conventional materials of construction such as wood, metal and glass. The properties of polymer nanocomposites can be fine-tuned to cater various needs by achieving proper synergy between the polymer matrix and filler material. Proper encapsulation and uniform dispersion of the nanofiller in the polymer matrix is crucial to achieving the desired properties of the nanocomposites for various applications.

The nanofiller montmorillonite clay which belongs to a group of Smectites family has attracted influential interest due to its high aspect ratio (1-100), and large interlayer galleries spacing (*d*-spacing) in-between clay layers. The addition of clay in polymer matrix makes it suitable for enhancing thermal and mechanical properties of pristine polymer. Nanocomposites with semiconductor oxides such as TiO_2 and ZnO have been used in solar

cells, light emitting diode, gas sensors, shielding resistance against harmful UV radiation etc. due to their optical properties. Recently, carbon-based modern materials such as graphene, carbon nanofibre, single and multiwall carbon nanotube that possess exceptional thermal, mechanical and electrical properties have been attempted as filler material for the nanocomposites. Polymer nanocomposites synthesized from carbon-based nanofiller are idle candidates for numerous applications in electronic and optical industries such as fabrication of supercapacitors, sensors, electromagnetic interference (EMI) shielding and electrostatic charge dissipation devices. Iron based nanocomposites employing nanoparticles of Fe_3O_4/Fe_2O_3 have been extensively applied in magnetic biosensors, EMI shielding, magnetic storage application, magnetic resonance application and biomedical application such as targeted drug delivery. These applications are essentially by virtue of the unique magnetic properties attained by the polymers after incorporation of nanoscale iron oxide particles within the polymer matrix.

Among various pristine polymers used for nanocomposite synthesis, polymethyl methacrylate (PMMA) is an important candidate for commercial application by virtue of its high optical transparency, good stability (against fluctuations of weather conditions) and good dimensional stability. PMMA has already been used (as a substitute for conventional polycarbonate plastic) in different applications ranging from aircraft glazing, lighting, dentures, food-handling equipment, contact lenses etc. Despite its versatile properties, pristine PMMA exhibits low mechanical strength (brittle behavior at high impact, and low ductility), negligible electrical conductivity and practically zero UV shielding. These shortcomings of pristine PMMA can be overcome by incorporation of proper nanofiller (with suitable properties) in the polymer matrix. Most importantly, the transparency of PMMA is least affected due to incorporation of the nanofiller material inside polymer matrix.

Conventional methods for synthesis of polymer nanocomposites include in-situ bulk polymerization (Wang et al., 2005; Aldosari et al., 2013,), in-situ emulsion and suspension polymerization (Tang et al., 2006a, Khatana et al., 2009; Hu et al. 2010; Wang et al., 2010; Zhang et al., 2014), melt intercalation polymerization (Wang et al., 2003; Kim et al., 2011) and solution intercalation or solvent blending method (Zhang et al., 2013; Chakraborty et al. 2014). A brief description of these techniques is given in the next section

1.2 Methods of polymer nanocomposite synthesis

1.2.1 In-situ emulsion polymerization

In-situ emulsion polymerization commences with impregnation of the nanofiller with liquid monomer. The dispersion of the nanofiller material in the reaction mixture occurs through surface encapsulation. A suitable water soluble initiator is then added and polymerization reaction is carried out under the effect of heat. There are various in-situ intercalative methods, such as in-situ bulk polymerization, in-situ suspension polymerization and in-situ emulsion polymerization, which are used for the synthesis of nanocomposite. Out of these methods, in-situ emulsion polymerization is most popular due to its simple procedure and other merits such as use of water as reaction medium (instead of toxic/expensive organic solvents). Latex particles of nanocomposites resulting from in-situ emulsion polymerization have narrow particle size distribution, high molecular weight and monodispersed nature. Moreover, use of high heat capacity / high latent heat reaction medium such as water helps in effective control the heat of reaction during polymerization. Surfactant is added to the reaction mixture for effective interphase mixing by reduction of interfacial tension. Above CMC (critical micellar concentration), the surfactant forms micelles in the reaction mixture. Monomer droplets with nanofiller materials dispersed inside it get encapsulated inside the surfactant micelles and undergo polymerization. This phenomenon not only limits the size

distribution of the nanocomposites to nanoscale range but also prevents formation of agglomerates. Effective mixing of the aqueous and organic phases of the reaction mixture and the solid nanofiller material is achieved by providing agitation or convection in the reaction mixture. The intensity of convection in reaction medium is critically important in the context of synthesis of nanocomposites, as it affects the dispersion of nanofiller and monomer in the reaction mixture. The intensity of convection also controls the encapsulation and dispersion of the nanofiller in the nanocomposite particles. Quite often, the agitation provided by mechanical stirring is inefficient in achieving high encapsulation and uniform dispersion of nanofiller in monomer droplets. This puts limit on enhancement of thermal, mechanical and electrical properties of polymer nanocomposite as compared to the pristine polymer with incorporation of the nanofiller in polymer matrix.

1.2.2 Solution Intercalation

This is a two-step process for synthesis of nanocomposites. In first step, the base polymer is dissolved in suitable solvents such as water, dichloromethane (DCM), acetone, chloroform, tetrahydrofuran (THF), dichloromethane (DCM), toluene etc. to obtain a uniform solution of polymer. In the second step, nanofiller material is dispersed in this solution using high speed mechanical agitation. Strong convection generated in the reaction mixture essentially causes intercalation of base polymer chains within the galleries of silicate layer. The solvent of the polymer solution is subsequently evaporated leaving behind the intercalated structure of resulting polymer nanocomposites.

The most undesirable feature of this method is energy-intensive recovery of organic solvent and its toxic nature. Agglomeration of the latex particles of polymer nanocomposites during solvent removal is also inevitable. This leads to weakening of the structure of polymer nanocomposites due to the defects left in the structure. The solution blending process has its

own difficulties, while application in industrial scale is hampered due to requirement of large quantities of expensive organic solvents.

Ultrasonic solution intercalation: More recently, the conventional technique of solution intercalation for nanocomposite synthesis has been coupled with high intensity sonication. Application of sonication to the polymer solution containing nanofiller leads to significant improvement in the dispersion of nanofiller in the base polymer. High intensity micro-convection/micro-turbulence generated by sonication causes very uniform mixing of nanofiller in polymer matrix. It also prevents the agglomeration of the polymer nanocomposite latex particles. Li et al. (2005) reported the effect of ultrasound and UV/ozone treatment on synthesis of graphite epoxy-based nanocomposites using acetone as a solvent media. Li et al. (2005) concluded that sonication provided exfoliated structure of nanofiller, which was manifested in terms of enhanced electrical conductivity of resulting nanocomposites. Safadi et al. (2002) synthesized multi-wall carbon nanotube/polystyrene nanocomposite using ultrasound-assisted solution intercalation with toluene as solvent. These nanocomposites had enhanced electrical conductivity, with percolation threshold concentration of nanofiller < 0.5 vol%, which essentially points to uniform dispersion of nanofiller in polymer matrix under influence of sonication.

1.2.3 Template synthesis

Template synthesis is also known as sol-gel method. This method is most commonly used for synthesis of silicate based polymer nanocomposites. In this technique, the clay minerals are synthesized within the polymer matrix using an aqueous solution (or gel) containing the polymer and the silicate building blocks. Generally, magnesium hydroxide sol and lithium fluoride are used as precursors for the silicate-based nanomaterial. In this technique, the long chain polymeric material aids the nucleation and growth of the inorganic

host crystals, which get trapped within the layers of the polymers, as they grow. Main disadvantage of this method is high thermal energy requirement, which may lead to decomposition of long chain polymer structure, and cause agglomeration of the resulting nanocomposite particles. This technique is widely applicable for the synthesis of (LDH) double-layer hydroxide-based nanocomposites. Synthesis of hectorite-type clay minerals can be performed at milder conditions. Carrado et al. (2000) have reported synthesis of hectorites from gels consisting of silica, lithium fluoride, hydroxide of magnesium, and various polymers like polyaniline, poly(vinyl alcohol), and polyacrylonitrile. The authors reported minor aggregation of some silicate layers, but most of the silicates remained uniformly distributed in the polymer matrix.

1.2.4 Melt intercalation

Principal merit of melt intercalation technique (as compared to solvent intercalation) is avoidance of use of any toxic organic solvent. In this process, the polymeric material is heated above its softening point and the filler material is inserted in molten polymer matrix. The final nanocomposites can be obtained by extrusion or injection. This technique essentially involves crawling of molten polymer into the interlayer space of the nanofiller to form either an intercalated or exfoliated nanocomposite. However, for this phenomenon to happen, the surface of the nanofiller should be sufficiently compatible with the polymer matrix. Melt intercalation is a popular method for synthesis of thermoplastic nanocomposites. Melt mixing has been employed for the dispersion of a wide range of materials such as clays, oxides, and carbon nanotubes in polymer melt. A practical merit of the technique of melt intercalation is its similarity and compatibility with industrial processes of polymer manufacture such as extrusion and injection molding. Despite these advantages, use of melt mixing method is limited due to operational constraints such as rapid increase of the viscosity

of polymer melt with incorporation of nanofiller, and formation of agglomerates of nanofiller material inside polymer matrix due to weak bonding between polymer molecules and surface of nanofiller. Wang et al. (2003) has synthesized intercalated structure of polyethylene/clay nanocomposite by melt intercalation method with using hexadecyl trimethyl ammonium bromide (C16) as reactive compatibilizer. Moussaif and Groeninckx (2003) have reported exfoliated structure of polyvinylidene fluoride (PVDF)/ organoclay nanocomposites by melt-extrusion using PMMA as an interfacial agent. Kim et al. (2006) reported carbon-based synthesis of polyethylene/graphene nanocomposites with exfoliation of graphene sheet in polyethylene matrix.

***Ultrasonic melt intercalation*:** Due to high viscosity of the polymer melt, complete exfoliation of the nanofiller material is not achieved in the polymer matrix during melt intercalation. Application of sonication during melt intercalation could overcome this limitation. Few authors have reported synthesis of different nanocomposites using ultrasound-assisted melt intercalation. Lee et al. (2004) reported synthesis of polypropylene /clay nanocomposites using ultrasound-assisted melt intercalation. Lee et al. (2004) used 20 kHz ultrasound with rated input power of 60 W for sonication of polymer melt. Under the effect of ultrasound, an exfoliated structure of clay platelets in the matrix of polypropylene was achieved. Swain and Isayev (2007) have synthesized high density polyethylene (HDPE)/organoclay Cloisite 20A nanocomposite using a single screw compounding extruder with ultrasonic slit die at frequency of 20 kHz. The author reported the 50% enhancement in *d*-spacing under sonication. Swain and Isayev (2007) claimed that use of sonication during nanocomposite synthesis by melt intercalation is an effective method for improving exfoliation and the dispersion of nanoclays in polymer matrix, which essentially is manifested in terms of enhanced physical properties of the nanocomposite as compared to pristine polymer.

1.2.5 Comparative analysis

Among various techniques for nanocomposite synthesis, emulsion polymerization has several distinct advantages for synthesis of polymer and its nanocomposites such as uniform dispersion of nanofiller in polymer matrix, better control over rate/yield of reaction, and low viscosity of the reaction mixture. Due to its different reaction mechanism than conventional bulk polymerization, emulsion polymerization has merit of simultaneously achieving high molecular weight as well as high rate of polymerization. Achieving fine emulsification between organic (polymer) and aqueous phase is crucial for high yield of emulsion polymerization. Conventional methods of providing agitation (or convection) in the reaction mixture using mechanical stirring to create emulsion are not effective. The cause leading to this effect is relatively large size of monomer droplets (> 100 nm) in the emulsion due to which these droplets cannot enter the micelles with nanoscale diameters (20-45 nm). As a result, the nanocomposites synthesized with emulsion polymerization employing mechanical stirring suffer from demerits such as low encapsulation and non-uniform distribution of nanofiller in polymer matrix, high polydispersity index and low kinetics of polymerization. This essentially emphasizes the crucial role of convection on kinetics and yield of nanocomposite synthesis through emulsion polymerization.

***Ultrasonic emulsion polymerization*:** A relatively new technique of introducing convection in emulsion polymerization reaction system is sonication or ultrasound irradiation. The first investigation on ultrasound-induced polymerization was reported by Lindstrom and Lamm (1951), who studied polymerization of acrylonitrile in aqueous medium. The study of Lindstrom and Lamm (1951) was essentially inspired by the previous work by Dainton (1948), who demonstrated polymerization of acrylonitrile in water solution initiated by free radicals produced by ionizing radiation from strong radioactive preparations. Initial research in the area of ultrasonic polymerization is attributed to group of Peter Kruus of Carleton

University who reported sonication-induced polymerization of several monomers like methyl methacrylate, styrene, bromobenzene and isoprene (Kruss et al., 1983, 1985, 1988). Ultrasonic polymerization had distinct advantages such as low bulk reaction temperature, high monomer conversion, higher polymerization rate, high molecular weight and narrow particle size distribution. Prior to the work of Kruus and co-workers, ultrasound was used for treating polymers, but most of the work was dedicated to depolymerization rather than polymerization (Basedow and Ebert, 1977; Tabata et al., 1980). Production of free radicals during sonication is attributed to implosive transient collapse of cavitation bubbles driven by pressure variation induced by ultrasound waves. The transient cavitation generates intense energy concentration on extremely small temporal and spatial scales. The implosive collapse (or compression) of the cavitation bubbles is adiabatic and the temperature and pressure inside the bubble reaches extreme (~ 5000 K, ~ 500 bar). At these conditions, the solvent vapor molecules entrapped in the bubble undergo thermal dissociation to generate the radical species. The cavitation bubble may get fragmented at the point of maximum compression with release of the chemical species inside it into the bulk liquid. These species are responsible for inducing/accelerating chemical reactions such as polymerization. In the context of synthesis of polymer nanocomposites, the physical effects of ultrasound and cavitation are also of relevance. Both ultrasound and cavitation induces micro-convection in the medium. The ultrasound wave passes through the liquid medium in the form of longitudinal wave comprising alternate compression/rarefaction cycles. This generates oscillatory motion of fluid elements around their mean position. The amplitude of this oscillatory motion is typically ~ 0.1–1 microns, and the time scale is of few microseconds (e.g. 50 μs for 20 kHz wave). In addition, the radial motion of cavitation bubbles also generates micro-convection in the form of oscillatory motion of fluid elements and shock waves (or acoustic waves). The shock (or acoustic) waves are generated due to sudden

reflection of the fluid elements from the gas-liquid interface – when the radial motion of the cavitation bubble comes to sudden halt. This effect is caused by the back-pressure exerted by the non-condensable gas present in the bubble during adiabatic compression. Thus, the micro-turbulence generated in the reaction mixture by both ultrasound and cavitation creates fine emulsification of the monomer/water solution. It not only leads to higher encapsulation of nanofiller material in the polymer but also uniform dispersion in the matrix. Both of these effects are highly beneficial towards enhancing properties of the nanocomposite over that of pristine polymer. Moreover, fine emulsification of aqueous/organic phases generates enormous interfacial area in reaction mixture that boosts the kinetics of the polymerization.

1.3 Types of nanofiller for the composites

Reinforcement of polymers and plastics with nano-scale fillers such as nanoclay, conducting/semiconducting/magnetic metal oxides (e.g. ZnO, TiO_2, Fe_3O_4), carbon nanotubes, carbon nanofibre, graphene and metal (Cu, Ag, Au) nanoparticles/nanowires has been widely practiced for developing functional composites and interface structures. Addition of the nanofillers in host polymer matrix significantly improves its physical properties and suitability for various applications. Encapsulation of silica-based nanoparticle or clays in polymer matrix such as nanoclay results in nanocomposites with enhanced thermal and mechanical properties. Addition of nanoscale semi-conductor metal oxide such as ZnO and TiO_2 in polymer matrix results in nanocomposites with enhanced resistance against UV radiation. ZnO-based polymer nanocomposites also have several other merits such as high excition binding energy, antireflection coating, effective antibacterial activity, enhanced thermal stability and scratch resistance. Titania-based metal oxides such as TiO_2 are known for its remarkable photocatalytic activity and enhanced thermal stability. More recently, carbon-based nanomaterials such as fullerenes, single and multi-wall carbon nanotube,

carbon nanofiber and graphene have attracted high attention as filler material for nanocomposites due to their exceptionally high physical properties (such as aspect ratio, electrical conductivity, thermal stability and mechanical strength), as compared to other conventional filler materials. The polymer composites synthesized with carbon-based nanofiller have significantly higher electrical conductivity and thermal / mechanical properties (Kuila et al., 2011; Yan et al., 2012). Iron-based nanomaterials such as Fe_2O_3/Fe_3O_4 have also attracted high interest of researchers as nanofillers in polymer matrix in view of potential industrial applications such as magnetic bioseparation, detection of biological entities (cell, protein, nucleic acids, enzyme, virus etc.), clinic diagnosis and therapy such as MRI (magnetic resonance image) and MFH (magnetic fluid hyperthermia) and targeted drug delivery. Polymer nanocomposites employing magnetic nanoparticles have various applications such as drug targeting, cell separation and purification, molecular biology, EMI shielding etc. Other filler materials like $CaCO_3$ combined with polymers such as polyaniline (PANI) have exhibited dual effect, such as improvement in mechanical and anticorrosion properties of resulting PANI/$CaCO_3$ nanocomposites (Bhanvase et al., 2010).

In this thesis, we have reported ultrasonic synthesis and characterization of nanocomposites of polymethyl methacrylate (PMMA) with four nanofillers, viz. (1) Cloisite 30B i.e. a type of montmorillonite nanoclay, (2) semiconductor ZnO, (3) reduced graphene oxide (RGO), and (4) iron oxide nanoparticle (Fe_3O_4). Our study also includes ultrasound-assisted synthesis of the nanofiller itself. For the convenience of the readers, we have given a brief description of these nanomaterials in next section.

1.3.1 Montmorillonite nanoclay

Silica is essentially 1-D nanoscale clay, which possesses layered structure. The thickness of individual clay platelets is ~ 1 nm and length/width of the platelets varies in the range of 200 - 600 nm with high aspect ratio. This layered silicate structure belong to the

group of swelling phyllosilicates or smectites. Majority of the smectites clay consist of platelet shaped crystals usually containing oxygen, silica, aluminium and magnesium. The crystal lattice of 2:1 phyllosilicates based MMT (montmorillonite) clay is a sheet type structure composed of two tetrahedral silicate sheets merged in an octahedral plane of alumina or silica (Fig. 1.1). The tetralayer silicate layer consists of SiO_4 groups linked together to form a hexagonal network of the repeating unit of composition Si_4O_{10}. Due to the isomorphous substitution of central anions in lower valence of tetrahedral and octahedral sheet, the layered silicates possess negative charge on their outer surface, which is counter-balanced by the inorganic cations located in the interlayer galleries of the clay. The characteristic dimensions of clays are *d* (001) spacing and its gallery (or interlayer) spacing. The gallery spacing is the gap between two parallel clay platelets within a clay aggregate, and the *d* (001) spacing is the vertical distance between clay platelet stacked one above another. Fig. 1.2 clearly depict the difference about the galleries spacing, interlayer *d* (001) spacing and clay platelets height.

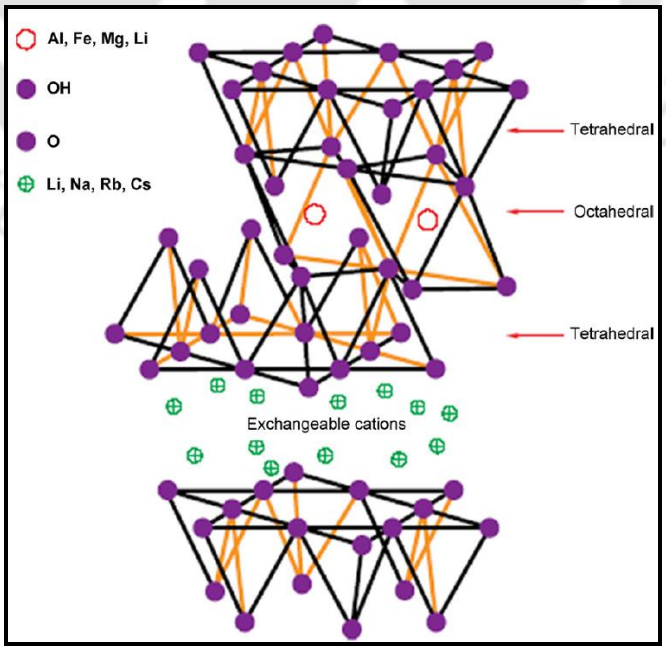

Figure 1.1: Schematic diagram of 2:1 (TOT) layered structure. (Adopted from Beyer, 2002 by permission of Elsevier Science Ltd., UK)

***Organic treatment of layered silicates*:** Naturally occurring silicates have layered structure and have hydrophilic character. Thus, the nanoparticles of silicates are not compatible with the polymer matrix, which has predominantly hydrophobic character. The surface of the clay must be made organophillic/hydrophobic in order to make it compatible as nanofiller with the host polymer. The chemical method for imparting hydrophobicity to the clay surface is known as organic treatment or surface modification of clay. Organic treatment or surface modification of clay is accomplished by the ion exchange between inorganic alkali cations on the surface of the clay with the cationic-organic surfactant such as alkylammonium ions and other onium salts. These organic cations lower the surface energy of the silicate surface and improve wettability of the surface with the hydrophobic polymer chain. Moreover, the long chains of surfactant molecules possessing positively charged ends are tethered to the surface of negatively charged silicate layer. This essentially results in pulling apart of the silicate layers resulting in an increase in gallery height (Fig. 1.2). The yardstick for assessing extent of surface modification of clay is the charge density, which is determined by the concentration of the exchangeable ions between clay galleries. The excess negative charge on layered silicates and their capability to exchange ions is expressed in terms of cation-exchange capacity (CEC, measured in mequiv/g). Lan et al. (1995) have reported that layered silicate minerals with cation exchange capacity (CEC) of 60-100 mol-equivalent/100 g of the mineral (such as montmorillonite / hectorite clay) provided better exfoliation after surface modification and cure compared to other clay minerals with higher CEC value. The higher the CEC value, the better the hydrophobicity of organomodified clay. Silicate layers belonging to smectites (2:1 TOT) family such as organomodified montmorillonite (o-MMT) possess the CEC value in range of 0.8-1.2 meq/g as compared to the kaolinite (CEC ~ 0.2 meq/g.) One of the commercially available organo-modified o-MMT clays, Cloisite 30B, has CEC capacity > 0.9 meq/g. This clay has also been used for ultrasonic synthesis of PMMA

nanocomposites in the present thesis.

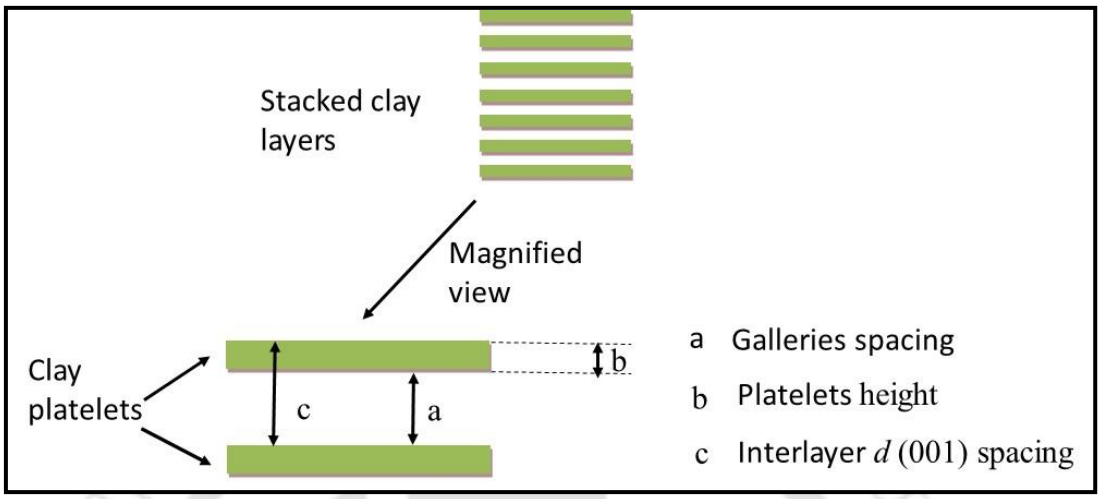

Figure 1.2: Schematic representation of interlayer *d* (001) spacing of clay.

***Dispersing nanoclay*:** Mere mixing of the polymer and nanofiller does not result in a nanocomposites with enhanced physical and chemical properties. Negligible intercalation of polymer into clay platelets due to weak interaction between the clay platelets and polymer results in a nanocomposite that has reduced physical/chemical properties than even the pristine polymer. The structure of nanocomposites can be divided into three possible phase depending upon the degree of separation of clay platelets, viz. (1) phase separated/unmixed structure, (2) intercalated structure, and (3) exfoliated structure, which are depicted in Fig. 1.3.

Phase separation in the nanocomposite matrix occurs for unfavorable polymer/clay interactions. It may also occur if the clay layers are too tightly bound together to allow penetration of polymer chains into its galleries. This essentially leads to agglomeration of large clusters/aggregates of clay in nanocomposite matrix. Intercalated structure is obtained when one or more polymer chain is injected in between the clay layers. This is a well-ordered multilayer structure with alternating polymeric and inorganic layers, with a repeat distance

between them. The exfoliated structures are obtained when the silicates layers are well separated from one another and individually dispersed in the continuous polymer matrix. Obtaining the exfoliated structure is the most desirable result in synthesis of polymer nanocomposites. The exfoliated structure provides the highest interactions among the polymer and silicates nanoparticles. This results in maximum improvement in the thermal and mechanical properties of the resulting nanocomposites.

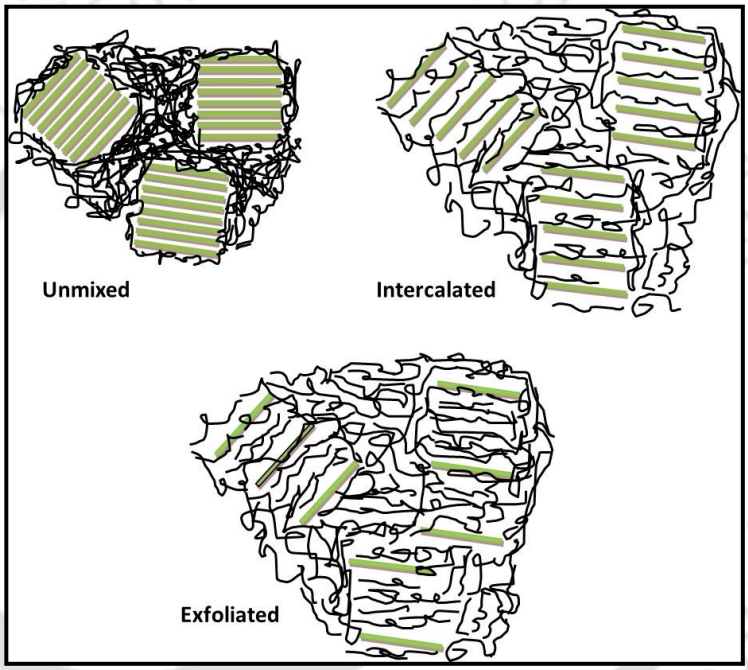

Figure 1.3: Schematic of structures of polymer/clay nanocomposites resulting from different levels of dispersion of nanoclay in polymer matrix.

1.3.2 Zinc oxide

Among the semiconductor metal oxides, nanoscale zinc oxide has received significant attention of the researchers for nanocomposite synthesis due to its unique physical and chemical properties, such as high excitons binding energy (60 meV), wide band-gap, better chemical stability and low growth temperature. By these virtues, nanoscale ZnO is suitable for numerous applications such as solar cells, gas sensors, photoelectricity switch, UV

protection layers and various optical devices. The basic crystal structure of ZnO occurs in two forms: (1) hexagonal wurtzite structure, and (2) cubic zinc blende structure. Out of these, wurtzite shows greater thermodynamic stability at ambient conditions. ZnO with wurtzite structure has deviations from stoichiometry due to presence of intrinsic defects such as O-vacancies and Zn-interstitials. This makes ZnO a natural n-type semiconductor. Undoped ZnO shows intrinsic n-type activity with very high electron density of 10^{21} cm^{-3} (Ozgur et al., 2005). The wurtzite structure has a hexagonal unit cell in addition with the two interpenetrating hexagonal close packed (hcp) sublattices. The hexagonal wurtzite structure lattice constants are: a = 3.25 Å and c = 5.2 Å. The ratio c/a ~ 1.60 is close to the ideal value for hexagonal cell c/a = 1.633. The bonding in ZnO is largely ionic (Zn^{2+}– O^{2-}) with the corresponding radii of 0.074 nm for Zn^{2+} and 0.140 nm for O^{2-}. This property accounts for preferential formation of wurtzite structure of ZnO.

For the uniform dispersion and better compatibility of nanoscale ZnO in polymer matrix, surface modification of ZnO is necessary. Pristine ZnO without the surface modification cannot distribute uniformly in polymer matrix as the hydrophilic surface of ZnO is not compatible with hydrophobic polymer. Compatibility of the ZnO with polymer matrix can be enhanced using various techniques such as absorption of suitable coupling agent (such as silane) on the surface of particle or grafting of polymer chains on the surface of the particle (Rong et al., 2002; Flesch et al., 2004). Common techniques employed for surface modification of inorganic particles before their use in synthesis of nanocomposites are described subsequently.

1.3.3 Iron oxide based nanofiller

The magnetic particles are promising nanofiller materials for nanocomposites for their wide application in magnetic fluid, drug delivery, resonance imaging, data storage, synthesis

of catalyst, protein purification and enzyme immobilization. The encapsulation of magnetic nanoparticles in polymer matrix makes resulting nanocomposite conductive and magnetic. Several methods have been reported in literature for synthesis of iron oxide nanoparticles, viz. co-precipitation, thermal decomposition and micro-emulsion based method. Among these methods, co-precipitation has been widely practiced due to its ease and simplicity. In this method, iron based salt such as iron chloride ($FeCl_3/Fe^{3+}$) and iron sulfate ($FeSO_4$ /Fe^{2+}) are used as precursors. An aqueous mixture of Fe^{3+}/Fe^{2+} in 2:1 molar ratio is used under mechanical stirring at room temperature. With the addition of ammonia solution (NH_4OH), black precipitate of Fe_3O_4 nanoparticles is obtained. These particles are further filtered and dried. The co-precipitation approach has been used extensively to produce ferrite nanoparticles of controlled sizes and desired magnetic properties (Gnanaprakash 2006, Ayyappan 2009). The method of co-precipitation, however, suffers from problem of Oswald ripening, which essentially is phenomenon of aggregation of colloidal particles resulting in lower surface energy. Steric stabilization of suspended nanoparticles provides resolution of this problem. The reaction scheme for synthesis of iron oxide by co-precipitation method is as follows:

$$FeSO_4 \longrightarrow Fe^{2+} + SO_4^{2-}$$
$$FeCl_3 \longrightarrow Fe^{3+} + 3Cl^-$$
$$Fe^{2+} + 2Fe^{3+} + 8OH^- \xrightarrow{co-precipitation} Fe_3O_4 + 4H_2O$$

1.3.4 Surface modification of inorganic particles

As noted previously, to enhance the dispersion of nanoscale ZnO in polymer matrix, the surface of the ZnO particles must be modified by using various techniques. Some common methods used for surface modification of inorganic or metal oxide particles for enhancing their compatibility for nanocomposite synthesis are described below.

Chemical method: This method involves the absorption of silane coupling agent on the unmodified inorganic nanoparticles. The polar surface of the inorganic nanoparticles is modified by the grafting of silane coupling agents. This improves the compatibility between the particle and polymer surfaces and the properties of composite materials. Fig. 1.4 shows alumina nanoparticle before and after surface modification using the silane coupling agent APTMS (3-aminopropyltriethoxysilane). The surface of the original (or pristine) nanoparticle is covered with only –OH groups, while the surface of the silane-modified nanoparticle is covered with 3-methacryloxypropyl trimethoxysilane molecules. The modified nanoparticles show comparatively better dispersion (as compared to unmodified nanoparticle) in both organic solvents (which are used as reaction media in conventional methods) and polymer matrices. Ma et al. (2008) improved the dispersion stability of ZnO nanoparticles by treatment with a silane coupling agent (γ-methacyloxypropyl trimethoxy silane, KH-570). Hong et al. (2006) also used same silane coupling agent during the synthesis of PMMA/ZnO nanocomposites. Surface modification of ZnO essentially resulted in addition of functional double bonds onto the surface of ZnO nanoparticles. The nanocomposites of PMMA/ZnO were synthesized by radical grafting polymerization in non-aqueous medium. Truong et al. (2010) treated the Al_2O_3 nanoparticle surface with two different silane coupling agents, (3-chloropropyl) trimethoxysilane and (octyl) triethoxysilane to enhance hydrophobic interactions with syndiotactic polypropylene matrix. Mallakpour and Barati (2011) reported surface modification of TiO_2 nanoparticles by reaction with a ϒ- aminopropyltriethoxy silane coupling agent. The silane coupling agent is adsorbed on the surface of the nanoparticles at its hydrophilic end and interacts with hydroxyl groups that are pre-existing on the nanoparticle's surface.

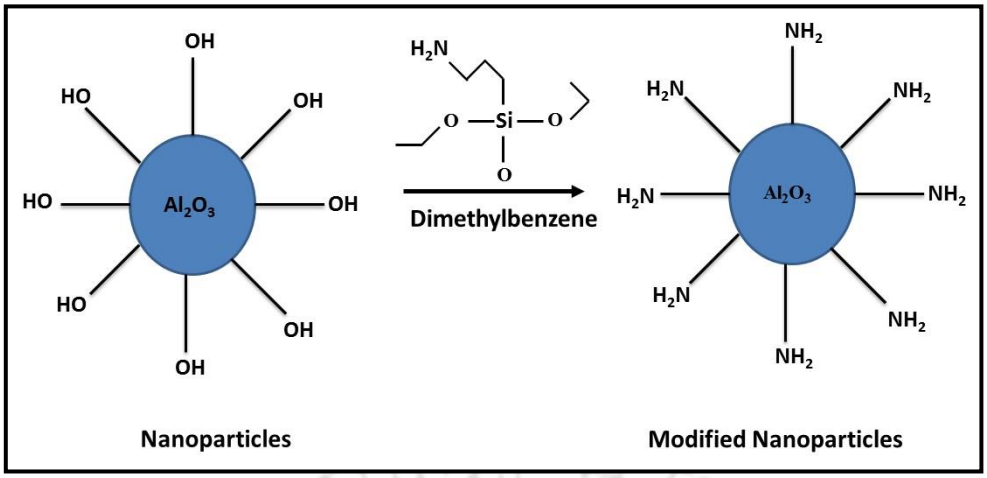

Figure 1.4: The surface modification of nanoparticles with 3-aminopropyltriethoxysilane.

Grafting polymer chains: This technique involves the grafting of synthetic polymer on the external surface of the inorganic nanoparticles. This changes the surface topology and increases the chemical functionality of nanoparticles. Generally, there are two methods for covalent grafting of polymer chains on the surface of inorganic nanoparticles, viz. (1) 'grafting to method', in which end-functionalized polymers chains react with the particle surface, and (2) 'grafting from method' in which polymer chains are grown from an initiator-terminated self-assembled monolayer (Kango et al., 2013). In both cases, a thin layer of polymeric brush is formed on the solid surface of nanoparticles. The schematic representation of grafting method is shown in Fig.1.5. The grafting approach involve a chemical reaction between (end) functionalized polymers and complementary reactive group on the surface. This reactive polymer can be synthesized via conventional, radical, anionic, and cationic polymerization methods, involving propagation of the grafted polymers from the surface of the particle .The major advantage of the grafting method over other polymer attachment techniques is that the polymer can be thoroughly characterized (prior to grafting) via various chemical and physical methods. Higher yield of grafting percentage of polymer-grafted-nanomaterial has been obtained by initiating the graft polymerization from the surface of the nanomaterials with polymer initiating groups. The polymerization process consists of radical,

anionic and cationic polymerization method, involving propagation of grafted polymers from the surface of particles. Liu and Wang (2008) grafted poly (hydroethyl acrylate) from the surface of ZnO nanoparticles via copper-mediated surface-initiated atom transfer radical polymerization (SI-ATRP) method. Tang et al. (2006b) modified the surface of inorganic ZnO nanoparticles by grafting of chain of polymethacrylic acid on the external surfaces of nanoparticles. The -OH groups on surface of ZnO nanoparticles interact with carboxyl groups (COO–) of PMMA to form a poly (zinc methacrylate) complex on the surface, which provides better compatibility with the organic polymer matrix. Zhang et al. (2011) successfully modified the surface of zinc oxide nanoparticles with methyl methylacrylate acetate (ZnMAAc), and developed ZnO/poly (methyl methacrylate)-(ZnO/PMMA) nanocomposite films via free-radical polymerization between methyl methacrylate (MMA) and ZnMAAc. In a recent study, Bach et al. (2012) grafted PMMA on Fe_3O_4 magnetic nanoparticles (MNPs) using the "grafting from" approach based on thiol-lactam initiated radical polymerization (TLIRP). Wu et al. (2012) successfully modified the surface of iron oxide (Fe_3O_4) nanoparticles with maleimide, and prepared PBZ magnetic nanocomposite using modified iron oxide nanoparticles and benzoxazine through in-situ Diels–Alder polymerization.

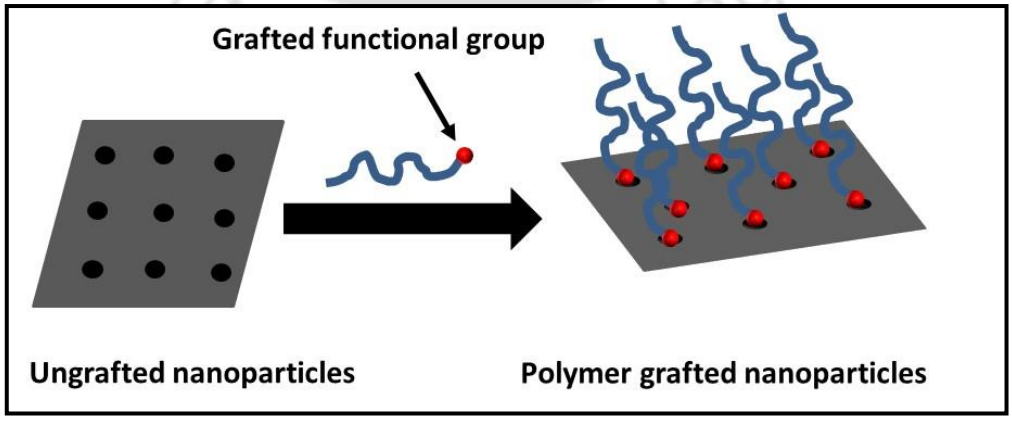

Figure 1.5: Grafting techniques of surface modification of nanoparticles.

***Surfactant method*:** Surface treatment of inorganic nanoparticles using surfactants is one of the simplest methods to improve the dispersion behavior of nanoparticles in aqueous systems. The polar groups present in the surfactants molecules are selectively adsorbed on nanoparticle surface as a result of electrostatic interactions. The surfactant reduces the physical forces between the nanomaterials, which decreases the inter-particle interaction and reduces the agglomeration. The resultant surfactant-modified nanomaterials can be effectively encapsulated into the polymer matrix. Various anionic surfactants such as oleic acid, polycarboxylic acids and their salts have been used for surface-modification of oxide nanoparticles, such as TiO_2, Al_2O_3, and Fe_2O_3.

1.3.5 Graphene based nanofiller

As noted earlier, carbon-based nanomaterials such as graphene, CNF and carbon nanotubes (CNTs) are increasingly being used as fillers for the nanocomposite synthesis due to their exceptional physical properties. Among carbon-based nanomaterials, graphene is the thinnest material in the form of 2-D layers of sp^2 bonded carbon atoms. Graphene is an ultra-modern material with extraordinary mechanical, thermal and electrical properties (e.g. Young's modulus = 1 TPa, Tensile Strength = 130 GPa, Thermal conductivity = 5000 W/mK, electrical conductivity = 10^4 S/cm). These unique properties make graphene a suitable material for the synthesis of polymer nanocomposites for diverse applications such as nanoelectronics, supercapacitors, chemical and biological sensors, flame retardant, electromagnetic interference shielding and packaging. Pristine graphene is not compatible with organic polymers and does disperse uniformly in the polymer matrix to form homogeneous nanocomposites. Therefore, pristine graphene is converted to graphene oxide prior to synthesis of the nanocomposite. The graphene oxide sheets contain highly oxygenated groups (diols, ketones, carboxyls and hydroxyl) on surface that enhance

interaction and compatibility of the nanofiller with the organic polymer. However, conversion of graphene to graphene oxide sharply reduces the electrical conductivity. This makes graphene oxide unsuitable as nanofiller for synthesis of conductive nanocomposites. However, surface modification of graphene is an essential step for obtaining uniform dispersion of graphene sheets in polymer matrix. Electrical conductivity of the polymer/graphene oxide nanocomposites can be increased by in-situ chemical reduction of GO, presumably by restoring the graphitic network of sp^2 bonds. Several methods have been reported in recent literature for synthesis of graphene nanosheets. One of the widely practiced methods is chemical vapor deposition (CVD) and epitaxial growth, which involves decomposition of ethylene on nickel surfaces (Eizenberg and Blakely, 1979; Aizawa, 1990). The second method is micromechanical exfoliation of graphite, which is also known as the 'scotch tape' or 'peel-off' method (Novoselov, 2004). Other common methods for graphene synthesis are: (1) epitaxial growth on electrically insulating surfaces such as silicon carbide (SiC), and (2) solution-based reduction and thermal treatment of graphene oxide with good electrical conductivity (Berger, 2006; Park and Ruoff, 2009).

Surface modification of graphene: As noted earlier, pristine graphene is non-compatible with polymer matrix. Thus, the graphene sheets are not intercalated by polymer chains, because graphene as a bulk material has a pronounced tendency to agglomerate in a polymer matrix**.** Chemical functionalization of graphene improves the solubility and interaction among the polymer and graphene. Various methods such as chemical modification, electrochemical modification, π- π interaction have been used for the surface modification of graphene. Out of these methods, chemical modification of graphene is most widely used due to its simplicity. In this method, the precursor graphene oxide is first dispersed in water followed by the addition of aq. KOH solution (Fig. 1.6). KOH being a strong base can confer

large negative charge through reactions with the reactive hydroxyl, epoxy and carboxylic acid groups on the graphene oxide sheets, resulting in extensive coating of the sheets with negative charges and K^+ ions. Further addition of hydrazine monohydrate to KOH-treated graphene oxide produces highly stable homogeneous suspension of hydrazine-reduced KOH-modified graphene (hKMG). This method has merit of being a facile approach for large-scale production of aqueous graphene dispersions without need for polymeric or surfactant stabilizers.

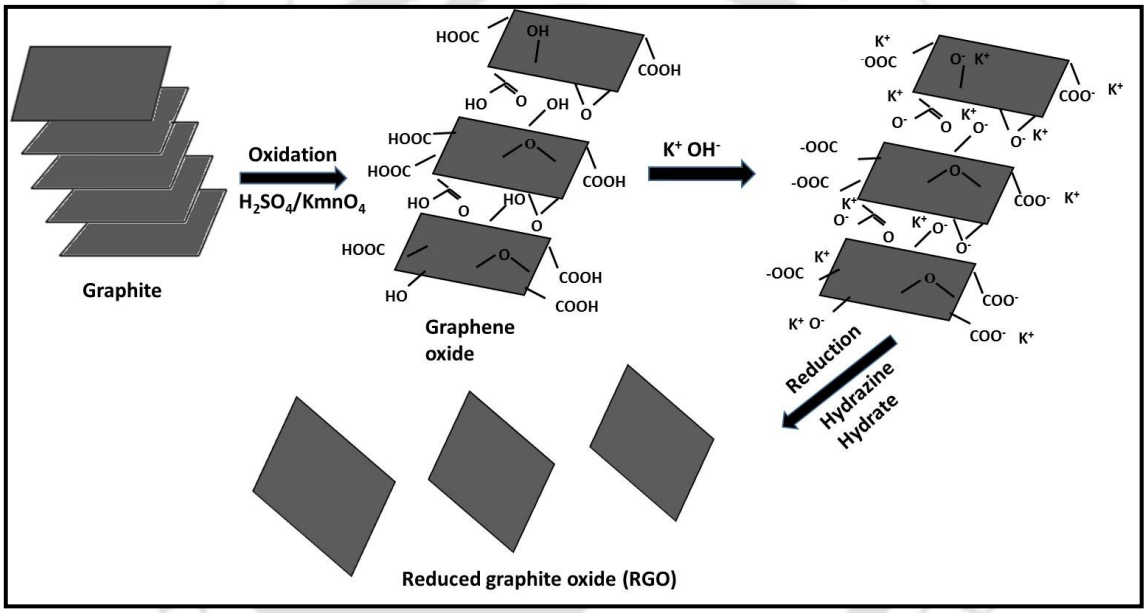

Figure 1.6: Reduction method used for the synthesis of RGO from the stacked graphite sheets using oxidation and reduction method.

1.4 Ultrasonic assisted synthesis of in situ emulsion polymer nanocomposites

1.4.1 Clay based polymer nanocomposites

Addition of clay nanofiller in polymer matrix dramatically enhances its gas permeability, flame retardation capability, and mechanical (especially thermal and mechanical) properties. Among various synthesis methods for polymer nanocomposites, in-situ emulsion polymerization is one of the environmental benign techniques, where water is

used as a dispersing medium. Above critical micellar concentration (CMC), the surfactant molecules form micelles entrapping monomer droplets with clay nanoparticles dispersed in them. During polymerization process, the galleries of layered silicates widen, which in turn leads to the intercalation of monomer and/or micelles within the silicate layers. In conventional technique of polymer/clay nanocomposites synthesis, mechanical stirring is employed, which cannot widen the clay galleries sufficiently. This essentially results in poorly intercalated or semi-exfoliated structure of the nanocomposites.

As noted earlier, ultrasound irradiation or sonication generates intense microturbulence in the medium, which essentially causes widening of the *d*-spacing of the nanofiller that result in effective intercalation of the monomer (Fig. 1.7). Secondly, microturbulence also causes fine emulsification of the aqueous and organic phases of the reaction mixture. Ultrasound treatment of aqueous clay suspension also stabilizes the colloidal system. The generation of high shear force during formation and collapse of the cavitation bubbles results in exfoliation of clay into single platelets, with easy dispersion into hydrophobic monomer phase (Borthakur et al., 2010). Moreover, transient collapse of cavitation bubbles causes generation of radicals through thermal dissociation of solvent. Transient cavitation predominantly occurs in vicinity of the clay particles. In-situ generation of radicals near the clay layers helps in polymerization of the intercalated monomer, which helps in increasing the *d*-spacing and exfoliation of the nanoclay in resulting nanocomposites.

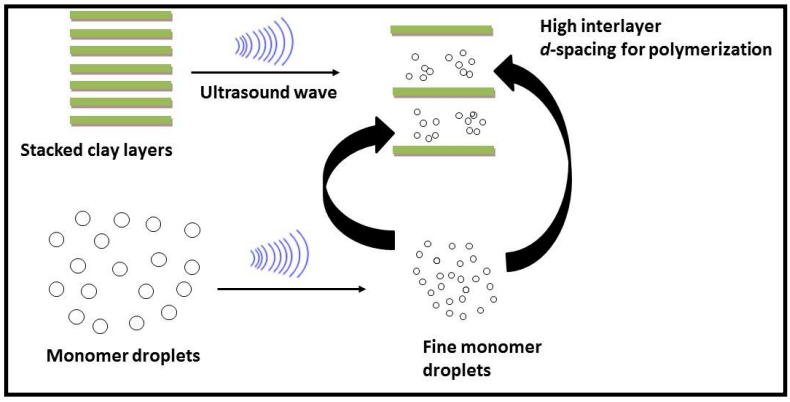

Figure 1.7: Schematic scheme of synthesis of polymer/clay nanocomposites under the presence of ultrasound.

1.4.2 Polymer-metal nanocomposite

Nanoscale metals particles have special characteristics that are suitable in numerous advanced functional applications. The major practical problems associated with these particles are: their easy aggregation due to high surface free energy, and fast oxidation (feeble stability) in air. Metal nanocomposites of polymers possess versatile functional properties suitable for many applications. Several methodologies and techniques have been reported in literature for the synthesis of metal nanocomposites as follows: (1) a metallic precursor is dissolved along with a polymer in a solvent, and then reduced to the metallic nanoparticles in-situ. The metal nanoparticles get entrapped in the polymer matrix as the solvent is removed by heating with stirring (Delamarche, 2003; Demir et al., 2004; Dos et al., 2004), (2) a metallic precursor is dissolved in a monomer, and then reduced to the metallic nanoparticles during polymerization (Haes et al. 2004), (3) a colloidal solution of metal nanoparticles is mixed with either a monomer or a polymer solution, followed by a procedure similar to (1) or (2) (Klabunde, 1989; Mibhele, 2003), and (4) a polymer matrix is impregnated with a solvent containing a metal precursor, and then is either treated by reduction agents or subjected to thermolysis (Boyes, 2003 and Yoda, 2004). A simple one-step synthetic route for nanocomposites of PMMA/Ag (with Ag as core and PMMA as shell)

has been reported by Xu et al. (2007). Xu et al. (2007) sonicated (50 kHz, 200–1200 W) an emulsion of MMA monomer and silver nitrate without addition of initiator. In-situ reduction of silver nitrate generated clusters of Ag nanoparticles, and the polymerization of monomer occurred on the surface of the clusters. Barkade et al. (2011) have attempted ultrasound-assisted (20 kHz, 600 W) in-situ mini-emulsion polymerization of aniline with different loading of silver nanoparticles and studied its application for ethanol vapor sensing. It has been reported that ethanol vapor sensing ability of the nanocomposite increases with the addition of silver nanoparticles in the polymer matrix. Sivakumar and Gedanken (2005) used sonochemical technique (20 kHz, 600 W) for the preparation of polyaniline/Au nanocomposite. In this study, authors concluded that ultrasonic route of nanocomposite synthesis yields particle size in nanoscale range, as compared to the conventional method, which yields particle size in micron range. Ultrasonic synthesis route also boosts kinetics of polymerization with increase in the yield of nanocomposites. Xia and Wang (2002) synthesized aniline/TiO_2 nanocomposites by ultrasound-assisted in-situ emulsion polymerization. Authors reported that aggregation of nano-TiO_2 in aqueous solution can be reduced drastically under sonication, and polymerization of aniline occurred over the surface of the crystalline TiO_2 nanoparticles resulting in core-shell structure. Ultrasonically synthesized polyaniline/TiO_2 nanocomposites possessed higher electrical conductivity than nanocomposites synthesized with mechanical stirring.

1.4.3 Polymer graphene nanocomposites

As noted earlier, the carbon-based materials form new potential filler materials for nanocomposite synthesis due to their exceptional properties.

Among carbon-based materials, although carbon nanotubes (CNTs) show comparable mechanical properties compared to graphene, still graphene, the latter is better nanofiller than

former for certain aspects/facets of nanocomposites, such as thermal and electrical conductivity. The improvement in physicochemical properties of the nanocomposites depends on distribution of graphene layers in the polymer matrix as well as interfacial bonding between graphene layers and polymer matrix. However, it is very difficult to disperse nanoscale graphene in the polymer emulsion through mechanical agitation due to its high surface energy, strong van der Waals interaction and low interface affinity toward polymer. To overcome these issues, ultrasound-assisted in-situ emulsion polymerization can be used for synthesis of polymer/CNTs composites. Markovic et al. (2006) have reported ultrasound-assisted synthesis of PANI/MWNTs nanocomposites by in-situ emulsion polymerization. Authors concluded that use of ultrasound irradiation ensures dispersion of the CNTs in aqueous solution without agglomeration during emulsion polymerization. The resulting nanocomposites showed enhanced electric conductivity and thermal stability as compare to neat PANI. Zelikman et al. (2010) and Suckeveriene et al. (2011) have used ultrasound-assisted in-situ dynamic inverse emulsion polymerization technique for the synthesis of PANI/MWNT nanocomposite with toluene as solvent. Both of these studies reported that the PANI coated MWNT could uniformly disperse in toluene (unlike coagulation/settling observed for pristine MWNT). Moreover, PANI/MWNT nanocomposites synthesized with sonication possessed enhanced mechanical properties and electrical conductivity.

1.4.4 Polymer-magnetic particle nanocomposites

Proper encapsulation and uniform dispersion of magnetite particles in the polymer matrix is challenging task in synthesis of polymer/magnetite nanocomposites. Surface modification of magnetite nanoparticles is required for proper dispersion and better compatibility of nanomagnetic material in polymer matrix. Surface modification of magnetic

material is often uneconomical due to requirement of expensive chemicals such as oleic acid and ricinoleic acid. For the synthesis of magnetite nanocomposites, ultrasound-assisted emulsion polymerization is an effective route as it obviates the need for surface modification of the nanofiller prior to nanocomposite synthesis. The previous literature reports uniform dispersion of magnetite nanoparticles in the polymer latex under influence of ultrasound.

Lu et al. (2006) have used ultrasound irradiation (40 kHz, 50 W) for the synthesis of polyaniline/Fe_3O_4 nanotubes with average particle size of resulting nanocomposites in the range of 100 nm. Qiu et al. (2007) have prepared polystyrene/Fe_3O_4 nanocomposite using sonication at frequency of 20 kHz. The polystyrene latex particles prepared in the presence of Fe_3O_4 nanoparticles were spherical in nature with size range of 20-80 nm. Mahdavian et al. (2008) used sonication of 35 kHz for the synthesis of poly (butyl acrylate–styrene)/Fe_3O_4 nanocomposites. In this study, the authors modified surface of iron oxide nanoparticles with surface modifying agent such as oleic acid. The resultant poly (butyl acrylate–styrene)/Fe_3O_4 nanocomposite showed core–shell morphology with well-dispersed hydrophobic nano-magnetite particles as core in polymeric shell. Gyergyek et al. (2010) have synthesized superparamagnetic PMMA/Fe_2O_3 nanocomposite using mini-emulsion polymerization. In this study, Gyergyek et al. (2010) initially dispersed relatively large loading (39 wt%) of magnetic iron-oxide nanoparticles in the reaction medium, followed by polymerization with mechanical agitation. The resultant PMMA/Fe_2O_3 nanocomposites had high content of iron oxide nanoparticles in the core with polymer shell (without particles) surrounding it. Gyergyek et al. (2010) have commented that in such morphology of nanocomposites, the iron oxide particles are well protected by the surface layer of the polymer.

1.5 Aim, scope and structure of the present thesis

Ultrasound-assisted in-situ emulsion polymerization is a well-known and well-studied technique for synthesis of numerous polymers and co-polymers. Previous papers from our group (Morya et al., 2008; Kanmuri and Moholkar, 2010) have provided mechanistic insight into this process by coupling experimental results with simulations of cavitation bubble dynamics. These studies have essentially concluded that beneficial effect of ultrasound and cavitation on emulsion co-polymerization system is of physical nature. Strong microturbulence generated in the reaction medium creates fine emulsification between aqueous and organic phases that boosts the kinetics of the reaction several fold. Use of ultrasound during emulsion polymerization has special relevance from view point of synthesis of nanocomposites. In this case, the role of ultrasound and cavitation is two-fold, viz. generation of fine emulsion and effective encapsulation/dispersion of the nanofiller material in the polymer matrix. Literature on ultrasound-assisted nanocomposite synthesis is also sizeable. However, most of this literature has black-box approach in that more emphasis is given on characterization of the nanocomposite than identifying mechanistic links between physical/chemical effects of cavitation/sonochemistry and the intrinsic chemistry of the process.

In the present thesis, we have attempted to give mechanistic accounts of ultrasonic synthesis of polymer nanocomposites. The model system that we have used is Polymethyl methacrylate as the base polymer and four different nanofillers, viz. Cloisite 30B clay, zinc oxide, reduced graphene oxide and iron oxide (or magnetite). Except for the clay, the other nanofillers have also been in-house synthesized using sonication. The experimental parameters have been optimized using statistical design of experiments. Variation in different physical properties (mechanical/ thermal/ electrical/ magnetic/ optical) of the nanocomposites has been mapped as a function of the loading of the nanofiller. The results have been

analyzed vis-à-vis the experimental conditions. The analysis of these studies has provided an insight into the inter-relation between properties of the nanocomposites and the properties of polymer and nanofiller in pristine form. Comparison of these properties with previous literature employing mechanical agitation has given a quantitative account of the enhancement in physical properties induced by sonication.

The thesis comprises of 6 chapters, the contents of which are as follows:

- Chapter 2 reports mechanistic insight into the influence of ultrasound and cavitation in synthesis of polymethyl methacrylate (PMMA) and its nanocomposite using the organo-modified Cloisite 30B clay. A statistical design of experiments (Central Composite Design with Response Surface Methodology) has been used to find optimum values of experimental parameters. The nanocomposites have been characterized for mechanical and thermal properties.
- Chapter 3 reports two-step ultrasonic method for in-situ synthesis of PMMA/ZnO nanocomposites. First step comprises nanoscale ZnO synthesis through ultrasound-assisted in-situ hydrolysis of zinc acetate. In second step, PMMA/ZnO nanocomposites have been synthesized via ultrasound-assisted in-situ emulsion polymerization in presence of native ZnO particles. ZnO loading has been varied in range of 1-5 wt%, and the effect of this parameter on the physical properties of the resultant PMMA/ZnO nanocomposites (especially optical, electrical and thermal properties) has been quantified and analyzed.
- Chapter 4 reports ultrasound–assisted synthesis of polymethyl methacrylate (PMMA) /reduced graphene oxide (RGO) nanocomposites by in–situ emulsion polymerization coupled with in–situ reduction of graphene oxide. The nanocomposites have been characterized for physical properties. The thermal degradation kinetics of the nanocomposites has also been assessed with common methods. It has been revealed

that RGO nanofiller gives significant enhancement in all physical properties of the nanocomposite at relatively much smaller concentrations than other nanofillers. These nanocomposites have been characterized for thermal, mechanical, electrical, and EMI shielding properties. Significant enhancement in physical properties, as compared to the previous literature, at low RGO loadings is attributed to uniform dispersion of RGO in PMMA matrix under sonication.

- Chapter 5 has treated synthesis of Poly(methyl methacrylate)/magnetite (PMMA/Fe_3O_4) nanocomposites with a two–step technique involving sonication. Initially, Fe_3O_4 nanoparticles have been synthesized by ultrasound–assisted co–precipitation, followed by synthesis of PMMA/Fe_3O_4 nanocomposites via ultrasound–assisted in–situ emulsion polymerization with varying Fe_3O_4 loadings. Incorporation of magnetite nanoparticles in PMMA matrix not only enhanced the thermal and mechanical properties, but also imparted excellent magnetic properties to the nanocomposite in terms of coercivity, magnetic saturation and magnetic remanence. These nanocomposites also possessed good electromagnetic interference shielding properties.
- Chapter 6 presents an overview of results of synthesis / characterization of four types of PMMA nanocomposites reported in preceding chapters. An analysis is presented as how the intrinsic properties of the nanofiller are reflected in terms of physical properties of the nanocomposites. Four nanofillers used in this thesis research, viz. organo-modified clay, zinc oxide, reduced graphene oxide and iron oxide (or magnetite), have been compared on the basis of their intrinsic properties and the properties of the PMMA nanocomposites using these fillers. Some recommendations for further research in the area of ultrasound-assisted synthesis of nanocomposites have also been given.

We would like to specifically mention that the review and analysis of the published literature in synthesis/characterization of each type of nanocomposite has been given in the corresponding chapter – prior to materials and methods section. We believe that such an approach for presentation of literature review would be more convenient that a separate chapter with collective literature review for all nanocomposites.

References

Aizawa T, Souda R, Otani S, Ishizawa Y, Oshima C, Anomalous bond of monolayer graphite on transition metal carbide surfaces, Phys. Rev. Lett. 64 (1990) 768–771.

Aldosari MA, Othman AA, Alsharaeh EH, Synthesis and characterization of the in situ bulk polymerization of PMMA containing graphene sheets using microwave irradiation, Molecules 18 (2013) 3152–3167.

Ayyappan S, Philip J, Raj B, Solvent polarity effect on physical properties of Co-Fe_2O_3 nanoparticles, J. Phys. Chem. C. 113 (2009) 590–596.

Bach LG, Islam MDR, Kim JT, Seo SY, Lim KT, Encapsulation of Fe_3O_4 magnetic nanoparticles with poly(methyl methacrylate) via surface functionalized thiol-lactam initiated radical polymerization. App. Surf. Sci. 258 (2012) 2959–2966.

Barkade SS, Naik JB, Sonawane SH, Ultrasound assisted miniemulsion synthesis of polyaniline/Ag nanocomposite and its application for ethanol vapor sensing, Colloids Surf. A. 378 (2011) 94–99.

Basedow AM., Ebert KH, Ultrasonic degradation of polymers in solution. In: Physical Chemistry (Series: Advances in Polymer Science), Springer, Berlin, Heidelberg, Vol. 22, PP. 83-148, 1977.

Berger C, Song Z, Li X, Wu X, Brown N, Naud C, et al., Electronic confinement and coherence in patterned epitaxial graphene, Science 312 (2006) 1191–1196.

Beyer G, Nanocomposites: a new class of flame retardants for polymers, Plast Addit. Compound 2002 4:22–28.

Bhanvase BA, Sonawane SH, New approach for simultaneous enhancement of anticorrosive and mechanical properties of coatings: Application of water repellent nano $CaCO_3$–PANI emulsion nanocomposite in alkyd resin, Chem. Eng. J. 156 (2010) 177–183.

Borthakur LJ, Das D, Dolui SK, Development of core–shell nano composite of poly (styrene-co-methyl acrylate) and bentonite clay by ultrasonic assisted mini-emulsion polymerization, Mater. Chem. Phys. 124 (2010) 1182–1187.

Boyes SG, Akgun B, Brittain WJ, Foster MD, Synthesis, characterization, and properties of polyelectrolyte block copolymer brushes prepared by atom transfer radical polymerization and their use in the synthesis of metal nanoparticles, Macromolecules, 36 (2003) 9539–9548.

Carrado, KA, Synthetic organo-and polymer-clays: preparation, characterization, and materials applications, Appl. Clay Sci. 17 (2000). 1–23.

Chakraborty S, Kumar M, Suresh K, Pugazhenthi G, Influence of organically modified Ni–Al layered double hydroxide (LDH) loading on the rheological properties of poly (methyl methacrylate) (PMMA)/LDH blend solution, Powder Technol. 256 (2014) 196–203.

Dainton, FS, On the existence of free atoms and radicals in water and aqueous solutions subjected to ionizing radiation, J. Phys. Chem, 52 (3) (1948). 490–517.

Demir MM, Gulgun MA, Menceloglu YZ, Erman B, Abramchuk SS, Makhaeva EE, et al., Palladium Nanoparticles by Electrospinning from Poly(acrylonitrile-co-acrylic acid)−$PdCl_2$ Solutions, Relations between preparation conditions, particle Size, and catalytic activity, Macromolecules, 37 (2004) 1787–1792.

Delamarche E, Geissler M, Vichiconti J, Graham WS, Andry PA, Flake JC, et al., Electroless deposition of NiB on 15 inch glass substrates for the fabrication of transistor gates for liquid crystal displays, Langmuir 19 (2003) 5923–5935.

Dos DS, Santos J, Goulet PJG, Pieczonka NPW, Oliveira ON, Aroca RF, Gold nanoparticle embedded, self-sustained chitosan films as substrates for surface-enhanced Raman scattering. Langmuir, 20 (2004) 10273–10277.

Eizenberg M, Blakely JM, Carbon monolayer phase condensation on Ni(III), Surf. Sci. 82 (1979) 228–236.

Flesch C, Delaite P, Dumas Bourgeat-Lami E, Duguet E, Grafting of poly (ε -caprolactone) onto maghemite nanoparticles, J. Polym. Polym. Chem. 42 (2004) 6011–6020.

Gnanaprakash G, Ayyappan S, Jayakumar T, Philip J, Raj B, A simple method to produce magnetic nanoparticles with enhanced alpha to gamma-Fe_2O_3 phase transition temperature, Nanotechnology 17 (2006) 5851–5857.

Gyergyek S, Makovec D, Mertelj A, Huskic M, Drofenik M, Superparamagnetic nanocomposite particles synthesized using the mini-emulsion technique, Colloids Surf. A 366 (2010) 113–119.

Haes AJ, Zou S, Schatz GC, Duyne RP, Nanoscale optical biosensor: short range distance dependence of the localized surface plasmon resonance of noble metal nanoparticles, J. Phys. Chem. B.108 (2004) 6961–6968.

Hong RY, Qian JZ, Cao JX, Synthesis and characterization of PMMA grafted ZnO nanoparticles, Powder Technol. 163 (2006) 160–168.

Hu H, Wang X, Wang J, Wan Li, Liu F, Zheng H, Chen R, Xu C, Preparation and properties of graphene nanosheets-polystyrene nanocomposites via in situ emulsion polymerization, Chem. Phys. Lett. 484 (2010) 247–253.

Kango S, Kalia S, Celli A, Njuguna J, Habibi Y, Kumar R, Surface modification of inorganic nanoparticles for development of organic–inorganic nanocomposites—a review. Prog. Polym. Sci. 38 (2013) 1232–1261.

Kanmuri S, Moholkar VS, Mechanistic aspects of sonochemical copolymerization of butyl acrylate and methyl methacrylate, Polymer 51 (2010) 3249–326.

Khatana S, Dhibar AK, Ray SS, Khatua BB, Use of pristine clay platelets as a suspension stabilizer for the synthesis of poly(methyl methacrylate)/clay nanocomposites, Macromol. Chem. Physic. 210 (2009), 1104–1113.

Kim SK, Kim NH, Lee JH, Effects of the addition of multiwalled carbon nanotubes on the positive temperature coefficient characteristics of carbon-black-filled high density polyethylene nanocomposites, Scripta. Mater. 55 (2006) 1119–1122.

Kim H, Kobayashi S, Abdurrahim MA, Zhang MJ, Khusainova A, Hillmyer MA, Abdala AA, Macosko CW, Graphene/polyethylene nanocomposites: Effect of polyethylene functionalization and blending methods, Polymer 52 (2011) 1837–1846.

Klabunde KJ, Habdas J, Cardenas V, Colloidal metal particles dispersed in monomeric and polymeric styrene and methyl methacrylate, Chem. Mater.1 (1989) 481–483.

Kruus, P, Polymerization resulting from ultrasonic cavitation, Ultrasonics 21.5 (1983) 201–204.

Kruus P, Patraboy TJ, Initiation of polymerization with ultrasound in methyl methacrylate, J. Phys.Chem. 89 (1985) 3379–3384.

Kruus P, Lawrie JAG, Neill MLO, Polymerization and depolymerization by ultrasound, Ultrasonic 26 (1988) 352–355.

Kuila T, Bose S, Khanra P, Kim NH, Rhee, KY, Lee, JH, Characterization and properties of in situ emulsion polymerized poly(methyl methacrylate)/graphene nanocomposites, Compos. Part A. 42 (2011) 1856–1861.

Lan T, Kaviratna PD, Pinnavaia TJ, Mechanism of Clay Tactoid Exfoliation in Epoxy-Clay Nanocomposites, Chem. Mater. 7 (1995) 2144–2150.

Liu P, Wang T, Poly(hydroethyl acrylate) grafted from ZnO nanoparticles via surface-initiated atom transfer radical polymerization, Current Applied Physics, 8 (2008) 66–70.

Lindstorm O, Lamm O, The chemical effect produced by ultrasonic waves, J. Phys. Colloid Chem. 55 (7) (1951) 1139–1146.

Li Jing, Jang K, Man LS, Conductive graphite nanoplatelet/epoxy nanocomposites: effects of exfoliation and UV/ozone treatment of graphite, Scripta. Mater. 53 (2005) 235-240.

Lee EC, Mielewski DF, Baird RJ, Exfoliation and dispersion enhancement in polypropylene nanocomposites by in-situ melt phase ultrasonication, Polym. Eng. Sci. 44 (2004) 1773–1782.

Lu X, Mao H, Chao D, Zhang W, Wei Y, Ultrasonic synthesis of polyaniline nanotubes containing Fe_3O_4 nanoparticles, J. Solid State Chem. 179 (2006) 2609–2615.

Ma SR, Shi LY, Feng X, Yu WJ, Lu B, Graft modification of ZnO nanoparticles with silane coupling agent KH570 in mixed solvent, J. Shanghai University12 (2008) 278–282.

Mahdavian AR, Sehri Y, Mobarakeh HS, Nanocomposite particles with core–shell morphology II. An investigation into the affecting parameters on preparation of Fe_3O_4-poly(butyl acrylate–styrene) particles via miniemulsion polymerization, Eur. Polym. J. 44 (2008) 2482–248

Mallakpour S, Barati A, Efficient preparation of hybrid nanocomposite coatings based on poly(vinyl alcohol) and silane coupling agent modified TiO_2 nanoparticles, Progress in Organic Coatings,71 (2011) 391–398.

Markovic MG, Matisons JG, Cervini R, Simon GP, Fredericks PM, Synthesis of new polyaniline/nanotube composites using ultrasonically initiated emulsion polymerization, Chem. Mater. 18 (2006) 6258–6265.

Mibhele ZH, Salemane MG, Sittert CGCE, Nedeljkovic JM, Djokovic V, Luyt AS, Fabrication and characterization of silver−polyvinyl alcohol nanocomposites, Chem. Mater.15 (2003) 5019–5024.

Morya NK, Iyer PK, Moholkar VS, A physical insight into sonochemical emulsion

polymerization with cavitation bubble dynamics, Polymer 49 (2008) 1910–1925.

Moussaif N, Groeninckx G, Nanocomposites based on layered silicate and miscible PVDF/PMMA blends: melt preparation, nanophase morphology and rheological behaviour, Polymer 44 (2003) 7899–7906.

Novoselov KS, Geim AK, Morozov SV, Jiang D, Zhang Y, Dubonos SV, et al., Electric field effect in atomically thin carbon films, Science 306 (2004) 666–669.

Ozgur U, Alivov YI, Liu C, Teke A, Reshchikov MA, Dogan S, Avrutin V, Cho SJ, Morkoç H, A comprehensive review of ZnO materials and devices, J. App. Phys. 98 (2005) 041301.

Park S, Ruoff RS, Chemical methods for the production of graphenes, Nat. Nanotechnol. 4 (2009) 217−224.

Qiu G, Wang Q, Wang C, Lau W, Guo Y, Polystyrene/Fe_3O_4 magnetic emulsion and nanocomposite prepared by ultrasonically initiated miniemulsion polymerization, Ultrason. Sonochem. 14 (2007) 55–61.

Rong MZ, Ji QL, Zhang MQ, Friedrich K, Graft polymerization of vinyl monomers onto nanosized alumina particles, Eur. Polym. J. 38 (2002) 1573–1582.

Safadi B, Andrews R, Grulke EA, Multiwalled carbon nanotube polymer composites: synthesis and characterization of thin films, J. Appl. Polym. Sci. 84 (2002) 2660–2669.

Sivakumar M, Gedanken A, A sonochemical method for the synthesis of polyaniline and Au-polyaniline composites using H_2O_2 for enhancing rate and yield, Synth. Met. 148 (2005) 301–306.

Swain SK, Isayev AI, Effect of ultrasound on HDPE/clay nanocomposites: Rheology, structure and properties. Polymer 48 (2007) 281–289.

Suckeveriene RY, Zelikman E, Mechrez G, Tzur A, Frisman I, Cohen Y, Narkis M, Synthesis of hybrid polyaniline/carbon nanotube nanocomposites by dynamic interfacial

inverse emulsion polymerization under sonication, J. Appl. Polym. Sci. 120 (2011) 676–682.

Tabata M, Miyazawa T, Kobayashi O. Sohma J, Direct evidence of main-chain scissions induced by ultrasonic irradiation of benzene solutions of polymers, Chem. Phys. Lett. 73 (1980) 178–180.

Tang E, Cheng G, Pang X, Ma X, Xing F, Synthesis of nano-ZnO/poly(methyl methacrylate) composite microsphere through emulsion polymerization and its UV-shielding property, Colloid Polym. Sci. 284 (2006a) 422–428.

Tang E, Cheng G, Ma X, Preparation of nano-ZnO/PMMA composite particles via grafting of the copolymer onto the surface of zinc oxide nanoparticles, Powder Technol. 161 (2006b) 209–214.

Truong LT, Larsen A, Holme B, Diplas S, Hansen FK, Roots J, Jorgensen, S, Dispersibility of silane-functionalized alumina nanoparticles in syndiotactic polypropylene, Surf Interface Anal. 42 (2010) 1046–1049.

Wang S, Hu Y, Zhongkai Q, Wang Z, Chen Z, Fan W, Preparation and flammability properties of polyethylene/clay nanocomposites by melt intercalation method from Na^+ montmorillonite, Mater. Lett. 57 (2003) 2675–2678.

Wang GA, Wang CC, Chen CY, The disorderly exfoliated LDHs/PMMA nanocomposites synthesized by in situ bulk polymerization, Polymer 46 (2005) 2443–2450.

Wang C, Yan J, Cui X, Cong D, Wang H, Preparation and characterization of magnetic hollow PMMA nanospheres via in situ emulsion polymerization, Colloids Surfaces A Physicochem. Eng. Asp. 363 (2010) 71–77.

Wu CS, Kao TH, Li HY, Liu YL, Preparation of polybenzoxazine-functionalized Fe_3O_4 nanoparticles through in situ Diels-Alder polymerization for high performance magnetic polybenzoxazine/Fe_3O_4 nanocomposites, Compos. Sci. Technol. 72 (2012) 1562–1567. (2012).

Xia H, Wang Q, Ultrasonic irradiation: a novel approach to prepare conductive polyaniline/nanocrystalline titanium oxide composites, Chem. Mater. 14 (2002) 2158–2165.

Xu GC, Xiong JY, Ji XL, Wang YL, Synthesis of nanosilver/PMMA composites via ultrasonically bi-in situ emulsion polymerization, J. Thermoplast. Compos. 20 (2007) 523–533.

Yan D, Xu L, Chen C, Tang J, Ji X, Li Z, Enhanced mechanical and thermal properties of rigid polyurethane foam composites containing graphene nanosheets and carbon nanotubes, Polym. Int. 61 (2012) 1107–1114.

Yoda S, Hasegawa A, Suda H, Uchimaru Y, Haraya K, Tsuji T, et al., Preparation of a platinum and Palladium/Polyimide Nanocomposite Film as a Precursor of Metal-Doped Carbon Molecular Sieve Membrane via Supercritical Impregnation, Chem. Mater. 16 (2004) 2363–2368.

Zhang L, Li F, Chen Y, Wang X, Synthesis of transparent ZnO/PMMA nanocomposite films through free-radical copolymerization of asymmetric zinc methacrylate acetate and in-situ thermal decomposition, J. Lumin. 131 (2011) 1701–1706.

Zhang Y, Zhuang S, Xu, X, Hu, J, Transparent and UV-shielding ZnO@PMMA nanocomposite films, Opt. Mater. 36 (2013) 169–172.

Zhang Y, Li M, Yang L, Yi K, Li Z,Yao J, Facilely prepared polypyrrole-graphene oxide-sodium dodecylbenzene sulfonate nanocomposites by in situ emulsion polymerization for high-performance supercapacitor electrodes, J. Solid State Electrochem. 18 (2014) 2139–2147.

Zelikman E, Suckeveriene RY, Mechrez G, Narkis M, Fabrication of composite polyaniline/CNT nanofibers using an ultrasonically assisted dynamic inverse emulsion polymerization technique, Polym. Adv. Technol. 21 (2010) 150–152.

CHAPTER 2

SONOCHEMICAL SYNTHESIS OF PMMA/CLOISITE 30B NANOCOMPOSITES: A MECHANISTIC INVESTIGATION

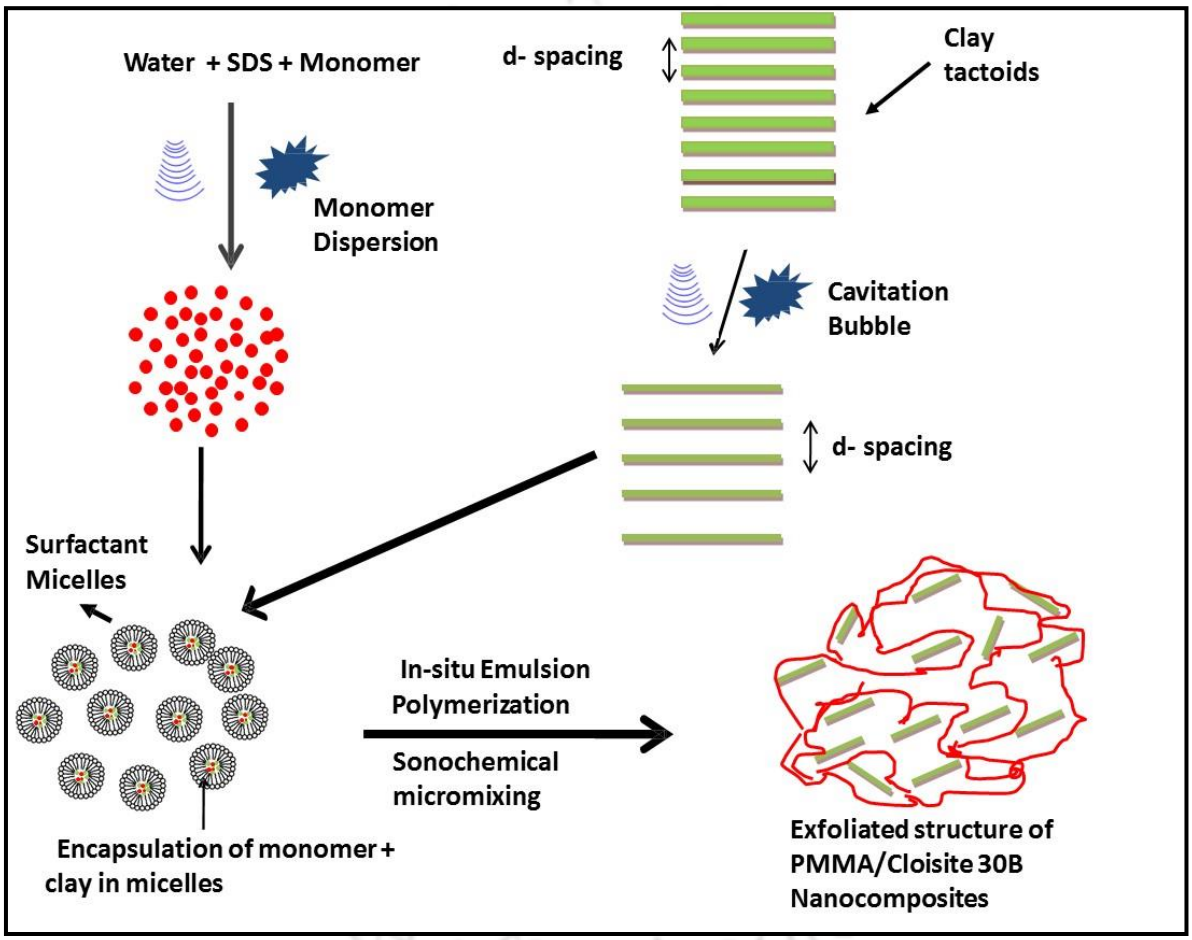

CHAPTER 2

Sonochemical Synthesis of PMMA/Cloisite 30B Nanocomposites: A Mechanistic Investigation

2.1 Introduction

Polymer nanocomposites are modern age materials that have remarkable combination of physical and mechanical properties as compared to the conventional polymer and metals. As noted in previous chapter, the nanoclays have attracted special attention as nanoscale filler material due to marked enhancement in properties of the original polymer. The polymer clay nanocomposites have been found to have better mechanical properties, barrier properties, thermal stability and flame retardance than the original polymer (Borthakur et al., 2010; Zelikman et al., 2010). Polymer clay nanocomposites have found applications in automobile, aerospace, packaging coating and rubber industries. The clays of smectite family that have layered silicate structure have been widely used for as fillers in nanocomposites. For proper incorporation of clay into the hydrophobic polymer matrix, the surface of clay need to be modified by replacing naturally occurring cations (which impart hydrophilic character to clay) by large organic cations. A major problem in synthesis of polymer nanocomposites is uniform dispersion of layered clay into the polymer matrix with complete exfoliation. The

organo–modification of the surfaces of clay platelets increases their compatibility with monomer, and also helps catalyzing polymerization from within monomer saturated tactoids Bhanvase et al., 2012). This helps in exfoliation of the silicate layers or platelets. Another mean of achieving exfoliation of the clay platelets is to subject the clay to high mechanical shear (Delozier et al., 2002). This could be achieved by strong agitation of clay suspension in suitable liquid. The shear generated by convection in the liquid causes widening of the galleries of the layered silicates. The convection generated by ultrasound also causes intercalation of the monomer or monomer swollen micelles (if surfactant is also added to the solution) into the silicate layers or platelets. The radical generated through initiator added to mixture polymerizes the intercalated monomer which further widen the *d*–spacing of the nanocomposites giving exfoliated structure (Bhanvase et al., 2011; Bhanvase et al., 2012).

Ultrasound assisted synthesis of polymer nanocomposites is a research area of intense activity. Ultrasound and its secondary effect cavitation are known to have several physical and chemical effects, which are beneficial towards the intensification of polymerization. Among various nanocomposites synthesized with ultrasound, PMMA–clay nanocomposites have been popular due to marked enhancement in physical and mechanical properties, as noted earlier. Several authors have studied synthesis of PMMA/clay nanocomposites using different methodologies. A summary of the previous literature on synthesis of PMMA/clay nanocomposites using different techniques is given in Table 2.1. Literature on ultrasound–assisted synthesis of PMMA/clay nanocomposite is limited. However, there are several papers that have treated the subject of ultrasonic polymerization of pristine PMMA (Chou and Stoffer, 1999; Bradley and Gieser, 2002; Bhanvase et al., 2012). Although the physical mechanism of ultrasound assisted polymer nanocomposite is broadly understood in following terms: (1) intense micro mixing generated by ultrasound and cavitation causes good dispersion of the particles or intercalation of hydrophobic polymer into hydrophilic silicate

layers or shear induced separation of silicate layers, and (2) polymerization of the monomer either in presence or absence in external initiator induced by radicals produced from transient cavitation, the exact links between polymerization chemistry and physics of cavitation bubble dynamics are not clearly established. In our previous papers, (Morya et al., 2008; Kanmuri and Moholkar, 2010) we have tried to explore the links between cavitation physics and polymerization chemistry for synthesis of homopolymer (butyl acrylate and vinyl acetate) and copolymer (butyl acrylate and methyl methacrylate). Our approach has been to couple the experimental results with the simulations of cavitation bubble dynamics. In this chapter, we have extended this theme for the synthesis of PMMA–montmorillonite clay (organo–modified version Cloisite 30B) nanocomposite. The approach used in this work is that of statistical experimental design with response surface methodology with extent of monomer conversion as the response. The results of statistical experimental design have been explained on the basis of known concepts of physics of cavitation bubble dynamics.

Table 2.1: Summary of literature on Polymethyl methacrylate (PMMA)/clay nanocomposites

Reference	Types of Filler material & polymerization	Experimental Conditions	Major Findings and Conclusions
Zhu et al. (2002)	PMMA/organo–clay (three different types hexadecyl allyl dimethyl ammonium chloride (Ally116), hexadecyl vinyl benzyl dimethyl ammonium chloride (VB16) & hexadecyl vinyl benzyl dimethyl ammonium chloride (Bz16) Bulk polymerization method	MMA/clay = 100 g/ 3 g, AIBN = 1 g, temprature = 60°–80°C, reaction time = 24 h with stirring	Clay with double bond give an exfoliated material while saturated clay shows intercalated; VB16 nanocomposite had higher *d*–spacing as compare to the Ally116 and Bz 16
Ryu et al. (2004)	PMMA/clay (cloisite 10 A, cloisite 20A) Two step process .1st step involve In situ free radical polymerization of MMA with clay & 2nd step PMMA melt mix with product of the 1st step	Combined with US and mechanical stirring based process; clay = 3 wt%, sonication = 10 min, AIBN = 0.1 phr (Parts per hundred), melt mixing temp = 230°C, rotor speed = 120 rpm, mixing time = 20 min	Highly exfoliated structure due to effect of US. 60 ~ 70°C increase in thermal decomposition temp as compare to pure PMMA; complex viscosity increase of PMMA/clay nanocomposite) by ultrasound technique as compare to without ultrasound.
Wang et al (2005)	PMMA/clay (modified by cationic surfactants).	Clay = 3 g, AIBN =1 g, MMA = 100 g, magnetic stirring, T = 60°C, time = 24 h	At $T_{10\%}$ wt loss PMMA/clay stability is higher as compared to $T_{5\%}$ wt loss. Dielectric properties decreased with formation of nanocomposite. PMMA/clay also resulted in increase in ignition temperature
Zhao et al. (2006)	PMMA /PDMS (Polydimethylsiloxane) clay and polystyrene (PS) / PDMS/clay nanocomposite In–situ polymerization in presence of supercritical CO_2	PMMA synthesis: T = 65°C, P = 241 bar, magnetic stirring, MMA =0.5 ml, 6 % PDMS–clay, AIBN (Azobisisobutyronitrile) = 0.6 wt%, time = 48 h	PDMS and supercritical CO_2 act as stabilizing agents for nanocomposites which enhance thermal stability of PMMA/clay up to 19 °C
Unnikrishnan et al. (2011)	PMMA/organo–clay; melt intercalation process	PMMA/clay (loading 3 and 5 wt %) Processing temperature = 180°C, Rotor speed = 50 rpm, mixing time = 30 min	Maleic anhydride used as a compatibilizer Thermal stability increased by 16–17°C Relatively small (Glass transition temperature) (T_g) increase by 2–4°C
Jung et al. (2012)	PMMA/ Organo clay (Cloisite 15A and Cloisite 30B); Solvent blending including supercritical process	T = 70°C, P = 350 bar, reaction time = 1 h, mechanical stirring, ultrasound (US)	Better intercalation with Cloisite 30 B than Cloisite 15 A; Enhanced thermal stability of the nanocomposite for ultrasound assisted process

Table 2.1 (continued.....)

Reference	Types of Filler material & polymerization	Experimental Conditions	Major Findings and Conclusions
Dhibar et al. (2012)	Polycarbonate (PC) and poly(methyl methacrylate)/ clay melt blending and *in–situ* suspension	PC/ PMMA used as 80/20 wt % in blending; T = 280^{o}C during melt mixing	The surface morphologies studied by Scanning Electron Microscope (SEM); Optical transparency of nanocomposite decreased with loading of clay.
Patra et al. (2012)	PMMA/clay(Cloisite 93A) Ultrasound (US) assisted emulsifier free emulsion polymerization techniques followed by mechanical stirring.	Clay (1, 2 & 3 wt%), KPS = 0.1 M, temp = 60^{o}C, Different power and frequency of US (10 min, 120W / 80 kHz, 120 W / 60 kHz, 80 W / 80kHz), total stirring time = 21 h	Ultrasound result partial exfoliated structure. Oxygen permeability reduced by 17% & LOI Increased about 31 % of PMMA/clay. Young modulus up to (400 MPa), Toughness (258 MPa), yield stress (19.98 MPa) as compared to pristine PMMA.
Tsai et al. (2013)	PMMA/O–MMT (organo–modified Montmorillonite clay) (CL–42, CL–120, CL–88); In–situ free radical polymerization in toluene	MMA/ O–MMT = 9.5 g / 0.5 g, toluene solvent, BPO (Benzoyl peroxide) used as an initiator, ~ 12 h stirring at 25^{o}C, polymerization temperature = 75^{o}C, polymerization time = 5 h	Increased in *d*–spacing of three different clays from 1.24, 1.53 and 1.48 nm to 4.10, 4.09 and 4.05, respectively; PMMA/clay nanocomposites exhibit higher optical UV (Ultraviolet) transmission (87%) and improved thermal stability and gas barrier properties.
Biswal et al. (2015)	PMMA/clay (using one unmodified MMT clay and three different modified MMT clay such as dellite 67G, Nanofill SE 3010 and Cloisite 11B	Polymerization temperature =70^{o}C, microwave irradiation = 40W, Polymerization time = 2 h	Delaminated or intercalated structure for all nanocomposites. All nanocomposites showed 20^{o}C enhancement in thermal decomposition temperature as compare to neat PMMA. PMMA/Nanofill SE 3010 exhibited highest reduction in gas permeability of 27%.
Lerari et al. (2015)	PMMA/clay with various loading of 1, 3 and 5 wt% by in house modification of the natural MMA clay into OMMT using HDTMA (hexadecyl trimethyl ammonium bromide). In situ bulk polymerization	Polymerization was done with combined effect of mechanically stirring followed by ultrasound (75 Hz). Polymerization temperature =80^{o}C. Polymerization time = 4h	The modified PMMA/clay nanocomposites showed higher *d*- spacing as compare to the unmodified one. Use of ultrasound enhanced the thermal stability of resulting PMMA/clay nanocomposites.

2.2 Experimental

2.2.1 Materials

Following chemical have been used in this experiments: Methyl methacrylate (MMA, GR grade) was procured from Hi–Media India Ltd. Organically modified clay, Cloisite 30B, were procured from Southern Clay Products, Inc. (USA). The surfactant, sodium dodecyl sulfate (SDS, AR grade) and potassium persulfate ($K_2S_2O_8$, AR grade) were purchased from Merck India Ltd. Prior to polymerization experiments, the inhibitor in MMA monomer was removed by adsorption. The monomer was filtered several times through a bed of neutral alumina powder to remove the inhibitors present in the monomer.

2.2.2 Experimental setup

Polymerization reactions were carried out in a reactor fabricated from SS–319. A schematic of the reactor is shown in Fig. 2.1. The dimensions of the polymerization reactor were: height 70 mm, inner diameter of jacket 65 mm, and reactor thickness 2 mm. The reactor had an outer jacket through which water was circulated to maintain the temperature of the reaction mixture at desired value during polymerization reaction. The reactor had a probe type microprocessor controlled programmable ultrasound processor (Sonics and Materials Inc., Model: VCX 500). This processor had a frequency of 20 kHz with maximum theoretical power rating of 500 W. The sonicator probe was fabricated from titanium alloy with grade Ti–6A1–4V, and had a diameter of 25 mm. The processor was operated at 40% of the maximum power, i.e. 200 W. The actual power input to the reaction mixture was determined using calorimetric technique (Sivasankar et al., 2007, Kanmuri et al., 2010). The acoustic pressure amplitude corresponding to this power input was 1.8 bar. This acoustic pressure amplitude is sufficient to create transient cavitation in the medium. At even higher power level, excessive cavitation gives rise to cloud of bubbles at the sonicator probe tip, which

decouples the probe surface from liquid and hinders effective power delivery to the reaction system.

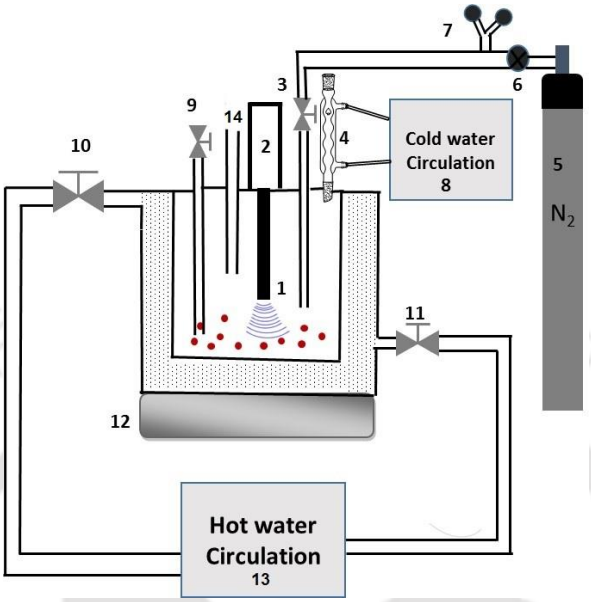

Figure 2.1: A schematic diagram of experimental set up of synthesis of polymer nanocomposites (1) ultrasound probe (2) ultrasonic generator (3) valve to control nitrogen flow (4) reflux condenser (5) nitrogen gas cylinder (6) two stage regulator to control the pressure (7) gauge pressure (8) cold water circulation tank (9) sample collecting point (10) hot water outlet valve (11) hot water inlet valve (12) supporting base to the reactor (13) hot water circulation tank (14) Nitrogen outlet

2.3 Experimental procedure of synthesis of PMMA

The experimental study was divided in two parts as follows: (1) Optimization of homopolymerization of MMA using statistical design of experiments (DoE) (Response Surface Method or RSM), (2) In–situ emulsion polymerization of MMA along with varying concentrations of Cloisite 30B clay for synthesis of nanocomposites. RSM is a very common and popular technique for optimization. Greater information on this technique can be found in several books (Montgomery 2004, Montgomery and Runger 2007). The sonication of the emulsion polymerization mixture was accomplished using monomer MMA, inorganic initiator potassium persulfate ($K_2S_2O_8$) and anionic surfactant SDS. The total sonication

reaction time was 60 min with continuous sonication. The temperature of the reaction was maintained using hot water circulation at $65^{o} \pm 2^{o}C$. The rate of polymerization (or extent of monomer conversion) was monitored by withdrawal of aliquots of reaction mixture at regular time interval. The monomer conversion was determined using gravimetric technique described by Bradley and Grieser (2002). After completion of the polymerization reaction, the total reaction volume was dried in vacuum oven at $60^{o}C$ for 15 h to remove the moisture and unconverted monomer. The final gross conversion of monomer was also determined by gravimetric technique, as stated earlier. The surfactants present on surface of dried latex particles were removed by washing several times with water followed by vacuum drying. The polymeric film of vacuum dried latex particles were prepared by dissolving these particles in organic solvent (dichloromethane). The solution was poured in a petridish for evaporation of the solvent.

2.4 Optimization of MMA polymerization

The statistical DoE for synthesis of pristine PMMA was based on three independent variables, viz. quantities monomer (MMA) concentration, initiator potassium persulfate (KPS) concentration and surfactant (SDS) in the reaction mixture. The actual values of these variables used for the experimental design for optimization at three levels (viz. –1, 0 and +1) are given in Table 2.2. The actual values of optimization variables were decided on the basis of typical values of similar parameters reported in literature (Borthakur et al., 2010; Bhanvase et al., 2012; Prasad et al., 2013). The different combinations of the values of these parameters (3 factors, 3 levels) for the complete Central Composite Design (CCD) experimental design are shown in Table 2.3 (for greater information on CCD design and its analysis, please refer to Montgomery and Runger (2007). The response variable (% polymerization or monomer conversion) was fitted with a full quadratic model (given in equation 2.1) in order to correlate

it to the experimental parameters or independent variables. This second order polynomial equation including all the interaction terms were used for finding the predicted response (Equation 2.1)

$$X = a_0 + a_1A + a_2B + a_3C + a_{11}A^2 + a_{22}B^2 + a_{33}C^2 + a_{12}AB + a_{13}AC + a_{23}BC \qquad (2.1)$$

Various notations in above equation are as follows: X = response variable (i.e. % polymerization or monomer conversion); a_0 = constant; a_1, a_2, a_3, a_{11}, a_{22}, a_{33}, a_{12}, a_{13}, a_{23} = regression coefficients; A, B, C = coded independent variables (refer to Table 2.2).

Table 2.2: Experimental factors and levels used in CCD

Variables	Symbol	Level		
		(–1)#	**(0)#**	**(+1)#**
Amount of MMA (g)*	A	5	10	15
Amount of KPS (g)*	B	0.03	0.39	0.75
Amount of SDS (g)*	C	0.3	1.65	3.00

* – Values of different variables chosen on the basis of published literature (Morgan and Harris, 2004; Borthakur et al., 2010; Bhanvase et al., 2012; Prasad et al., 2013) # – numbers in the bracket represent coded values of the variables.

2.5 Synthesis of PMMA/Cloisite 30B nanocomposites

The optimized values of the independent variables (surfactant concentration, monomer concentration and initiator concentration) for maximum value of the response (monomer conversion) were determined from the Response Surface Method analysis. The polymer nanocomposites were synthesized using these optimized values of experimental parameters. However, in the synthesis of polymer nanocomposites, an additional factor comes into picture, i.e. the clay concentration in the reaction mixture. The following values of this parameter were used for nanocomposites synthesis (wt% monomer): 1, 2, 4 and 5%. The reaction kinetics of polymer nanocomposites formation was monitored using a similar

gravimetric procedure (as for the pristine polymer, described earlier). The gross monomer conversion was also determined using gravimetric analysis.

2.6 Characterization of PMMA/Cloisite 30B nanocomposites

The latex particles of PMMA and PMMA/Cloisite 30B nanocomposites have been characterized for chemical composition and physical/structural morphology using following techniques. **(1) TEM:** Structural morphology PMMA/Cloisite 30B nanocomposite was assessed Transmission Electron Microscopy (Jeol, Model: JEM 2100). **(2) FTIR:** Fourier Transform Infrared (FTIR) spectra of the latex samples were recorded at room temperature using FTIR spectrophotometer (Shimadzu, Model: IRAffinity–1). **(3) X-Ray Diffraction:** Change in the interlayer *d*-spacing in as-synthesized nanocomposites was analyzed using X-ray diffractograms. Analysis of the as-synthesized nanostructures was carried out in ambient (air) atmosphere using X–ray diffractometer (D8 Advanced, Bruker, equipped with Cu –Kα radiation, λ = 1.54 Å, scan speed = 0.05^{o} s^{-1}) in the range of 2θ = 1–30^{o}. **(4) Particle size distribution and Zeta Potential:** The size distribution and particle stability of neat PMMA and PMMA/Cloisite 30B particles was determined by dynamic light scattering (DLS) instrument (Beckman Coulter, Switzerland; Model Delsa Nano C) **(5) Optical transparency:** Optical transparency of film of dimensions 20 X 20 mm with 0.3 mm thickness of neat PMMA and PMMA/Cloisite 30B nanocomposites was done by using UV– Vis spectrometer (Perkin elmer) in visible light wavelength of 400– 800 nm. **(6) Thermo–gravimetric analysis:** Thermal stability of neat PMMA and its nanocomposite was determined using TGA instrument (NETZSCH TG 209F1 Libra) with heating rate of 10^{o}C/min under nitrogen environment. **(7) Differential scanning calorimeter:** The glass transition temperature of neat PMMA and its nanocomposite was determined using DSC instrument (Metler Toledo–1 series) with heating rate of 10^{o}C/min under nitrogen environment **(8) Tensile strength,**

Young's modulus and percentage elongation: The mechanical properties of the neat PMMA and its nanocomposite were determined with Universal Testing Machine (INSTRON 8801, UK).

Table 2.3: Response surface central composite design and the response (MMA conversion)

Sl. No.	A MMA (g)	B KPS (g)	C SDS (g)	Conversion (%) Experimental	Conversion (%) Fitted by model
1	5 (–1)	0.03 (–1)	3.00 (+1)	50.8 ± 0.65	50.6
2	15 (+1)	0.39 (0)	1.65 (0)	75.3 ± 0.82	74.9
3	10 (0)	0.39 (0)	1.65 (0)	73.5 ± 0.35	73.4
4	15 (+1)	0.75 (+1)	3.00 (+1)	82.6 ± 0.71	82.2
5	10 (0)	0.75 (+1)	1.65 (0)	82.2 ± 0.21	82.6
6	10 (0)	0.39 (0)	3.00 (+1)	68.8 ± 0.47	69.7
7	10 (0)	0.03 (–1)	1.65 (0)	59.5 ± 0.23	58.7
8	10 (0)	0.39 (0)	1.65 (0)	73.2 ± 0.18	73.4
9	15 (+1)	0.75 (+1)	0.3 (–1)	84.5 ± 0.32	84.8
10	10 (0)	0.39 (0)	1.65 (0)	73.1 ± 0.51	73.4
11	15 (+1)	0.03 (–1)	0.3 (–1)	61.1 ± 0.10	61.5
12	5 (–1)	0.75 (+1)	0.3 (–1)	79.5 ± 0.28	79.6
13	5 (–1)	0.39 (0)	1.65 (0)	69.8 ± 0.37	69.8
14	5 (–1)	0.03 (–1)	0.3 (0)	58.1 ± 0.76	58.6
15	15 (+1)	0.03 (–1)	3.00 (+1)	55.5 ± 0.84	55.6
16	10 (0)	0.39 (0)	0.3 (–1)	76.2 ± 0.29	74.9
17	5 (–1)	0.75 (+1)	3.00 (+1)	75.3 ± 0.62	74.9
18	10 (0)	0.39 (0)	1.65 (0)	73.2 ± 0.33	73.4
19	10 (0)	0.39 (0)	1.65 (0)	73.3 ± 0.75	73.4
20	10 (0)	0.39 (0)	1.65 (0)	73.3 ± 0.19	73.4

Note: Total volume of reaction mixture = 60 mL. Numbers in the bracket represent coded values of the variables, while numbers outside bracket represent the actual value of the parameter (refer to Table 2.2).

Table 2.4: Statistical analysis of experimental results

(A) Regression coefficients for quadratic model fitted to CCD experimental design

Term	Coefficient	SE coeff	*t*–Stat	*p*–value
Constant	73.4036	0.2233	328.757	0
MMA (*A*)	2.55	0.2054	12.416	0
KPS (*B*)	11.91	0.2054	57.989	0
SDS (*C*)	–2.64	0.2054	–12.854	0
MMA × MMA (A^2)	–1.0591	0.3917	–2.704	0.022
KPS × KPS (B^2)	–2.7591	0.3917	–7.045	0
SDS × SDS (C^2)	–1.1091	0.3917	–2.832	0.018
MMA × KPS (*AB*)	0.575	0.2296	2.504	0.031
MMA × SDS (*AC*)	0.5	0.2296	2.177	0.054
KPS × SDS (*BC*)	0.85	0.2296	3.702	0.004

(B) Analysis of variance (ANOVA)

Sources	DF	Sq. SS	Adj SS	Adj MS	*F*–value	*p*–value
Regression	9	1656.39	1656.39	184.04	436.30	0
Linear	3	1553.20	1553.20	517.73	1227.36	0
Square	3	92.76	92.76	30.92	73.30	0
Interaction	3	10.42	10.42	3.47	8.24	0.005
Residual Error	10	4.22	4.22	0.42	–	–

Note: R^2 = 99.75%, R^2 (pred) = 98.11%, R^2 (adj) = 99.52%. For greater information on regression coefficients and the ANOVA, please refer to Montgomery and Runger (2007)

2.7 Results and Discussion

2.7.1 Optimization of MMA polymerization

The conversions of MMA achieved in 20 experimental sets of the CCD DoE are indicated in Table 2.3. A quadratic regression model was fitted to the results using coded values for the experimental parameters (Minitab 15 software, trial version). The fitted model equation is as follows:

$$X = 73.4036 + 2.55A + 11.91B - 2.64C - 1.05A^2 - 2.75B^2 - 1.1091C^2 + 0.575AB + 0.5AC + 0.85BC \quad \textbf{(2.1)}$$

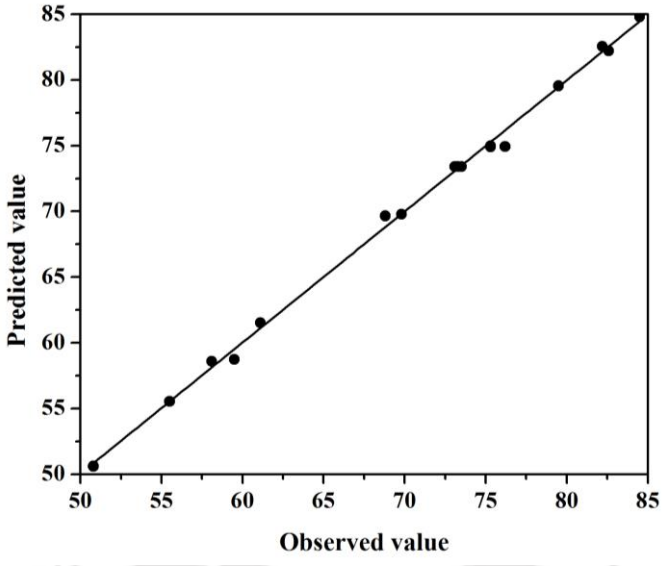

Figure 2.2: Relation between the observed (Experimental) and predicted value of MMA conversion

It could be seen from Table 2.3 that the experimental values of the conversion and the values obtained from the quadratic model fitted to the data match closely. The parity plot of experimental and predicted (by model) values is given in Fig. 2.2. It could be seen that all point fall very closely to 45^{o} line through origin, which shows fitness of the plot. The significance of the linear, square and interaction coefficients in the model equation was determined by ANOVA (Analysis of variance). Greater details on this technique can be found in texts by Montgomery and Runger (2007). *F*– and *p*–values of the coefficients are given in Table 2.4A and B. A high *F*–value and *p*–value less than 0.05 for a coefficient are indicative of the significance level of the coefficient. The *p*–value of all three linear regression coefficient is 0.0 (Table 2.4A), while the *p*–values of interaction coefficients are higher. This is an indication that the influence of each of the optimization variable is essentially independent of each other. This result is also corroborated by the *F*–values of regression coefficients. The *F*–value for linear coefficients (1227.36) is far higher than the *F*–value for interaction coefficients (8.24) as given in Table 2.4B. The overall *F*–value for model is

436.30 which indicate good fitness of the model to experimental data. The fitness of the quadratic regression model is also confirmed by the determination coefficient R^2 = 0.9975, R^2(adj) = 0.9952, and R^2(pred) = 0.9811, respectively.

The response surface 3–D plots depicting interactive effect of any two variables on the response (conversion) value are shown in Fig. 2.3A, B and C. The optimization plot of the experimental design is given in Fig. 2.4. It could be seen the optimum combination of values of quantities of monomer, initiator and surfactant in the 60 mL reaction mixture are MMA = 15 g, initiator (potassium persulfate, KPS) = 0.75 g and surfactant (SDS) = 0.8727 g. The optimum values of all three parameters in the range of variables were also confirmed using Microsoft Excel solver that uses the quasi–Newton as well as conjugate gradient method for finding the solution using all three variables. The synthesis of PMMA/Cloisite 30B nanocomposites was carried out using these optimized values of experimental parameters. However, the quantity of clay added to the reaction mixture was varied. The next section describes the results of nanocomposites synthesis.

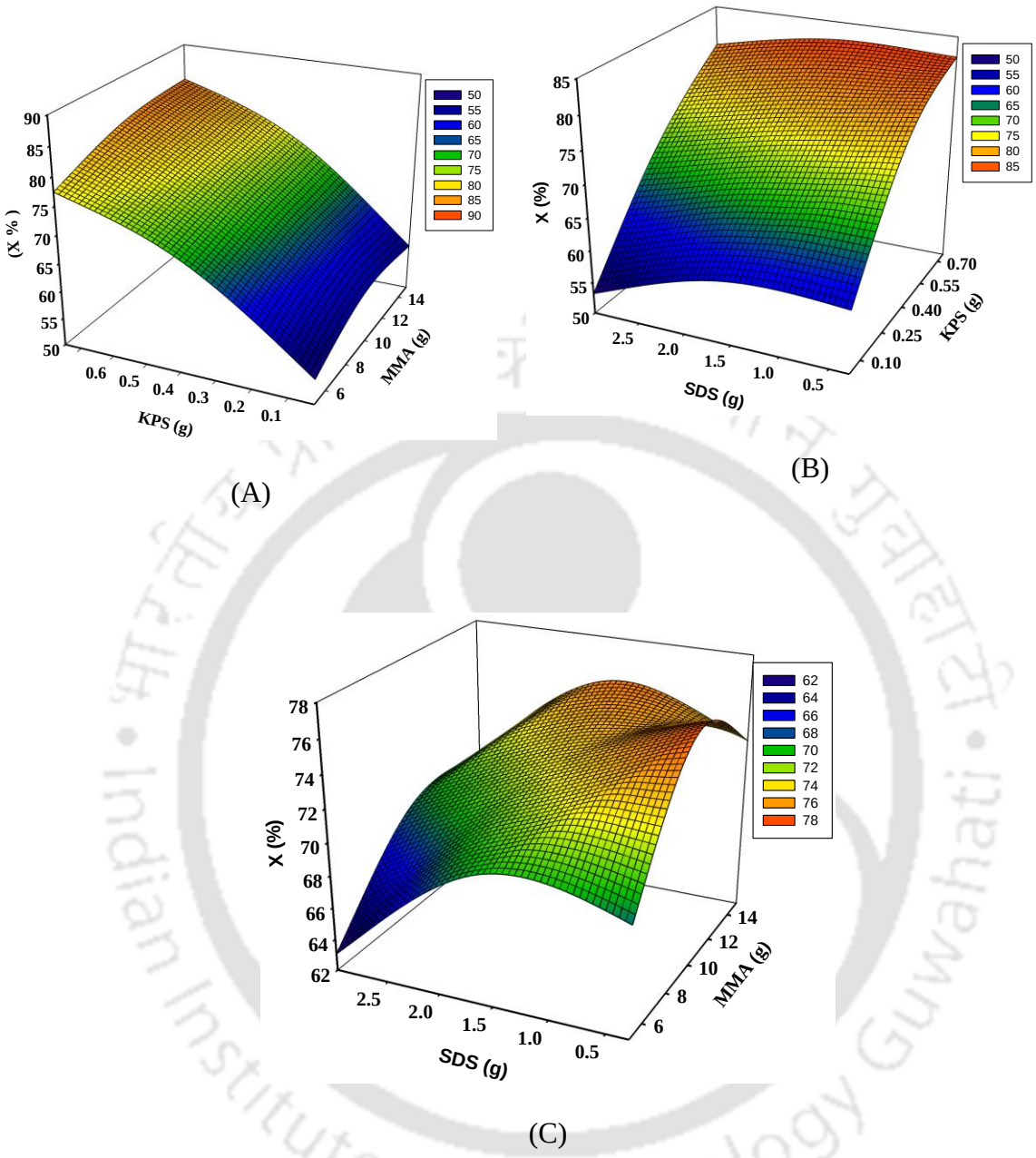

(A)

(B)

(C)

Figure 2.3: Results of statistical optimization of PMMA polymerization. Response surface plots depicting variation in the response variable, i.e., monomer conversion (X%), as a function of any two experimental parameters (or independent variables) (A) monomer (MMA) quantity and initiator (KPS) quantity; (B) initiator (KPS) quantity and surfactants (SDS) quantity; (C) monomer (MMA) quantity and surfactants (SDS) quantity.

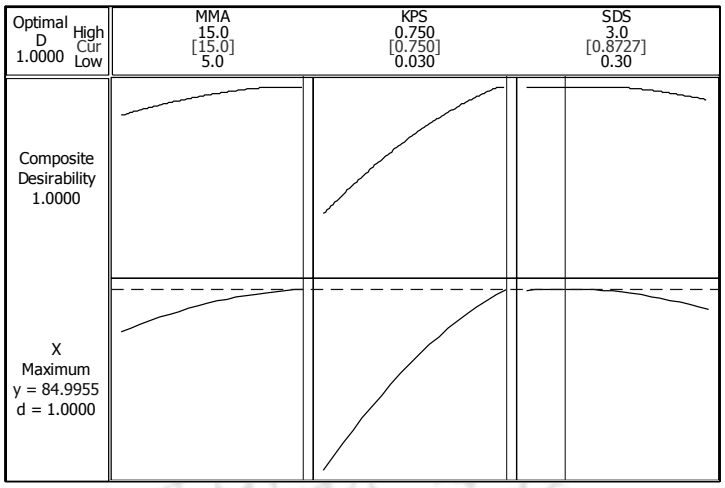

Figure 2.4 Results of statistical optimization of PMMA polymerization. Optimization plot for the CCD statistical experimental design depicting optimum values of the three experimental parameters (or independent variables).

2.7.2 Kinetic analysis of PMMA and PMMA/Cloisite 30B nanocomposite synthesis

The time profiles of monomer conversion and rate of polymerization during synthesis of only PMMA and PMMA/Cloisite 30B nanocomposites are shown in Figs. 2.5A and B**,** respectively. The extent of monomer conversion as well as the rates of MMA polymerization during synthesis of PMMA/Cloisite 30B nanocomposites decreases as compared to the neat PMMA. Moreover, the polymerization rate shows inverse variation with the amount of Cloisite 30B clay in reaction mixture. A possible explanation for these results can be given along following lines: Polymerization of MMA is essentially a radical induced process, which is extremely fast due to high energy and instability of radicals. Due to strong micro–turbulence generated by ultrasound and cavitation, the concentration of the initiator is uniform throughout the medium. Consequently, radicals also form uniformly throughout the medium. Micro–turbulence generated by ultrasound creates fine dispersion or emulsion (in the form of droplets of micro– or even nanoscale dimensions) of monomer into the reaction volume. These droplets are very rapidly polymerized by the radicals. Hence, the initial monomer conversion rate is quite fast and results in ~ 50% monomer conversion in first 10

min of reaction. However, thereafter the rate of polymerization decreases sharply with consumption of free radicals and also the reactant concentration. During synthesis of PMMA/ Cloisite 30B nanocomposites, the polymerization rate shows reduction due to two possible reasons: (1) strong micro–turbulence causes intercalation of monomer between silicate layers of the clay. However, the polymerization of intercalated monomer may be hindered due to mass transfer limitations. (2) Some initiator as well as a growing nuclei of polymer may get adsorbed onto the clay surface. These phenomena not only hinder dissociation of initiator into radicals but also cause hindrance of growth of polymer nuclei resulting in reduction in net monomer conversion.

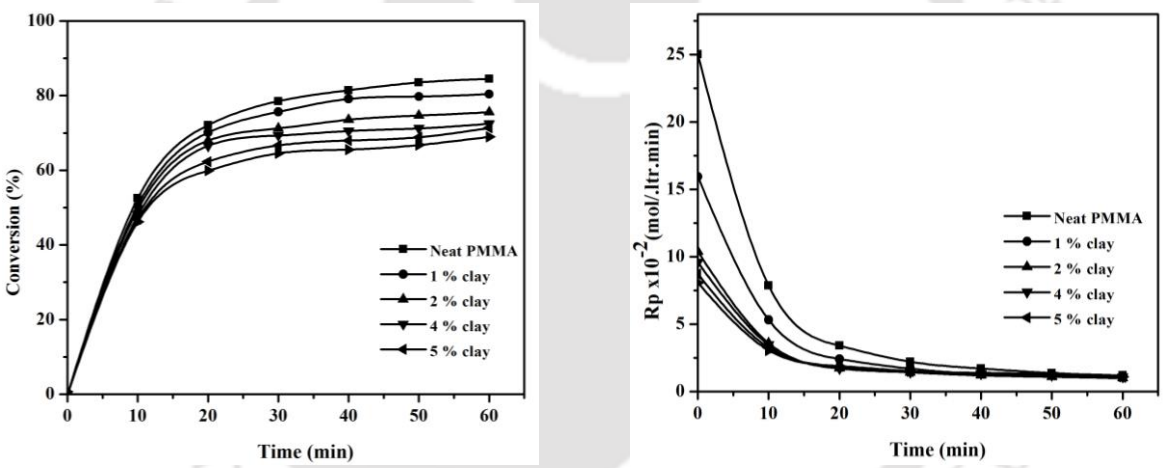

(A) (B)

Figure 2.5: (A) Time profiles of monomer conversion during synthesis of pristine PMMA and PMMA/Cloisite 30B nanocomposites in ultrasound–assisted emulsion polymerization. (B) Time history of monomer conversion rate during ultrasonic synthesis of PMMA and PMMA/ Cloisite 30B nanocomposites.

2.7.3 Comparative analysis of kinetics with literature

The kinetic rate constant depends on numerous factors – one of which is the agitation applied to the system. Since we have carried out synthesis of PMMA/clay nanocomposites using ultrasound, we have compared our analysis with results of Bhanvase et al. (2012). Bhanvase

et al. (2012) have plotted trends in rate of polymerization (for different initiator concentrations) with respect to time and have fitted these trends with polynomials. For initiator concentration of 0% and 0.5%, the polynomial order for rate vs time curve is 3, while for initiator concentration of 1–5%, the polynomial order is 5. Although analysis of Bhanvase et al. (2012) helps to perceive that order of polymerization with respect to monomer is higher than 1; Bhanvase et al. (2012) have not done the conventional kinetic (integral) analysis to determine the actual order of polymerization reaction with respect to monomer concentration. In our study, we have determined the optimum concentration of initiator as 0.75 g (5%). We have done the conventional integral kinetic analysis of the monomer conversion profile for this initiator concentration. The results are depicted in Fig. 2.6. The third order kinetic model has been found to fit best to the monomer conversion profile in synthesis of only PMMA as well as its nanocomposites with different loading of clay material. These results are similar to those reported by Bhanvase et al. (2012) and more recently by Bhanvase et al. (2014). The third order rate constant of only PMMA formation is 0.07 $(L/mol)^2 \cdot min^{-1}$, whereas it decreases for 1, 2, 4 and 5% loading of clay as 0.03, 0.02, 0.01, 0.01 $(L/mol)^2 \cdot min^{-1}$, respectively. This decrease in rate constant signifies slower of polymerization rate with continuous increasing the concentration of clay loading. This result is attributed to hindered polymerization of intercalated monomer in the silicate layers of clay or adsorption of initiator onto the clay, which hinders its decomposition into radicals. Polymer nuclei may also get adsorbed onto the clay which hinders their growth. All of these phenomena are manifested in terms of reduction in rate constants of polymerization.

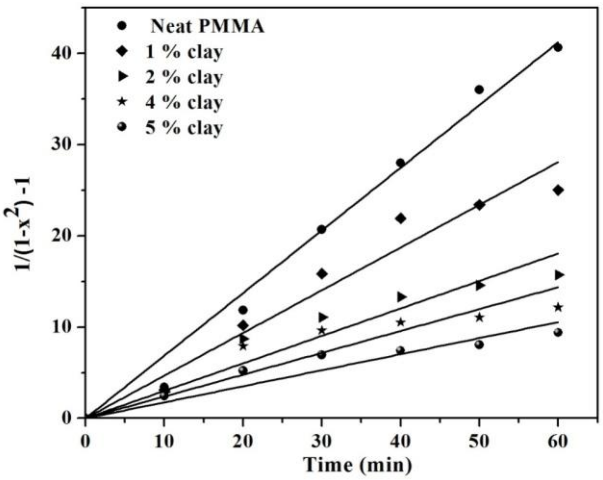

Figure 2.6: Results of integral analysis of reaction kinetics of polymerization for: neat PMAM and PMMA/ Cloisite 30B (1-5 wt%) nanocomposite. The third order kinetics with respect to monomer gives the best fit.

2.7.4 Characterization of PMMA/Cloisite 30B nanocomposites

TEM analysis: The morphology of the inner structure of the PMMA/Cloisite 30B nanocomposites (synthesized with clay loading of 1, 2, 4 and 5 wt%) is evident from the TEM micrographs depicted in Figs. 2.7A–D. The dark sheets or lamellar structures in the micrographs represent the clay platelets in PMMA matrix formed due to exfoliation of the clay particles. These dark layers of clay structures are present almost uniformly through the matrix of PMMA/Cloisite 30B nanocomposites for low clay loading of 1 and 2 wt%. However, TEM images of nanocomposites synthesized with higher loading (for 4 and 5 wt %) clearly show crowded or clustered regions of dark layers indicating agglomeration of the clay platelets inside the copolymer matrix. Agglomeration of the nanofiller material (in the present context the exfoliated platelets of the clay) inside polymer matrix has marked implications on the properties of the nanocomposites, as evident from the thermal and mechanical analyses presented in subsequent sections.

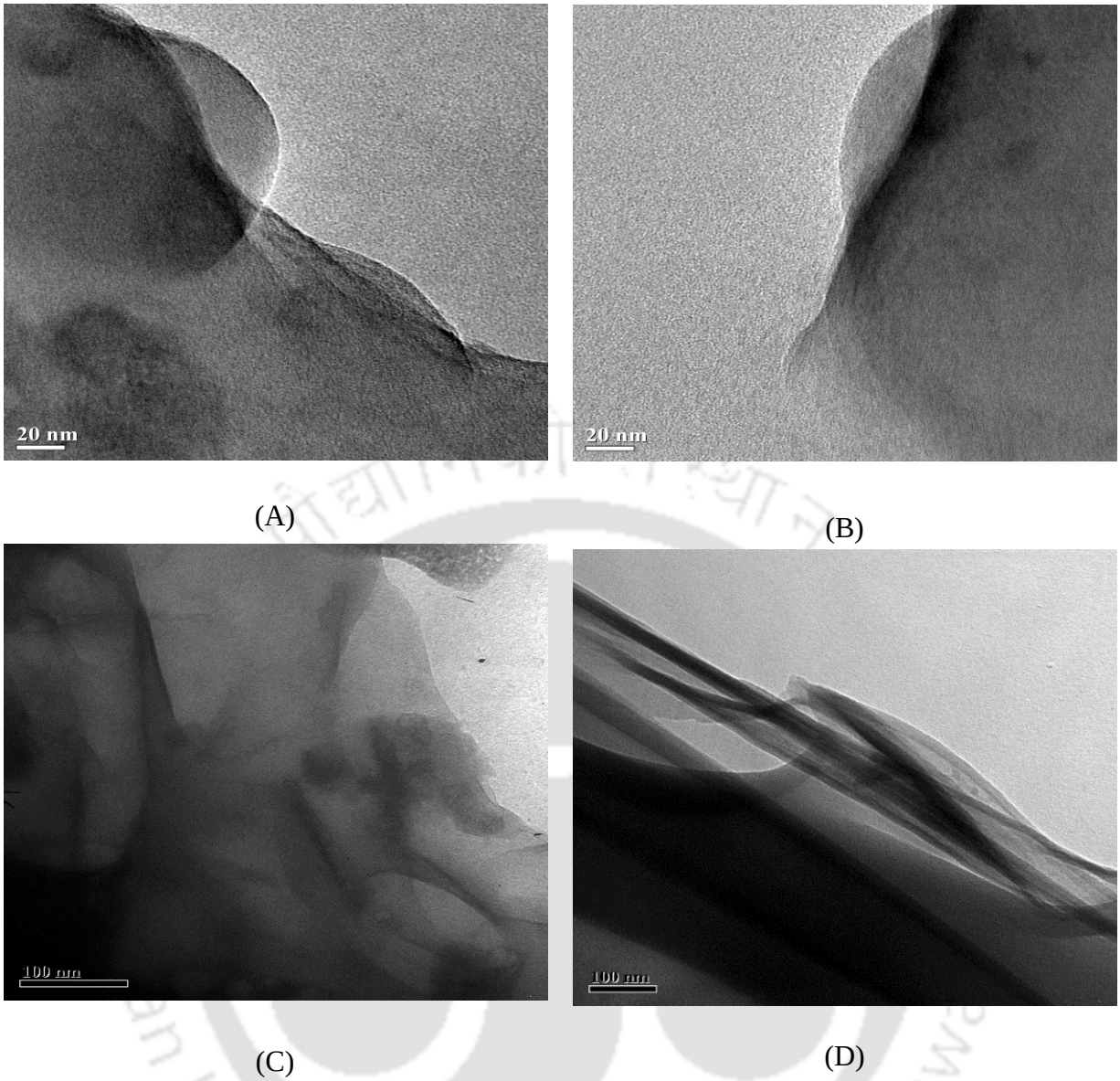

Figure 2.7: TEM micrographs PMMA/Cloisite 30B (A) 1 % (B) 2% (C) 4 % and (D) 5% loading of Cloisite 30 B respectively.

FTIR analysis: FTIR spectra of the organo–modified Cloisite 30B clay, neat PMMA and PMMA/Cloisite 30B nanocomposites (synthesized with different clay loadings) are shown in Fig. 2.8(A)**.** Sharp peak at 3636 cm^{-1} illustrates Si–O–H stretching on surface of the clay. Peaks at 2924, 2842 and 1475 cm^{-1} show asymmetric, symmetric and bending stretching of C–H bonds in $–CH_2$ group respectively, in addition to in–plane scissoring vibrations. Al–OH stretching peak is at 917 cm^{-1}, while and peak at 1040 cm^{-1} represents Si–O and Si–O–Si

stretching. Peaks at 3395 and 1639 cm^{-1} indicate H–O–H stretching and O–H bending, respectively. The peak at 1639 cm^{-1} also represents bending vibrational mode of hydrated water molecules and weakly bonded water molecules. Peaks in the range of 1374–1465 cm^{-1} correspond to N–H bending in the surfactant used for organo–modification of clay. The characteristic peak at 1730 cm^{-1} in FTIR spectrum of neat PMMA exhibits C = O stretching vibration of acrylate carboxyl group. The peaks in the range of 1395–1450 cm^{-1} represent deformation vibration of CH_3 and CH_2 groups in pure PMMA compound. Peaks in range of 1260–1040 cm^{-1} indicate C–O–C single bond stretching vibration**.** Fig. 2.8 A clearly represents that the transition of asymmetric of C = O stretching to C–O–C symmetric vibration after formation of PMMA/ Cloisite 30B nanocomposite. Further, peaks in range between 3636 and 3440 cm^{-1} in FTIR of PMMA/Cloisite 30B nanocomposite are attributed to Al–O–H stretching, while peak at 1040 cm^{-1} corresponds to Si–O–Si and Si–O stretching. These peaks confirm existence of Cloisite 30B nanoclay in the PMMA matrix. FTIR shown in Fig. 2.8 A was obtained for clay loading of 1, 2, 4 and 5 wt%. It could be observed from Fig. 2.8A that as Cloisite 30B loading during the synthesis of PMMA nanocomposite increases, the intensities of the peaks at 3636, 3440 and 1040 cm^{-1} become stronger indicating greater loading of clay in the polymer matrix.

XRD Analysis: The X-ray diffractogram of the clay in pristine form as well as clay subjected in sonication mode is shown in Fig. 2.8B.1. The X-ray diffractograms (in the range of 2θ = 1–30^o) of PMMA/Cloisite 30B nanocomposites are shown in Fig. 2.8B.2. The X-ray diffractograms in Fig. 2.8B.1, however, reveal an additional facet of beneficial effect of ultrasound and cavitation on the nanocomposites synthesis. The X-ray diffractogram of sonicated clay clearly show the shift of the characteristic peak corresponding to change in *d*-spacing between clay platelets. The initial diffraction peak of pristine Cloisite 30B nanoclay

at 2θ = 4.85°, shifts to 2θ = 4.1° after sonication of clay continuous mode. Thus, the initial *d*-spacing of 1.82 nm between platelets of pristine Cloisite 30B nanoclay increases to 2.16 nm after sonication. This result highlights and corroborates the role of microturbulence generated by ultrasound and cavitation in the exfoliation of the clay.

The X-ray diffractograms essentially help in determination of the structure of the clay present in nanocomposites – whether in intercalated or exfoliated form. XRD analysis is not only another tool (than FTIR) for confirmation of presence of clay in the nanocomposites but also its structure – whether intercalated or exfoliated as the characteristics peak changes with galley height (or spacing between the silicate layers) of the clay. If the nanocomposite formed in the synthesis has intercalated structure, the XRD peak is seen at larger *d*–spacing than the original organo–clay. However, if a completely exfoliated structure forms in the nanocomposites, no peak is seen. Fig. 2.8B.2 shows the X–ray diffractogram of pure Cloisite 30B and different nanocomposites synthesized using varying concentration of the Cloisite 30B clay. X–ray diffraction peaks were recorded in the range of 2θ = 1°–30°. The *d* (001) spacing is determined from peak positions using Bragg's law. Pure clay exhibits the *d* (001) peak at 2θ = 4.85°. However, for all nanocomposites synthesized at clay concentrations in the range of 1 wt% to 5 wt%, no diffraction peak is seen. This essentially indicates that equilibrium between exfoliation and intercalation structures in the PMMA/ Cloisite 30B nanoclay is driven completely towards exfoliation by ultrasound and cavitation, and the individual clay platelets are dispersed in the polymer matrix. The effect of ultrasound on exfoliation is evident by comparison of our results with those of Patra et al. (2012). Patra et al. (2012) used a combination of sonication and mechanical stirring during synthesis of nanocomposites. The mixture of monomer, initiator and clay was stirred for 1 h and then sonicated for just 10 min for ultrasound frequencies of 60 to 80 kHz. This was followed by

mechanical stirring for 20 h. On the contrary, we have used continuous sonication for 1 h during the entire synthesis. Moreover, the frequency of ultrasound used by us was 20 kHz. At lower frequency, the transient cavitation effects are much stronger (as explained in greater details subsequently). Patra et al. (2012) could achieve only intercalated/partial exfoliated structure at clay concentration of 3 wt% using mechanical stirring. However, Patra et al (2012) achieved exfoliated structure of PMMA/clay nanocomposites under the effect of ultrasound with input of 120 W power and 80 kHz acoustic frequency. However, in the present study, complete exfoliation is observed at clay concentration as high as 5 wt%. Krishna and Pugazhenthi (2011) have also confirmed formation of exfoliated structure at clay concentrations lower than 5 wt% for polystyrene/ montmorillonite clay nanocomposites. The exfoliated nature of poly(styrene–co–methyl acrylate)–bentonite clay nanocomposite has also been ascertained by Borthakur et al. (2010) For clay loading of 1% and 2 wt%, Borthakur et al. (2010) have found partial exfoliation, while for clay loading of 0.5 wt%, complete (or 100%) exfoliation was observed. The reason cited by Borthakur et al. (2010) for exfoliation is increase in the hydrophobicity of intergalleries of clay due to presence of long chain alkyl chains of surfactant. This assists intercalation and exfoliation of the clay with insertion of monomer molecules and subsequent polymerization. Exfoliation of montmorillonite clay in polystyrene with chlorobenzene as solvent during ultrasound–assisted polymerization has also been reported by Morgan and Harris (2004) for clay loading of 2 – 3 wt%. Morgan and Harris (2004) have proposed that sonication provided additional energy for separation of the platelets of the large clay tactoid and dispersion of these platelets into the solvent. Morgan and Harris (2004) have also hypothesized that sonication helped formation of crude "solvation sphere" of chlorobenzene around each clay platelet. The polymer mixes with the solvated clay to form a uniform mixture and complete exfoliation.

Particle size and zeta potential analysis*:* The results of size distribution measurement of only

PMMA and PMMA/ Cloisite 30B nanocomposites particles are shown in Fig. 2.8C and Table 2.5. The cumulative average particle size of only PMMA was determined as 79.9 nm. The range of average particle size of PMMA/ Cloisite 30B nanocomposites for different clay loading was observed in the range of 100.5 – 114.7 nm. These sizes are far smaller than the particle size obtained using mechanical stirring. For example, Patra et al. (2012) have reported a size of 648 nm for PMMA/ clay nanocomposites). This effect is attributed to fine emulsification produced by sonication applied continuously during polymerization. Greater discussion on this is given in subsequent section, in which the physical mechanism of formation of polymer nanocomposites is discussed. The average particle size of the nanocomposites increased with the Cloisite 30B concentration in the reaction mixture and also in polymer matrix. A possible reason for this could be aggregation of the clay particles with intercalated monomer Bhanvase et al. (2012); Prasad et al. (2013) have also reported similar trends in particle size for PMMA/$CaCO_3$ nanocomposite.

The homogeneity and colloidal stability of nanocomposites was measured by zeta potential. Table 5B illustrates different values of zeta potential of resulting latex particle. The zeta potential value of only PMMA particles was –52.09 mV which decreased in the range of –49.47 to –45.02 mV for nanocomposites with varying Cloisite 30B concentration. This reduction essentially indicates increase in latex stability. This effect is rather contrary to that reported by Yilmaz et al. (2010) for acrylate/ montmorillonite composites in which the zeta potential of nanocomposites increased indicating lower stability of the latex. However, in case of ultrasound assisted synthesis, the uniform arrangement of silicate layers in polymer matrix may help overcome the surface tension forces, which leads to stabilization of the polymer nanocomposites. Fine emulsification of monomer in the reaction mixture can also cause reduction in polymer nanocomposite particle, which contributes to emulsion stability.

All of these factors contribute to reduction in zeta potential with nanocomposite formation. A similar trend of zeta potential reduction with nanocomposite formation with increasing clay content is also reported by Bhanvase et al. (2012).

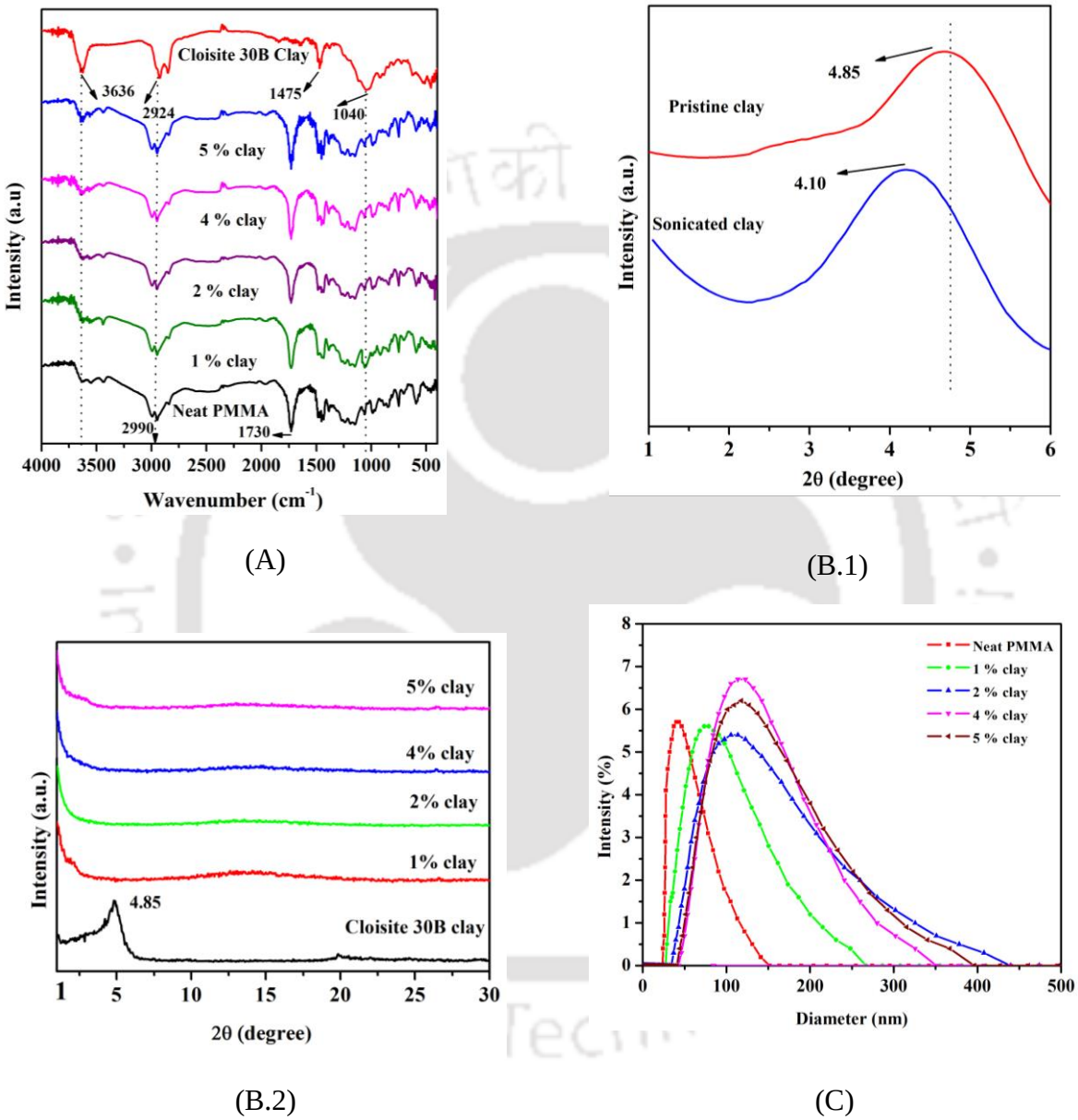

Figure 2.8: Characterization of the neat PMMA and PMMA/Cloisite 30B nanocomposites. (A) FTIR spectra of pristine Cloisite 30B clay, neat PMMA and PMMA/Cloisite 30B nanocomposite (1-5 wt% clay). (B.1) X-ray diffractograms of pristine Cloisite 30B nanoclay and the clay after sonication (B.2) X–ray diffractograms of Cloisite 30B Clay and PMMA/clay Nanocomposites synthesized with ultrasound. (C) Particle size distribution of the neat PMMA and PMMA/Cloisite 30B nanocomposites.

Thermogravimetric analysis: The thermal stability of synthesized neat PMMA and its nanocomposites with cloisite 30B were performed under nitrogen atmosphere with heating rate of 10^{o}C min^{-1}. All samples were run in duplicate and the average values of these are reported. The thermal degradation of PMMA due to the heating effect occurred in three different temperature range (Kashiwagi et al., 1986).The first step temperature degradation measured in temperature range of 160-240^{o}C. This is due to the scission of weak head to head linkage of PMMA chain and presence of impurities involved during synthesis of PMMA. The second degradation step occurred at 290^{o}C due to the decomposition of PMMA chains ends. The third and final degradation occurs in between temperature range of 300-400^{o}C due to the random scission of polymer chains (Ferrial et al., 2003). The thermal degradation behaviour of neat PMMA and its nanocomposites with Cloisite 30 B clay (1, 2, 4 and 5 wt %) are depicted in Fig. 2.9A.1. During heating, the weight loss of the neat PMMA and its nanocomposites were occurred in various steps. The initial step weight loss was occurred due to the evaporation of moisture which were remained in the sample after completion of vacuum drying.

The change in the weight loss for neat PMMA and PMMA/Cloisite 30B nanocomposites is almost similar up to temperature of 240^{o}C. This indicates the thermal stability of neat PMMA and its nanocomposites exhibit similar behavior of thermal decomposition up to this temperature. After this, the dramatically change in weight loss occurred above temperature of 240^{o}C. The thermal degradation at different weight loss ($T_{5\%}$, $T_{10\%}$ and $T_{50\ \%}$) of neat PMMA and PMMA/Cloisite 30B (1, 2, 4 and 5 wt %) are shown in Table 2.5B. For comparison of 5 wt% weight loss ($T_{5\%}$), the synthesized neat PMMA exhibit thermal degradation at 267.4 ^{0}C. Whereas, the loading of nano clay with 1 and 2 wt % enhance the thermal stability 7.32, 9.26, ^{o}C respectively as compared to the neat PMMA. Further increase in loading for 4 and 5 wt %, the reduction in thermal stability occur for $T_{5\%}$.

The possible reason for reduction in thermal stability is due to present of cationic surfactants in Cloisite 30 B clay. This cationic surfactants is thermally unstable in this temperature range and form agglomerates at higher loading. This combined effect are responsible for the breakage of weak head to head bond linkage of PMMA chain. This result, reduction in thermal stability of PMMA/Cloisite 30B nanocomposites at higher loading of clay. For comparison of weight loss at $T_{10\%}$ the neat PMMA exhibit thermal degradation at 277.2 ^{0}C. Whereas, the loading of nano clay with 1, 2, 4 and 5 wt % enhance the thermal stability 12.5, 19.5, 25.1 and 30.1 ^{o}C respectively as compared to the neat PMMA. The expanded view of the TGA image is shown in Fig.2.9 A.2 This enhanced thermal stability at $T_{10\%}$ weight loss of nanocomposites were due to the two following reason. First one is due to disappearance of unstable cationic surfactants molecules, and the second is due to addition of nano clay in PMMA matrix, which act as a superior insulator which provide hindrance in the diffusion of volatile products which strengthen the weak head to head carbon linkage which provide cross link structure, result enhance its thermal stability (Gilman, 1999 and Maiti et al 2002). The decomposition temperature at which ($T_{50\%}$) 50 % of weight loss occurs are also shown in Table 2.5B. The temperature at which 50 wt % loss occurred of pristine PMMA was observed at 326^{o}C. The incorporation of nanoclay from 1, 2, 4 and 5 wt % in PMMA matrix increase the thermal stability at 50 % weight loss with, 14.1, 30.7, 43.3 and 55.9^{o}C respectively as compare to the neat PMMA. Thus, we can observe, the ultrasound assisted synthesis of PMMA/Cloisite 30B nanocomposites increase the thermal stability of PMMA after loading of clay nano material due to following reasons. The first one is have proposed that the effect of ultrasound caused an additional energy transferred to the clay material which increase the interlayer *d*-spacing of the clay platelets which helps the uniform dispersion of these platelets into the polymer matrix (Morgan and Harris, 2004). The second reason is due to high thermal stability of cloisite 30B clay which contain the single tallow

modifier with a methyl and two hydroxyl groups which make the more thermal stability to the clay material (Unnikrishnan et al., 2011).

DTG analysis Fig. 2.10A the maxima of the DTG peak indicates the temperature corresponding to maximum rate of degradation rate. All maxima DTG curves for the PMMA/Cloisite 30B nanocomposites show shift towards right hand side as compared to maxima peak for only PMMA. The maximum degradation rate temperature for neat PMMA is 376^{o}C, while that for PMMA/cloisite 30B nanocomposites for 1, 2 and 4 and 5 wt % cloisite 30B this increased up to up to 4, 9, and 12 and 17^{o}C respectively. Thus, the thermal behaviour DTG analysis supports the conclusion of TGA analysis and confirm that the addition of silicate layers in matrix of PMMA significantly improve the thermal stability of PMMA/cloisite 30B in a greater extent.

DSC (Differential scanning calorimeter) analysis: The DSC analysis represents the effect of Cloisite 30B concentration in the PMMA/Cloisite 30B nanocomposites on the molecular mobility of PMMA chains. The glass transition temperature of polymer matrix is an indicator of this property. The DSC study results of neat PMMA and PMMA/Cloisite 30B nanocomposites at various clay concentration levels has been carried out. Fig. 2.10B and Table 2.5 gives the results of the analysis. In the DSC curve, the glass transition temperature is determined as the point of inflection between onset and end set of temperature. As per the results shown in Table 2.5A, glass transition temperature of neat PMMA is improved significantly after nanocomposites formation. The increase in T_g shows a maxima with clay concentration in that the highest increase of 9^{o}C (T_g = 125^{o}C) is seen for nanocomposite with Cloisite 30B concentration of 4 wt%. The increase in glass transition temperature is attributed to incorporation of silicate platelets or layers (with high aspect ratio) in the PMMA matrix. The segmental motion of polymer chains is restricted at organic–inorganic interface due

confinement of PMMA chains between the silicate layers. The interactions between silicate surface and polymers in the nanocomposites also lead to reduced mobility of the polymer chain. Several other papers have also reported increase in glass transition temperature of nanocomposites in comparison of the sulfate. For polystyrene/ MMT nanocomposites synthesized with melt intercalation, (Zidelkheir et al., 2006), the rise in glass transition temperature is rather limited, i.e. 3^{o}C, as compared to 8^{o}C rise in the present study for 3 wt% clay. We attribute this result to higher concentration and more uniform distribution of clay platelets in the polymer matrix with use of ultrasound during synthesis. An increase in glass transition temperature of similar magnitude as the present study has also been reported by Krishna and Pugazhenthi (2011) or polystyrene/clay nanocomposites. However, at even higher loading of clay (> 2%), agglomeration of clay may occur in polymer matrix, (Bhanvase et al., 2012), which leads to decrease in T_g. The T_g is highest (125^{o}C) for 4% clay loading and further start decreasing with increase in clay loading due to agglomeration of clay in polymer matrix. These results indicate that the optimum clay loading for PMMA/ Cloisite 30B nanocomposite is 4 wt%.

Optical Transparency: The optical transparency of neat PMMA and PMMA/Cloisite 30B nanocomposites (for loading 1–5 wt%) are depicted in Fig. 2.10C. by a UV–Vis spectrometer. The neat PMMA shown highly optical transparency with more than 85% in the visible light range. The addition of nanoclay lower the optical transparency. The lowest transparency was reported 84% for the 5 wt% loading of clay in the PMMA matrix. The reduction in transparency was due to the absorption of visible light due to presence of clay nanosheets in PMMA matrix.

Table 2.5: Summary of PMMA and PMMA/Cloisite 30B nanocomposites characterization

(A) Particle size analyses, zeta potentials and glass transition temperatures

Name of Sample	Average diameter (nm)	Zeta potential (mV)	Glass transition Temperature (°C)
Neat PMMA	79.9	–52.1	116
PMMA/clay (1 wt%)	100.5	–47.7	121
PMMA/clay (2 wt%)	104.6	–49.5	122
PMMA/clay (4 wt%)	113.7	–47.1	125
PMMA/clay (5 wt%)	114.7	–45.0	113

(B) Thermogravimetric analysis

Name of Sample	$T_{5\%}$ (°C)	$T_{10\%}$ (°C)	$T_{50\%}$ (°C)	$\Delta T_{10\%}$ (°C)	$\Delta T_{50\%}$ (°C)
PMMA	267.4	277.2	326	–	–
PMMA/clay (1 wt%)	274.7	289.7	340.1	12.5	14.1
PMMA/clay (2 wt%)	276.6	296.7	356.7	19.5	30.7
PMMA/clay (4 wt%)	267.3	302.3	369.3	25.1	43.3
PMMA/clay (5 wt%)	240.4	308.1	381.9	30.9	55.9

Note:$T_{5\%}$ – temperature corresponding to 5% weight loss, $T_{10\%}$ – temperature corresponding to 10% weig loss $T_{50\%}$ – temperature corresponding to 50% weight loss

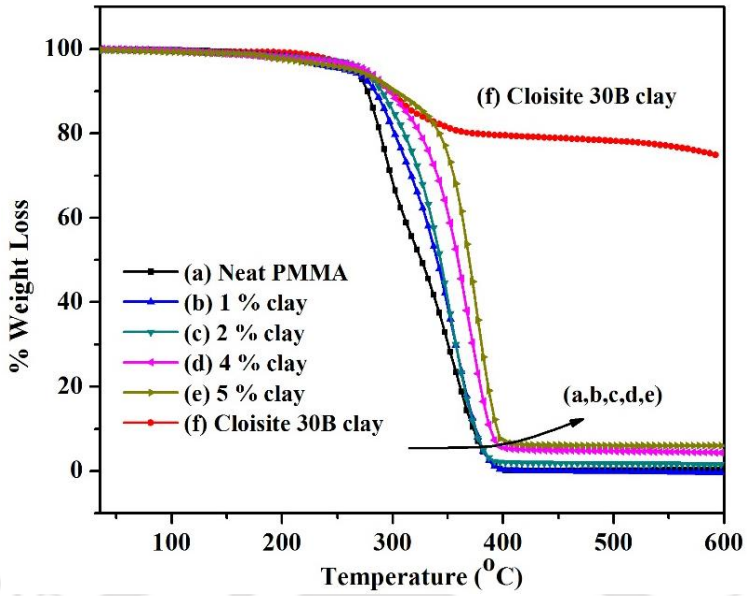

(A.1)

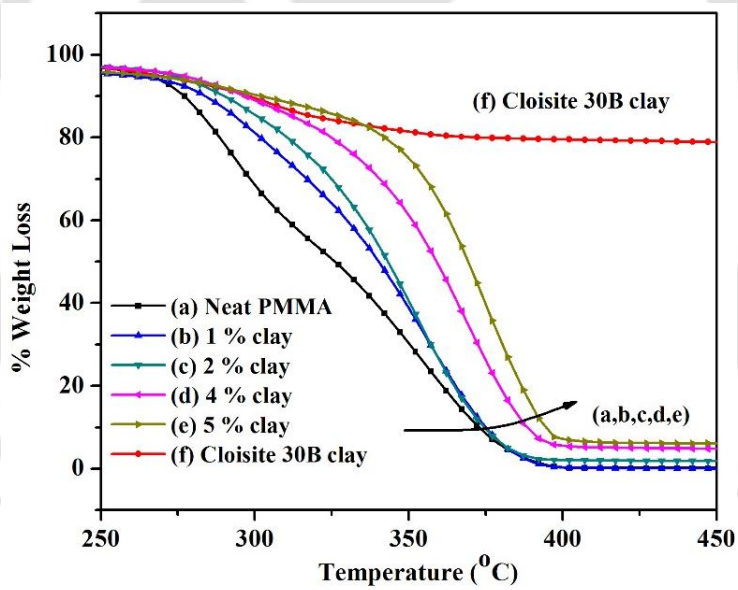

(A.2)

Figure 2.9: Analysis of thermal properties of neat PMMA and PMMA/Cloisite 30B nanocomposites synthesized with varying clay loading. (A.1) Thermogravimetric (TGA) curves in full temperature range; (A.2) Expanded view of TGA curves in the temperature range of 250–500 °C.

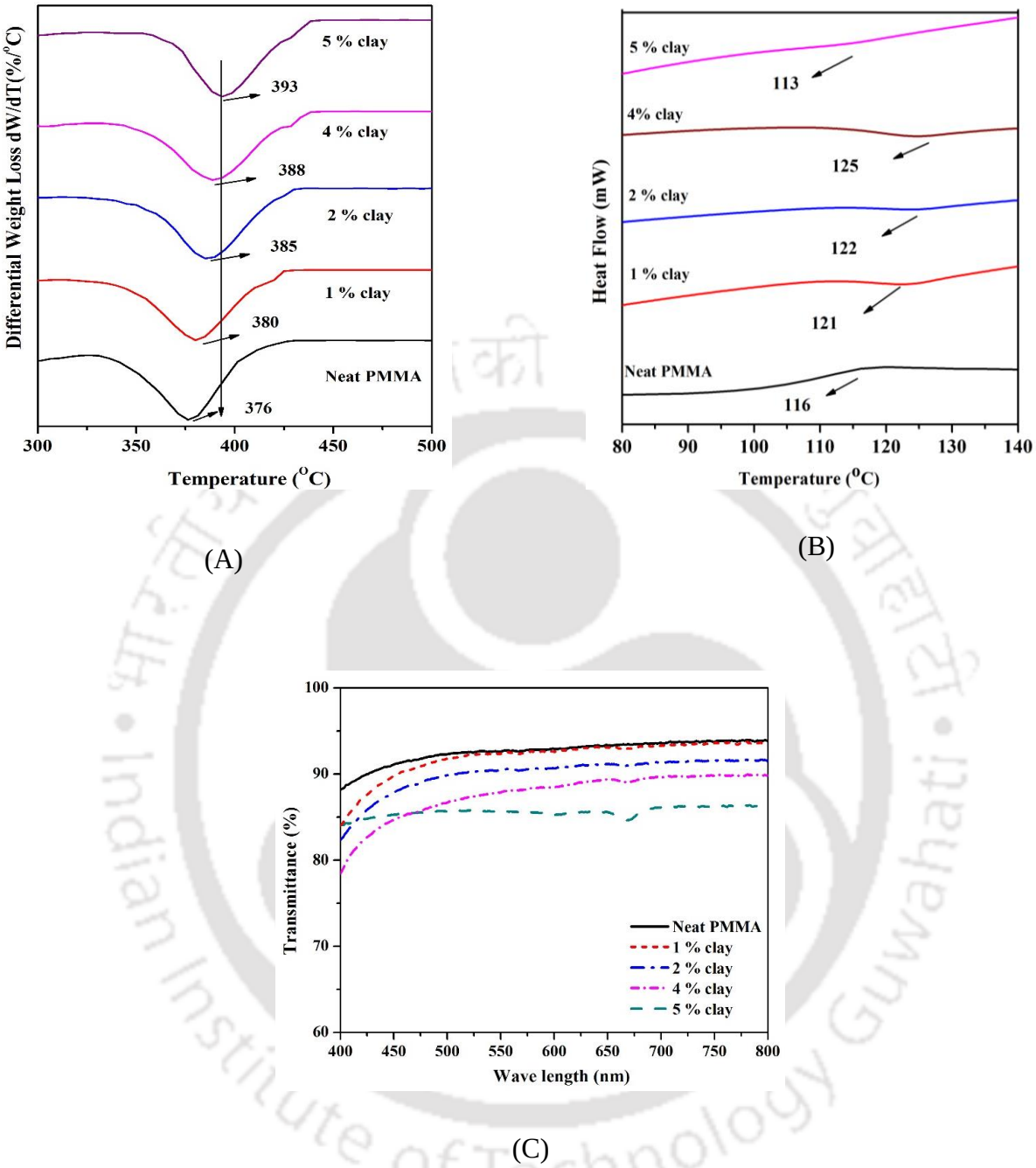

Figure 2.10: (A) Analysis of differential Thermogravimetric (DTG) curves. (B) Differential Scanning Calorimetric (DSC) curves. (C) Optical Transparency of neat PMMA and PMMA/Cloisite 30B nanocomposites.

Mechanical Properties: Three mechanical properties of as-synthesised neat PMMA and its nanocomposites with varying clay loading have been assessed, viz. tensile strength, Young's modulus and percentage elongation. The tests for measurement for mechanical properties have been conducted with Universal Testing Machine (UTM) as per ASTM D 882 standard

test method. Specimen film of neat PMMA and nanocomposites with dimensions 100 mm × 50 mm × 0.15 mm have been used at a crosshead speed of 0.5 mm/min. The trends in three mechanical properties have been shown in Figs. 2.11A–C. The trends in tensile strength of the nanocomposites vis-a-vis neat PMMA are shown in Fig. 2.11A. The tensile strength of neat PMMA is 32.74 MPa. With addition of clay (1, 2, 4 and 5 wt %), the nanocomposites reveal reduction in the tensile strength. For 5 wt % clay loading it was reported minimum value of 22.1 MPa. The decrease in tensile strength with addition of clay material was due to the more brittle and amorphous nature of PMMA polymer (Kumar et al., 2014). The loading of clay platelets further make it more brittle and reduce its tensile strength as compare to the neat PMMA. Incorporation of clay increase the young's modulus of PMMA chain. The trends in Young's modulus (Fig. 2.11B) indicate opposite trends as compare to the tensile strength. The neat PMMA depict Young's modulus of 1.17 GPa. Addition of Cloisite 30B nanoclay in PMMA matrix with 1, 2 and 4 wt% rises the Young's modulus to 1.4, 1.7 and 2.2 GPa, respectively. The possible reason for increase in Young 's modulus could be that addition of clay provides more neighboring sites of hydrogen molecules present in PMMA chain, which strengthens the structure of PMMA and increases its stiffness which resists its elastic deformation and making the nanocomposites more brittle. However for nanocomposite with 5 wt% clay loading, the Young's modulus shows reduction to 1.9 GPa. For large clay concentration of 5 wt%, however, the distribution of clay platelets in the PMMA matrix can be non-uniform, leading to agglomeration/segregation of the same, which could be form weak spot in the matrix leading to reduction in Young 's modulus. These spots also act as locations of stress concentration, which could result in development and propagation of cracks. Fig. 2.11C depicts the trends in percentage elongation of neat PMMA and its nanocomposites with varying clay loading. The percentage strain at break, decreased

with clay loading in the PMMA matrix. Neat PMMA shows the highest elongation with increase in in 3.92 % as compare to its original length. The clay loading continuously decreases the elongation. For 5 wt% clay loading, the strain corresponds to mere only 0.7 percent increase in length, as compared to the neat PMMA. The decrease in strain at break with clay loading is attributed to more stiff and brittle material. Incorporation of clay in polymer matrix provides resistance for polymer chain mobility, which reduces the elongation ability for nanocomposite.

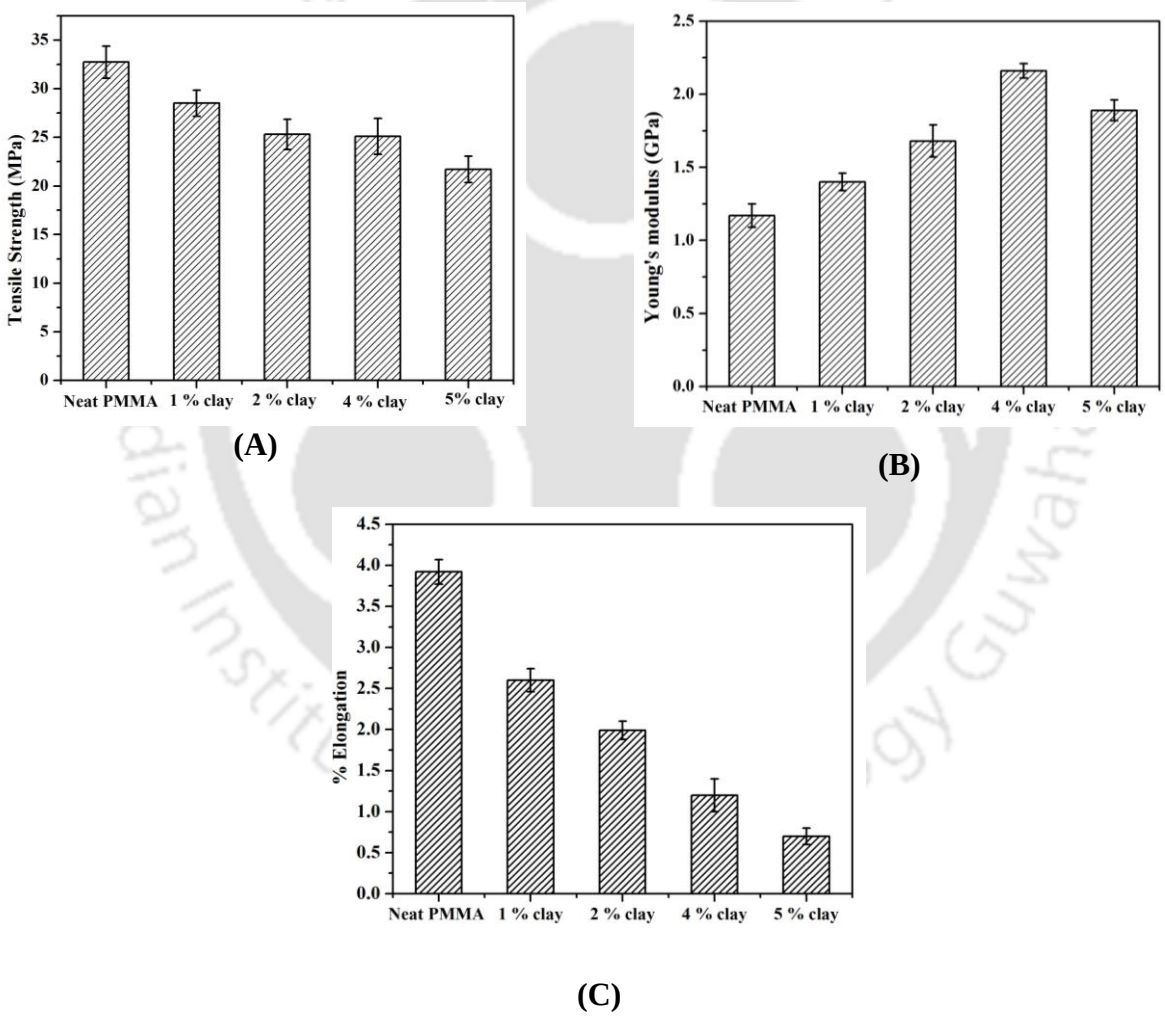

Fig. 2.11 (A): Tensile Strength of PMMA)/clay), (B)Young's Modulus of PMMA)/clay (C) % Elongation of PMMA)/ clay

2.8 Discussion and Mechanistic (Physical) Analysis)

After presentation of the results of this study, we try to give physical justification and reasoning for our results. In the first place, we need to distinguish between the physical and chemical effects of ultrasound and cavitation. As noted earlier, the principal physical effect of ultrasound and cavitation is generation of intense microturbulence, (Kuppa et al., 2010) while the chemical effect of generation of highly reactive radicals by thermal dissociation of solvent vapor trapped in the bubble during collapse (Sivasankar et al., 2007). The micro–turbulence generated by the ultrasound and transient cavitation has two components, shock waves and micro–streaming/ micro–convection. These two components have a distinct effect on chemical reactions, especially the heterogeneous reactions, due to their very nature. The shock waves are intermittent and sporadic character in terms of time as well as space, while the micro–streaming (or micro–convection) is a oscillatory yet continuous motion of fluid elements. In our earlier work, we have distinguished between effects of these two components on chemical system using extensive simulations of cavitation bubble dynamics. (Midathana et al., 2009; Reddy et al., 2009; Nalajala et al., 2010; Chakma et al., 2011; Choudhury et al., 2013; Goswami et al., 2013). Ultrasound and cavitation can help overcome reaction barrier due to nucleation generated by shock waves. In case of solid particle synthesis, ultrasound and cavitation can also cause specific growth of the particles that gives a typical morphology and characteristics. In the present context of polymer nanosynthesis, both physical and chemical effects of cavitation and ultrasound play a role. However, the relative contribution of the two effects is not same, as explained below:

The shock waves produced by transient cavitation cause de–agglomeration of the clay particles and it also disperses the monomer in the form of fine emulsion (e.g. droplets of nanoscale dimensions) in the reaction volume. Some monomer droplets can also get

entrapped inside micelle. However, the shock waves are not much useful for causing intercalation of monomer (or monomer swollen micelles) into silicate layers of clay and subsequent exfoliation of the same. The microstreaming generated by ultrasound (which is fast oscillatory motion of fluid elements during passage of ultrasound wave) can cause intercalation (or penetration) of the monomer molecules between silicate layers. The micelles of the surfactant, which enclose the monomer droplet, can also get intercalated inside the silicate layers – provided their diameter is smaller than the spacing between silicate layers. Some adsorption of the monomer swollen micelle can also occur on surface of the clay particle. The polymerization of these entities is done by radicals. As noted earlier, transient cavitation produces in–situ radicals. However, this source of radicals is highly sporadic in space as well as time, and hence, does not contribute much to polymerization. The polymerization is mainly affected by radicals generated from externally added initiator. Since the concentration of initiator in the reaction volume is uniform, so is the radical concentration and extent of polymerization. Thus, initiator concentration plays a decisive role in synthesis of PMMA/ Cloisite 30B nanocomposite – which is reflected by high regression coefficient in the quadratic model of the DoE. These results are physically very similar to those observed by us for degradation of textile dyes in sono–Fenton process.[44] In some cases, the radicals and other chemical species generated by cavitation events may cause scavenging of the radicals generated by initiator (Bolla et al., 2012; Bhasarkar et al.,2013).

Since the convection generated by ultrasound is sufficiently strong to cause intercalation of monomer into the silicate layers, the role of surfactant is rather secondary. Surfactant reduces the surface tension of the medium and adversely affects the cavitation phenomena. The intensity of transient cavitation and the magnitudes of their physical effect reduce with increase in surface tension. Thus, the regression coefficient in the quadratic model of the DoE corresponding to surfactant concentration has a negative value.

2.9 Conclusions

In the present chapter, we have reported mechanistic investigations in ultrasound assisted synthesis of PMMA/Cloisite 30 B nanocomposite. The role of ultrasound and cavitation is revealed to be mostly physical. The micro–turbulence generated by ultrasound/ cavitation creates fine emulsion of monomer and water. The actual polymerization process is affected by the radicals generated by the initiator and not transient cavitation. Due to highly sporadic nature of transient cavitation (in time and spatial domain), the net contribution of cavitation generated radicals to polymerization is negligible. The shock waves generated by the transient cavitation assist de–agglomeration and uniform dispersion of clay particles in the reaction volume. Convection generated by micro–streaming by ultrasound assists intercalation of the monomer or monomer swollen micelles between the silicate layers of clay. Overall kinetics of polymerization is revealed to be third order with respect to monomer. Although thermal properties of PMMA/Cloisite 30 B nanocomposite have been enhanced as compared to neat PMMA, there is no direct proportionality between the properties and quantity of clay. All properties have been revealed to have an optimum clay concentration at which they are at their maximum. We believe that the mechanistic insight into ultrasound assisted synthesis of PMMA/Cloisite 30 B nanocomposite gained in this study will form useful inputs for research.

References

Borthakur LJ, Das D, Dolui SK, Development of core–shell nano composite of poly (styrene-co-methyl acrylate) and bentonite clay by ultrasonic assisted mini-emulsion polymerization, Mater. Chem. Phys. 124 (2010) 1182–1187.

Bhanvase BA, Pinjari DV, Gogate PR, Sonawane SH, Pandit AB, Process intensification of encapsulation of functionalized $CaCO_3$ nanoparticles using ultrasound assisted emulsion polymerization, Chem. Eng. Process. Process Intensif. 50 (2011) 1160–1168.

Bhanvase BA, Pinjari DV, Gogate PR, Sonawane SH, Pandit AB, Synthesis of exfoliated poly(styrene-co-methyl methacrylate)/montmorillonite nanocomposite using ultrasound assisted in situ emulsion copolymerization, Chem. Eng. J. 181–182 (2012) 770–778.

Bhasarkar JB, Chakma S, Moholkar VS, Mechanistic features of oxidative desulfurization using sono-Fenton-peracetic acid (ultrasound/Fe^{2+}-CH_3COOH-H_2O_2) system, Ind. Eng. Chem. Res. 52 (2013) 9038–9047.

Bhanvase, BA, Sonawane, SH, Pinjari, DV, Gogate PR, Pandit AB, Kinetic studies of semibatch emulsion copolymerization of methyl methacrylate and styrene in the presence of high intensity ultrasound and initiator, Chem. Eng. Process. Process Intensif. 85 (2014) 168–177.

Biswal T, Behera P, Prafulla Sahoo PK, Microwave assisted synthesis and gas barrier properties of PMMA/clay nanocomposites, Eur. J. Biomedical and Pharmaceutical sciences, 2 (2015) 479–493.

Bolla MK, Choudhury HA, Moholkar VS, Mechanistic features of ultrasound-assisted oxidative desulfurization of liquid fuels, Ind. Eng. Chem. Res**.** 51 (2012) 9705–9712.

Bradley M, Gieser F, Emulsion Polymerization Synthesis of Cationic Polymer Latex in an Ultrasonic Field, J. Colloid Interface. Sci. 251 (2002), 78–84.

Chakma S, Moholkar VS, Mechanistic features of ultrasonic desorption of aromatic pollutants, Chem. Eng. J. 175 (2011) 356–367.

Chou HC, Stoffer JO, Ultrasonically initiated free radical-catalyzed emulsion polymerization of methyl methacrylate, J. Appl. Polym. Sci. 72 (1999) 797–825.

Choudhury HA, Choudhary A, Sivakumar AM, Moholkar VS, Mechanistic investigation of the sonochemical synthesis of zinc ferrite, Ultrason. Sonochem. 20 (2013**)** 294–302.

Delozier DM, Orwoll RA, Cahoon JF, Johnston NJ, Jr Smith JG, Connell JW, Preparation and characterization of polyimide/organoclay nanocomposites, Polymer 43 (2002) 813–822.

Dhibar S, Kar P, Khatua BB, Preparation of highly exfoliated and transparent polycarbonate/clay nanocomposites by melt blending of polycarbonate and poly (methyl methacrylate)/clay, J. Appl. Polym. Sci. 125 (2012) 601–609.

Ferriol M, Gentilhomme A, Cochez M, Oget N, Mieloszynski JL, Thermal degradation of poly(methyl methacrylate) (PMMA): modelling of DTG and TG curves, Polym. Degrad. Stab. 79 (2003) 271–281.

Gilman JW, Flammability and thermal stability studies of polymer layered–silicate (clay) nanocomposites, Appl. Clay Sci. 15 (1999) 31–49

Goswami PP, Choudhury HA, Chakma S, Moholkar VS, Sonochemical synthesis of cobalt ferrite nanoparticles, Ind. Eng. Chem. Res.52 (2013) 17848–17855.

Jung HT, Lee SS, Park M, Kim H, Lim S, Preparation of poly(methyl methacrylate)/clay nanocomposites using supercritical fluid process, Compos. Interfaces 19 (2012) 565–572.

Kanmuri S, Moholkar VS, Mechanistic aspects of sonochemical copolymerization of butyl acrylate and methyl methacrylate, Polymer 51 (2010) 3249–326.

Kashiwagi T, Inaba A, Brown JE, Hatada K, Kitayama T, Masuda E, Effects of weak linkages on the thermal and oxidative degradation of poly(methyl methacrylates) Macromolecules. 19 (1986) 2160–2168.

Krishna SV, Pugazhenthi G, Influence of Processing Conditions on the Properties of Polystyrene (PS)/organomontmorillonite (OMMT) nanocomposites prepared via solvent blending method, Int. J. Polym. Mater. 60 (2011) 144–162.

Kumar M, Kumar V, Upadhyaya P, Pugazhenthi G, Fabrication of poly (methyl methacrylate)(PMMA) nanocomposites with modified nanoclay by melt intercalation, Compos. Interface. 21 (2014) 819–832.

Kuppa R, Moholkar VS, Physical features of ultrasound-enhanced heterogeneous permanganate oxidation, Ultrason. Sonochem. 17 (2010) 123–131.

Lerari B, Benaboura D, Preparation method effect on thermal properties of PMMA/Clay nanocomposites, Moroccan J. Chem. 3 (2015) 202-211. |

Maiti P, Nam PH, Okamoto M, Kotaka T, Gasegawa N, Usuki A, Influence of crystallization on intercalation, morphology, and mechanical properties of polypropylene/clay nanocomposites, Macromolecules 35 (2002) 2042–2049.

Midathana VR, Moholkar VS, Mechanistic studies in ultrasound-assisted adsorption for removal of aromatic pollutants, Ind. Eng. Chem. Res. 48 (2009) 7368–7377.

Montgomery DC, Design and analysis of experiments (5th ed.). John Wiley & Sons (Asia) Pte. Ltd., Singapore, 2004.

Montgomery DC, Runger GC, Applied statistics and probability for engineers (4th ed.). John Wiley & Sons, Inc., U.K., 2007.

Morgan AB, Harris JD, Exfoliated polystyrene clay nanocomposites synthesized by solvent blending with sonication, Polymer 45 (2004**)** 8695–8703.

Morya NK, Iyer PK, Moholkar VS, A physical insight into sonochemical emulsion polymerization with cavitation bubble dynamics, Polymer 49 (2008) 1910–1925.

Nalajala VS, Moholkar VS, Investigations in the physical mechanism of sono crystallization, Ultrason. Sonochem, 18 (2010) 345–355.

Patra SK, Prusty G, Swain SK, Ultrasound assisted synthesis of PMMA/clay nanocomposites: Study of oxygen permeation and flame retardant properties, Bull. Mater. Sci. 35 (2012) 27–32.

Prasad K, Sonawane S, Zhou M, Ashokkumar M, Ultrasound assisted synthesis and characterization of poly(methyl methacrylate)/$CaCO_3$ nanocomposites, Chem. Eng. J. 219 (2013) 254–261.

Reddy BR, Sivasankar T, Sivakumar M, Moholkar VS, Physical facets of ultrasonic cavitational synthesis of zinc ferrite particles, Ultrason. Sonochem. 17 (2010) 416–426.

Ryu JG, Lee JW, Development of poly(methyl methacrylate)-Clay Nanocomposites by Using Power Ultrasonic Wave, Macromol. Res. 10 (2002) 187–193.

Ryu JG, Park SW, Kim, H, Lee JW, Power ultrasound effects for in situ compatibilization of polymer–clay nanocomposites, Mater. Sci. Eng. 24 (2004) 285–288.

Sivasankar T, Paunikar AW, Moholkar VS, Mechanistic approach to enhancement of the yield of a sonochemical reaction, AIChE J. 53 (2007) 1132–1143.

Tsai TY, Lin MJ, Chuang YC, Chou PC, Effects of modified clay on the morphology and thermal stability of PMMA/clay nanocomposites, Mater. Chem. Phys. 138 (2013) 230–237.

Unnikrishnan L, Mohanty S, Nayak SK, Ali A, Preparation and characterization of poly(methyl methacrylate)–clay nanocomposites via melt intercalation: Effect of organoclay on thermal, mechanical and flammability properties, Mater. Sci. Eng. A 528 (2011) 3943–3951.

Wang HW, Shieh CF, Chang KC, Chu HC, Synthesis and dielectric properties of poly (methyl methacrylate)–clay nanocomposite materials. Journal of applied polymer science, 97 (2005) 2175–2181.

Yilmaz O, Cheaburu CN, Durraccio D, Gulumser G, Vasile C, Preparation of stable acrylate/montmorillonite nanocomposite latex via in situ batch emulsion polymerization: effect of clay types, Appl. Clay Sci. 49 (2010) 288–297.

Zelikman E, Suckeveriene RY, Mechrez G, Narkis M, Fabrication of composite polyaniline/CNT nanofibers using an ultrasonically assisted dynamic inverse emulsion polymerization technique, Polym. Adv. Technol. 21 (2010) 150–152.

Zhao Q, Samulski ET, A comparative study of poly(methyl methacrylate) and polystyrene/clay nanocomposites prepared in supercritical carbon dioxide, Polymer 47, (2006) 663–671.

Zhu J, Start P, Mauritz KA, Wilkie CA,Thermal stability and flame retardancy of poly (methyl methacrylate)-clay nanocomposites. Polymer Degradation and Stability, 77 (2002) 253–258.

Zidelkheir B, Boudjemaa S, Abdel GM, Djelloui B, Preparation and characterization of polystyrene/montmorillonite nanocomposite by melt intercalative compounding, Iran. Polym. J. 15, (2006) 645–653.

CHAPTER 3

INVESTIGATIONS IN TWO-STEP ULTRASONIC SYNTHESIS OF PMMA/ZNO NANOCOMPOSITES BY IN–SITU EMULSION POLYMERIZATION

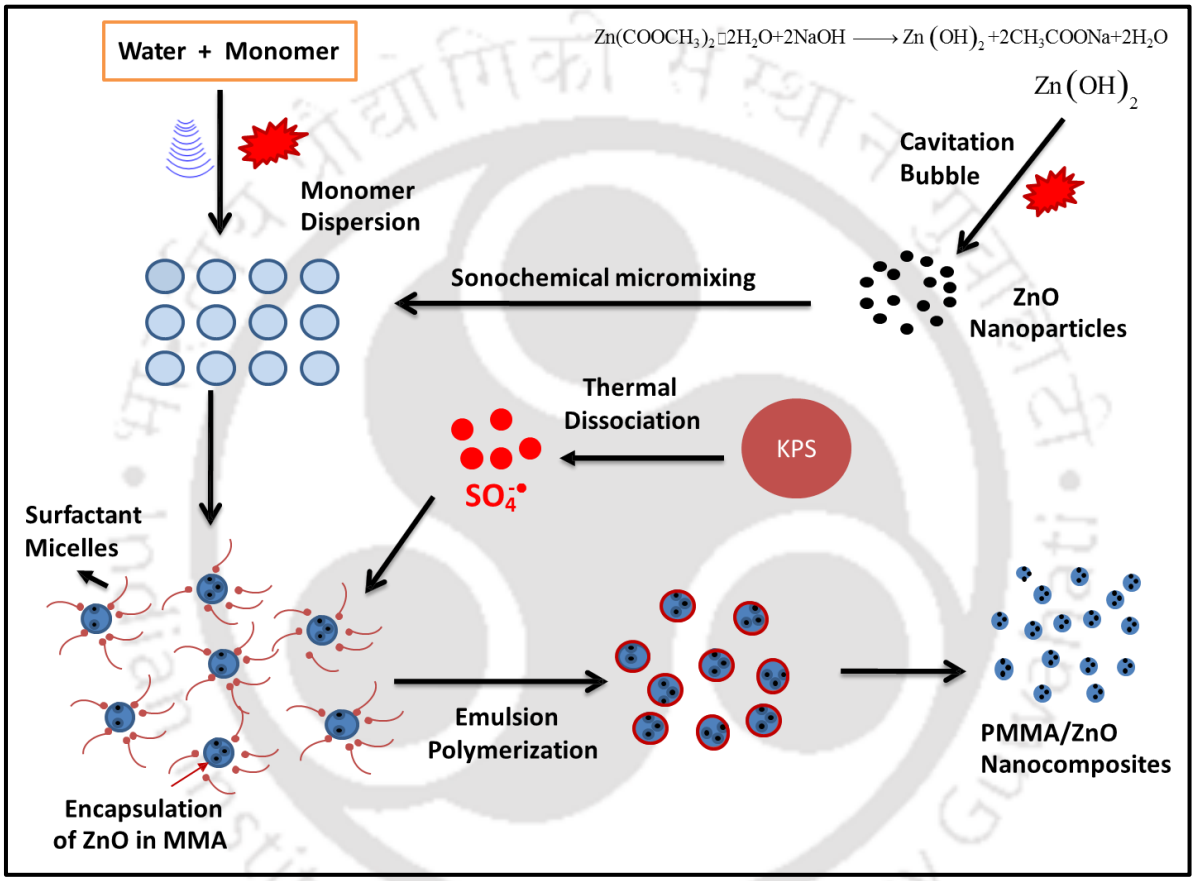

CHAPTER 3

Investigations in Two-Step Ultrasonic Synthesis of PMMA/ZnO Nanocomposites by In–situ Emulsion Polymerization

3.1 Introduction

Among various nanoscale filler materials employed for synthesis of polymer nanocomposites, the semiconductor metal oxides are of special interest due to their applicability in diverse areas such as light emitting diode (LED), solar cells and others non–optical devices (Dawidczyk et al., 2008; Vodnik et al., 2010; Mostafaei and Zolriasatein, 2012). These nanocomposites have processibility, flexibility and transparency by virtue of the polymer matrix, while optical properties are granted by the semiconductor nanoparticles.

Among different nanoscale semiconductor materials used as fillers in polymer nanocomposites, zinc oxide (ZnO) has shown high potential due to its unique electrical and optical properties (Li et al., 2012; Liao et al., 2012; Ocak et al., 2015). Nanoscale zinc oxide (ZnO) has a wide band gap of 3.37 eV in the UV region, due to which it is an efficient UV absorber (Huang et al., 2010; Matsuyama et al., 2012). Moreover ZnO also has large excitonic binding energy (60 meV), high chemical stability and large growth temperature. Significant literature has been published in the synthesis of ZnO with wide range of size and structure (Wahab et al., 2007; Bhatte et al., 2011; Kumar et al.; 2013). Among different polymer nanocomposites employing ZnO, the nanocomposite with polymethyl–methacrylate (PMMA) have been widely investigated for their applicability in UV protecting film and

plates, antireflective coating, transport barrier, or protective layers and enhanced thermal stability (Anzlovar et al., 2010; Chakraborthy et al., 2013; Soumya et al., 2014). Several earlier papers have addressed the matter of synthesis of PMMA/ZnO nanocomposite. This literature has also reported different techniques for synthesis of ZnO nanocomposites that have variety of shape and morphologies. A summary of previous literature , on synthesis of PMMA/ZnO nanocomposites is presented in Table 3.1.

For achieving efficient properties of polymer nanocomposites, uniform and homogenous distribution of the nano filler into the polymer matrix is of crucial importance. The nanoparticles or nanocrystals have tendency to agglomerate due to high free surface energy. Surface modification of zinc oxide with stabilizing polymer hydrophobic ligands such as alkyl silanes, oligomeric alkyl silicones, alkyl phosphonic acid and fatty acid is a common technique used for avoiding agglomeration of the ZnO particles (Liu et al., 2006; Tang et al., 2006; Abbasian et al., 2013). Methyl methacrylate and other acrylic monomers are grafted on to the modified surface of the particles . Surface modification of ZnO particles also helps in enhancing their miscibility with polymer matrix. Another technique adopted for uniform and homogenous distribution of ZnO nanoparticles in PMMA matrix is in–situ polymerization, which include in–situ polymerization of MMA monomer in presence of surface modified of ZnO particles and /or in situ preparation of ZnO particles in polymer matrix using different techniques (Zhang et al., 2011; Zhang et al., 2013).

In the present study, we have reported a new two–step methodology of ultrasound–assisted in–situ emulsion polymerization for synthesis of PMMA/ZnO nanocomposites. In the first step of this technique, ZnO nanoparticles have been synthesised by ultrasound–induced hydrolysis of zinc acetate to zinc hydroxide, followed by in–situ thermal decomposition of zinc hydroxide to nanoscale ZnO through transient cavitation bubbles. In the second step, the in–situ emulsion polymerization of MMA monomers with ZnO particles

(in native form – without surface modification) has been carried out under ultrasound irradiation. This technique essentially uses the physical and chemical effects of ultrasound for dual purpose: (1) synthesis of zinc oxide nanoparticles with narrow size distribution, and (2) polymerization of MMA monomers with uniform and homogeneous encapsulation of ZnO particles in the matrix without the requiring surface modification. We have also carried out extensive characterization of synthesised PMMA/ZnO nanocomposites for the thermal, mechanical, electrical and optical properties under different loading of zinc oxide particles. The ultrasound–assisted technique for in–situ synthesis of PMMA/ZnO nanocomposites is much simpler and easier than previously reported techniques, and yet highly effective in imparting the nanocomposite desired thermal, mechanical, electrical and optical properties, as explained in subsequent sections.

Table 3.1: Summary of previous literature on PMMA/ZnO nanocomposites

Reference No.	Polymerization technique	Experimental Conditions	Major Findings and Conclusions
Hong et al. (2006)	In situ emulsion polymerization ZnO particles formed by homogeneous precipitation Grafting of PMMA onto ZnO nano particles introducing functional double bonds	Radical grafting polymerization in non-aqueous medium Polymerization temperature = 85°C, polymerization time = 2.5 h	Increased thermal stability of PMMA/ZnO composite as compared to the neat PMMA The grafting technique reduces the aggregation of the ZnO nanoparticles.
Tang et al. (2006)	Grafting of PMMA on the surface of nano-ZnO particles Radical copolymerization of methyl methacrylate and methacrylic acid	Modification of ZnO surface followed by In situ emulsion polymerization. T = 75°C, reaction time = 8 h, magnetic stirring (250 rpm).	Uniform dispersion of ZnO nano particles in PMMA matrix. Increase the UV-shielding properties of the PMMA/ZnO nanocomposites
Liu and Su (2006)	Synthesis of oleic acid modified zinc oxide particles In-situ polymerization of modified ZnO particles with methyl methacrylate in toluene solvent	Modification of the surface of ZnO followed by 30 min sonication. T = 75°C, reaction time = 5 h followed by 30 min sonication	Improved thermal stability of PMMA/ZnO nanocomposites obtained as compare to the PMMA only. UV Visible analysis shown high absorption in the ultraviolet region and low absorption in the visible region.
Agrawal et al. (2010)	Solvent blending method DMAc (N,N-dimethylacetamide) was used as a solvent for dispersion of ZnO particles in PMMA matrix	. Dispersion was done at 70°C for 2 h followed by 30 min sonicatoion.	Increase in thermal, mechanical and optical properties with small loading of ZnO. High transparent and keeping better resistance of UV light
Kulyk et al. (2011)	Solvent blending method PMMA/ZnO was blended with 1,2,2-trichloroethane	Spin coating Technique used for preparation of thin film of PMMA/ZnO Angular speed (1000 rpm)	Highly transparent thin film of PMMA/ZnO nanocomposite The binding energy of donor-bound excitons was found 51 meV at 20°C.

Table 3.1 (*continued…*)

Zhang et al (2011)	In situ emulsion polymerization by synthesis of poly (methyl methacrylate)-co-poly(zinc methacrylate acetate);	Free – radical copolymerization of Acetic and methacrylic acid in presence of ZnO T = 70°C, , reaction time = 4 h	Thermal stability of PMMA/ZnO increased significantly as compare to the pristine PMMA Uniform dispersion of ZnO nano crystals without any agglomerations. The transparent ZnO/PMMA nanocomposite films exhibited good optical properties
Sharma et al. (2011)	The nanocomposite was prepared with Solvent casting method Dichloromethane used as a solvent for PMMA blending	Synthesis of ZnO by reacting with Zinc acetate dihydrate with NaOH 2-mercaptoethanol were used as a capping agent during the synthesis of ZnO	Stability and uniform particle size distribution of ZnO nanoparticles in PMMA matrix. PMMA/ZnO nanocomposite showed increased in green luminescence at 527 nm
Zhang et al.(2013)	Solvent blending method were used Chloroform were used as solvent with addition of TPM as a coupling agent	Successfully synthesis of the modified of ZnO nano particles by sol-gel route. T = 70°C, reaction time = 2 h. magnetic stirring time = 1.5 h	Transparent PMMA/ZnO nanocomposite. High UV-absorbing capability Improved the thermal stability of PMMA/ZnO nanocomposites as compare to the pristine PMMA.
Abbasian et al. (2013)	Synthesis was done by Atom transfer radical polymerization Copper was used as a metal catalyzed radical polymerization for the hybrid linkage in between PMMA and ZnO	Synthesis of ZnO by precipitation method followed by its surface Modification. ATRP polymerization of PMMA followed by grafting of ZnO nano particles.	Surface modification of ZnO reduced the aggregation of ZnO. DSC analysis showed the increase in T_g of PMMA/ZnO nanocomposites. TGA showed the improved thermal stability of PMMA/ZnO nanocomposites composites as compare to the neat PMMA.

3.2 Experimental

3.2.1 Materials

Following chemicals have been used in this study: methyl methacrylate (MMA, monomer, GR grade, Hi–Media), zinc acetate (Merck), sodium hydroxide (Merck), sodium dodecyl sulfate (SDS, surfactant, Merck, AR grade) and potassium persulfate (KPS, Merck, AR grade). Before the polymerization reactions, the inhibitor in MMA monomer was removed by adsorption technique. MMA was passed two times through a bed of neutral alumina powder to remove the inhibitors present in the monomer.

3.2.2. Step 1: Synthesis of nano sized ZnO

4.38 g zinc acetate dihydrate was dissolved in 100 mL of Millipore water, 20 mL of 1 M NaOH solution was added to this solution and the mixture was sonicated in a jacketed glass reactor (detailed given in next section) using a probe type micro–processor controlled programmable ultrasound processor with frequency of 20 kHz (Sonics and Materials Inc., Model: VCX 500) and a diameter of 25 mm in continuous mode. The total reaction time was 60 min. The processor was operated at 40% of the maximum power, i.e. 200 W. The reaction temperature was maintained at 25 ± 2^{o}C by circulating cold water in the jacket of reaction flask. After 45 min of sonication, an additional quantity of 5–10 mL NaOH was added to reaction mixture to ensure completion of conversion of zinc acetate. At the end of reaction, the white colored solid product was separated by centrifugation (10 min, 4000 rpm), and then washed with distilled water 3 to 4 times to remove sodium acetate. The white precipitate was filtered and washed with the methanol several times to remove ionic impurities, and finally vacuum dried at 60^{o}C for 12 h. Dried ZnO was then calcined at 500^{o}C for 4 h, and further used for characterization and synthesis of nanocomposites.

***Reaction mechanism and growth of ZnO nano powder*:** The synthesis of ZnO nanoparticles has a two–step reaction mechanism, as depicted by the following reactions:

$$Zn(COOCH_3)_2 \cdot 2H_2O + 2NaOH \longrightarrow Zn(OH)_2 + 2CH_3COONa + 2H_2O$$

$$Zn(OH)_2 \xrightarrow{Ultrasound} ZnO + H_2O$$

The first step is formation of zinc hydroxide from hydrolysis of zinc acetate. The zinc hydroxide is then decomposed by transient cavitation bubbles to yield ZnO. This phenomenon could be explained as follows: cavitation is essentially nucleation, growth and transient collapse of tiny gas bubble driven by pressure variation induced by propagation of ultrasound wave (Mason and Lorimer, 2002; Nalajala et al., 2011; Patidar et al., 2012). During the transient collapse, the temperature and pressure conditions inside the bubble reach extreme (> 5000 K, > 500 bar) (Moholkar et al., 2003; Reddy et al., 2010; Bhanvase et al., 2012). At these conditions, the thin liquid film in contact with the bubble surface (or bubble–liquid interfacial region) also gets heated to moderate temperatures (500 to 600 K). The zinc hydroxide molecules present in this film can undergo thermal decomposition to yield ZnO. It should be noted that transient cavitation also gives rise to formation of free radicals such as $^{\bullet}H$ and $^{\bullet}OH$ through dissociation of vapor molecules entrapped in the bubble. These radicals also assist the first step of hydrolysis of zinc acetate to zinc hydroxide. However, the context of present study, as the hydrolysis reaction is carried out in alkaline medium (with addition of NaOH), the hydrolysis is predominantly due to OH^- ions, and the role of $^{\bullet}OH$ radicals is expected to be relatively small.

3.2.3. Step 2: Synthesis of PMMA/ZnO nanocomposites

The polymerization reactions for synthesis of PMMA/ZnO nanocomposites were carried out in a jacketed glass reactor. The optimum values of reaction parameters for maximum monomer conversion (from results of Chapter 2). were as follows: SDS = 0.87 g,

MMA = 15 g and KPS = 0.75 g. The ZnO loading in the reaction mixture was varied in the range of 1-5 wt% of monomer. All experiments were conducted using Millipore water as the bulk medium. Total volume of reaction mixture was 60 mL. The dimensions of the polymerization reactor were: height 70 mm, inner diameter = 50 mm, inner diameter of jacket = 62 mm, and reactor thickness 2 mm. The reactor had an outer jacket for water circulation to maintain temperature of reaction mixture at desired value (65 ± 2^{o}C). In order to avoid induction of oxygen in the reaction mixture, nitrogen (at flow rate of 2 L/min) was sparged through reaction mixture during reaction. Moreover, a blanket of nitrogen was maintained above surface of the reaction mixture. The rate of polymerization (or extent of monomer conversion) was monitored by withdrawal of aliquots of reaction mixture at regular time interval. The monomer conversion was determined using gravimetric technique described by Bradley and Grieser (2002). After completion of the polymerization reaction, the total reaction mixture was dried in vacuum oven at 65^{o}C for 15 h to remove the moisture and unconverted monomer. To remove the surfactants present in the dried latex particles of PMMA/ZnO nanocomposite, the particles were washed several times with water followed by filtration. The surfactants free PMMA/ZnO nanocomposite particles were further vacuum dried and used for characterization.

3.2.4 Characterization of ZnO and PMMA/ZnO nanocomposites

Two reaction products, viz. nanosize ZnO particles and PMMA/ZnO nanocomposites were characterized for physical/ structural morphology with following techniques: **(1) XRD*:*** The crystallinity and crystal phases of the synthesized nanostructures were analyzed with X–ray diffraction (XRD, D8 Advanced, Bruker) spectroscopy with Cu –Kα radiation (λ = 1.54 Å) in the range of 2θ = 5–70^{o}. **(2) FTIR*:*** Fourier Transform Infrared Spectroscopy was carried out at room temperature by the FTIR spectrophotometer (Shimadzu). **(3) UV–Visible:** UV–visible spectroscopy of thin film was performed using Lambda 35 spectrometer from

Perkin Elmer. **(4) Thermo–gravimetric analysis:** Thermal stability of the samples was determined by TGA instrument (NETZSCH TG 209F1 Libra) with heating rate of 10^{o}C/min under nitrogen environment. **(5) Differential scanning calorimeter:** The glass transition temperature of PMMA/ZnO nanocomposites was determined by DSC instrument (Metler Toledo–1 series) with heating rate of 10^{o}C/min under nitrogen environment **(6) Electrical properties:** The electrical conductivity and dielectric loss of nanocomposites was determined by forming circular pellets of nanocomposites with silver painted on both sides. Analysis was performed at 25^{o}C in the frequency range of 100 Hz to 2 kHz using the LCR meter (Wayne Kerr Electronics Pvt. Ltd., Model 1J43100). **(7) Tensile strength, Young's modulus and percentage elongation:** The mechanical properties of the PMMA/ZnO nanocomposites were determined with Universal Testing Machine (INSTRON 8801, UK). **(8) FE–SEM, TEM and EDX:** Structural and elemental morphology of ZnO and PMMA/ZnO nanocomposite was assessed using Field Emission Scanning Electron Microscopy (Zeiss, Model: Sigma), Transmission Electron Microscopy (Jeol, Model: JEM 2100) and Energy Dispersive X-ray Spectroscopy (Zeiss, Model: Sigma) micrographs. For FE-SEM analysis, the nanocomposite material was deposited in the form of thin film on carbon tape. The surface of the thin nanocomposite film was gold-sputtered using magnetron device. The micrographs of the nanocomposite film were obtained using FESEM microscope. The samples for the TEM analysis were prepared by initially dispersing nanocomposite samples (at a concentration of 0.5 mg/mL) in dimethyl formamide (DMF) in the form of fine particles using sonication (or ultrasound irradiation). A drop of this solution was placed on a copper grid (200 mesh). Finally the images were recorded at an accelerating voltage of 200 kV. **(9) Particle size distribution:** Particle size distribution of ZnO and PMMA/ZnO nanocomposite particles was determined by dynamic light scattering (DLS) instrument (Beckman Coulter, Switzerland; Model Delsa Nano C). The procedure followed for the particle size distribution was as

follows: a few drops of the reaction solution, which contained the latex particles of either neat PMMA or its ZnO Nanocomposites, were taken in an glass tube after completion of polymerization, and were diluted with millipore water. The diluted samples were further sonicated for 5 min for deagglomeration and uniform dispersion/suspension of the latex particles. This suspension was analyzed for particle size and zeta potential measurement using the DLS equipment.

3.3 Results and Discussion

We present the results of our study in following sequence: (1) characterization of sonochemically synthesized ZnO nanoparticles, (2) kinetic analysis ultrasonic synthesis of PMMA/ZnO nanocomposites, and (3) characterization of the PMMA/ZnO nanocomposites.

3.3.1 Characterization of ZnO

***FE–SEM micrographs, EDX spectrum and particle size distribution*:** FE–SEM micrographs of ZnO nanoparticles in native (original) and calcined form are shown in Figs. 3.1A and B, respectively. The morphology of the original ZnO nanoparticles is that of rod–type with wide variation in sizes. The length of ZnO nanorods is in the range 100–400 nm and width in the range of 20–50 nm. Moreover, there is strong agglomeration among the particles. As seen from Fig. 3.1B, the morphology of the ZnO changes significantly after calcination. The calcined ZnO particles have either cubical or hexagonal morphology and with narrower size distribution (or more uniform size) due to growth and reorganization of ZnO nanoparticles through Ostwald ripening process. The EDX spectrum of the calcined ZnO particles depicted in Fig. 3.1C clearly shows presence of Zn and O as elementary components without any traces of acetate and hydroxide impurities. EDAX spectrum also shows a small peak at 2.1, which corresponds to gold (Au) deposited on the surface of the particle during coating of the sample. The particle size distribution (PSD) analysis of calcined ZnO is shown in Fig. 3.1D.

The PSD measurement yields following parameters: (1) $d(0.5)$ – mass median diameter, (2) $d(0.1)$ – particle size below which 10 wt% of total particles lie, (3) $d(0.9)$ – particle size below which 90 wt% of total particles lie and (4) d_{peak} – peak diameter. For the calcined ZnO particles, these parameters are: $d(0.1)$ = 42.7 nm, $d(0.5)$ = 81.2 nm, $d(0.9)$ = 161.1 nm, d_{peak} – 96.4 nm. The span or width of the PSD was calculated as: $[d(0.9) - d(0.1)]/d(0.5)$ = 1.46. The calcination of ZnO particles leads to narrower and uniform crystal structure due to removal of unwanted impurities such as hydroxyl and acetate ions.

***XRD Analysis*:** The X–ray diffractograms of original and calcined ZnO particles are shown in Fig. 3.2A. Calcined ZnO nanoparticles show sharper diffraction peaks in the X–ray diffractogram as compared to the original particles, which indicate higher crystallinity of ZnO nanoparticles after calcination. The peaks at ($2\theta \sim 8^{o}$) in original ZnO correspond to sodium acetate and other impurities. Calcination of ZnO at 400^{o}C removes these impurities in addition to reorganization (Ostwald ripening process) of ZnO granules with initial wide size distribution, which imparts them better crystallinity with more uniform size distribution. X–ray diffractogram of calcined ZnO (Fig. 2A) shows planes (1 0 0), (0 0 2), (1 0 1), (1 0 2), (1 1 0), (1 0 3), (1 1 2), which correspond to hexagonal wurtzite structure of ZnO. The peaks at various planes can be used to determine the crystallite size using Scherrer formula: $D = K\lambda/\beta\cos\theta$, where K = shape factor (typical value 0.89), λ = X–ray wavelength (1.54A^{o}), β = peak broadening at half maximum, and θ = Braggs or diffraction angle. The sizes of calcined ZnO particles have been calculated using Scherrer formula are in the range of ~ 22–58 nm and listed in Table 3.2.

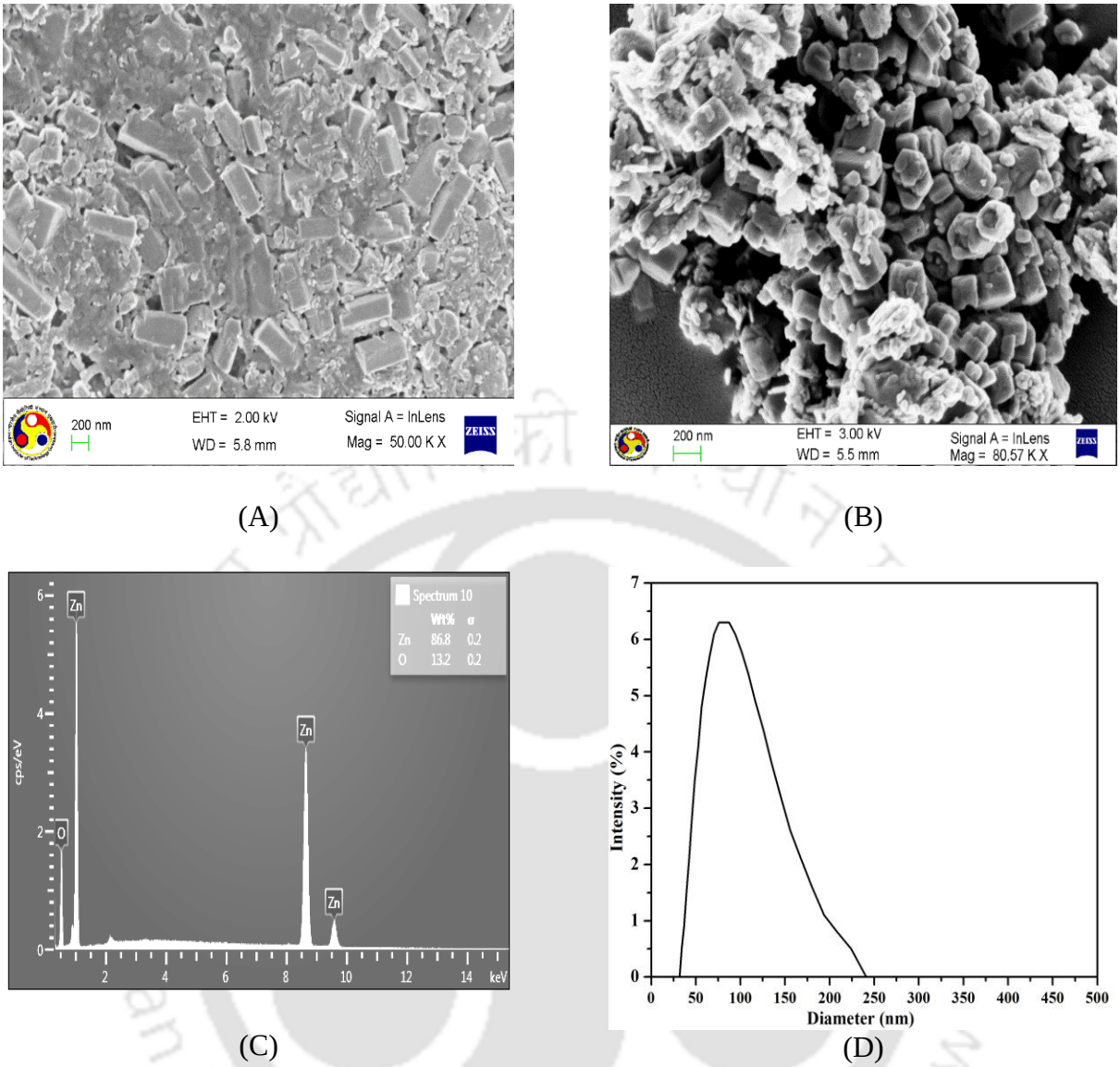

Figure 3.1: Characterization of ultrasonically synthesized ZnO nanoparticles. (A) FE-SEM micrographs of uncalcined ZnO. (B) FE-SEM micrograph of calcined ZnO. (C) EDX spectrum of calcined ZnO. (D) Particles size distribution analysis of calcined ZnO.

Table 3.2: Determination of ZnO crystal size on the basis of Scherrer's formula

Plane (*hkl*)	Braggs angle 2θ (deg)	FWHM (deg)	Size (nm)
(1 0 0)	32.50	0.27	32.01
(0 0 2)	34.80	0.15	57.98
(1 0 1)	36.50	0.30	28.75
(1 0 2)	47.50	0.32	28.34
(1 1 0)	56.55	0.35	26.93
(1 0 3)	62.80	0.32	30.40
(1 1 2)	67.95	0.45	22.24

FTIR Spectrum: The quality and composition of the original and calcined ZnO particles has been assessed using FTIR spectroscopy at room temperature in the range of 400–4000 cm^{-1}. The FTIR spectra of original and calcined ZnO particles are shown in Fig. 3.2B. Broad peak in the range of 3200–3700 cm^{-1} in the spectrum of original or uncalcined ZnO particles illustrates O–H stretching and is attributed to residual water and NaOH (used during synthesis) on surface of ZnO. IR bands in the range of 600 – 1700 cm^{-1} correspond to C=O, C–O and C–H vibrations, respectively which are attributed to the impurities present on the surface of the ZnO particles. The band at 459 cm^{-1} corresponds to Zn–O stretching bond, which is characteristic of wurtzite phase of crystalline ZnO. This peak is present in the spectra of both original and calcined ZnO particles; however, the peak in spectrum of calcined ZnO is much sharper due to higher crystallinity of the particles due to calcination, as noted earlier.

***Thermogravimetric analysis*:** Thermogravimetric analysis (TGA) of the original and calcined ZnO particles has been shown in Figs. 3.2C and D, which depict the percentage weight loss profiles with temperature, and the derivative (differential thermogravimetry or DTG) curves of the same. The weight loss profile of original or uncalcined ZnO depicts weight losses at different temperature ranges. The weight loss at 100°C corresponds to removal of bound moisture left after drying. Weight losses in the range of 125°–324°C correspond to removal of zinc hydroxide, zinc acetate and sodium acetate remained on the surface of ZnO particles after synthesis. These weight losses are clearly evident in the peaks of DTG curves depicted in Fig. 3.2D. Large peak near 400°C in the DTG curve corresponds to thermal decomposition of residual or unconverted $Zn(OH)_2$ present in the ZnO product after sonication. TGA and DTG profiles of calcined ZnO, however, show absence of peaks corresponding to weight losses. The step of calcination removes moisture and impurities left on the surface of ZnO particles after synthesis, and also causes thermal decomposition of any residual or

unconverted $Zn(OH)_2$ in the product.

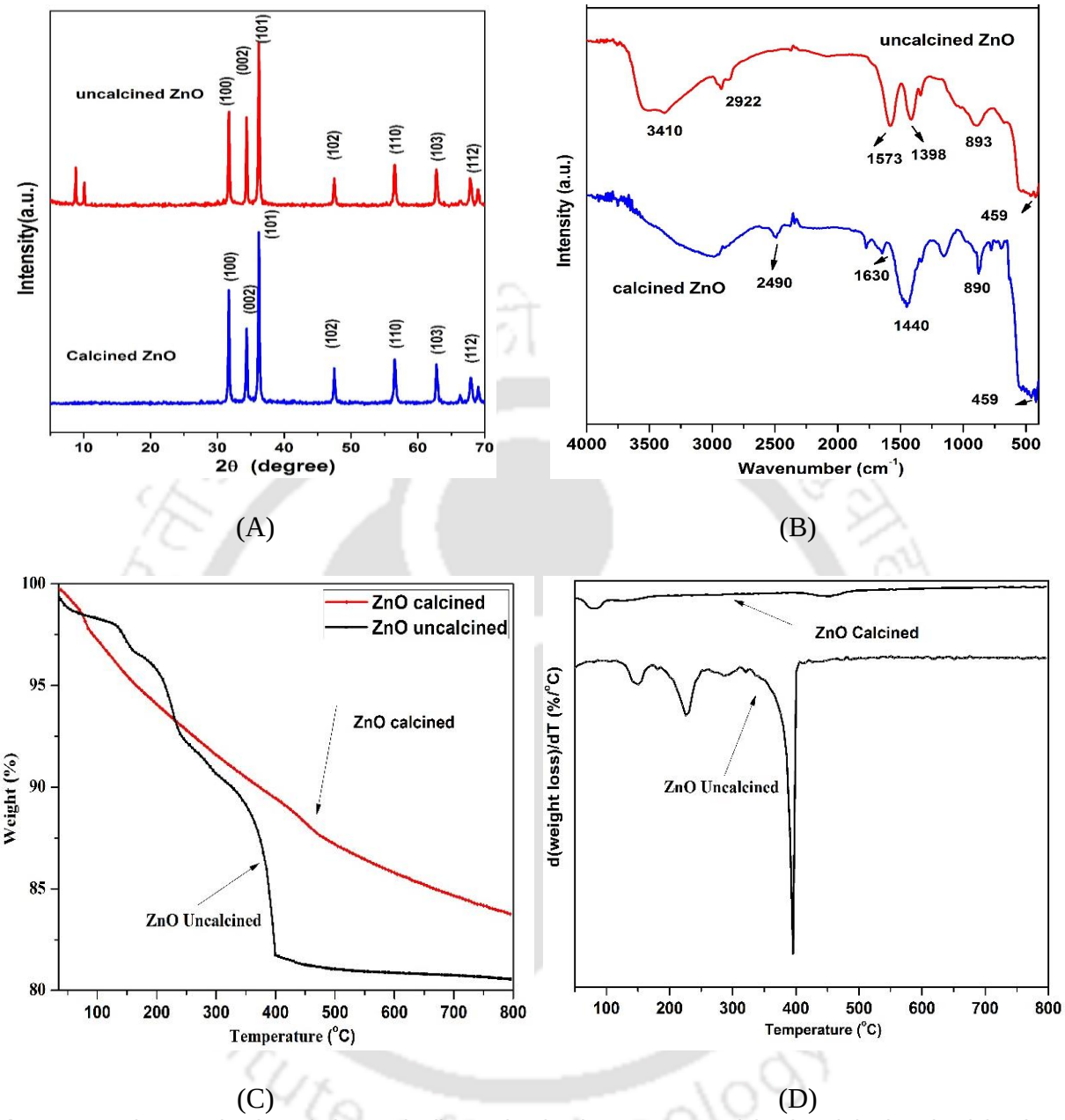

Figure 3.2: Characterization of ultrasonically synthesized ZnO nanoparticles in original and calcined form. (A) X-ray Diffractograms. (B) FTIR spectra (C) Thermogravimetric analysis (TGA) profiles of ZnO, (D) Differential Thermo -gravimetric (DTG) analysis of ZnO.

3.3.2 Kinetic analysis of In–situ synthesis of PMMA/ ZnO nanocomposites

Strong microturbulence generated by ultrasound and cavitation in the reaction mixture generates fine emulsion (in the form of droplets of micro– or even nanoscale dimensions) of monomer and water, in addition to uniform mixing of the initiator. This leads to uniform generation of the polymerization radicals in the reaction volume. Microtubulence also generates uniform dispersion of ZnO nanoparticles in the reaction volume and their entrapment inside monomer droplets. The time profiles of MMA conversion and rates of MMA polymerization in presence of different loadings of ZnO particles are shown in Figs. 3.3A and B, respectively. The initial rate of MMA polymerization is extremely rapid and more than 55% conversion is obtained with first 10 min of the reaction. The conversion rate falls very rapidly thereafter with ~ 75% conversion in 30 min and ~ 79% conversion at the end of 1 h. The rapid fall in the monomer conversion rate is attributed to consumption of both monomer and initiator due to which the rate of generation of radical species is reduced. In the present context, there are two sources of polymerization radicals, viz. initiator and transient collapse of cavitation bubbles. However, as demonstrated in previous chapter, the contribution of the radicals generated through cavitation bubbles is insignificant due to spatial non–uniformity in generation.

An interesting feature of the kinetics of MMA polymerization in presence of ZnO is marked reduction in initial polymerization rate with increasing ZnO concentration. A plausible explanation for this phenomenon is given as follows: during emulsification induced by ultrasound, the monomer droplets enter into the micelles of surfactant. The radicals generated in the bulk solution enter these micelles and polymerize the monomer droplets. ZnO particles added to the solution can adsorb on the surface of these micelles and cause restriction to mass transfer across micelles due to which the rate of polymerization reduces. Moreover, ZnO particles adsorbed onto the micelle surface may also cause hindrance to entry

of monomer droplet into the micelle. Monomer droplets present in "free form" in bulk solution may not undergo polymerization as rapidly and as efficiently as intra–miceller monomer due to limited interaction probability with the radicals. The reduction in polymerization rate shows direct variation with the quantity of ZnO present in the reaction mixture. Addition of surfactant to reaction mixture avoids agglomeration and deposition of the latex (PMMA/ZnO) nanoparticles onto the ultrasound probe, due to which the intensity of the ultrasound waves may reduce.

Analysis of kinetic data on MMA polymerization with different ZnO loadings with integral approach is shown in Figs. 3.3C. Third order (with respect to MMA monomer) kinetic model has been found to best fit the monomer conversion profiles with different ZnO loadings. It should be noted that similar kinetic behavior for MMA polymerization (or order of reaction with respect to MMA monomer) has also been reported by Bhanvase et al. (2012) in presence of clay. The third order rate constant of MMA polymerization in absence of ZnO is 0.07 $(L/mol)^{2}\cdot min^{-1}$, which shows sharp reduction as 0.05, 0.04, 0.03 $(L/mol)^{2}\cdot min^{-1}$, for 1, 2, 4 and 5 wt% loading of ZnO, respectively. An interesting study on kinetics of MMA polymerization in presence of aluminum powder has been published by Liu et al. (2010), in which contrary observation of increase in kinetics of polymerization with concentration of the nanofiller material has been reported. However, there is significant difference in the synthesis procedure followed by Liu et al. (2010) and the present study. The major difference is in the relative quantities of monomer and filler material. Liu et al. (2010) have used 10 g of aluminum powder for 6 g of monomer MMA. Liu et al. (2010) have reported that rate of polymerization varies directly with the concentration of the aluminum powder (with an exponent of 0.521). A probable reason underlying this result is that due to very large excess of aluminum powder in comparison to MMA monomer. The surface of aluminum powder offers sites for adsorption and polymerization of the MMA, and thus the rate of

polymerization increases with concentration of aluminum powder.

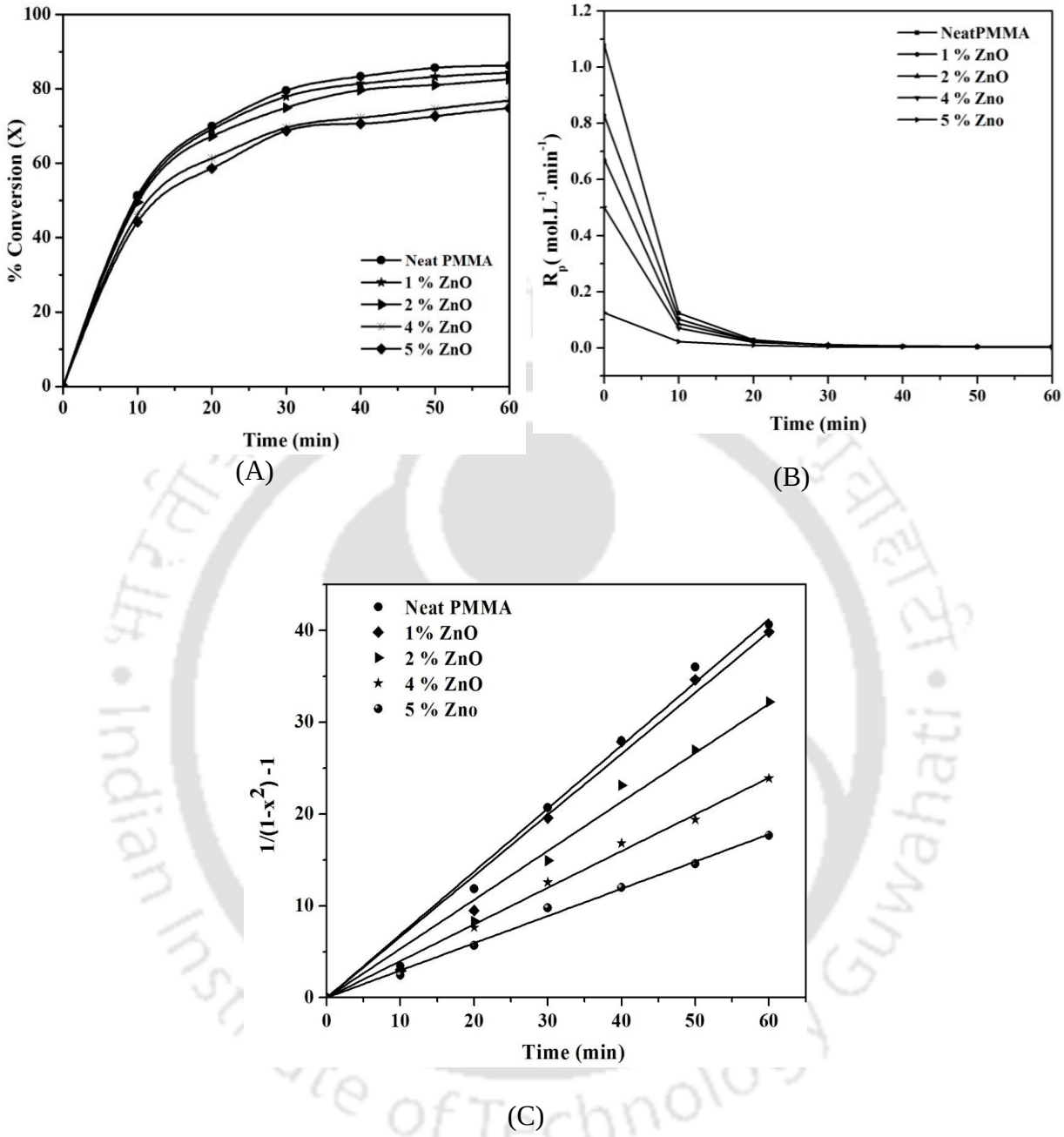

Figure 3.3: Kinetic analysis of synthesis of PMMA/ZnO nanocomposites. (A) Time profile of monomer (MMA) conversion with varying loading of the ZnO nanoparticles. (B) Time profile of the reaction rate with varying loading of the ZnO nanoparticles (C) Determination of kinetic constant of PMMA/ZnO nanocomposites.

3.3.3 Characterization of PMMA/ZnO nanocomposites

FE–SEM and TEM analysis: FE–SEM micrographs of the PMMA/ZnO nanocomposites synthesized with various ZnO loadings are depicted in Figs. 3.4A–D. Fig. 3.4A shows the micrograph of PMMA/ZnO nanocomposite synthesized with the lowest ZnO loading of 1 wt%. This micrograph shows uniform dispersion of ZnO particles in PMMA matrix. As the loading of ZnO particles is increased, interaction among the particles also increases, resulting in agglomeration of ZnO nanoparticles in the polymer matrix. This feature is evident from micrographs depicted Figs. 3.4B, C and D for PMMA/ZnO nanocomposites synthesized with ZnO loading of 2, 4 and 5 wt%. Fig. 3.4D shows highest agglomeration of ZnO particles. The causes underlying agglomeration of ZnO particles are two fold: (1) increasing concentration (or density) of particles in limited volume of the polymer matrix, and (2) formation of Zn–O–Zn bonds between the particles.

The TEM micrographs of PMMA/ZnO nanocomposites synthesized with varying ZnO loadings are shown in Fig. 3.5A–D. These micrographs confirm encapsulation of the ZnO nanoparticles into the polymer matrix. The translucent portion of the micrograph represents the polymer matrix while the black dots represent the ZnO nanoparticles. The size of the black dots is the smallest in Fig. 3.5A (nanocomposite with 1 wt% ZnO) with more–or–less uniform dispersion. On the other hand, relatively larger back dots seen in Figs. 3.5 B, C and D represent agglomerations of the ZnO particles in PMMA matrix.

XRD Analysis: Fig. 3.6A shows the X–ray diffractograms of PMMA and PMMA/ZnO nanocomposite with various loading of ZnO. For all nanocomposites, X–ray diffraction peaks have been recorded in the range of 2θ = 1–50^{o}. At lower 2θ value ~15^{o}, PMMA matrix (with no ZnO) shows a broad peak due to its amorphous nature. For PMMA/ZnO nanocomposites synthesized with loading of 1, 2, and 5 wt% of nanosize ZnO, new sharps peaks appear in the diffractogram in the range of 2θ = 20–40^{o}. These peaks essentially confirm presence of ZnO

nanoparticles (or nanocrystals) in the PMMA matrix with uniform dispersion. These peaks also indicate that incorporation of ZnO nanoparticles into the PMMA imparts the nanocomposite matrix more crystalline structure.

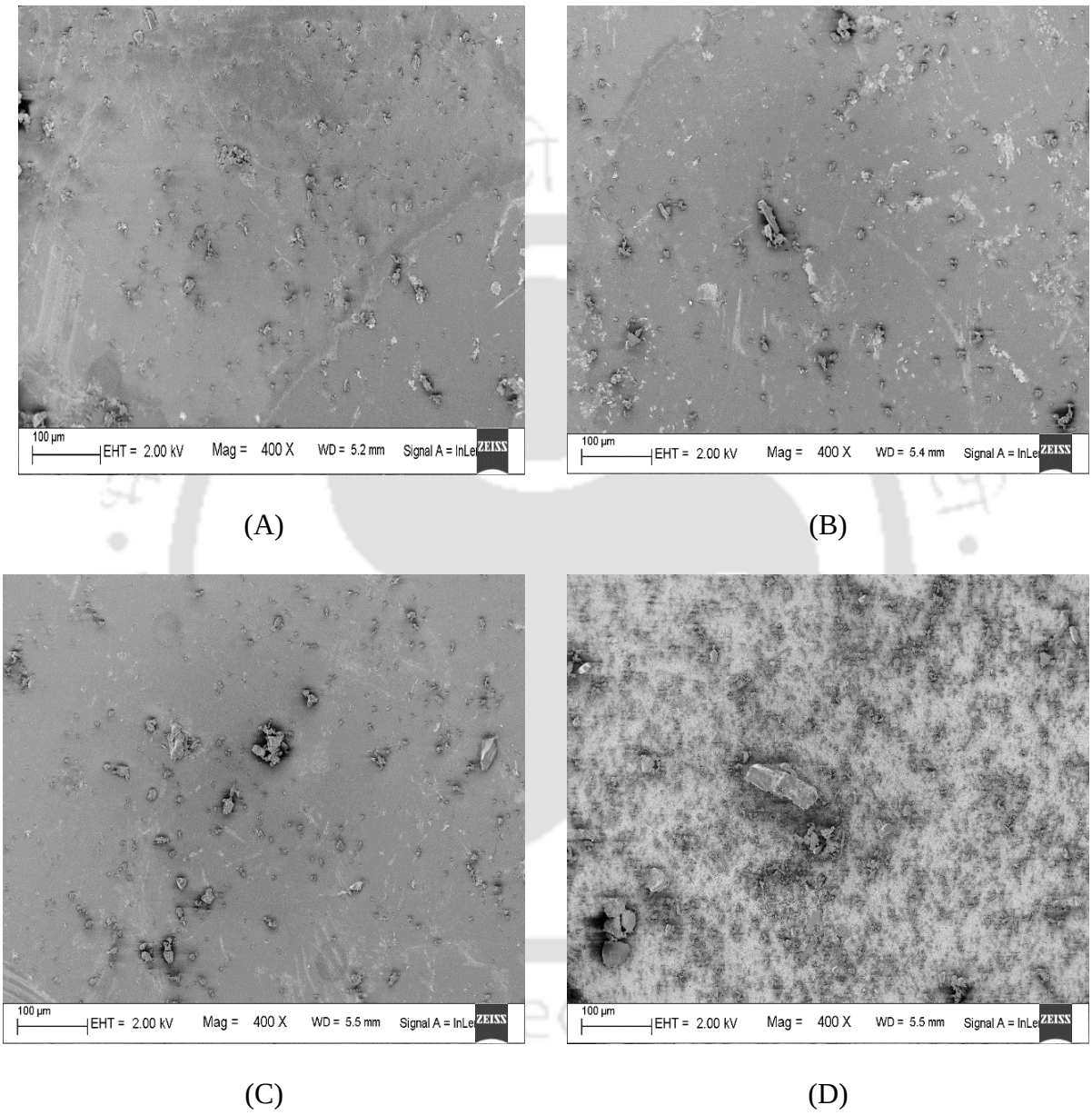

Figure 3.4: Field Emission Scanning Electron Microscope (FE-SEM) images of PMMA/ZnO nanocomposites synthesized with varying loading of calcined ZnO nanoparticles. (A) 1 wt% loading, (B) 2 wt% loading (C) 4 wt% loading (D) 5 wt% loading. For 4 wt% and 5 wt% loading, agglomeration of particles in the central portion of micrograph is clearly visible.

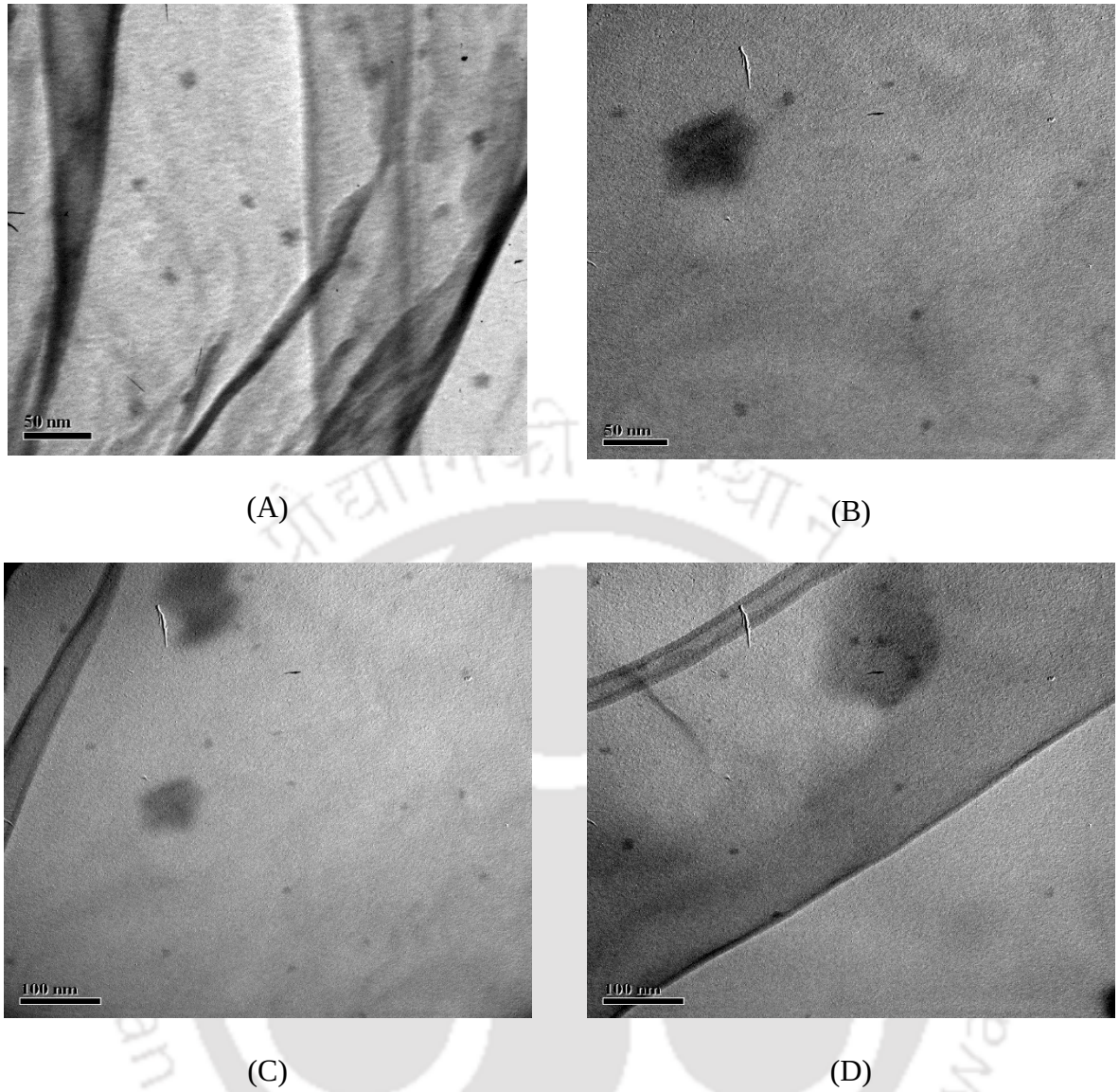

Figure 3.5: TEM micrographs of PMMA/ZnO nanocomposites synthesized with varying loading of ZnO nanoparticles (A) 1 wt% loading, (B) 2 wt% loading, (C) 4 wt% loading, (D) 5 wt% loading

FTIR analysis: FTIR spectra of ZnO, PMMA and PMMA/ ZnO nanocomposites (synthesized with different ZnO loadings) are shown in Fig. 3.6B. In the FTIR spectrum of calcined ZnO, the characteristic stretching mode of Zn–O vibration bands is seen in the range of 400 and 480 cm^{-1}. The broad peak in the range of 3400–3650 cm^{-1} corresponds to O–H stretching vibration of adsorbed water molecules during sample preparation. The characteristic peak at 1730 cm^{-1} in the spectrum of PMMA is attributed to C=O stretching vibration of acrylate carboxyl group. The peaks in the range of 1395–1450 cm^{-1} represent

deformation vibration of $–CH_3$ and $–CH_2$ groups in PMMA. Peaks in range of 1260–1040 cm^{-1} indicate C–O–C single bond stretching vibration. The introduction of ZnO nanoparticles in PMMA matrix (or formation of PMMA/ZnO nanocomposite) is confirmed by appearance of the characteristic Zn–O vibration band at 459 cm^{-1} in the spectrum of PMMA, which itself is characterized by peak at 1730 cm^{-1}.

***Particle size and zeta potential analysis*:** The results of size distribution measurements of PMMA and PMMA/ ZnO nanocomposites particles with varying ZnO loading are shown in Fig. 3.6C. The summary of this analysis is given in Table 3.3 that depicts cumulant (weight–averaged) diameter range of particles of PMMA and PMMA/ZnO nanocomposites. It could be inferred that cumulant diameters of PMMA and PMMA/ZnO nanoparticles ranged between 72.9 and 109.7 nm, which are significantly smaller than typical sizes of the PMMA nanocomposites (200–400 nm) reported in literature (Anzlovar et al., 2010; Bhanvase et al., 2011; Bhanvase et al., 2012). The principal cause underlying this effect is intense microturbulence and micromixing generated by sonication which creates extremely fine emulsion of reaction mixture with dispersion of monomer in the nanoscale droplets. This aspect is discussed at greater length in subsequent section, with reference to the predominant physical mechanism of polymer nanocomposite formation in presence of sonication or ultrasound irradiation. The span of the particle size distribution is seen to broaden with ZnO loading. Particles of PMMA alone show narrow size distribution, which successively broadens for the PMMA/ZnO nanocomposites with increasing ZnO loading from 1 to 5 wt%. A possible reason for increase in particle size distribution with ZnO loading could be aggregation of the ZnO particles.

The homogeneity and colloidal stability of nanocomposites has been estimated on the basis of zeta potential values. Zeta potential values of PMMA and PMMA/ZnO latex particles with varying ZnO loading are given in Table 3.3. The zeta potential value of only

PMMA particles was –64.32 mV, which demonstrates excellent stability of the latex particles [49]. With incorporation of ZnO nanoparticles in PMMA matrix, the (absolute) zeta potential value decreases indicating reduction in stability. For ZnO loading between 1–4 wt%, the zeta potential values are in the range of –43.6 to –45.7 mV, which correspond to good stability. For 5 wt% ZnO loading, high concentration of particles leads to agglomeration of particles inside the PMMA matrix. This results in further reduction in zeta potential to –38.7 indcating moderate stability (Greenwood et al., 1999).

Table 3.3: Summary of characterization of PMMA/ZnO nanocomposites: Particle size analyses, zeta potentials and glass transition temperatures

Name of Sample	Average diameter (nm)	Zeta potential (mV)	Glass transition temperature (^oC)	Electrical conductivity at 1 kHz (μS/cm)
Neat PMMA	72.9	-64.32	116.0	0.028
PMMA/ZnO (1 wt%)	77.7	-45.72	122.0	0.030
PMMA/ZnO (2 wt%)	81.7	-49.13	122.5	0.036
PMMA/ZnO (4 wt%)	91.2	-43.59	121.0	0.073
PMMA/ZnO (5 wt%)	109.7	-38.72	119.0	0.207

Table 3.4: Results of thermogravimetric analysis of PMMA and PMMA/ZnO nanocomposites

Name of Sample	$T_{5\%}$ (^oC)	$T_{50\%}$ (^oC)	Char Value (% at 600^oC)	% Encapsula-tion of ZnO
PMMA	267.40	326	0.28	--
PMMA/ ZnO (1 wt%)	271.25	366	0.30	0.32
PMMA/ ZnO (2 wt%)	279.32	367.52	2.28	2.46
PMMA/ ZnO (4 wt%)	279.86	368.10	4.26	4.82
PMMA/ ZnO (5 wt%)	278.56	367.22	6.85	7.76

Note: $T_{5\%}$ - temperature corresponding to 50% weight loss; $T_{50\%}$ – temperature corresponding to 50% weight loss

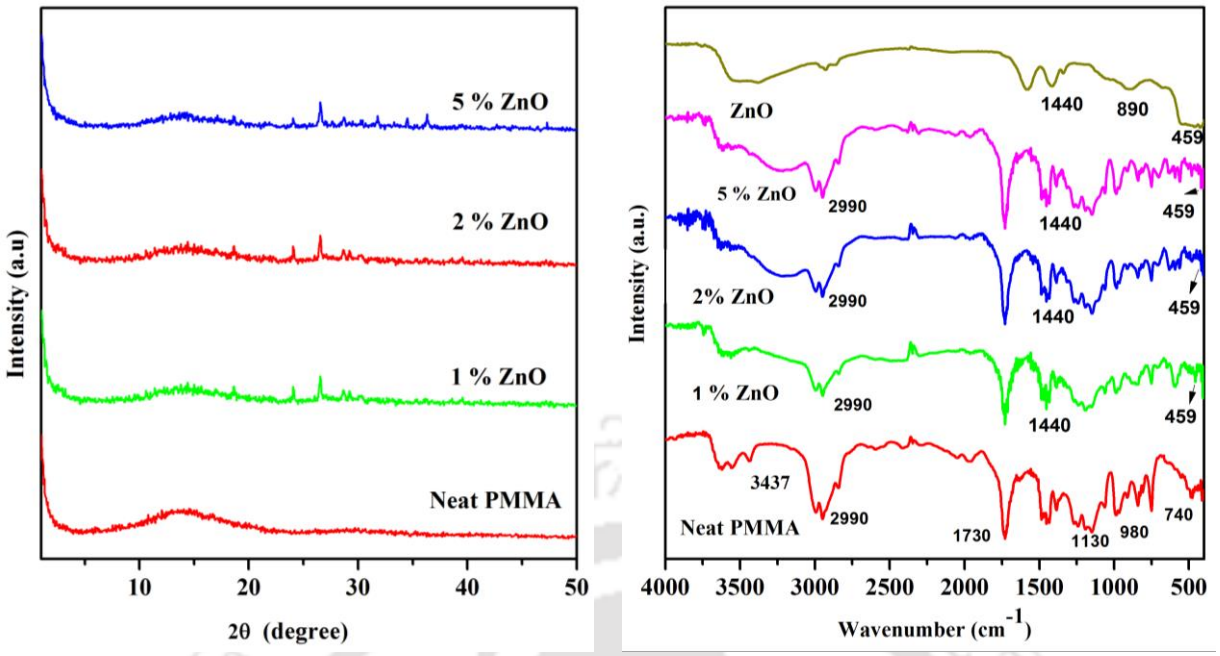

(A) (B)

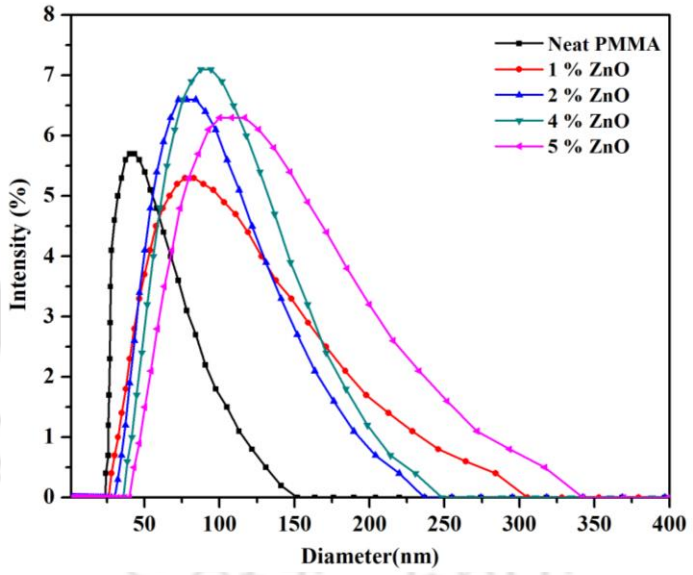

(C)

Figure 3.6: Characterization of PMMA/ZnO nanocomposite particles synthesized with varying loading of ZnO nanoparticles. (A) X-ray diffractograms of PMMA and PMMA/ZnO nano-composites; (B) FTIR spectra of PMMA/ZnO nanocomposites; (C) Analysis of particle size distribution of PMMA/ZnO nanocomposites.

***Thermogravimetric analysis**:* The thermal stability of PMMA/ZnO nanocomposites can be assessed with thermogravimetric analysis (TGA). TGA analysis of neat PMMA and PMMA/ZnO nanocomposites has been done under nitrogen environment with heating rate of $10^{o}C\ min^{-1}$. The TGA curves for neat PMMA and PMMA/ZnO nanocomposites are shown in Fig. 3.7A.1. The expanded view of the TGA curves in the temperature range of 250 to 400^{o}C are shown in Fig. 3.7A.2. The results of the TGA analysis are summarized in Table 3.4, which lists the temperatures for 5% and 50% weight loss of the samples. It could be observed from the result given in Table 3.4 that incorporation of ZnO nanoparticles in PMMA matrix increases degradation temperatures for both 5 and 50% weight loss indicating enhanced thermal stability. This is possible a consequence of hindrance offered by the ZnO nanoparticles to diffusion of volatile products of thermal decomposition through the PMMA matrix. For 5% weight loss, the rise in degradation temperature of PMMA/ZnO nanocomposites is 4 to 13^{o}C higher than neat PMMA for 1 to 5 wt% ZnO loading. Maxima in degradation temperature is seen for 4% ZnO loading. However, for 50% weight loss, a large rise of 40^{o}C is seen for nanocomposite with ZnO loading of 1 wt%. Thereafter, the degradation temperature is almost similar (± 2^{o}C) for all nanocomposites with 2 to 5 wt% ZnO loadings. The rise in degradation temperature for 50% weight loss is attributed to resistance offered by ZnO nanoparticles present in the PMMA matrix to homolytic scission of vinyl group in PMMA chain. The cross–linking of the polymeric chains induced by ZnO nanoparticles could also contribute to enhanced thermal stability in higher temperature range (Das et al., 2011).

The extent of encapsulation of ZnO particles in the polymer matrix has also been determined using TGA data. As evident from Fig. 3.7A.1, the thermal degradation of PMMA commences from 150^{o}C. The final temperature attained during TGA analysis is 600^{o}C, at which the entire polymer matrix is expected to get removed through thermal degradation. The

final matter that remains at the end of TGA analysis is the nanofiller material. 10 mg sample of PMMA/ZnO nanocomposites was used for the TGA analysis. Depending on the weight of residual material left at the end of TGA analysis for nanocomposites synthesized with different ZnO loadings, the percentage encapsulation of ZnO in polymer matrix has been depicted in Table 3.4.

The Differential Thermogravimetric (DTG) curves that depict the rates of thermal decomposition (or the derivatives of the TGA curves) of the PMMA/ZnO nanocomposites are given in Fig. 3.8A. Peaks of the DTG curves essentially indicate the temperature corresponding to maximum rate of degradation. As observed from Fig. 3.8A, the peak of the DTG curve for neat PMMA occurred at 376^{o}C, while the peaks of DTG curves for PMMA/ZnO nanocomposites occurred at enhanced temperatures of 385, 386.1, 386.4, 386.4^{o}C for 1, 2, 4 and 5 wt% ZnO loading, respectively. Thus, DTG analysis also confirms increase in the thermal stability of the PMMA/ZnO nanocomposites as compared to neat PMMA. Increased thermal degradation temperatures for PMMA/ZnO nanocomposites in our study are attributed to relatively smaller size of the ZnO particles (with higher surface area) and more uniform dispersion of these particles in the PMMA matrix under intense microturbulence due to sonication. Due to these features, the random thermal scission of PMMA chains is effectively prohibited by the ZnO particles. Rise in the cystallinity of the PMMA matrix after incorporation of the nanofiller ZnO, as evident from the XRD analysis of the nanocomposites presented earlier, also contributes to enhanced degradation temperature (or enhaced thermal stability). This feature is discussed in greater detail subquently during analysis of the mechanical properties of the nanocomposites.

DSC (Differential scanning calorimeter) analysis: The influence of incorporation of the ZnO nanoparticles inside the PMMA matrix on the molecular mobility of the PMMA chains can be assessed using DSC analysis. The molecular mobility is characterized by the property

of glass transition temperature (T_g). The DSC heating curves of neat PMMA and PMMA/ZnO nanocomposites are shown in Fig. 3.8B, and the values of glass transition temperatures are summarized in Table 3.3. T_g of neat PMMA is revealed to be 116^{o}C. PMMA/ZnO nanocomposite synthesized with 1 wt % loading of ZnO shows an enhanced T_g of 122^{o}C. Increase in T_g is attributed to restriction of the segmental motion of polymer chains in PMMA matrix with incorporation of ZnO nanoparticles. A similar result has also been reported by Hong et al. (2006) who observed increase in T_g of polystyrene with incorporation of ZnO in the polymer matrix. The trend in T_g of PMMA/ZnO nanocomposites, however, shows a maxima (122.5^{o}C) for 2 wt% ZnO loading. For higher ZnO loading of 4 and 5 wt%, T_g shows minor reduction. This result is possibly a consequence of non–uniform distribution of ZnO particles in PMMA matrix due to agglomeration at higher loading. These results indicate that the optimum ZnO loading for PMMA/ ZnO nanocomposite is 2 wt%.

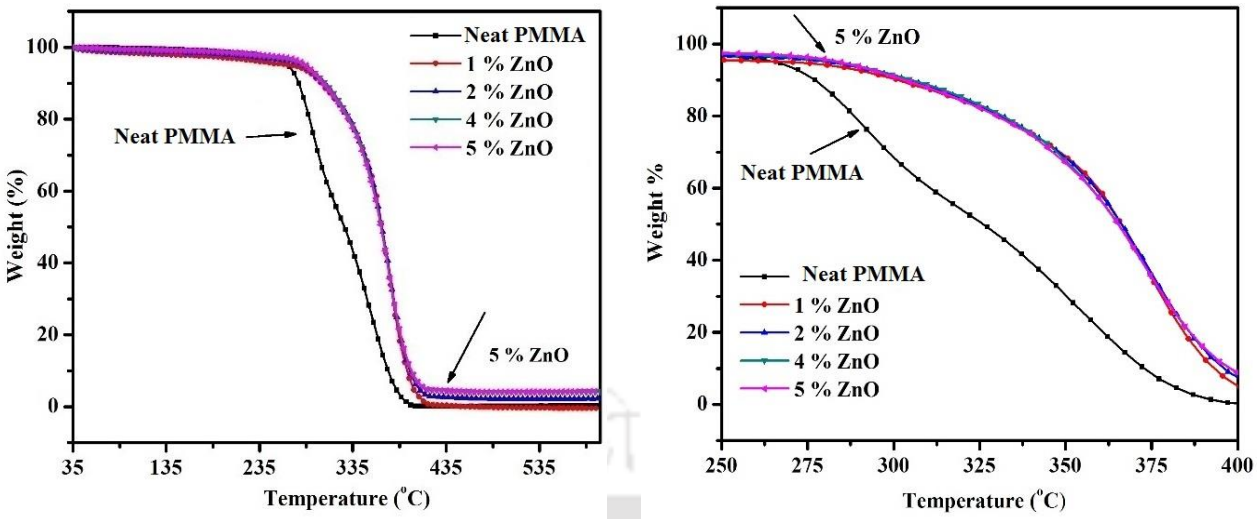

(A.1) (A.2)

Figure 3.7: Characterization of PMMA/ZnO nanocomposites synthesized with varying loading of ZnO nanoparticles. (A.1) Thermogravimetric (TGA) curves in full temperature range, (A.2) Expanded view of TGA curve in the temperature range of 250° to 400°C.

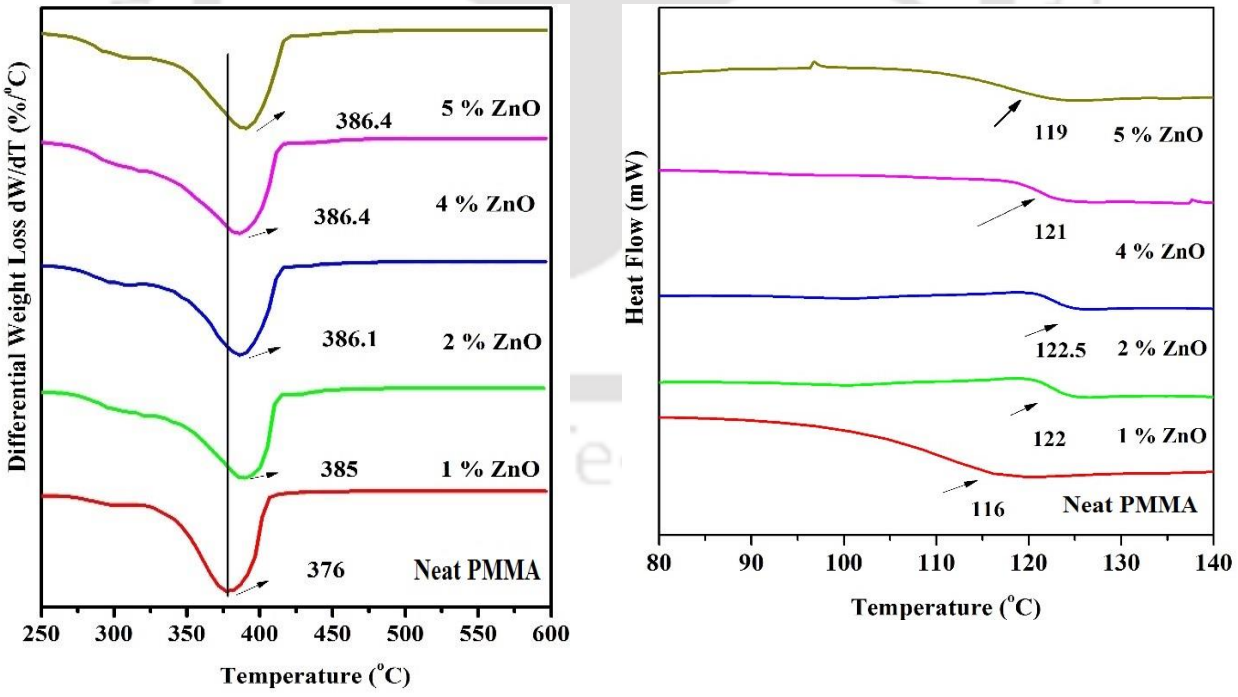

(A) (B)

Figure 3.8: Characterization of PMMA/ZnO nanocomposites synthesized with varying loading of ZnO nanoparticles. (A) Differential Thermogravimetric (DTG) curves of PMMA/ZnO nanocomposites. (B) Differential Scanning Calorimetric (DSC) curves of PMMA/ZnO nanocomposites

UV–Visible spectroscopy: The UV–Vis spectra of neat PMMA and PMMA/ZnO nanocomposites are shown in Fig. 3.9A. The UV absorption capacity of the neat PMMA is very poor, which is reflected in no absorption peak in its UV–Visible spectrum. For the PMMA/ZnO nanocomposites, an absorption peak is seen at 372 nm corresponding to the exciton state in the bulk ZnO (Kulyk et al., 2011). The intensity of this peak also rises with the ZnO loading. This is attributed to the quantum effect of the nanoparticles when the size of the particles is reduced to nanoscale. Moreover, no shift in this absorption length is observed (due to quantum confinement effect) because the predominant or peak size of the ZnO nanoparticles (96.4 nm) is much higher than the exciton Bohr radius of ZnO = 2.34 nm (Kulyk et al., 2011; Lin et al., 2005).

Electrical properties*:* The electrical conductivities of neat PMMA and PMMA/ZnO nanocomposites with variable frequency of current are illustrated in Fig. 3.9B with the values for 1 kHz frequency listed in Table 3.3. The electrical conductivity of neat PMMA is the lowest, and shows proportionate increase with ZnO loading during synthesis of nanocomposite. The highest electrical conductivity 0.2067 μS/cm is obtained for PMMA/ZnO nanocomposite with 5 wt% ZnO loading. This essentially means that the electrical conductivity of PMMA is significantly enhanced by incorporation of the ZnO nanoparticles in the polymer matrix. Moreover, the conductivity for PMMA and all nanocomposites is found to be a function of frequency of the current and vary proportionately with it. As noted by Abdul Rahman et al. (2013) who studied the electrical and optical properties of sago starch/ZnO nanocomposites, the increase in the conducticity of the nanocomposite is attributed to various factors such as number of charge carriers, mobility of free charge and availability of connections of the polar domains as the conduction pathway. In the present context, incorporation of ZnO nanoparticles in PMMA polymer matrix results in increment of the charge carriers leading to rise in conductivity.

Variations in the dissipation factor or loss tangent (tan δ) of the neat PMMA and PMMA/ZnO nanocomposites are shown in Fig. 3.9C. In the frequency range of 200 – 2000 Hz, neat PMMA has the highest dissipation factor, which reduces with increasing concentration of ZnO in the polymer matrix. The least dissipation factor is obtained for PMMA/ZnO nanocomposite with 5 wt% ZnO loading. Moreover, for nanocomposites with ZnO loadings of 4 and 5 wt%, the dissipation factor is also revealed to remain constant over large frequency range of 100 to 2000 Hz. An explanation for these results can also given as follows Abdul Rahman et al., (2013): the conduction path of the nanocomposite is a function of concentration of the filler ZnO particles. For neat PMMA and nanocomposites with low concentration of ZnO particles (for smaller loading of ZnO), the number of free charge carriers present in the polymer matrix is small leading to large interparticle distances or shorter conducting paths. As a consequence, the probability of charge trapping or charge neutralization is high, which results in higher dissipation factor (or higher tangent loss). Reverse is true for nanocomposites with high concentration of filler ZnO particles (for higher ZnO loading during synthesis). In this case, the interparticle distances are shorter, the conduction paths are longer leading to lesser charge trapping and neutralization and smaller dissipation factor.

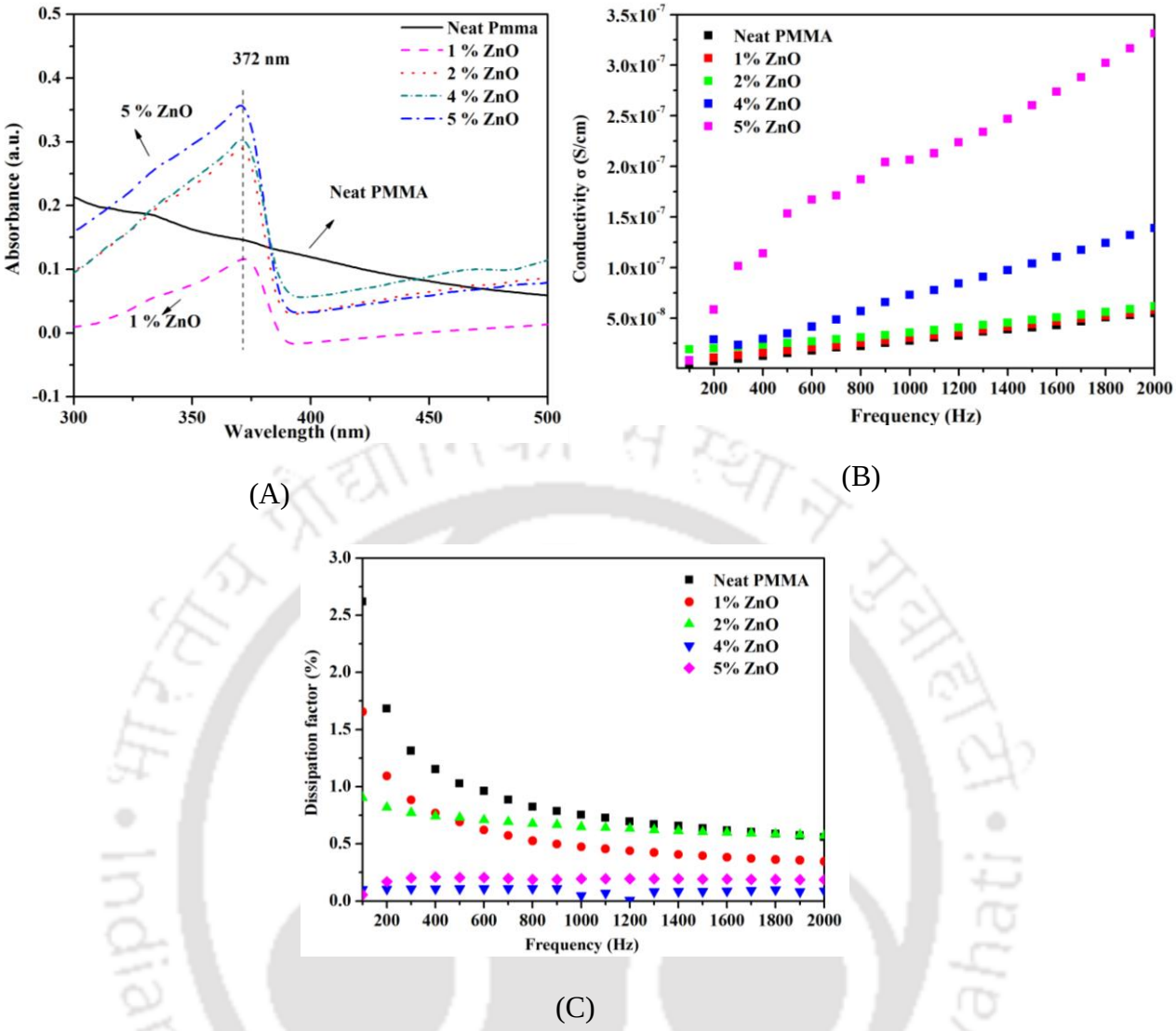

Figure 3.9: Characterization of PMMA/ZnO nanocomposites synthesised with varying loading of calcined ZnO nanoparticles. (A) UV–visible absorption spectra. (B) Electrical conductivity. (C) Dissipation factor.

Mechanical properties: Assessment of three mechanical properties of neat PMMA and PMMA/ZnO nanocomposites, viz. tensile strength, Young's modulus and percentage elongation, has been done. The tests for measurement of these mechanical properties were done using Universal Testing Machine, as noted earlier. As per ASTM D882 standard test method, specimen films of neat PMMA and PMMA/ZnO nanocomposite with dimensions 100 mm × 25 mm × 0.4 mm have been used at a cross head speed of 0.5 mm/min. The gauge length of each film was maintained at 50 mm. The results of assessment of mechanical properties are depicted in Fig. 3.10. Trends observed in different mechanical properties and

the plausible reasoning for the same are given below.

Tensile strength: The results of tensile strength test depicted in Fig. 3.10A reveal that the neat PMMA has maximum tensile strength of 32.74 MPa. The PMMA/ZnO nanocomposite with 1 wt% ZnO loading has a higher tensile strength of 36.57 MPa. Nanocomposites with higher ZnO loadings of 2, 4 and 5 wt% show reduction in the tensile strength. The maximum tensile strength of nanocomposites with 2, 4 and 5 wt% ZnO loading have been 27.77, 26.36 and 25.8 MPa respectively.

Increased tensile strength of PMMA matrix at lower concentrations of the filler ZnO particles could be a combined result of uniform dispersion of ZnO nanoparticles in the polymer matrix (due to intense microturbulence generated by ultrasound), strong interfacial interaction and adhesion between phases (possibly through H–bonds) and increase in the crystallinity of the material. Increase in the tensile strength of the nanocomposite films could also be due to the limit of moving scale of chain segments of the PMMA matrix with addition of ZnO, as noted by Li et al. (2009). Tanniru et al. (2006) have noted that local and global conformations of the polymers within host galleries of nanoparticles are quite different than those in bulk or neat polymer due to confinement of polymer chains and specific polymer–surface interactions, and that polymer chain dynamics is affected by confinement and polymer–surface interactions. Tanniru et al. (2006) have also noted that the interphase around the nanofiller (ZnO) particle is a characteristic of the crystalline nature of the particle–matrix surface. Reduction in tensile strength for higher ZnO loading is possibly a consequence of non–uniform distribution and agglomeration/segregation of ZnO particles in polymer matrix that could form "weak spots" in the matrix resulting in reduction of the tensile strength. As noted by Esthappan (2012), increased concentration of ZnO nanoparticles in polymer matrix can reduce the interfacial contact area resulting in formation of defects in the nanocomposites that reduce the tensile strength. Tanniru et al. (2006) have noted that for a matrix with

aggregate of nanofiller particles, the stress field will be concentrated around the aggregate such that cracks will propagate easily and rapidly causing premature failure.

Young's modulus: This mechanical property shows similar trends as the tensile strength for neat PMMA and PMMA/ZnO nanocomposites with different ZnO loading. Results shown in Fig. 3.10B reveal that Young's modulus for nanocomposite with 1 wt% ZnO loading is 1.47 GPa, which is notably higher than the Young's modulus of 1.14 GPa for neat PMMA. For higher ZnO loading of 2, 4 and 5 wt%, the Young's modulus shows consistent reduction. The least Young's modulus of 1.09 GPa is obtained for PMMA/ZnO nanocomposite with 5 wt% ZnO loading. Explanation for these trends in Young's modulus could be given along similar lines as for the trends in tensile strength stated earlier.

Percentage elongation: Trends in percentage elongation of neat PMMA and PMMA/ZnO nanocomposites (for 1 – 5 wt% ZnO) are shown in Fig. 3.10C. As compared to neat PMMA, the percentage elongations for all PMMA/ZnO nanocomposites showed marked rise. Neat PMMA had percentage elongation of 3.92%, which increased to 17.56% for PMMA/ZnO nanocomposite for 1 wt% ZnO. However, an inverse variation in percentage elongation was observed with concentration of the ZnO particles in PMMA matrix (or the loading of ZnO). This is evident from the percentage elongation values of 13.1, 11.8 and 10.98% for the PMMA/ZnO nanocomposites with 2, 4 and 5 wt% ZnO loadings, respectively. An explanation for trends in percentage elongation can be given as follows: for smaller concentration of ZnO particles (1 wt% loading), the limited confinement of polymer chains (with increased crystallinity) and filler–matrix interfacial interactions improve the ability of the nanocomposite matrix to absorb energy during deformation process, which results in marked rise in percentage elongation. However, at higher loading of ZnO, higher concentration of nanoparticles in the matrix restricts the ductile flow of polymer chains, which is reflected in reduced percentage elongations.

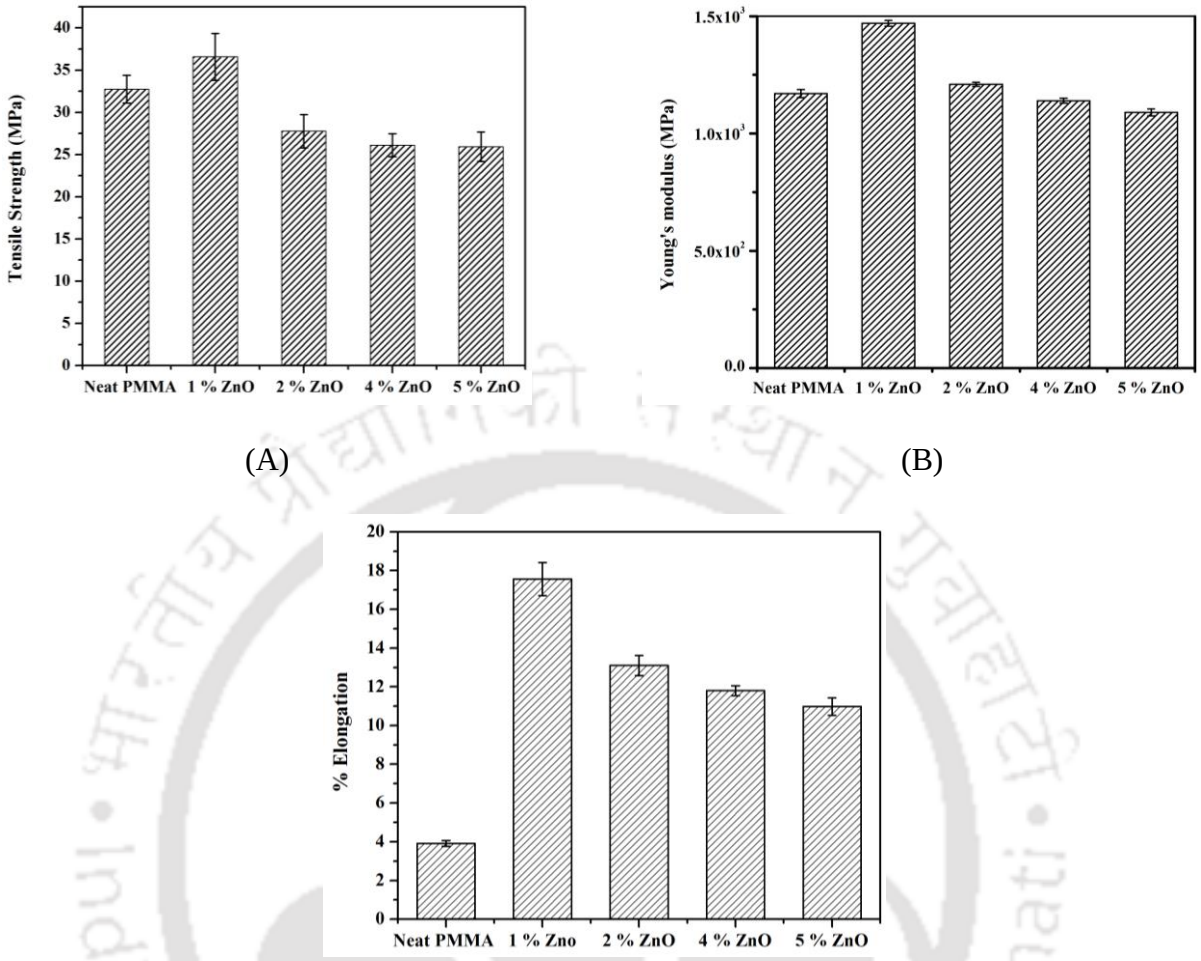

Figure 3.10: Mechanical properties of PMMA/ZnO nanocomposites synthesised with varying loading of calcined ZnO nanoparticles. (A) Tensile Strength; (B) Young's (or elasticity) modulus; (C) Percentage (%) elongation**.**

3.4 Discussion and mechanistic analysis

This study has put forth a novel sonochemical technique for synthesis of PMMA/ZnO nanocomposites. The principal merit of this technique is that it does not require surface modification of ZnO nanoparticles prior to nanocomposite synthesis. Nonetheless, PMMA/ZnO nanocomposites synthesised with this technique have enhanced thermal, and optical properties as compare to neat PMMA. This essentially is manifestation of the physical and chemical effects of the ultrasound and cavitation on both synthesis of nanoscale ZnO particles and PMMA/ZnO nanocomposites. The physical effect of ultrasound and cavitation

is generation of intense microturbulence and micromixing in the medium, while the chemical effect involves generation of highly reactive radicals such as $^{\bullet}OH$, $O^{\bullet}$ or $^{\bullet}HO_2$ through thermal dissociation of gas and vapor molecules present in the bubble at the moment of transient collapse – when the temperature and pressure conditions in the bubble reach extreme (> 5000 K, > 500 bar). In our previous papers (Morya et al., 2008; Kanmuri et al., 2010) we have presented extensive simulations of cavitation bubble dynamics using the diffusion limited model (Toegel et al., 2000). At the moment of transient collapse, the bubble core is extremely hot, with temperatures exceeding 5000 K. Although these conditions last for a very short duration (~ 50 ns or so), some heat transfer does occur through the bubble interface to the liquid. As a consequence, a thin layer of liquid (thickness of a few micrometers) sticking to the bubble interface gets heated to moderate temperatures of about 500–600 K (Kotronarou et al., 1991; Yasui, 1997) and Chemical compounds present in this interfacial region may undergo thermal decomposition at these temperatures.

As far the synthesis of ZnO nanoparticle is concerned, the initial hydrolysis of the zinc acetate to zinc hydroxide is mainly effected by the OH^- ions provided by NaOH. $^{\bullet}OH$ radicals generated through transient cavitation could also contribute to the hydrolysis of aceteate. However, due to relatively far lesser concentration of the radicals and spordaic nature of cavitation events, acetate hydrolysis is mainly affected by the OH^- ions. The decomposition of $Zn(OH)_2$ occurs in the interfacial region of the cavitation bubble during transient collapse, when this region gets heated due to heat transfer from extremely hot bubble core, as noted earlier. As a consequence, ZnO nanoparticles have relatively smaller size with large surface area, and narrow size distribution. The shockwaves generated by transient cavitation helps in averting agglomeration of the particles.

The microturbulence generated by ultrasound and cavitation is also responsible for fine emulsification between the aqueous (water) and organic (monomer) phases. The process

of emulsification not only distributes the monomer in the form of fine droplets in the bulk medium, but also assists encapsulation of nanoparticles inside the monomer droplets, both in the bulk medium as well as intra–micelle region. These droplets are subsequently 'spot' polymerized by the radicals. Again, there are two sources of polymerizing radicals in the medium, viz. the radicals originating from the thermal decomposition of KPS initiator, and the radicals generated through the transient cavitation. However, due to large and volumetrically more uniform concentration, the polymerization is mainly affected by radicals generated from initiator (from previous chapter). Thus, the role of cavitation in the synthesis of PMMA/ZnO nanocomposites is mainly physical in that it assists formation of ZnO nanoparticles of smaller size and narrower size distribution, and helps in uniform dispersion of these particles in polymer matrix leading to high surface interaction/ adhesion, which is equivalent to surface modified particles.

It is the noteworthy to compare the result of present study with previous literature that would vividly illustrate the efficacy of sonchemical technique for nanocomposite synthesis reported in this study. First and foremost impact of sonication is in terms of enhancement of polymerization kinetics. Against the long polymerization periods (6–20 h) and high temperatures (60–150^{o}C) reported in the literature (Hong et al., 2006; Kulyk et al., 2011; Chakraborthy et al., 2013) sonochemical polymerization is complete within 1 h at moderature temperature of 65^{o}C. The size of the nanocomposite particles obtained with present technique (< 100 nm) is significantly smaller than the typical sizes (> 200–400 nm) reported in the literature (Anzlovar et al., 2010; Bhanvase et al., 2011; Bhanvase et al., 2012). The maximum degradation temperatures in the present study (340–430^{o}C) are higher than previous literature. For example, Anzlovar et al. (2010) have reported maximum degradation temperature of 375^{o}C for PMMA/ZnO nanocomposite synthesied in a glass mould with 1 wt% ZnO loading, while Abbasian et al. (2013) have reported maximum degradation

temperature of 348^{o}C for ZnO (APS–modified) loading of 0.6 wt%. The glass tranisition temperature of synthesised PMMA/ZnO nanocomposites is in the range of 110–121^{o}C, which is significantly higher than the temperature of 95.3^{o}C reported by Hong et al. (2006) for nanocomposites of PS/ZnO (with PMMA grafting). The optical properties of as–synthesized PMMA/ZnO nanocomposites are also enhanced, in that the maximum UV absorption band is shifted to 350–375 nm, as against the band of 375–400 nm reported by Soumya et al. (2014). It is also notable that all properties of sonochemically synthesized nanocomposites show a maxima for low concentration of filler in polymer matrix (corresponding to 1 or 2 wt% ZnO loading during synthesis) for which uniform dispersion of the nanofiller in the polymer matrix is achieved. This observation is in concurrence with previous literature.

3.5 Conclusions

The two–step sonochemical methodology for nanocomposite synthesis reported in this study has distinct merits of being faster and simpler than previous techniques reported in literature. The first step of the sonochemical methodology yields nanoscale (< 100 nm) ZnO particles with narrow size distribution. Moreover, this methodology obviates the need of surface modification of the ZnO particles, and achieves uniform encapsulation and dispersion of the ZnO particles (in native form) in the PMMA matrix. Fine emulsification generated through intense micromixing by sonication gives almost 10–fold boost to kinetics of polymerization at moderate temperature. The gross manifestation of these facets of sonochemical methodology is synthesis of PMMA/ZnO nanocomposites with enhanced thermal, mechanical, electrical and optical properties. The merits of sonochemcal synthesis are essentially manifestations of the physical effect of generation of intense micro–convection and micro–mixing due to sonication. The methodology of PMMA/ZnO nanocomposite synthesis presented in this study also forms a general framework, which could

be extended to synthesis of ZnO–based nanocomposites with other polymers such as polystyrene,poly propylene and polyvinyl alcohol.

References

Abbasian M, Aali NK, Shoja SE, Synthesis of poly(methyl methacrylate)/zinc oxide nanocomposite with core–shell morphology by atom transfer radical polymerization, J. Macromol. Sci. Part A 50 (2013) 966–975.

Agrawal M, Gupta S, Zafeiropoulos NE, Oertel U, Habler R, Stamm M, Nano–level mixing of ZnO into poly(methyl methacrylate), Macromol. Chem. Phys. 211 (2010) 1925–1932.

Anzlovar A, Orel ZC, Zigon M, Poly(methyl methacrylate) composites prepared by in situ polymerization using organophillic nano–to–submicrometer zinc oxide particles, Eur. Polym. J. 46 (2010) 1216–1224.

Bhatte KD, Fujita SI, Arai M, Pandit AB, Bhanage BM, Ultrasound assisted additive free synthesis of nanocrystalline zinc oxide, Ultrason. Sonochem. 18 (2011) 54–58.

Bhanvase BA, Pinjari DV, Gogate PR, Sonawane SH, Pandit AB, Process intensification of encapsulation of functionalized CaCO3 nanoparticles using ultrasound assisted emulsion polymerization, Chem. Eng. Process. Process Intensif. 50 (2011) 1160–1168.

Bhanvase BA, Pinjari DV, Gogate P.R, Sonawane SH, Pandit AB, Synthesis of exfoliated poly(styrene–co–methyl methacrylate)/montmorillonite nanocomposite using ultrasound assisted in situ emulsion copolymerization, Chem. Eng. J. 181–182 (2012) 770–778.

Bradley M, Grieser F, Emulsion polymerization synthesis of cationic polymer latex in an ultrasonic field, J. Colloid Interface Sci. 251 (2002) 78–84.

Chakraborty H, Sinha A, Mukherjee N, Ray D, Chattopadhyay P. Protim, A study on nanoindentation and tribological behaviour of multifunctional ZnO/PMMA nanocomposite, Mater. Lett. 93 (2013) 137–140.

Das A, Wang DY, Leuteritz A, Subramaniam K, Greenwell HC, Wagenknecht U, Heinrich G, Preparation of zinc oxide free, transparent rubber nanocomposites using a layered double hydroxide filler, J. Mater. Chem. 21 (2011) 7194–7200.

Dawidczyk TJ, Walton MD, Jang WS, Grunlan JC, Layer–by–Layer assembly of UV–resistant poly(3,4–ethylenedioxythiophene) thin films, Langmuir 24 (2008) 8314–8318.

Esthappan SK, Polypropylene/metal oxide nanocomposites: Fiber spinning and evaluation, Ph.D. Dissertation, Department of Polymer Science and Rubber Technology, Cochin University of Science and Technology, Kochi (Kerala), India, May 2012.

Greenwood R, Kendall K, Electroacoustic studies of moderately concentrated colloidal suspensions, J. Eur. Ceram. Soc. 19 (1999) 479–488.

Hong RY, Qian JZ, Cao JX, Synthesis and characterization of PMMA grafted ZnO nanoparticles, Powder Technol. 163 (2006) 160–168.

Huang HC, Hsieh TE, Preparation and characterizations of highly transparent UV–curable ZnO–acrylic nanocomposites, Ceram. Int. 36 (2010) 1245–1251.

Kanmuri S, Moholkar VS, Mechanistic aspects of sonochemical copolymerization of butyl acrylate and methyl methacrylate, Polymer 51 (2010) 3249–3261.

Kotronarou A, Mills G, Hoffmann MR, Ultrasonic irradiation of p–nitrophenol in aqueous solution. J. Phys. Chem. 95 (1991) 3630–3638.

Kulyk B, Kapustianyk V, Krupka O, Sahraoui B, Optical absorption and photoluminescence properties of ZnO/PMMA nanocomposite films, J. Phys.: Conf. Ser. 289 (2011) 012003.

Kumar SS, Venkateswarlu P, Rao VR,. Rao GN, Synthesis, characterization and optical properties of zinc oxide nanoparticles, Int. Nano Lett. 3 (2013) 30

Li H, Schirra LK, Shim J, Cheun H, Kippelen B, Monti OLA, et al., Zinc oxide as a model transparent conducting oxide: A theoretical and experimental study of the impact of hydroxylation, vacancies, interstitials, and extrinsic doping on the electronic properties of the Polar ZnO (0002) surface, Chem. Mater. 24 (2012) 3044–3055.

Li, JH, Hong RY, Li MY, Li HZ, Zheng Y, Ding J, Effects of ZnO nanoparticles on the mechanical and antibacterial properties of polyurethane coatings, Prog. Org. Coat. 64

(2009) 504–509.

Liao W, Gu A, Liang G, Yuan L, New high performance transparent UV–curable poly(methyl methacrylate) grafted ZnO/silicone–acrylate resin composites with simultaneously improved integrated performance, Colloids Surf. A 396 (2012) 74–82.

Lin KF, Cheng HM, Hsu HC, Lin LJ, Hsieh WF, Band gap variation of size–controlled ZnO quantum dots synthesized by sol–gel method, Chem. Phys. Lett. 409 (2005) 208–211.

Liu H, Sun R, Yi J, Ye H, Tang X, Li Y, Kinetics of Methyl Methacrylate Grafting Polymerization onto Flaky Aluminum Powder, J. Appl. Polym. Sci. 115 (2010) 3040–3044.

Liu P, Su Z, Preparation and characterization of PMMA/ZnO nanocomposites via in–situ polymerization method, J. Macromol. Sci., Part B: Phys. 45 (2006) 131–138.

Mason TJ, Lorimer JP, Applied Sonochemistry: Uses of Power Ultrasound in Chemistry and Processing, Wiley–VCH Verlag GmbH & Co., 2002.

Matsuyama K, Mishima K, Kato T, Irie K, Mishima K, Transparent polymeric hybrid film of ZnO nanoparticle quantum dots and PMMA with high luminescence and tunable emission color., J. Colloid Interface Sci. 367 (2012) 171–177.

Moholkar VS, Warmoeskerken MMCG, Integrated approach to optimization of an ultrasonic processor, AIChE J. 49 (2003) 2918–2932.

Morya NK, Iyer PK, Moholkar VS, A physical insight into sonochemical emulsion polymerization with cavitation bubble dynamics, Polymer 49 (2008) 1910–1925.

Mostafaei A, Zolriasatein A, Synthesis and characterization of conducting polyaniline nanocomposites containing ZnO nanorods, Prog. Nat. Sci. Mater. Int. 22 (2012) 273–280.

Nalajala VS, Moholkar VS, Investigations in the physical mechanism of sono crystallization, Ultrason. Sonochem. 18 (2011) 345–355.

Ocak SB, Selçuk AB, Aras G, Orhan E, Electrical analysis of Al/ZnO/p–Si, Al/PMMA/p–Si and Al/PMMA/ZnO/p–Si structures: Comparison study, Mater. Sci. Semicond. Process. 38 (2015) 249–256.

Patidar P, Khanna S, Moholkar VS, Physical features of ultrasound assisted enzymatic degradation of recalcitrant organic pollutants. Ultrason. Sonochem. 19 (2012) 104–118.

Rahman MAA, Mahmud S, Alias AK, Nor AFM, Effect of nanorod zinc oxide on electrical and optical properties of starch–based polymer nanocomposites, J. Phys. Sci, 24 (2013) 17–28.

Reddy BR, Sivasankar T, Sivakumar M, Moholkar VS, Physical facets of ultrasonic cavitational synthesis of zinc ferrite particles, Ultrason. Sonochem. 17 (2010) 416–426.

Sharma S, Vyas R, Shrivastava S, Vijay YK, Effect of swift heavy ion irradiation on photoluminescence properties of ZnO/PMMA nanocomposite films, Phys. B (Amsterdam, Neth.) 406 (2011) 3230–3233.

Soumya S, Mohamed AP, Paul L, Mohan K, Ananthakumar S, Near IR reflectance characteristics of PMMA / ZnO nanocomposites for solar thermal control interface films, Sol. Energy Mater. Sol. Cells 125 (2014) 102–112.

Tang E, Cheng G, Ma X, Preparation of nano–ZnO/PMMA composite particles via grafting of the copolymer onto the surface of zinc oxide nanoparticles, Powder Technol. 161 (2006) 209–214.

Tanniru M, Yuan Q, Misra KDK, On significant retention of impact strength in clay–reinforced high–density polyethylene (HDPE) nanocomposites, Polymer 47 (2006) 2133–2146.

Toegel R, Gompf B, Pecha R, Lohse D, Does water vapor prevent upscaling sonoluminescence? Phys. Rev. Lett. 85 (2000) 3165–3168.

Vodnik VV, Bozanic DK, Dzunuzovic E, Vukovic J, Nedeljkovic JM, Thermal and optical

properties of silver–poly(methylmethacrylate) nanocomposites prepared by in–situ radical polymerization, Eur. Polym. J. 46 (2010) 137–144.

Wahab R, Ansari SG, Kim YS, Seo HK, Shin HS, Room temperature synthesis of needle–shaped ZnO nanorods via sonochemical method, Appl. Surf. Sci. 253 (2007) 7622–7626.

Yasui K, Alternative model for single–bubble sonoluminescence. Phys. Rev. E 56 (1997) 6750–6760.

Zhang L, Li F, Chen Y, Wang X, Synthesis of transparent ZnO/PMMA nanocomposite films through free–radical copolymerization of asymmetric zinc methacrylate acetate and in–situ thermal decomposition, J. Lumin. 131 (2011) 1701–1706.

Zhang Y, Zhuang S, Xu X, Hu J, Transparent and UV–shielding ZnO@PMMA nanocomposite films, Opt. Mater. (Amst). 36 (2013) 169–172.

CHAPTER 4

ULTRASOUND–ASSISTED SYNTHESIS AND CHARACTERIZATION OF PMMA/REDUCED GRAPHENE OXIDE NANOCOMPOSITES

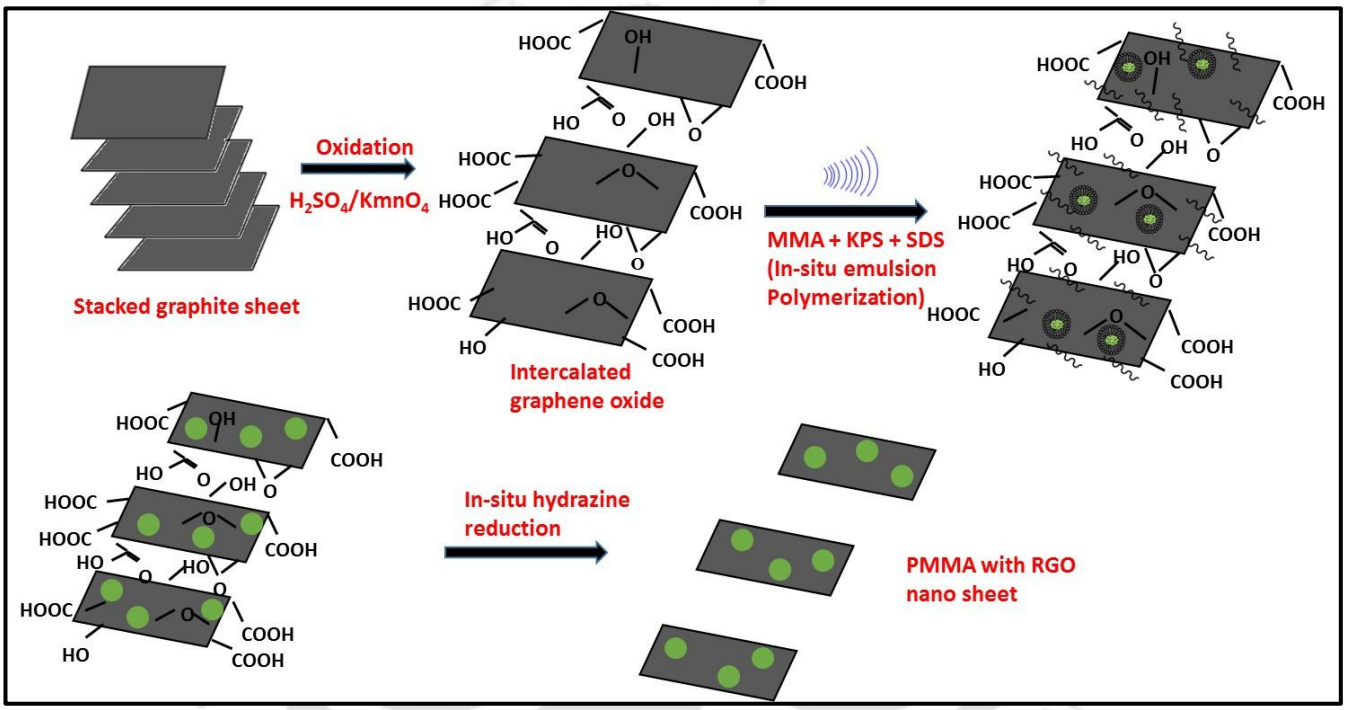

CHAPTER 4

Ultrasound–Assisted Synthesis and Characterization of PMMA/Reduced Graphene Oxide Nanocomposites

4.1 Introduction

Among different nanofiller materials for synthesis of nanocomposites, graphene has attracted special attention due to its extraordinary mechanical, thermal and electrical properties. For the synthesis of nanocomposites, the graphene sheets are frequently used in functionalized form of reduced graphene oxide. Reduced graphene oxide (RGO) sheets bear hydroxyl and epoxide functional groups on their basal planes, in addition to carbonyl and carboxyl groups located at sheet edges. Functionalization of graphene sheets enhances their compatibility with polymer matrix (Worsely et al., 2007; Park et al., 2008). The published literature reports several methodologies and techniques for the synthesis of graphene based nanocomposites such as in–situ polymerization, solution mixing, melt extrusion, solution casting, self–assembly and atom transfer radical polymerization (Ping et al., 2004; Fang et al., 2009; Steurer et al., 2009; Kim et al., 2011; Ren et al., 2011). PMMA/RGO nanocomposites have received special attention due to their potential application in electromagnetic interference (EMI) shielding and microwave absorbing materials. Several authors have reported synthesis of PMMA/RGO nanocomposites with markedly enhanced thermal, mechanical and electrical properties using variety of techniques. Zhang et al. (2013) have synthesized functional PMMA/graphene nanocomposites microcellular foams by blending

PMMA with graphene sheets followed by foaming with subcritical CO_2. These microcellular foams possessed superior electrical and EMI shielding properties. Jang et al. (2009) have reported synthesis of functionalized graphene sheet (FGS)/PMMA nanocomposites. FGS/PMMA nanocomposite (1 wt% FGS) had 7 orders of magnitude higher conductivity than pristine PMMA. Goncalves et al. (2010) have reported synthesis of PMMA grafted GO nanocomposites (GPMMA) via atom transfer radical polymerization. These nanocomposites were soluble in chloroform. PMMA nanocomposite films have been prepared using different percentages of GPMMA. Even for concentrations as low as 1 wt%, these nanocomposite films showed remarkably high mechanical properties. Morimune et al. (2012) have reported an environmentally benign method for synthesis of GO/PMMA nanocomposites that employs soap–free emulsion polymerization using water as the processing medium. The PMMA/GO nanocomposites synthesized with this method had excellent mechanical, thermal and O_2 barrier properties with nanodispersion of GO in polymer matrix. Aldosari et al. (2013) have synthesized PMMA/RGO nanocomposites using microwave irradiation. In this study, the nanocomposites were synthesized with two different approaches, viz. conventional bulk polymerization, and nanocomposites reduction with hydrazine hydrate in presence of microwave irradiation. The latter approach yielded nanocomposites with better thermal properties. Microwave irradiation enhanced thermal delamination, intercalation and exfoliation of RGO sheets, which contributed to betterment of the thermal properties. Summary of other studies reporting synthesis/characterization of PMMA/GO nanocomposites is given in Table 4.1.

Uniform exfoliation and dispersion of the GO nanosheets and effective in–situ GO reduction are vital to achieve enhanced physical properties of the nanocomposites. One of the physical factors that govern exfoliation and dispersion of GO nanosheets is convection intensity in the reaction mixture, which in turn, is inversely proportional to viscosity of the

reaction medium. In the conventional bulk radical polymerization, the reaction proceeds with fast kinetics, which results in rapid increase of solution viscosity. As a consequence, uniform exfoliation and dispersion of GO nanosheets may not be achieved. The in–situ emulsion polymerization, on the other hand, has aqueous bulk medium with low viscosity, and thus higher intensity of convection for a given energy input. This makes in–situ emulsion polymerization a suitable technique for synthesis of nanocomposites. Ultrasound-assisted in–situ emulsion polymerization is a relatively novel technique for nanocomposite synthesis. Ultrasound and its secondary effect, cavitation, introduces energies in reaction system at extremely small temporal and spatial scales. Ultrasound and cavitation induce intense micro–turbulence in the medium (Suslick, 1988; Mason and Lorimer, 1989; Morya et al., 2008; Kuppa et al., 2010; Bhasarkar et al., 2013). Implosive collapse of transient cavitation bubbles also generates radical species. These effects lead to higher encapsulation and better dispersion of nanofiller in the polymer matrix as compared to conventional methods employing mechanical agitation. Nanocomposites synthesized with sonication have better physical properties than those synthesized with conventional techniques, as demonstrated in our previous chapters.

In this chapter, we report synthesis of PMMA/RGO nanocomposites with ultrasound–assisted in–situ emulsion polymerization. These nanocomposites have been characterized for thermal, mechanical and electrical properties. In addition, we have analysed kinetics of thermal decomposition of these nanocomposites with Coats-Redfern and Criado models. As explained in subsequent sections, ultrasound–assisted in–situ emulsion polymerization is an effective technique for synthesizing nanocomposites with optimal combination of thermal, mechanical and electrical properties.

Table 4.1: Summary of literature on synthesis and characterization of PMMA/RGO nanocomposites

Reference	Mode of synthesis	Experimental conditions	Major findings and conclusions
Zheng et al. (2003)	PMMA with the expanded graphite filler by solvent blending method	(1) Preparation of expanded graphite (EG) using HNO3 and H2SO4. (2) PMMA/graphite composite synthesis by solvent blending method using chloroform	Electrical conductivity of PMMA/graphite = 1 × 10^{-5} S cm^{-1}; Higher storage modulus (3.4 GPa) and loss modulus (380 MPa) of PMMA/EG as compare to the pristine PMMA
Jang et al. (2009)	Synthesis of PMMA/ Graphite oxide (GO) nanocomposites using macroazoinitiator (MAI).	Two–step process: (1) GO preparation by Hummer's method, (2) PMMA/ GO nanocomposite synthesis. Reaction mixture: GO = 2.5 parts per 100 parts MMA. Temperature = 65°C, Reaction Time = 6 h. MAI with poly(ethylene oxide) segment gets intercalated between lamellae of GO to induce the intergallery polymerization of MMA and exfoliate the GO.	Enhancement in electrical conductivity up to 1.78 × 10^{-7} S/cm (50–fold higher than intercalated nanocomposite). Highest tensile modulus = 1160 MPa Highest T_g = 128°C. Thin GO with high aspect ratio is finely dispersed and reinforced PMMA matrix in both exfoliated and intercalated nanocomposites.
Pramoda et al. (2010)	PMMA/ Octadecyl–amine (ODA) functionalized graphene nano–composites by in situ polymerization method	(1) Reaction of ODA functionalized graphite oxides with methacryloyl chloride to incorporate polymerizable functionality at the graphene surfaces. (2) In situ polymerization of MMA at 60°C to obtain covalently bonded PMMA–graphene nanocomposites.	$T_{5\%}$ of neat PMMA = 274°C, $T_{5\%}$ of PMMA/graphene (0.1 wt%) = 293°C. $T_{5\%}$ of PMMA/graphene (0.5 wt%) = 300°C. Max degradation temp PMMA/ graphene (0.5 wt%) = 360°C
Putz et al. (2010)	PMMA/layered graphene oxide nanocomposites by vacuum–assisted self-assembly (VASA) technique.	PMMA/GO were formed by adding a diluted graphene oxide dispersion solution in PMMA with DMF (10–30 mg in 400 mL of DMF).	The resulting nanosheets prepared by VASA technique exhibit a high degree of order with tunable intersheet spacing.
Kuila et al. (2011)	PMMA/ graphene, In situ emulsion polymerization method	Two–step process: (1) GO preparation by Hummer's method, (2) PMMA/ RGO nanocomposite synthesis. Reaction mixture: GO = 0.1 g, MMA = 30 g, AIBN = 0.1 g, SDS = 2 g. Temperature = 80°C, Time = 7 h. Addition of N_2H_4, reflux for 16 h.	Graphene acts as reinforcing filler in PMMA matrix. Enhanced storage moduli and glass transition temperatures. Increase in thermal stability by 35°C. Electrical conductivity with 1 wt% GO = 1.5 S m^{-1}
Pham et al. (2011)	Highly conductive PMMA/ RGO nanocomposites by surfactant free emulsion polymerization	Self–assembly of +ve charged PMMA latex and –ve charged GO sheets through electrostatic interactions, followed by hydrazine reduction. Use of cationic free radical initiator. Reaction mixture: 0.1 g GO, PMMA = 100 g, Reaction time = 8 h at 80°C.	10°C rise in decomposition temperature of PMMA/RGO (1 wt%). Electrical conductivity of PMMA/RGO (0.6 vol%) = 1 S/m. For 1.0 vol % RGO, thermal conductivity > 10 S/m. Max conductivity for 2.7 wt % RGO ~ 64 S/m

Table 4.1: (*continued*…..)

Reference	Mode of synthesis	Experimental conditions	Major findings and conclusions
Wang et al. (2012)	PMMA/ functionalized Graphene (GP) nanocomposites (GPMMA) via in–situ free radical polymerization. GP functionalization with N–methyl–2–pyrrolidone (NMP)	(1) Synthesis of functionalized GP: graphite (4.0 g) + NMP (80 mL) + sonication for 6 h. (2) Synthesis of GPMMA: NMP solution (0.5 mg/mL) + MMA (10.0 g) + sonicated for 2 h + AIBN (0.05 g). Reaction 80^{o}C for 48 h under magnetic stirring.	PMMA/GPMMA composites show improved mechanical properties for 0.5 wt% GPMMA due to good dispersion of GPMMA and strong GPMMA/PMMA interfacial adhesion. Highest Young modulus = 5.24 MPa, Tensile strength = 66.08 MPa, $T_{5\%}$ – degradation temp increase by ~ 40^{o}C (for 1 wt% GPMMA)
Li et al. (2013)	Synthesis of transparent PMMA nanocomposites using electrospun graphene–incorporated–Nylon 6 (Gr/PA–6) nanofibers	Gr–doped PA–6 solutions (Gr/PA–6 mass ratios of 0, 0.5, 1.0 wt%) and pristine PA–6 granules dissolved in Gr/HFIP dispersions with sonication. PMMA solution and Gr/PA–6 suspensions (varied Gr loadings) simultaneously electrospun into hybrid fibers via self–blending co–electrospinning.	High–performance Gr/PA–6/PMMA nanocomposites. Significant enhancement of mechanical properties at Gr loading of ~ 0.01 wt%; 56% and 113% improvement in tensile strength and modulus, respectively. > 250% increase of toughness. Transmittance maintained > 70% in the visible wavelength range of 400–800 nm.
Tripathi et al.- (2013)	Synthesis of nanocomposite by 3 methods: (1) in situ poly–merization, (2) bulk poly–merization of MMA in presence of PMMA beads, (3) in situ polymerization of MMA/ RGO followed by sheet casting.	Two step process: (1) Preparation of GO by modified Hummer's method. (2) Reaction mixture: GO = 100 mg, MMA = 10 mL, AIBN = 0.1 g (0.5 wt%), ultrasonic dispersion for 1 h. Final polymerization in water bath at 70^{o}C for 4 h.	Electrical conductivity of 2 wt% RGO–loaded PMMA composite increased by factor of 10^{7} for in situ polymerized nanocomposites, whereas, 10^{8} times increase in conductivity for nanocomposites synthesized by casting method.
Ji et al. (2014)	PMMA/ Thermally reduced graphene (TRG) oxides composites through UV–curing method	Reaction mixture: MMA = 10 g, photo–initiator = 10 mg, TRGs (containing 55%, 20% and 1% C=O bonds) = 50 mg. Sonication for 2 h, stirring for 12 h at room temperature. Coating of solution on glass template followed by UV–curing.	Better dispersion capability of TRGs with higher carboxylic group contents gives enhanced thermal stability, mechanical strength, thermal conductivity and gas permeability. Highest T_g = 122.5^{o}C, T_d = 269.9^{o}C

4.2 Materials and Methods

4.2.1 Materials

The experiments have been conducted with the following chemicals: methyl methacrylate (MMA, GR grade, Hi–Media India Ltd), surfactant sodium dodecyl sulfate (SDS, AR grade, Merck India Ltd), potassium persulfate ($K_2S_2O_8$, AR grade, Merck India Ltd), graphite powder (synthetic, < 20 μm, Sigma Aldrich, Switzerland), hydrazine hydrate (N_2H_4, reagent grade, 50–60%, Sigma Aldrich, Switzerland). The inhibitor in MMA monomer was removed by adsorption on neutral alumina powder.

4.2.2 Preparation of graphene oxide (GO) nanosheets

GO nanosheets were synthesized according to the modified Hummer's method using graphite powder (Hummers and Offeman, 1958). Exfoliation of graphite oxide into GO nanosheets was achieved by 20 kHz ultrasound irradiation.

4.2.3 Synthesis of PMMA/RGO nanocomposites

The polymerization reactions for synthesis of polymethyl methacrylate/reduced graphene oxide (PMMA/RGO) nanocomposites were carried out in a jacketed glass reactor. The reactor had an outer jacket through which water was circulated to maintain the reaction temperature at ~ 65 ^{o}C. In order to avoid induction of oxygen in the reaction mixture, the polymerization reaction was carried out under the flow of nitrogen gas (at flow rate of 2 L/min). In a typical experiment, the reaction mixture comprised MMA monomer (15 g), surfactant SDS (0.87 g) and initiator KPS (0.75 g dissolved in 100 mL water) along with nanofiller material GO (0.2 wt% MMA). This mixture was sonicated in continuous mode using a probe type (probe tip dia.: 25 mm) micro–processor controlled programmable ultrasound processor with frequency of 20 kHz (Sonics and Materials Inc., Model: VCX–500, Max power 500 W). The processor was operated at 40% of the maximum theoretical power, i.e. 200 W. The actual acoustic power dissipated in the reaction medium was determined by

calorimetric method, and the pressure amplitude of the ultrasound waves generated by the sonicator probe was calculated as 2 bar. Reaction mixture was heated to the desired temperature after initial sonication (~ 10 min) of the reaction mixture to achieve uniform dispersion of the nanofiller. This was followed by continuous sonication of the reaction mixture for 1 h at 65 ^{o}C for polymerization. After completion of the polymerization reaction, the pH of the reaction mixture was adjusted to 10 by addition of NaOH solution. Next, 5 mL hydrazine monohydrate (N_2H_4) was added to reaction mixture as reducing agent, with further sonication for 2 h at 95 ^{o}C. In this reaction, the GO nanosheets in the reaction mixture (encapsulated in the polymer matrix) are essentially reduced to RGO, resulting in the PMMA/RGO nanocomposite. It needs to be pointed out that unlike conventional procedure of reducing the GO separately (prior to nanocomposite synthesis), the present procedure involves in–situ reduction of GO within polymer matrix (subsequent to nanocomposite synthesis). This procedure is expected to have merit of greater encapsulation and more uniform dispersion of nanofiller into the polymer matrix as the polymerization proceeds while the nanofiller is still in functionalized form of GO. Functional groups present on GO can form bonds with the polymer matrix, which possibly enhance the compatibility of the nanofiller with the polymer matrix. The reaction mixture was vacuum dried at 70 ^{o}C for 15 h to obtain latex particles of PMMA/RGO nanocomposites after removal of water and unconverted monomers. The nanocomposite particles were washed several times with distilled water to remove surfactant present on the surface of the particles. The surfactant-free particles were further vacuum dried. For preparation of the nanocomposite film, these particles were dissolved in dichloromethane for 12 h under stagnant conditions without any external agitation. Then, this solution was sonicated at room temperature under mild conditions in an ultrasound bath (Elma, Transsonic T–460, 35 kHz, 35 W) to achieve volumetrically uniform concentration of the nanocomposite. The solution was poured into

petri–dish. The solvent was evaporated to obtain a thin film of PMMA/RGO nanocomposite, which was used for characterization and determination of thermal and mechanical properties of the nanocomposite.

4.2.4 Characterization of PMMA/RGO nanocomposites

PMMA/RGO nanocomposites were characterized for composition, and physical and structural morphology using standard techniques. The Raman spectra of graphite, GO and PMMA/RGO nanocomposites samples were recorded using Laser Micro Raman System (Horiba Jobin Vyon, Model: Lab Ram HR). These spectra were recorded using laser at 488 nm excitation with Raman shift between 1000 and 2000 cm^{-1}. Infrared (IR) absorption spectroscopic analysis was carried out at room temperature in the range of 400–4000 cm^{-1} with FTIR spectrophotometer (Shimadzu, Model: IRAffinity–1). The crystalline structure of graphite powder and graphene oxide and exfoliation of RGO in the PMMA matrix were analyzed by X–ray diffraction (XRD, D8 Advanced, Bruker) spectroscopy with Cu–Kα radiation (λ = 1.54A˚) in the range of 2θ = 1–50º. Thermal stability of the graphite, GO and PMMA/RGO nanocomposites was determined by thermogravimetric analysis (TGA) (NETZSCH TG, Model: 209F1 Libra) at a heating rate of 10 ºC/min in N_2 atmosphere. The glass transition temperatures (T_g) of the pristine PMMA polymer and PMMA/RGO nanocomposites were determined with DSC analysis (Make: Mettler Toledo–1 series) at a heating rate of 10 ºC/min in N_2 atmosphere. Structural and morphological analysis of RGO and PMMA/RGO nanocomposite was done by Field Emission Scanning Electron Microscopy (FE–SEM, Zeiss, Model: Sigma) and Transmission Electron Microscopy (TEM, Make: Jeol, Model: JEM 2100). Mechanical properties of the PMMA/RGO nanocomposites (viz. tensile strength, Young's modulus and percentage elongation) were determined using Universal Testing Machine (INSTRON 8801, UK). A specimen size 100 mm × 25 mm × 0.4 mm was used based on ASTM D882 standard at a cross head speed of 0.5 mm/min. The gauge length

of each film was maintained at 50 mm. The powder of the PMMA/RGO nanocomposites was compression molded into a rectangular cavity, with the dimensions of 22.9×10.2×2.8 mm^3, at 220 ^oC and 38 MPa for 10 min with a Carver compression molder (Carver Inc., Wabash, IN). The compression molded samples were employed for electrical characterization. For electrical conductivity < 10^{-6} S cm^{-1}, a Keithley 6517A electrometer connected to a Keithley 8009 test fixture was employed. For samples with conductivity > 10^{-6} S cm^{-1}, a Loresta GP resistivity meter (MCP-T610 model, Mitsubishi Chemical Co., Japan) connected with an ESP four-pin probe was used. The electromagnetic interference (EMI) shielding effectiveness (SE) was determined with an Agilent Network Analyzer (Model E5071C) within the X-band frequency range (8.2–12.4 GHz). EMI SE of a material is a measure of the material's ability to attenuate the intensity of EM waves, defined as the logarithm of the ratio of incident power to transmitted power, and its unit is expressed in dB:

$$EMI\ SE = 10\log\left(\frac{P_i}{P_o}\right) \quad (4.1)$$

where P_i is the incident power and P_o is the transmitted power.

4.3 Results and Discussion

4.3.1 Characterization of nanocomposites

***Raman spectroscopy*:** The Raman spectra for the graphite, graphene oxide (GO), and PMMA/RGO nanocomposites are shown in Fig. 4.1A. Raman spectrum of graphite powder in Fig. 4.1A shows a single characteristic peak, corresponding to G–band at ~1585 cm^{-1}. After oxidation of graphite into graphene oxide (GO), the Raman spectrum of GO shows two characteristic peaks, viz. D–band at ~1355 cm^{-1} and G–band at ~1600 cm^{-1}. The D–band essentially represents the sp^3 state of carbon and is also an evidence of the disruption of the sp^2 hybridized structure (or aromatic π–electrons) of the GO sheets. The D-band also

represents the disorders induced due to presence of various defects in graphene sheets (Georgakilas et al., 2012). The ratio of the intensities of D- and G- bands (I_D:I_G ratio) represents the relative population of the sp^3:sp^2 hybridized carbon atoms. The increase in I_D:I_G ratio indicates the increase in defects to the basal plane of graphene. These defects break the translational symmetry of the lattice structure of the carbon based materials. The I_D:I_G ratio for GO was 1.0. Raman spectra of PMMA/RGO nanocomposites also show D- and G-bands at the same wavelengths as in the Raman spectrum of GO albeit with much less intensity. Appearance of the D- and G- band peaks in the Raman spectrum of the PMMA/RGO nanocomposite is essentially a confirmation of the presence of RGO nanosheets inside the PMMA polymer matrix. However, the I_D:I_G ratio for PMMA/RGO nanocomposite is higher than that for the GO, i.e. 1.10, 1.1 and 1.2 for PMMA/RGO nanocomposites with 0.2, 0.4 and 1.0 wt% RGO loading, respectively. Rise in I_D:I_G ratio represents conversion of sp^2–state carbons to sp^3–state carbons. This could possibly be a consequence of covalent bond formation between PMMA chains and surface of RGO sheets, which partially disrupts the sp^2 carbon network (wang et al., 2012). This phenomenon is vital to maintenance of filler–matrix adhesion, which is manifested in terms of enhanced mechanical, electrical and thermal properties. Another probable cause leading to this effect could be creation of structural defects such as vacancies and topological defects produced during polymerization and reduction process, as hypothesized by Hu et al. (2010). Notably, I_D:I_G ratio of 1.2 for nanocomposite synthesized with 1.0 wt% RGO in the present study is significantly smaller than I_D:I_G ratio of 1.41 reported by Tripathi et al. (2013) for PMMA/RGO (1 wt%) nanocomposites synthesized by in–situ bulk polymerization. This essentially indicates the efficacy of the ultrasound technique for incorporation of nanofiller in polymer matrix in terms of higher exfoliation of RGO in polymer matrix with lesser defects.

***FTIR analysis*:** FTIR spectra of the graphite, GO, PMMA and PMMA/RGO with 0.2, 0.4 and 1.0 wt% loadings) are shown in Fig. 4.1B**.** Major peaks and their assignments in the FTIR spectra of GO are as follows: 1728 cm^{-1}: C=O; 1202 cm^{-1}: C–O–C; 1050 cm^{-1}: C–OH. Peaks at 3360 cm^{-1} and in between 2500–3000 cm^{-1} confirm the presence of hydroxyl (–OH) and carboxylic (–COOH) groups, respectively. All peaks are clear indications of conversion of graphite into graphene oxide (Krishnamoorthy et al., 2013; Tripathi et al., 2013). Various peaks and their assignments in FTIR spectrum of neat PMMA are as follows: 1730 cm^{-1}: strong C=O stretching vibration of acrylate carboxyl group; 2924, 2842 and 1475 cm^{-1}: asymmetric, symmetric and bending stretching of C–H bonds, respectively; range of 1395–1450 cm^{-1}: deformation vibration of $–CH_3$ and $–CH_2$ groups. Reduction in the intensity of peaks at 2924 and 1730 cm^{-1} in the FTIR spectrum of PMMA/RGO nanocomposites (as compared to pristine PMMA) represents strong intermolecular attractions between RGO and long chains of PMMA, and also ascertains effective incorporation of RGO nanosheets in the PMMA matrix.

***XRD analysis*:** The XRD patterns of graphite, GO, neat PMMA and its nanocomposites with RGO are shown in Fig. 4.1C. The graphite powder shows single sharp peak at 26.5° due to (002) graphitic plane. The graphite powder possesses highly crystalline hexagonal structure with interlayer *d*–spacing of 3.3 A°. The XRD pattern of GO shows a relatively less intense peak at 2θ = 10.6°, corresponding to interlayer *d*–spacing of 8.32 A°. This peak represents (001) plane. Rise in interlayer *d*–spacing of the GO is essentially a consequence of creation of new functional groups on graphene surface during oxidation. X–ray diffractogram of pristine PMMA shows a broad peak at 2θ = 13° that corresponds to crystalline regions (with ordered packing) of polymer. On the contrary, XRD patterns of PMMA/RGO nanocomposites synthesized with GO loading of 0.2 and 0.4 wt% do not show presence of any broad peak,

which essentially points to complete exfoliation of the nanofiller in the PMMA matrix. It is noteworthy that a weak peak at 2θ = 2.2° is seen in the XRD pattern of PMMA/RGO nanocomposites synthesized with 1.0 wt% GO loading. This essentially is a consequence of agglomeration of the nanofiller in the polymer matrix at high concentrations.

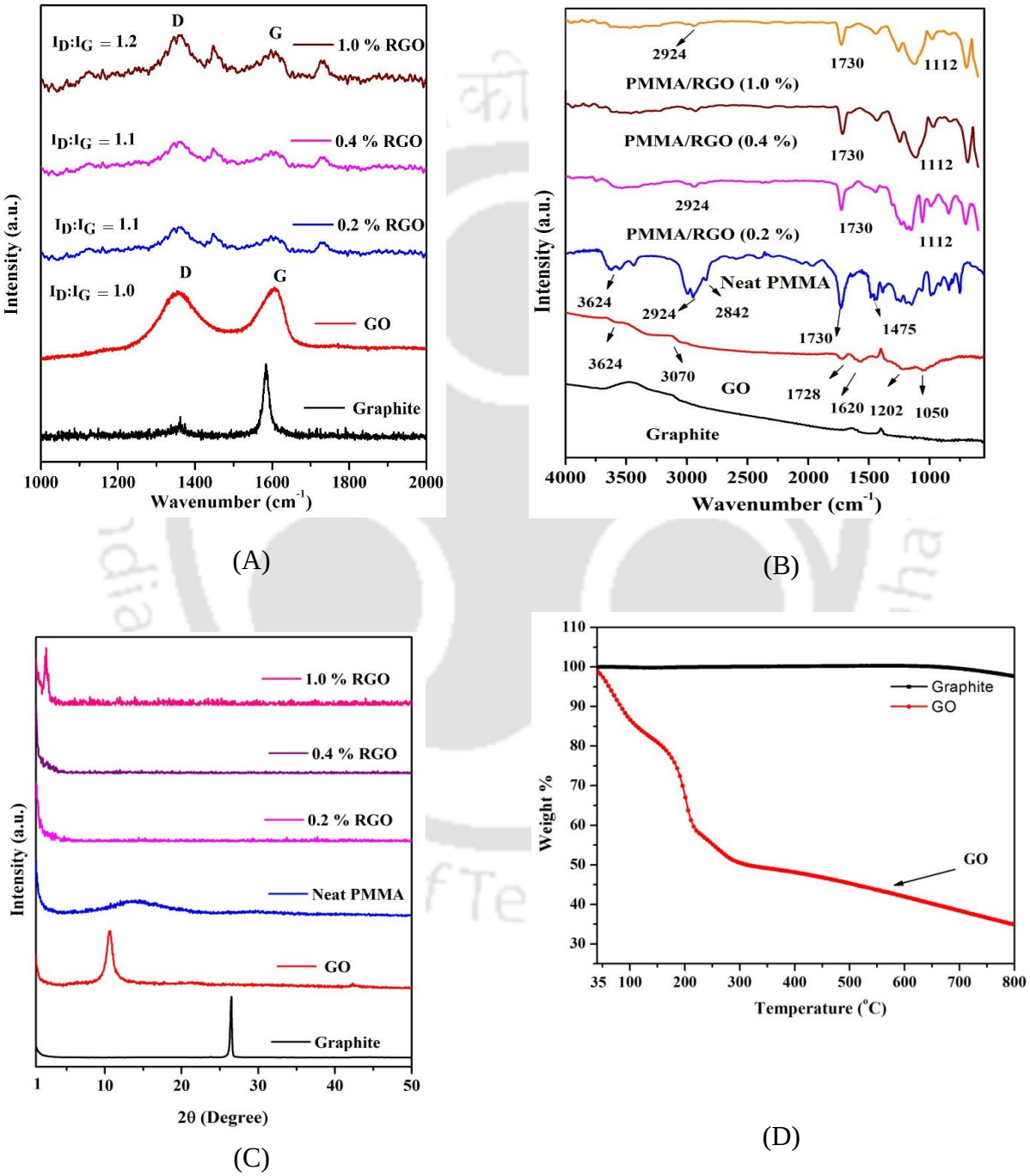

Figure 4.1: (A) Raman spectra of graphite, GO and PMMA/RGO nanocomposites for different loadings of RGO; (B) FTIR spectra of PMMA/RGO nanocomposites; (C) XRD diffractograms of graphite, GO and PMMA/RGO nanocomposites; (D) Thermogravimetric curves for graphite and GO.

***Thermogravimetric analysis (TGA)*:** TGA curves depicting percentage weight loss profile with temperature for graphite and GO are depicted in Fig. 4.1D. The graphite powder shows high thermal stability with just 10–12% total weight loss till 800 ^{o}C. TGA curve of GO shows weight loss in three distinct steps, i.e. (1) weight loss till 120 ^{o}C due loss of trapped water between GO sheets,[2,29] (2) weight loss between 120–230 ^{o}C, decomposition of functional groups such as C–O, C=O, and –OH, attached to the surface of GO layers (Stankovich et al., 2007; Mcallister et al.,2007), and (3) weak mass loss in the temperature range of 230–700 ^{o}C, which corresponds to the removal of unstable carbon due to emission of gases such as CO, CO_2 due to the pyrolysis of oxygen functional groups in the main structure (Fan et al., 2010; Elachaby et al., 2012).

TGA profiles of pristine PMMA and PMMA/RGO nanocomposites have been depicted in Fig. 4.2A.1. Magnified view of the TGA curves in the temperature range of 200–350 ^{o}C is shown in Fig. 4.2A.2. The results of the TGA analysis are summarized in Table 4.2A, which lists the temperatures $T_{5\%}$ and $T_{50\%}$, corresponding to 5% and 50% weight loss, respectively, for pristine PMMA and PMMA/RGO nanocomposites. Increments in thermal degradation temperatures, viz. $\Delta T_{5\%}$ and $\Delta T_{50\%}$, of the nanocomposites with respect to pristine PMMA have also been listed in Table 4.2A. For RGO loading of 1.0 wt%, low temperature ($T_{5\%}$) thermal stability shows rise of 23.85 ^{o}C, while high temperature ($T_{50\%}$) thermal stability shows rise of almost 50 ^{o}C. Most notably, the nanocomposites synthesized in the present study show marked rise in thermal stability in both low ($T_{5\%}$) and high ($T_{50\%}$) temperature range.

The first step of thermal degradation is expected to be due to weak interactions such as head to head linkages and van der Waals bonds. Presence of exfoliated nanosheets of RGO possibly strengthens these weak bonds, resulting in enhanced thermal stability. Moreover, uniform distribution of graphene nanosheets in the PMMA matrix under strong

microturbulence generated by sonication results in strong chemical bonding between PMMA and RGO sheets, giving reinforcing effect to the nanocomposite. Uniformly distributed RGO nanosheets also hinder and prevent diffusion and emission of gases and volatile products resulting from thermal degradation of nanocomposites through polymer matrix, leading to slowing down of degradation kinetics.

***Differential thermogravimetric (DTG) analysis*:** DTG curves for pristine PMMA and PMMA/RGO nanocomposites are depicted in Fig. 4.2B. The peaks of the DTG curves represent temperatures corresponding to maximum thermal degradation and are called inflection points. As compared to pristine PMMA, the nanocomposites show higher inflection point, which vary proportionately with RGO loading. Highest inflection point of 393 ^{o}C is obtained for PMMA/RGO (1.0 wt%) nanocomposite. The rise in the inflection point could be attributed to homogeneous distribution and exfoliation of the RGO nanosheets in the PMMA matrix, and strong interactions between the nanofiller and the polymer matrix. These interactions essentially resist random scission of polymer chains, leading to thermal degradation.

Table 4.2: (A) Results of thermogravimetric (TGA) analysis of pristine PMMA and PMMA/RGO nanocomposites

Sample	$T_{5\%}$(°C)	$T_{50\%}$(°C)	$\Delta T_{5\%}$(°C)	$\Delta T_{50\%}$(°C)
Pristine PMMA	267.4	326.1	–	–
PMMA/RGO (0.2 wt %)	283.2	373.0	15.8	46.9
PMMA/RGO (0.4 wt %)	288.2	375.2	20.8	49.1
PMMA/RGO (1.0 wt %)	291.3	375.8	23.9	49.7

Note: $T_{5\%}$ – Temperature corresponding to 5% weight loss; $T_{50\%}$ – Temperature corresponding to 50% weight loss; $\Delta T_{5\%}$ - increase in $T_{5\%}$ for nanocomposite with respect to neat PMMA; $\Delta T_{50\%}$ - increase in$T_{50\%}$for nanocomposite with respect to neat PMMA.

Table: 4.2: (B) Arrhenius (or kinetic) parameters of thermal decomposition of pristine PMMA and PMMA/RGO nanocomposites obtained using Coats–Redfern method*

Sample	Reaction order (*n*)	Activation energy (kJ/mol)	Pre–exponential factor (*A*)	Correlation coefficient
Neat PMMA	1.0	68.02	1.83×10^5	0.98
PMMA/RGO (0.2 wt%)	0.2	108.61	5.92×10^7	0.99
PMMA/RGO (0.4 wt%)	0.2	108.63	6.24×10^7	0.99
PMMA/RGO (1.0 wt%)	0.2	111.27	9.83×10^7	0.99

* Heating rate 10 °C/min

Table 4.2: (C) Algebraic functions representing reaction conversion (g(α)) in a solid state process under different prevalent mechanisms

Mechanism	g (α)	Solid state process
A_2	$[-\ln(1-\alpha)]^{1/2}$	Nucleation and growth: Avrami eq. (1)
A_3	$[-\ln(1-\alpha)]^{1/3}$	Nucleation and growth: Avrami eq. (2)
A_4	$[-\ln(1-\alpha)]^{1/4}$	Nucleation and growth: Avrami eq. (3)
R_2	$\left[1-(1-\alpha)^{1/2}\right]$	Phase boundary controlled reaction: contraction area
R_3	$\left[1-(1-\alpha)^{1/3}\right]$	Phase boundary controlled reaction: contraction volume
D_1	α^2	1–D diffusion
D_2	$(1-\alpha)\ln(1-\alpha)+\alpha$	2–D diffusion
D_3	$\left[1-(1-\alpha)^{1/3}\right]^2$	Three– D diffusion: Jander equation
D_4	$(1-(2/3)\alpha)-(1-\alpha)^{2/3}$	Three– D diffusion: Ginstlinge–Brounshtein equation
F_1	$-\ln(1-\alpha)$	First order random nucleation having one nucleus on individual particle
F_2	$\left[(1-\alpha)^{-1}\right]-1$	Second order random nucleation having two nucleus on individual particle
F_3	$(1/2)\left[(1-\alpha)^{-2}\right]-1$	Third order random nucleation having three nucleus on individual particle

Differential Scanning Calorimetry (DSC) analysis: Presence of nanofiller material inside polymer matrix influences the molecular mobility of the PMMA chains. This phenomenon can be assessed with DSC analysis. The DSC curves for the pristine PMMA and PMMA/RGO nanocomposites are shown in Fig. 4.2C. The point of inflection in the DSC curve (between onset and endset temperatures) essentially represents the glass transition temperature (T_g). It can be seen that incorporation of RGO in the polymer matrix increases T_g. This is essentially a manifestation of restriction of the segmental motion of polymer chains in the PMMA matrix with incorporation of the RGO nanosheets and strong surface interactions between RGO nanosheets and PMMA matrix. Trend in T_g of PMMA/RGO nanocomposites, however, shows a maxima with RGO loading during synthesis. The highest T_g of 124.5 ^oC is obtained for RGO loading of 0.4 wt%. For RGO loading > 0.4 wt%, T_g shows minor reduction. This could possibly be a consequence of relatively non–uniform distribution and agglomeration of the RGO nanosheets in PMMA matrix at higher loading.

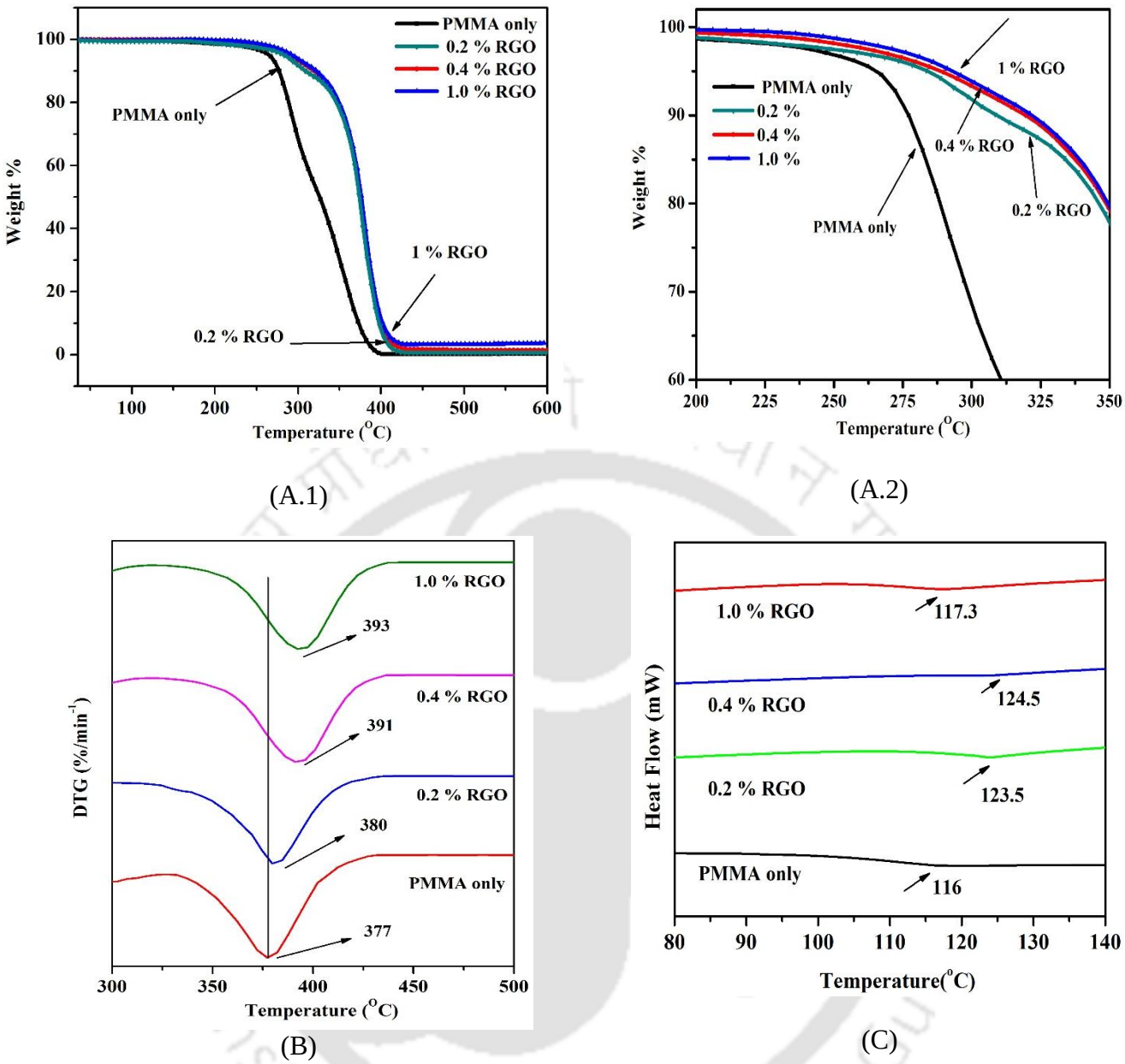

Figure 4.2: (A.1) Thermogravimetric analysis (TGA) curves for pristine PMMA and PMMA/RGO nanocomposites (A.2) Magnified view of the curves in the temperature range of 200 to 350°C. (B) Inflection points in differential thermogravimetric (DTG) curves for PMMA/RGO nanocomposites. (C) Differential scanning calorimetric (DSC) curves for PMMA/RGO nanocomposites.

Kinetic analysis of thermal degradation: The TGA and DTG analyses of PMMA/RGO nanocomposites have revealed that incorporation of RGO nanosheets in the PMMA matrix enhances the resistance of the nanocomposites against thermal degradation. In order to get further insight into the enhanced thermal stability of the nanocomposites, the TGA data have been analyzed to get kinetic parameters of thermal degradation, viz. activation energy, reaction order and pre–exponential factor, and also the predominant reaction mechanism of

thermal degradation. For this analysis, we have employed two common methods, viz. Coats–Redfern method and Criado method. These methods have been described in detail in the published literature by Krishna and Pugazhenthi (2011) and Bianchi et al. (2013). We have given herewith the final equations of these methods, which have been used for the analysis.

The Coats–Redfern method essentially fits the weight vs temperature data obtained in TGA analysis to the following expressions for different reaction orders (n):

For 1st order kinetics ($n = 1$)

$$\ln\left(-\frac{\ln(1-\alpha)}{T^2}\right) = \ln\left[\frac{AR}{\beta E_a}\left(1-\frac{2RT}{E_a}\right)\right] - \frac{E_a}{RT} \qquad (4.2)$$

For non–1st order kinetics ($n \neq 1$)

$$\ln\left(\frac{1-(1-\alpha)^{1-n}}{T^2(1-n)}\right) = \ln\left[\frac{AR}{\beta E_a}\left(1-\frac{2RT}{E_a}\right)\right] - \frac{E_a}{RT} \qquad (4.3)$$

Notation: α = non dimensional weight of the sample, $\alpha = (m_o - m_t)/(m_o - m_\infty)$, where m_o : initial weight of sample, m_t : instantaneous weight of sample at any time t, m_α : final weight of the sample, A : pre–exponential or frequency factor, E_a : activation energy for thermal degradation, R : universal gas constant, T : temperature, and β : heating rate of the sample. In the above equations, the term $2RT/E_a$ on the RHS can be ignored as it has numerical value << 1. Thus, the plots of LHS of equations 4.2 and 4.3 versus $1/T$ have slope of $-E_a/R$ and intercept of $\ln(AR/\beta E_a)$, from which the activation energy and pre–exponential factor can be calculated. However, for non–1st order kinetics, this analysis is implicit as the numerical value of the reaction order, n, needs to be assumed for the calculation of the R.H.S. of equation 4.3. The order of reaction is determined by plotting LHS of equation 4.3 using experimental profile of α versus T with different assumed values of n, and fitting a straight line to this plot. The best fit of the plot is determined by maximizing the regression

coefficient, R^2. The n value corresponding to the plot with R^2 closest to 1 is considered as the reaction order of thermal degradation. The kinetic parameters of activation energy (E_a) and pre–exponential factor (A) can be determined from the slope and intercept of this plot. Fig. 4.3 shows the Coats– Redfern plots for pristine PMMA and PMMA/RGO nanocomposites. The results of these plots are summarized in Table 4.2B. For the pristine PMMA, plot for n = 1 has the highest value of R^2, while for all nanocomposites (for RGO loading of 0.2, 0.4 and 1.0 wt%), plots corresponding to n = 0.2 have best fit to experimental data with $R^2 > 0.99$. An inspection of the kinetic parameters listed in Table 4.2B reveals that both E_a and A increase markedly with incorporation of RGO nanosheets in the PMMA matrix. For RGO loading of 0.2 wt%, the activation energy of thermal decomposition increases over 60% from 68.02 kJ/mol for pristine PMMA to 108.61 kJ/mol for PMMA/RGO nanocomposite. It is notable, however, that E_a shows miniscule variation with RGO loading, demonstrating almost similar E_a for 0.2, 0.4 and 1.0 wt% RGO loading. The reaction order for thermal degradation also shows marked reduction with incorporation of RGO nanosheets in the PMMA matrix. For pristine PMMA, the reaction order for thermal degradation is 1, while for all nanocomposites the reaction order is 0.2. Reduction in reaction order essentially indicates more uniform degradation of nanocomposite with time, which could be a consequence of good dispersion and distribution of RGO in PMMA matrix. This feature is also confirmed by solid state reaction mechanism determined using Criado analysis as explained in the following paragraph.

Criado method essentially determines the reaction mechanism of the solid state process using the conversion vs temperature data. In this method, standard curves of function z(α) versus α are plotted using the equation:

$$Z(\alpha) = \frac{\beta}{A} g(\alpha) \frac{d\alpha}{dT} \exp\left(\frac{E_a}{RT}\right) \qquad (4.4)$$

where $g(\alpha)$ is a function that represents different reaction mechanisms of solid state process. Table 4.2C provided lists some common forms of function $g(\alpha)$, corresponding to various reaction mechanisms.

The Arrhenius parameters E_a and A are determined from Coats–Redfern method. A plot of $Z(\alpha)$ versus α is also made using the experimental data with the following equation.

$$Z(\alpha) = \frac{d\alpha}{dT}\frac{E_a}{R}\exp\left(\frac{E_a}{RT}\right)P(x) \qquad (4.5)$$

where the function $P(x)$ is:

$$P(x) = \frac{\exp(-x)}{x}\frac{x^3 + 18x^2 + 86x + 96}{x^4 + 20x^3 + 120x^2 + 240x + 120}, \text{ where } x = E_a/RT \qquad (4.6)$$

The reaction mechanism of thermal degradation can be determined by comparing the theoretical curves for various $g(\alpha)$ functions and the experimental curve. $g(\alpha)$ function for the theoretical curve, which shows closest overlap with the experimental curve, represents reaction mechanism of thermal degradation of nanocomposites.

The results of Criado analysis are given in Fig. 4.4. It can be seen from Fig. 4.4A that the degradation profile of pristine PMMA has closest match with theoretical curve for $g(\alpha)$, corresponding to mechanism F1 (random nucleation having one nucleus on individual particle mechanism. On the other hand, the degradation of all PMMA/RGO nanocomposites have closest overlap with theoretical curve for $g(\alpha)$ corresponding to mechanism D1 (1–D diffusion). This result essentially points that the presence of RGO nanofiller in the PMMA matrix enhances the thermal stability of the nanocomposites by changing the reaction mechanism of degradation. A plausible explanation for this result can be given as follows: As hypothesized in several previous studies, (Kasiwagi et al., 1986; Ferriol et al., 2003) the thermal degradation of pristine PMMA chains is initiated by scission at head–to–head linkage at 160 ^{o}C, due to the relatively low H–H bond energy. This results in formation of a chain

radical that undergoes depropagation. With further increase in temperature to 270 ^{o}C, thermal degradation proceeds by scission at unsaturated ends (formed due to termination by disproportion) to the vinyl groups through homolytic β–scission. Finally, at around 350 ^{o}C, the degradation predominantly occurs through random scission of polymer chains in pristine PMMA. The degradation profile of pristine PMMA depicted in Fig. 4.4 is for the higher temperature range of 317–377^{o}C. In concurrence with the discussion given above, the predominant degradation mechanism of degradation of pristine PMMA in this temperature range is random nucleation or random scission of polymer chains.

The predominant thermal degradation mechanism of PMMA/RGO nanocomposites is 1–D diffusion. Incorporation of RGO nanosheets in the PMMA matrix has some distinct effects, which contribute to enhancement of thermal stability, as follows: (1) RGO nanosheets restrict the mobility of polymer chains and scavenge/capture the free radicals, formed during pyrolysis and initiate/propagate scission of PMMA chains, (2) the nanofiller material offers hindrance to diffusion/discharge of the volatile products of thermal decomposition through the PMMA matrix, and (3) strong surface interaction between RGO nanosheets and PMMA matrix induced by nanofiller, in addition to cross–linking of PMMA chains, resists the homolytic scission of vinyl groups in PMMA chains. All of these effects contribute to resisting of random nucleation and enhance thermal resistance of material. This is essentially manifested in terms of change of reaction mechanism for thermal degradation from random nucleation to 1–D diffusion.

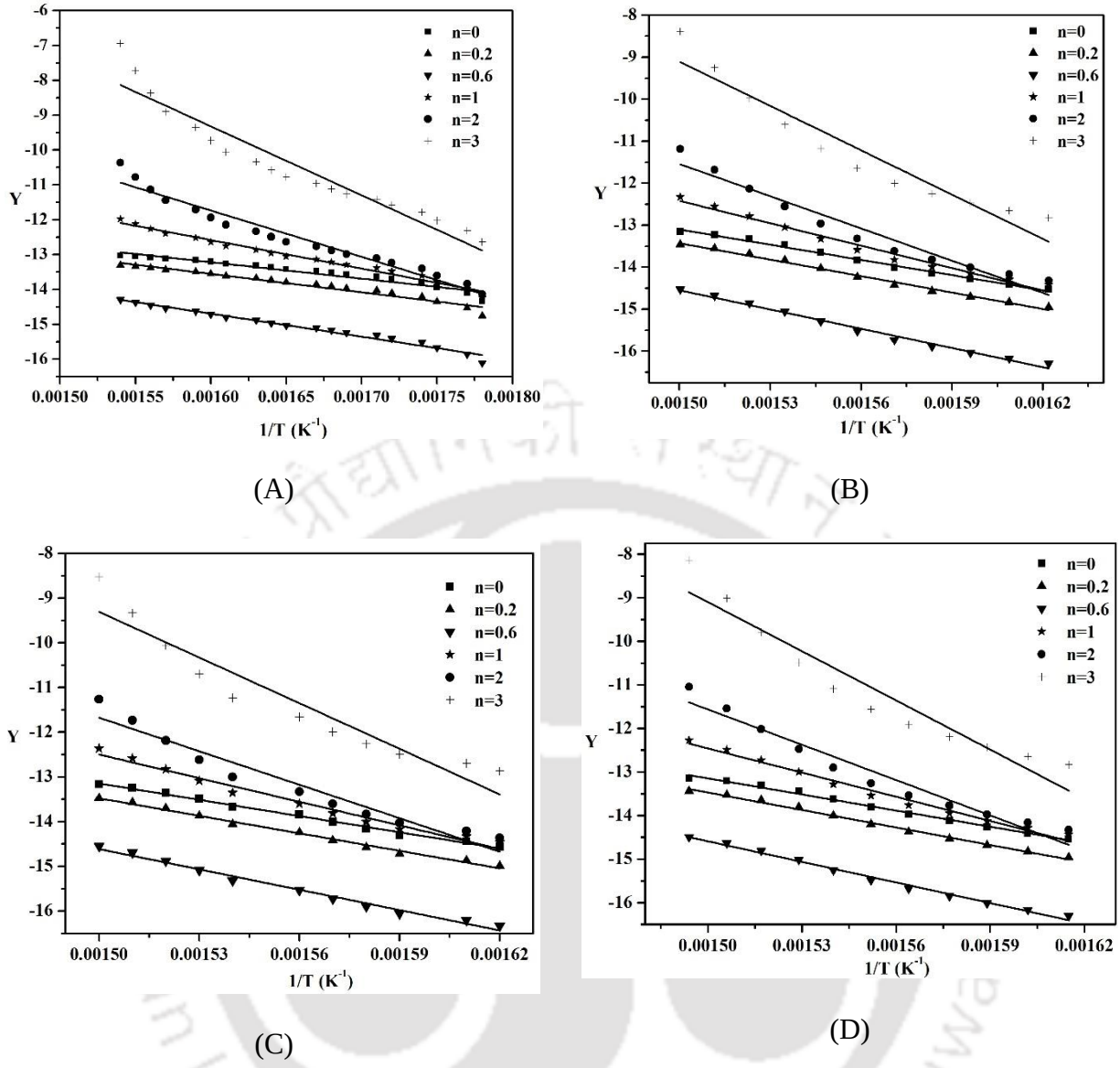

Figure4.3: Coats–Redfern plots (*Y* versus 1/*T*) for determination of the Arrhenius (or kinetic parameters) of thermal decomposition of neat PMMA and PMMA/RGO nanocomposites synthesized with different RGO loadings (A) neat PMMA; (B) PMMA/RGO (0.2 wt%); (C) PMMA/ RGO (0.4 wt%); (D) PMMA/RGO. (1.0 wt%)

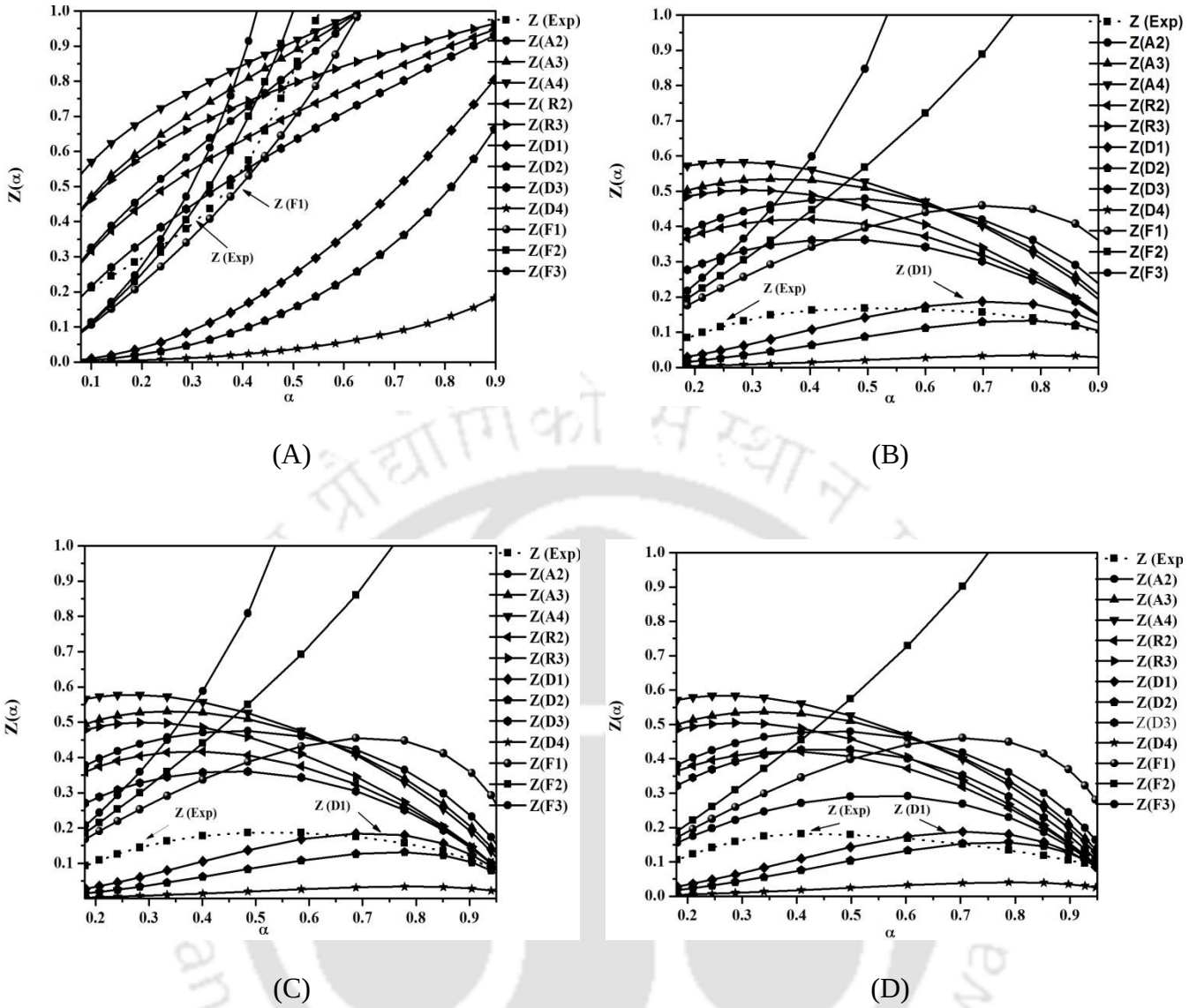

Figure 4.4: Determination of prevalent mechanism of thermal degradation of PMMA/RGO nanocomposites with Criado model using different algebraic functions of g(α), (A) Neat PMMA; (B) PMMA/RGO (0.2 wt%); (C) PMMA/RGO (0.4 wt%); (D) PMMA/RGO (1.0 wt%).

Morphological studies–FE–SEM and TEM analysis: FE–SEM micrographs of the PMMA/RGO nanocomposites synthesized with various RGO loadings are depicted in Fig. 4.5. Uniform dispersion of RGO particles in the PMMA matrix is seen in Fig. 4.5A and B for the lowest RGO loading of 0.2 and 0.4 wt% respectively. As the loading of RGO increases, density of RGO within the PMMA matrix and interactions among the nanoparticles also increase, leading to agglomeration. This feature is evident from micrographs depicted in Figs. 4.5 C for PMMA/RGO nanocomposites synthesized with

RGO loadings of 1.0 wt%.

TEM micrographs of pristine GO and PMMA/RGO nanocomposites are shown in Fig. 4.6. These micrographs confirm encapsulation of the RGO nanosheets into the PMMA matrix. TEM micrograph of pristine GO in Fig. 4.6A shows some single and some multiple layers of wrinkled nanosheets. For relatively low concentrations of RGO (0.2 and 0.4 wt%), presence of RGO nanosheets with some wrinkles in the polymer matrix can be seen in Figs. 4.6B and C. However, these sheets are mostly in single layers due to uniform spread in the polymer matrix. For higher RGO loading of 1.0 wt%, agglomeration of nanosheets with multilayers in the polymer matrix is evident, represented by dark shade in the central region of the micrograph (Fig. 4.6D). The TEM micrographs essentially confirm efficacy of sonication in achieving uniform spread of RGO nanosheets in the polymer matrix, which is manifested in terms of maximum surface interactions between nanofiller and polymer matrix, and enhanced physical properties.

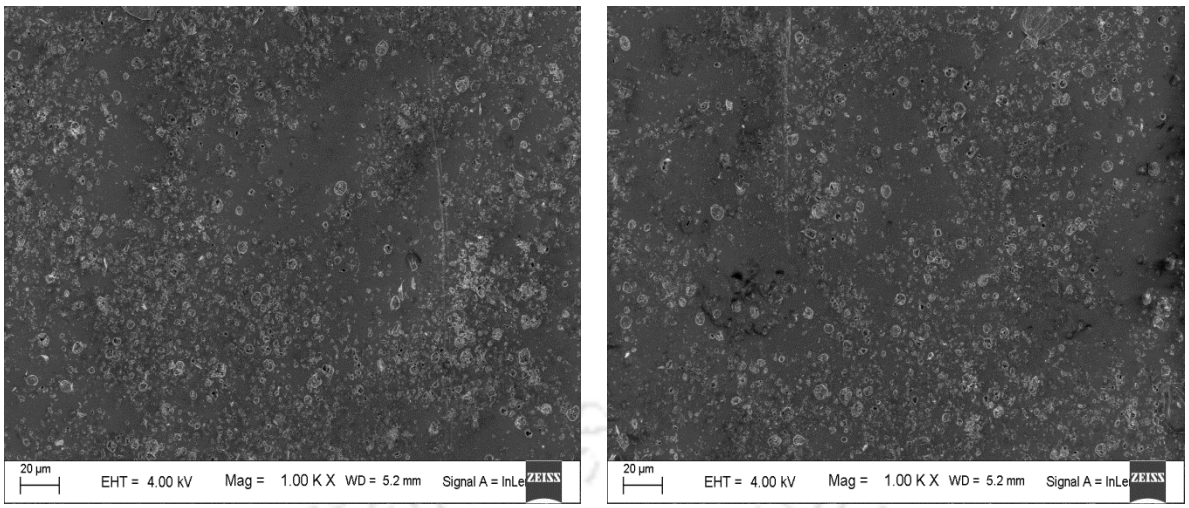

(A) (B)

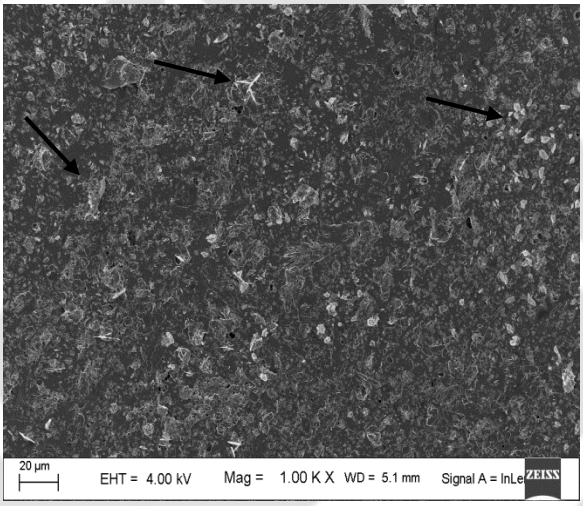

(C)

Figure 4.5: Field emission scanning electron microscope (FE–SEM) images of PMMA/RGO nanocomposites synthesized with different loadings of GO. (A) 0.2 wt% loading, (B) 0.4 wt% loading, (C) 1.0 wt% loading. Agglomerations of the nanofiller material is visible in some portions of the nanocomposite for 1.0 wt% loading.

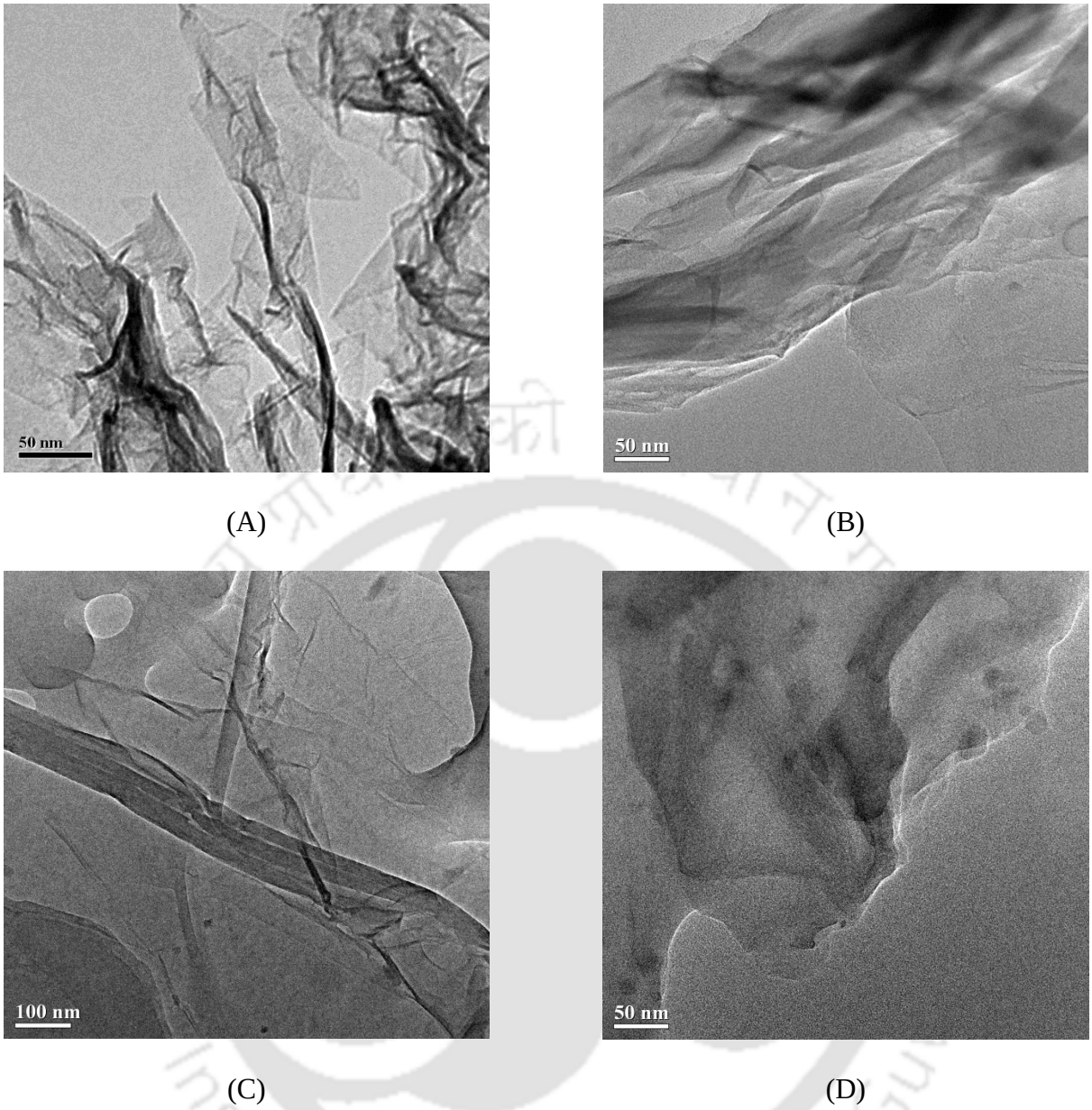

Figure 4.6: Transmission Electron Microscope (TEM) images. (A) Pristine GO, (B) PMMA/RGO (0.2 wt%), (C) PMMA/RGO (0.4 wt%), (D) PMMA/RGO. (1.0 wt%).

4.3.2 Physical properties of nanocomposites

Mechanical properties: Three mechanical properties of PMMA/RGO nanocomposites, viz. tensile strength, Young's modulus and percentage elongation were determined using standard procedures. The results of this analysis are given in Fig. 4.7. Tensile strength testing results shown in Fig. 4.7A reveal maximum tensile strength of 32.7 MPa for the pristine PMMA. With incorporation of RGO nanosheets in the polymer matrix, the tensile strength initially

increased to 40.4 MPa till RGO loading of 0.4 wt%. Thereafter, the tensile strength showed reduction to 18.87 MPa for the RGO loading of 1.0 wt%, respectively. Increase in the tensile strength of PMMA/RGO nanocomposite is attributed to effective encapsulation and uniform exfoliation/dispersion of RGO nanosheets in the PMMA matrix under intense microturbulence generated by sonication. Strong interfacial and adhesive interactions between functionalized RGO nanosheets and PMMA matrix also contributed to enhancement in stiffness of the composite. As noted by Liang et al. (2009) the mechanical performance of RGO nanocomposites would be significantly enhanced by large aspect ratio of the graphene sheets, the molecular level dispersion of the graphene sheets in PMMA matrix, and strong interfacial adhesion due to H-bonding between graphene and PMMA matrix. Oxygen containing function groups bound to the surface of the graphene sheets can also improve interfacial bonding between graphene and PMMA matrix. These factors essentially favour effective stress transfer across PMMA/RGO interface, which results in significant enhancement of tensile strength and Young's modulus. At higher nanofiller loading of 1.0 wt%, agglomeration effect and poor stress transfer characteristics deteriorated the mechanical properties.

Trends in Young's moduli of the PMMA/RGO nanocomposites (depicted in Fig. 4.7B) are similar to those observed in tensile strength. With incorporation of RGO nanosheets in the PMMA matrix, Young's modulus showed significant rise. For 0.2 and 0.4 wt% RGO loading, the PMMA/RGO nanocomposites have Young's moduli of 2.10 and 2.6 GPa, respectively. This is a marked rise over the Young's modulus of 1.17 GPa for pristine PMMA. However, for higher RGO loading of 1.0 wt%, the Young's moduli reduced to 1.13 GPa. Higher Young's moduli of the nanocomposite are manifestations of increase in stiffness of the polymer matrix with incorporation of the nanofiller. Reduction in Young's modulus at higher concentration (1.0 wt%) of the nanofiller is essentially a consequence of

agglomeration of the nanofiller material inside the PMMA matrix.

Trends in percentage elongation of pristine PMMA and PMMA/RGO nanocomposites synthesized with different RGO loadings are shown in Fig. 4.7C. Percentage elongation of pristine PMMA was 3.92%, which increased to 5.94% and 9.3 % with incorporation of RGO nanosheets in the polymer matrix for 0.2 and 0.4 wt% RGO loading. For higher RGO loading, however, reduction in percentage elongation occurs. Smaller concentrations of nanofiller material in polymer matrix cause limited confinement of polymer chains. Moreover, interfacial interactions among the RGO nanosheets and polymer matrix enhance energy absorption capacity of the nanocomposite matrix during deformation induced by shear stress. These effects are essentially manifested in terms of increase in percentage elongation. Nonetheless, restricted ductile flow of polymer chains at higher concentration of nanofiller in the polymer matrix results in reduction of the percentage elongation. Similar trends in the mechanical properties of the PMMA/RGO nanocomposites have also been observed by other authors, e.g. Wang et al. (2012) and Tripathi et al. (2013).

PMMA/RGO nanocomposites (with similar RGO loading) synthesized in the present study possess better mechanical and thermal properties as compared to the previous literature in which PMMA/RGO nanocomposites were synthesized with conventional techniques. $T_{5\%}$ and $T_{10\%}$ temperatures of nanocomposites (viz. 291 ^{o}C and 320 ^{o}C, respectively) in the present study are significantly higher than $T_{5\%}$ = 281 ^{o}C reported by Yuan et al. (2012) for 1.5 wt% RGO and $T_{10\%}$ = 299 ^{o}C reported by Aldosari et al. (2013) for 2.0 wt% RGO. Yuan et al. (2012) also reported max degradation temperature of 371 ^{o}C, which is lower than temperature of 393 ^{o}C (1.0 wt% RGO) observed in the present study. The glass transition temperature of 124.5 ^{o}C obtained in the current study is higher than that reported by Kuilla et al. (2011) (T_g = 114.9 ^{o}C), Yuan et al. (2012) (T_g = 122 ^{o}C) and Aldosari et al. (2013) (T_g = 120 ^{o}C). Mechanical properties of the PMMA/RGO nanocomposites synthesized in our study

(tensile strength = 40.37 MPa, Young's modulus = 2.59 GPa and percentage elongation = 9.28%) are better than those reported by Tripathi et al. (2013) for 1.0 wt% RGO loading, viz. tensile strength = 23 MPa, Young's modulus = 0.87 GPa and percentage elongation = 2.6%.

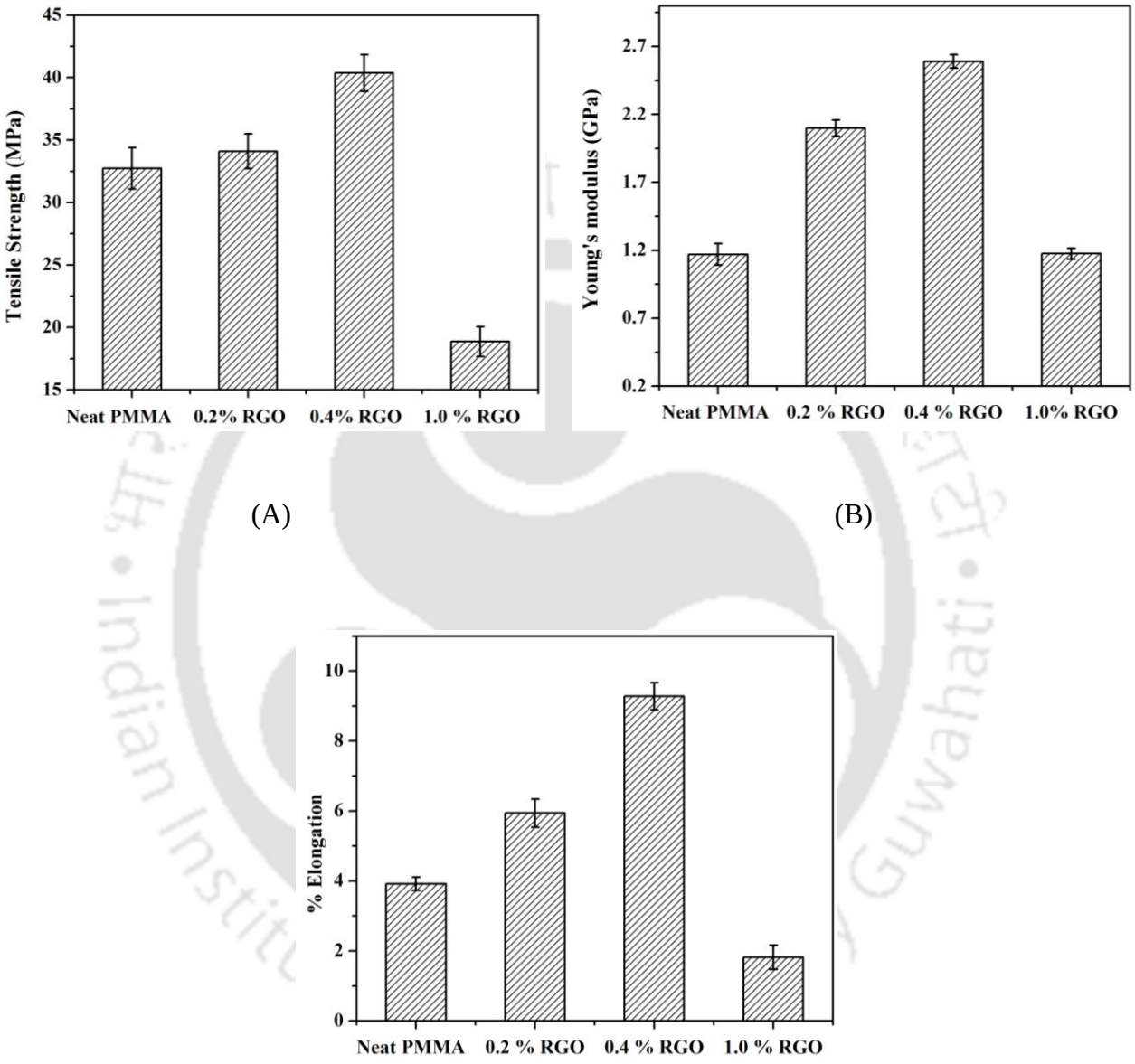

Figure 4.7: Mechanical properties of the pristine PMMA and PMMA/RGO nanocomposites. (A) Tensile strength; (B) Young's modulus; (C) % Elongation before break.

Electrical conductivity: Fig. 4.8A shows the percolation curve of the RGO/PMMA nanocomposites. With incorporation of RGO in the PMMA matrix, the electrical conductivity of nanocomposites showed marked rise, and the rise was directly proportional to the RGO loading. The percolation threshold occurs in the RGO loading range of 0.2 - 0.4 wt%, where the nanocomposite transformed from an insulative material into a conductive material. This transformation is due to the formation of conductive network of RGO nanofiller spanning the PMMA matrix. For maximum RGO loading of 1.0 wt%, the electrical conductivity rose by 8 orders of magnitude from 2.3×10^{-15} S/cm (for neat PMMA) to 2×10^{-7} S/cm. Such a large increase in electrical conductivity at relatively low nanofiller concentration signifies decent exfoliation of the RGO nanosheets with uniform distribution in the PMMA matrix

EMI Shielding: EMI shielding is a protection used to safeguard the performance of electrical and electronic equipment against EMI failure. Mandatory conformity of electromagnetic compatibility (EMC) regulations is a chief factor endorsing global demand for EMI solutions. Furthermore, increased environmental issues and health hazardousness due to EMI have compelled the regulatory bodies to adjust more strict EMC standards worldwide. Metals are common materials to attenuate EM wave; however, their drawbacks such as weight and cost necessitate the development of new sets of materials. Polymers are decent substitution for metals; nonetheless, neat polymers are transparent to EM wave due to their insulative nature. However, incorporating conductive nanofillers within the polymer matrix leads to the formation of conductive nanocomposites with the ability to attenuate EM wave. In other words, conductive polymeric nanocomposites are meritorious substitutions for metals to attenuate EM wave, due to inherent properties of polymers such as light weight, low cost, easy processability, corrosion resistance, etc. coupled with high electrical conductivity coming from conductive network of nanofiller.

EMI shielding in conductive nanocomposites consists of two chief mechanisms, viz. reflection and absorption. Reflection arises from the impedance mismatch between two media, i.e. two media with different electrical conductivity, real permittivity, and/or magnetic permeability. Absorption in conductive nanocomposites originates from Ohmic loss and polarization loss. Ohmic loss comes from the dissipation of energy by nomadic charges through conduction, hopping, and tunnelling mechanisms, whereas polarization loss derives from the reorientation of electric dipoles in each half cycle of EM wave (Chung et al., 2000; Yang et al., 2007; Arjmand and Sundararaj, 2015) EMI SE of the PMMA/RGO nanocomposites has been calculated using equation 4.1 (in the unit of dB), stated earlier. Fig. 4.8A shows the overall SE (SE_o) of the generated nanocomposites as a function of frequency in the X-band frequency range for different RGO loadings. It can be inferred from Fig. 4.8A that SE_o of PMMA/RGO nanocomposites vary proportionately with RGO loading. The increase in SE with RGO loading is attributed to increased number of nomadic charges at higher RGO loading. Moreover, it is well established at higher nanofiller loading the conductive network is stronger, leading to more mean free path for electrons to move in each half cycle of alternating field, thereby leading to more dissipation of electrical energy and thus enhanced SE (Pawar et al., 2016). Figure 4.8B depicts the average shielding by reflection (SE_r), shielding by absorption (SE_a) and overall shielding effectiveness (SE_o) of the generated nanocomposites over the X-band. SE_o of PMMA/RGO nanocomposites is contributed by both absorption and reflection, although the contribution from absorption is higher than reflection for all loadings of the nanofiller. For instance, PMMA/RGO nanocomposites at nanofiller loading of 1.0 wt% demonstrated a combination of SE_r = 1.44 dB and SE_a = 1.83 dB by absorption. On the contrary, for neat PMMA SE_o had combination of SE_r = 1.36 dB and SE_a = 1.22 dB, indicating greater contribution to shielding efficiency by reflection.

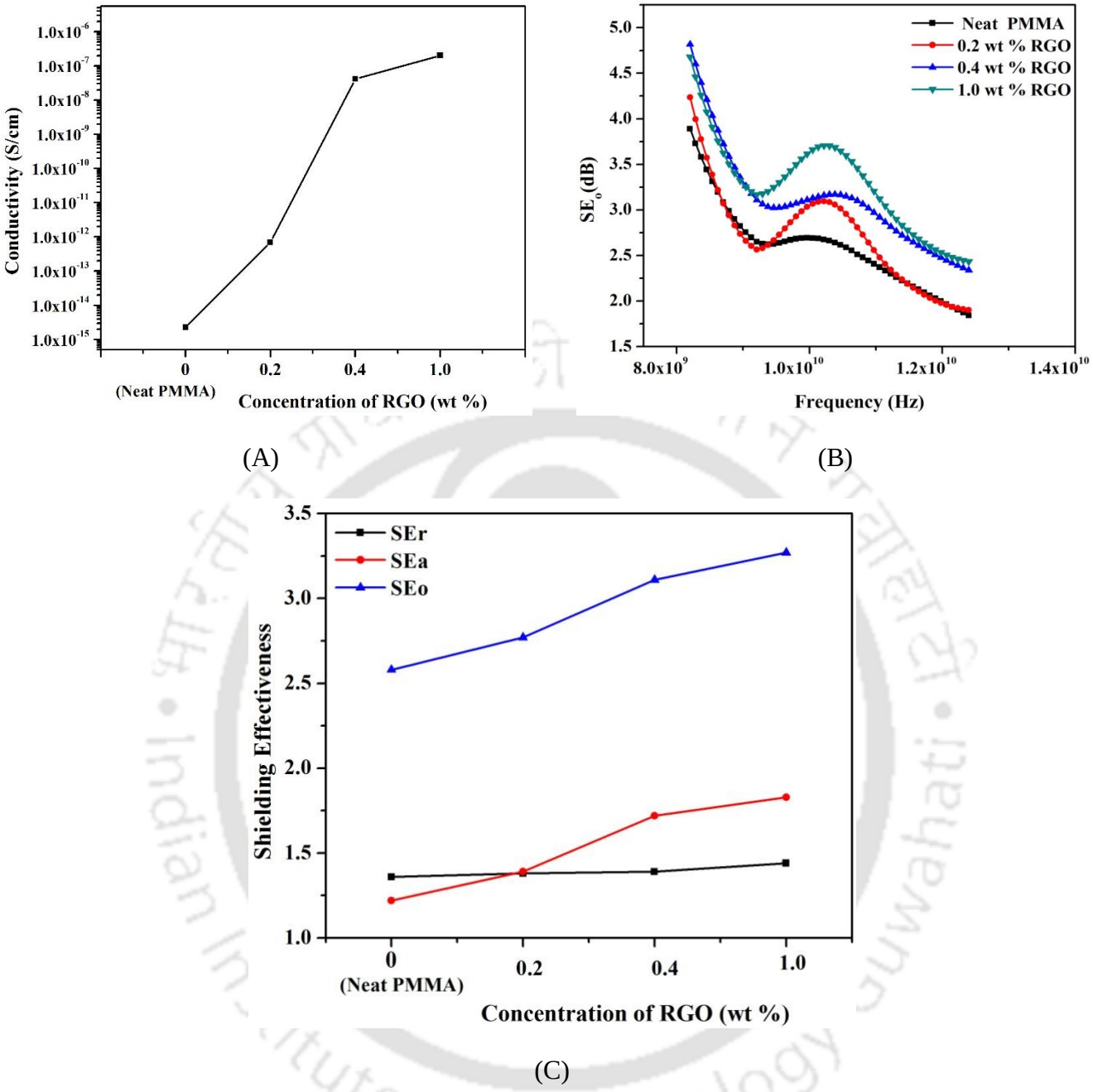

Figure 4.8: Electrical properties of PMMA/RGO nanocomposites. (A) Electrical conductivity. Electromagnetic interference (EMI) shielding properties of PMMA/RGO nanocomposites synthesized with varying RGO loadings. (B) Trends in overall shielding with frequency in the X-band (8.2–12.4 GHz). (C) Trends in EMI shielding efficiency with RGO loading (SE_a : shielding by absorption, SE_r : shielding by reflection, SE_o : overall shielding).

Table 4.3: Comparison of physical properties of neat PMMA and its RGO nanocomposites synthesized with conventional and ultrasound–assisted techniques

Type of properties	Property measure / Technique	Neat PMMA[#]	PMMA/RGO nanocomposite (conventional synthesis)[#]	PMMA/RGO nanocomposite (present study)[#]
Thermal Properties	Degradation temperature for different weight losses (TGA)	$T_{5\%}$ = 267.4 °C $T_{10\%}$ = 274 °C $T_{50\%}$ = 326.1°C (present study) $T_{5\%}$ = 249°C (Yuan et al., 2012) $T_{5\%}$ = 201.1°C (Ji et al., 2014) $T_{10\%}$ = 290°C (Aldosari et al., 2013)	$T_{5\%}$ = 281 °C (1.5 wt%) (Yuan et al., 2012) $T_{10\%}$ = 299 °C (2.0 wt%) (Aldosari et al., 2013) $T_{50\%}$ = 372 °C (2.0 wt%) (Aldosari et al., 2013)	$T_{5\%}$ = 291 °C (1 wt%) $T_{10\%}$ = 320 °C (0.4 wt%) $T_{50\%}$ = 375 °C (1.0 wt%)
	Max. Degradation temperature (DTG)	377 °C (present study) 330 °C (Pramoda et al., 2010) 369 °C (Yuan et al., 2012)	360 °C (0.5 wt%) (Pramoda et al., 2010) 371 °C (1.5 wt%) (Yuan et al., 2012) 268.9 °C (0.5 wt%) (Ji et al., 2014)	380 °C (0.2 wt%) 391 °C (0.4 wt%) 393 °C (1.0 wt%)
	Glass transition temperature (DSC)	116 °C (present study) 103.6 °C (Kuila et al., 2011) 103.2 °C (Ji et al., 2014) 107 °C(Yuan et al., 2012) 117 °C (Aldosari et al., 2013)	114.9 °C (1 wt%) (Kuila et al., 2011) 122.5 °C (0.5 wt%) (Ji et al., 2014) 122 °C (1.5 wt%) (Yuan et al., 2012) 120 °C (2.0 wt%) (Aldosari et al., 2013)	124.5 °C (0.4 wt%)
Mechanical Properties	Tensile strength	32.74 MPa (present study) 24.2 MPa (Tripathi et al., 2013)	23.0 MPa (1 wt%) (Tripathi et al., 2013)	40.37 MPa (0.4 wt%)
	Young's modulus	1.17 GPa (present study) 0.750 GPa (Tripathi et al., 2013)	0.865 GPa (1 wt%) (Tripathi et al., 2013)	2.59 GPa (0.4 wt%)
	Percentage elongation	3.92% (present study) 2.8% (Tripathi et al., 2013)	2.6% (1 wt%) (Tripathi et al., 2013)	9.28% (0.4 wt%)

RGO loading during nanocomposite synthesis (wt% MMA) is mentioned in the bracket.

4.4 Conclusions

PMMA/RGO nanocomposites synthesized using ultrasound-assisted emulsion polymerization have shown marked enhancement in physical properties as compared to neat PMMA at very low concentrations (≤ 1.0 wt%) of the nanofiller. Moreover, the physical properties of PMMA/RGO nanocomposites in the present study are significantly better than those reported in the previous literature (employing conventional techniques of synthesis) for similar RGO concentrations, as illustrated in Table 4.3. These results are essentially attributed to effective exfoliation of RGO nanosheets and uniform dispersion in the PMMA matrix under influence of strong microconvection generated by ultrasound and cavitation. High aspect ratio of the RGO nanosheets and high surface interaction between polymer matrix and nanofiller also contribute to enhancement of physical properties. It needs to be mentioned that relatively low concentration of nanofiller (≤ 1.0 wt%) employed in the present study is aimed at achieving a good balance between thermal/mechanical and electrical properties of the nanocomposites. This is evident from the results of the present study, which reveal highest thermal and mechanical properties (viz. maximum thermal degradation temperature, glass transition temperature, tensile strength, Young's modulus, percentage elongation) at RGO loading of 0.4 wt%, while the highest electrical properties (viz. conductivity and electromagnetic interference shielding efficiency) are at RGO loading of 1.0 wt%. PMMA/RGO nanocomposites with optimal combinations of physical properties (viz. max thermal degradation temperature = 393 ^{o}C, glass transition temperature = 125 ^{o}C, tensile strength = 40.37 MPa, Young's modulus = 2.59 GPa, percentage elongation = 9.28%, electrical conductivity = 2×10^{-7} S/cm, EMI shielding effectiveness = 3.28 dB) synthesized in the present study illustrate the efficacy of the technique of ultrasound-assisted in-situ emulsion polymerization.

References

Aldosari MA, Othman AA, Alsharaeh EH, Synthesis and characterization of the in situ bulk polymerization of PMMA containing graphene sheets using microwave irradiation, Molecules, 18 (2013) 3152–3167.

Arjmand M, Sundararaj U, Electromagnetic interference shielding of nitrogen-doped and undoped carbon nanotube/polyvinylidene fluoride nanocomposites: A comparative study, Compos. Sci. Technol. 118 (2015) 257–263.

Bhasarkar JB, Chakma S, Moholkar VS, Mechanistic features of oxidative desulfurization using sono–Fenton–peracetic acid (Ultrasound/Fe^{2+}–CH_3COOH–H_2O_2) system, Ind. Eng. Chem. Res. 52 (2013) 9038–9047.

Bianchi Q, Repenning GB, Canto LB, Mauler RS, Oliveira RVB, Kinetics of thermo–oxidative degradation of PS–POSS hybrid nanocomposite, Polym. Test. 32 (2013) 794–801.

Chakma S, Moholkar VS, Physical mechanism of sono–Fenton process, AIChE J. 59 (2013) 4303–4313.

Chung DDL, Materials for electromagnetic interference shielding, J. Mater. Eng. Perform. 9 (2000) 350–354

ElAchaby M, Arrakhiz FZ, Vaudreuil S, Essassi EM, Qaiss A, Piezoelectric β–polymorph formation and propertiesenhancement in graphene oxide—PVDF nanocomposite films, Appl. Surf. Sci, 258 (2012) 7668–7677.

Fan Z, Wang K, Wei T, Yan J, Song L, Shao B, An environmentally friendly and efficient route for the reduction of graphene oxide by aluminum powder, Carbon. 48 (2010) 1686–1689.

Fang M, Wang K, Lu H, Yang Y, Nutt S, Covalent polymer functionalization of graphene nanosheets and mechanical properties of composites, J Mater. Chem. 19 (2009) 7098–7105.

Ferriol M, Gentilhomme A, Cochez M, Oget N, Mieloszynski JL, Thermal degradation of poly(methyl methacrylate) (PMMA): modelling of DTG and TG curves, Polym. Degrad. Stab. 79 (2003) 271–281.

Georgakilas V, Otyepka M, Bourlinos AB, Chandra V, Kim N, Kemp KC, Hobza P, Zobril R, Kim KS, Functionalization of graphene: Covalent and non–covalent approaches, derivatives and applications, Chem. Rev. 112 (2012) 6156–6214.

Gonçalves G, Marques PAAP, Barros–Timmons A, Bdkin I, Singh MK, Emami N, et al., Graphene oxide modified with PMMA via ATRP as a reinforcement filler, J. Mater. Chem. 20 (2010) 9927–9934.

Hummers WS, Offeman RE, Preparation of graphitic oxide, J. Am. Chem. Soc. 80 (1958) 1339.

Jang JY, Kim MS, Jeong HM, Shin CM, Graphite oxide/poly(methyl methacrylate) nanocomposites prepared by a novel method utilizing macro azoinitiator, Compos. Sci. Technol. 69 (2009) 186–191.

Ji WF, Chang KC, Lai MC, Li CW, Hsu SC, Chuang TL, et al., Preparation and comparison of the physical properties of PMMA/thermally reduced graphene oxides composites with different carboxylic group content of thermally reduced graphene oxides, Compos. Part A: Appl. Sci. Manuf. 65 (2014) 108–114.

Kanmuri S, Moholkar VS, Mechanistic aspects of sonochemical copolymerization of butyl acrylate and methyl methacrylate, Polymer 51 (2010) 3249–3261.

Kashiwagi T, Inaba A, Brown JE, Hatada K, Kitayama T, Masuda E, Effects of weak linkages on the thermal and oxidative degradation of poly(methyl methacrylates) Macromolecules. 19 (1986) 2160–2168.

Kim H, Kobayashi S, Abdurrahim MA, Zhang MJ, Khusainova Hillmyer MA, Abdala AA, Macosko CW, Graphene/polyethylene nanocomposites: Effect of polyethylene functionalization and blending methods, Polymer 52 (2011) 1837–1846.

Krishna SV, Pugazhenthi G, Properties and thermal degradation kinetics of polystyrene/organoclay nanocomposites synthesised by solvent blending method: Effect of processing conditions and organoclay loading, J. Appl. Polym. Sci. 120 (2011) 1322–1336.

Krishnamoorthy K, Kim GS, Kim SJ, Graphene nanosheets: Ultrasound assisted synthesis and characterization, Ultrason. Sonochem, 20 (2013) 644–649.

Kuila T, Bose S, Khanra P, Kim NH, Rhee KY, Lee JH, Characterization and properties of in situ emulsion polymerized poly(methyl methacrylate)/graphene nanocomposites, Compos. Part A: Appl. Sci. Manuf. 42 (2011) 1856–1861.

Kuppa R, Moholkar VS, Physical features of ultrasound-enhanced heterogeneous permanganate oxidation, Ultrason. Sonochem. 17 (2010) 123–131.

Li B, Yuan H, Zhang Y. Transparent PMMA–based nanocomposite using electrospun graphene–incorporated PA–6 nanofibers as the reinforcement. Compos. Sci. Technol. 89 (2013) 134–141.

Liang J, Huang Y, Zhang L, Wang Y, Ma Y, Guo T, Chen Y, Molecular-level dispersion of graphene intoPoly(vinyl alcohol) and effective reinforcement of their nanocomposites, Adv. Funct. Mat. 19 (2009) 1–6.

Mason TJ, Lorimer JP, Sonochemistry: theory, application and uses of ultrasound in chemistry, New York: Ellis Horwood; 1989.

Mcallister MJ, Li J, Adamson DH, Schniepp HC, Abdala AA, Liu J et al., Single sheet functionalized graphene by oxidation and thermal expansion of graphite, Chem. Mater. 19 (2007) 4396–4404.

Morimune S, Nishino T, Goto T, Ecological approach to graphene oxide reinforced poly(methyl methacrylate), Nanocomposites 4 (2012) 3596–3601.

Morya NK, Iyer PK, Moholkar VS, A physical insight into sonochemical emulsion polymerization with cavitation bubble dynamics, Polymer 49 (2008) 1910–1925.

Park S, An J, Piner RD, Jung I, Yang D, Velamakanni A, et al., Aqueous suspension and characterization of chemically modified graphene sheets, Chem Mater. 20 (2008) 6592–6594.

Pawar SP, Arjmand M, Gandi M, Bose S, Sundararaj U, Critical insights in understanding effects of synthesis temperature and nitrogen doping towards charge storage capability and microwave shielding in nitrogen-doped carbon nanotube/polymer nanocomposites, RSC Advances 6 (2016) 63224–63234.

Pham VH, Cuong TV, Dang TT, Hur SH, Kong BS, Kim EJ, et al. Superior conductive polystyrene–chemically converted graphene nanocomposite. J. Mater. Chem. 21 (2011) 11312–11316.

Ping WW, Yuan PC, Preparation and characterization of poly(methyl methacrylate)–intercalated graphite oxide/poly(methyl methacrylate) nanocomposite, Polym. Eng. Sci. 44 (2004) 2335–2339.

Pramoda KP, Hussain H, Koh HM, Tan HR, He CB, Covalent bonded polymer–graphene nanocomposites, J. Polym. Sci. A: Polym. Chem. 48 (2010) 4262–4267.

Putz KW, Compton OC, Palmeri MJ, Nguyen ST, Brinson LC. High–nanofiller–content graphene oxide–polymer nanocomposites via vacuum–assisted self–assembly. Adv. Funct. Mater. 20 (2010) 3322–3329.

Qian Y, Wu H, Yuan D, Li X, Yu W, Wang C, In situ polymerization of polyimide–based nanocomposites via covalent incorporation of functionalized graphene nanosheets for enhancing mechanical, thermal, and electrical properties, J. Appl. Polym. Sci. 132 (2015) 42724.

Ren L, Wang X, Guo S, Liu T, Functionalization of thermally reduced graphene by in situ atom transfer radical polymerization, J Nanoparticle Res. 13 (2011) 6389–6396.

Stankovich S, Dikin DA, Piner R, Kohlhaas KM, Kleinhammes A, Jia Y et al., Synthesis of graphene–based nanosheets via chemical reduction of exfoliated graphite oxide, Carbon 45 (2007) 1558–15565.

Steurer P, Wissert R, Thomann R, Mulhaupt R, Functionalized graphenes and thermoplastic nanocomposites based upon expanded graphite oxide. Macromol. Rapid Commun. 2009;30:316–327.

Suslick KS, Ultrasound: its chemical, physical and biological effects. New York: VCH Publishers; 1988.

Tripathi SN, Saini P, Gupta D, Choudhary V, Electrical and mechanical properties of PMMA/reduced graphene oxide nanocomposites prepared via in situ polymerization, J. Mater. Sci. 48 (2013) 6223–6232.

Wang J, Shi Z, Ge Y, Wang Y, Fan J, Yin J, Solvent exfoliated graphene for reinforcement of PMMA composites prepared by in situ polymerization, Mater. Chem. Phys. 136 (2012) 43–50

Worsley KA, Ramesh P, Mandal SK, Niyogi S, Itkis ME, Haddon RC, Soluble graphene derived from graphite fluoride, Chem Phys Lett. 445 (2007) 51–56.

Yang, Y, Wu G, Ramalingam S, Hsu, SL, Kleiner L, Tang FW, Spectroscopic analysis of amorphous structure in fluorinated polymers, Macromolecules 40 (2007) 9658–9663.

Yuan XY, Zou LL, Liao CC, Dai JW, Improved properties of chemically modified graphene/poly(methyl methacrylate) nanocomposites via a facile in–situ bulk polymerization, Express Polym. Lett. 6 (2012) 847–858.

Zhang HB, Yan Q, Zheng W, He Z, Yu Z. Tough graphene–polymer microcellular foams for electromagnetic interference shielding, ACS Appl. Mater. Interfaces.3 (2011):918–924.

Zheng W, Wong S. Electrical conductivity and dielectric properties of PMMA / expanded graphite composites. Compos. Sci. Technol. 63 (2003) 225–235.

CHAPTER 5

ULTRASOUND-ASSISTED SYNTHESIS AND CHARACTERIZATION OF MAGNETITE NANOPARTICLES AND PMMA/MAGNETITE NANOCOMPOSITES

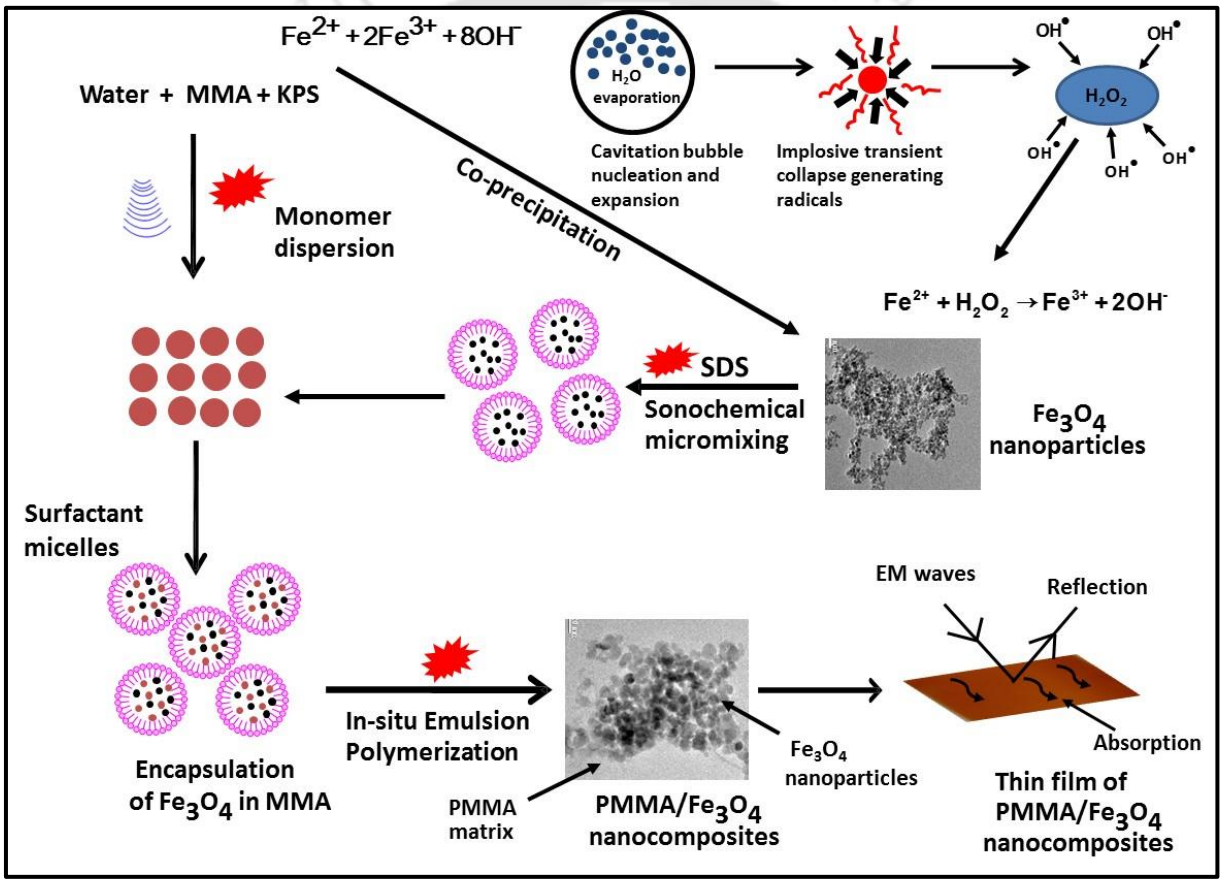

CHAPTER 5

Ultrasound-Assisted Synthesis and Characterization of Magnetite Nanoparticles and PMMA/Magnetite Nanocomposites

5.1 Introduction

Among various nanofillers, ferrofluid based magnetic nanoparticles have attracted significant interest due to the remarkable enhancement in thermal, electrical, magnetic and optical properties of the pristine polymers after their incorporation in the polymer matrix. Magnetic polymer nanocomposites have been used in numerous applications such as EMI shielding, enhancement in electrical conductivity, biomedical applications including drug delivery, biomedicine, magneto–optical devices, biosensors, magnetic resonance imaging (MRI), magnetic recording etc (Moser et al., 2002; Ramirez et al., 2003; Kaushik et al., 2008; Kim et al., 2008; Mahdavian et al., 2008). Superparamagnetic iron oxide based polymer nanocomposites are most commonly used due to their high magnetic saturation and narrow particle size distribution. Polymethyl methacrylate (PMMA) has been a versatile polymer due to its high impact strength, environmental stability and good transmittance. However, PMMA suffers from demerits such as negligible electrical conductivity, low thermal stability, lack of any magnetism, and low ductility. Various physical properties of PMMA such thermal

stability, magnetic properties (magnetic saturation), electrical conductivity, EMI shielding and mechanical properties. can be enhanced by addition of filler material such as magnetic nanoparticles. Several previous papers have addressed the matter of synthesis of PMMA/Fe_3O_4 nanocomposites using techniques such as in situ emulsion polymerization, solvent blending method, melt mixing method, atom transfer free radical polymerization (ATRP), suspension polymerization and reverse microemulsion. A summary of previous literature on synthesis, characterization and application of PMMA/Fe_3O_4 nanocomposites is presented in Table 5.1.

The principal factors that govern enhancement in physical properties of nanocomposites are extent of encapsulation and nature of dispersion of the nanofiller material in polymer matrix. Both of these factors depend on surface interactions and compatibility of the nanofiller material with polymer matrix, in addition to the extent of monomer conversion in the reaction system during polymerization. Polymer nanocomposites synthesized using conventional methods mentioned previously have demerit of non–uniform dispersion and agglomeration of the magnetic nanoparticles in polymer matrix (Table 5.1). A possible means of enhancing the polymer–nanofiller compatibility, which would be manifested in terms of greater nanofiller encapsulation and uniform dispersion in the polymer matrix is surface modification of the filler material. Usual methods of surface modifications include absorption of silane coupling agent or grafting of polymeric chains on external surface of inorganic filler particles (Fan et al., 2006; Shen et al., 2006; Bach et al., 2012). Use of surfactants for surface modification or surface treatment of inorganic nanoparticles is one of the simplest and economical methods to improve the dispersion behaviour of nanoparticles in aqueous systems (Nsib et al., 2006; Hong et al., 2009; Gyergyek et al., 2010). The polar groups present in the surfactants molecules are selectively adsorbed on nanoparticle surface as a result of electrostatic interactions. The surfactant reduces the physical forces between the

nanomaterials which decrease the inter particle interaction and controlling the agglomeration of nanoparticles. Conventionally used anionic surfactant of oleic acid is not much useful for surface treatment of magnetic nanoparticles, as the saturation magnetization (M_s) of surfaced modified magnetic nanoparticles reduce sharply as compared to the native nanoparticles.

In the present study, we have reported a new ultrasound–assisted two–step methodology for synthesis of PMMA/Fe_3O_4 nanocomposites. In the first step, Fe_3O_4 nanoparticles have been synthesized using co–precipitation technique which includes in–situ oxidation of Fe^{2+} to Fe^{3+} induced by radicals generated from transient cavitation bubbles. In the second step, in–situ emulsion polymerization of MMA monomers with Fe_3O_4 nanoparticles (in native form – without surface modification) has been carried out under ultrasound irradiation. We have also carried out extensive characterization of synthesized PMMA/Fe_3O_4 nanocomposites for the thermal, mechanical, electrical and magnetic properties under different loading of iron oxide particles. The ultrasound–assisted technique for in–situ synthesis of PMMA/Fe_3O_4 nanocomposites is much simpler and easier than previously reported techniques, and yet highly effective in imparting the nanocomposite desired thermal, mechanical, electrical and magnetic, as explained in subsequent sections.

Table 5.1: Summary of literature on synthesis and characterization of PMMA/Fe_3O_4 nanocomposites.

Reference	Mode of synthesis	Experimental conditions	Major findings and conclusions
Wilson et al. (2004)	PMMA/Fe_3O_4 nanocomposites using melt blending method	Two–step process: (1) iron oxide nanoparticles were prepared using a microwave plasma technique, (2) synthesis of PMMA/Fe_3O_4 nanocomposites with various loading of Fe_3O_4 such as 0.5, 1 and 10 wt% using melt blending technique at 210 °C.	PMMA/Fe_3O_4 nanocomposite showed saturated magnetization (M_s) = 0.091, 0.41 and 11.5 emu/g for 0.5, 1 and 10 wt% nanofiller concentration, respectively, at room temperature. SEM micrograph exhibit the uniform dispersion of Fe_3O_4 nanoparticles in PMMA matrix
Banert et al. (2006)	PMMA/Fe_3O_4 nanocomposites by solvent blending method	Two–step process: (1) preparation of magnetic fluid by co-precipitation method using $FeSO_4 \cdot 7H_2O$ and $FeCl_3 \cdot 6H_2O$, followed by surface modification with oleic acid. Fe^{3+}/Fe^{2+} = 2:1 molar ratio, Temp = 70 °C, (2) PMMA/Fe_3O_4 nanocomposites were synthesized using addition of dichloromethane in above magnetic fluid.	Super-paramagnetic behaviour of PMMA/Fe_3O_4 nanocomposite with saturated magnetization (M_s) = 18.33 Am^2/kg for loading of 22.8 wt% Fe_3O_4. Oleic acid used as a surface modifying agent for Fe_3O_4 nanoparticles. Glass transition temperature (T_g) of PMMA/Fe_3O_4 = 103 °C
Hong et al. (2009)	Synthesis of PMMA/Fe_3O_4 nanocomposites by double-miniemulsion polymerization method	Two–step process: (1) preparation of ferro-fluid using oleic acid coated Fe_3O_4 nanoparticles using co-precipitation method. (2) synthesis of PMMA/Fe_3O_4 nanocomposites using in-situ double mini-emulsion technique with AIBN as initiator. Reaction mixture: hexadecane = 0.12 g, SDS = 0.15 g, distilled water = 20 g, temperature = 80 °C, reaction time = 90 min	TGA analysis reveals reduction of mass loss with addition of Fe_3O_4 in PMMA. Saturation magnetization (M_s) = 65.6 and 47.7 emu/g for native and oleic acid coated Fe_3O_4 respectively. For PMMA/Fe_3O_4 (~ 17 wt% Fe_3O_4) nanocomposite, M_s = 23.7 emu/g
Gyergyek et al. (2010)	Synthesis of PMMA/Fe_3O_4 nanocomposites by miniemulsion polymerization method	Two–step process: (1) preparation of magnetic fluid by co-precipitation method using $FeSO_4 \cdot 7H_2O$ and $FeCl_3 \cdot 6H_2O$, using NH_4OH in addition with ricinoleic acid (RA). Fe^{3+}/Fe^{2+} = 2:1 molar ratio, RA = 5 g, Temp = 80 °C, (2) synthesis of PMMA/Fe_3O_4 nanocomposites, MMA = 5 g in addition with above synthesized ferro fluid, water + SDS = 63 g with varying concentration of SDS, Temp = 60 °C, reaction time = 16 h	SDS controlled the particles size of the nanocomposite in the range of 25 - 49 nm. Use of ricinoleic acid provided stable dispersion of iron oxide nanoparticles with reduction in M_s value. PMMA/Fe_3O_4 nanocomposites exhibit superparamagnetic behaviour (M_s = 27.3 emu/g) with Fe_3O_4 loading of ~ 39 wt%

Table 5.1: (*continued…*)

Reference	Mode of synthesis	Experimental conditions	Major findings and conclusions
Lan et al. (2011)	PMMA/Fe_3O_4 nanocomposites by miniemulsion polymerization method	Two–step process: (1) synthesis of Fe_3O_4 using precursor ferric acetylacetonate [Fe $(acac)_3$] and 1,2-hexadecanediol with oleic acid as surface modifier. (2) synthesis of PMMA/Fe_3O_4 nanocomposites: SDBS = 12 mg, PVA = 508 µL, MMA = 293 µl, Fe_3O_4 ferrofluid = 400 µl, ultrasound power = 130 W, magnetic stirring = 300 rpm, Temp = 80 °C, time = 5 h.	Mean particle size of Fe_3O_4 and PMMA/Fe_3O_4 was 8 and 90 nm, respectively. VSM results reveal that PMMA/Fe_3O_4 nanocomposites are super-paramagnetic with M_s value = 39 emu/g.
Kirchberg et al. (2012)	PMMA/Fe_3O_4 nanocomposites by solvent blending method	Two–step process: (1) preparation of Fe_3O_4 nanoparticles by co-precipitation method using ricinoleic and oleic acid as a surface modifying agent. (2) synthesis of PMMA/Fe_3O_4 nanocomposite by solvent blending method using dichloromethane. Reaction mixture: hexadecane = 0.12 g, SDS = 0.15 g, distilled water = 20 g, Temp = 80 °C, reaction time = 90 min with AIBN as initiator.	No significant improvement in the T_g of PMMA/Fe_3O_4 nanocomposites as compared to neat PMMA. TGA result revealed enhancement in degradation temperature of PMMA with addition of Fe_3O_4 nanoparticles surface modified with ricinoleic and oleic acid.
Bansod et al. (2014)	PMMA/Fe_2O_3 nanocomposites by solvent blending method	Single step process: PMMA with Fe_2O_3 (loading such as 10, 20, 30, 40, 50 and 60 wt%) mixed in acetone as organic solvent.	SEM micrographs revealed crystalline morphology of nanocomposites with size range of 80-100 nm. Nanocomposites with 30 wt% Fe_2O_3 loading exhibit best optical and electrical properties. TGA analysis showed improvement in the thermal stability of resulting nanocomposites.

5.2 Experimental

5.2.1 Materials

Iron(II) sulfate ($FeSO_4 \cdot 7H_2O$), iron(III) chloride ($FeCl_3$) and ammoium hydroxide (30 wt%) were purchased from SRL, India. Methyl methcrylate (MMA) monomer, GR grade was supplied by Hi–Media, India. The surfactants sodium dodecyl sulfate (SDS) and inorganic initiator potassium persulfate (KPS, AR grade) were procured from Merck, India. The inhibitor (hydroquinone) in MMA monomer was removed prior to polymerization reactions by adsorption on neutral alumina powder.

5.2.2 Synthesis of nano sized Fe_3O_4 and PMMA/Fe_3O_4 nanocomposite

Iron oxide (Fe_3O_4) nano particles were synthesized by dissolving mixture of iron(II) sulfate and iron(III) chloride in mole ratio of 1:2 in 60 mL of Millipore water. Initially, the iron salt solution was thoroughly mixed for 30 min at room temperature. Next, ammonium hydroxide (NH_4OH) solution was added dropwise to the solution of iron salts simultaneously with mechanical stirring till the pH of the solution reached 10. This resulted in precipitation of deep black particles of Fe_3O_4. These particles were analyzed for size distribution and zeta potential. In an alternate procedure, Fe_3O_4 particles were synthesized using same protocol as above except that mechanical stirring at the time of addition of NH_4OH was replaced with sonication. The sonication was carried out in continuous mode for 30 min under nitrogen atmosphere. The resulting Fe_3O_4 particles were analyzed for size distribution and zeta potential. The sonication of reaction mixture at frequency of 20 kHz was carried out using a probe type micro–processor controlled programmable ultrasound processor (Sonics and Materials Inc., Model: VCX 500). The processor was operated at 40% of the maximum power, i.e. 200 W. Actual acoustic power delivered to the reaction mixture was determined using calorimetric techniques. Using calorimetric measurements, the amplitude of the ultrasound wave generated by the sonicator probe was determined as 2 bar (Sivasankar et al., 2007; Chakma et al., 2013). After completion

of sonication, the entire reaction mixture was centrifuged and washed with water several times to remove unreacted iron salts. Finally, the black precipitate of Fe_3O_4 was vacuum dried at 65 ^oC. The dried Fe_3O_4 particles were used for synthesis of PMMA/Fe_3O_4 nanocomposite.

***Chemical mechanism of Fe_3O_4 synthesis*:** The overall chemistry of synthesis of Fe_3O_4 nanoparticles is represented as follows:

$$FeSO_4 \longrightarrow Fe^{2+} + SO_4^{2-}$$
$$FeCl_3 \longrightarrow Fe^{3+} + 3Cl^-$$
$$Fe^{2+} + 2Fe^{3+} + 8OH^- \xrightarrow{co-precipitation} Fe_3O_4 + 4H_2O$$
$$H_2O \xrightarrow{ultrasound} H^\bullet + OH^\bullet$$
$$H^\bullet + H^\bullet \longrightarrow H_2$$
$$OH^\bullet + OH^\bullet \longrightarrow H_2O_2$$
$$Fe^{2+} + H_2O_2 \longrightarrow Fe^{3+} + 2OH^-$$
$$3Fe^{3+} + 8OH^- \longrightarrow Fe_3O_4 + 4H_2O$$

Low yield (19.3 g/L) is the major drawback of the conventional Fe_3O_4 synthesis through coprecipitation of Fe(II)/Fe(III) salt mixture with mechanical shaking. The resulting Fe_3O_4 particles also have large impurity of unconverted salts. Application of ultrasound concurrently during coprecipitation step with NH_4OH addition helps in enhancement of Fe_3O_4 yield (21.6 g/L). The synergistic effect of ultrasound can be explained as follows: sonication of the reaction mixture gives rise to phenomena of transient cavitation. Dissociation of the water vapor molecules in the transient cavitation bubble result in generation of $H^\bullet$ and $^\bullet OH$ radicals. These radicals are released into the liquid medium with transient collapse and fragmentation of the cavitation bubble. The $^\bullet OH$ radicals can recombine to generate H_2O_2. The in–situ generated H_2O_2 helps in enhancing oxidation of Fe^{2+} to Fe^{3+}, which are further converted to Fe_3O_4 by OH^- ions. In–situ generation of H_2O_2 is also corroborated by reduction in final pH of the solution (11.35 with mechanical stirring to 8.12 with sonication) attained after NH_4OH addition. Moreover, as explained in subsequent sections, strong micro–turbulence and high shear generated by ultrasound also helps in reduction of mean size of Fe_3O_4 particles and narrowing

down of the size distribution of the particles.

Ultrasound–assisted synthesis of PMMA/Fe_3O_4 nanocomposites by in–situ emulsion polymerization was carried out in two steps. In first step, a mixture of surfactant SDS (0.87 g), Millipore water (100 mL) and Fe_3O_4 nanoparticles (with varying loading of 0.15, 0.3 and 0.75 g) was sonicated using ultrasound probe (frequency of 20 kHz, power rating 200 W) for 30 min at 65 ^oC. This procedure was expected to enhance the stability of Fe_3O_4 nanoparticles through adsorption of SDS molecules on the particle surface. The particle size distribution and zeta potential of the treated Fe_3O_4 particles was measured with dynamic light scattering (DLS) instrument (Beckman Coulter, Switzerland; Model Delsa Nano C). Table 5.2 depicts the result of this analysis. It could be seen that the zeta potential of the Fe_3O_4 nanoparticles showed marked increase after SDS treatment indicating greater stability against agglomeration. In order to assess efficacy of ultrasound in enhancing stability and zeta potential of the Fe_3O_4 particles, the above experiment was also performed using mechanical stirring instead of sonication. From results in Table 5.2, it could be inferred that mechanical stirring did not enhance the zeta potential of Fe_3O_4 particles to the same extent as sonication. Thus, step 1 resulted in generation of surfactant–stabilized suspension of Fe_3O_4 nanoparticles in water.

In second step of PMMA/Fe_3O_4 nanocomposite synthesis, in–situ emulsion polymerization of monomer MMA in presence of Fe_3O_4 nanoparticles was carried out in a jacketed borosilicate glass reactor. For this purpose, 15 g MMA along with 0.75 g KPS (initiator) was added to the suspension of Fe_3O_4 particles generated in the first step. The varying loading of 0.15, 0.3 and 0.75 g Fe_3O_4 nanoparticles essentially corresponded to 1, 2 and 5 wt% monomer. The polymerization reaction was carried out at 65±2 ^oC for 60 min. The temperature of reaction mixture was controlled by circulation of water through the reactor jacket. Prior to polymerization, the dissolved oxygen in the reaction mixture was removed by purging nitrogen. Moreover, during the polymerization reaction as well, nitrogen was purged through the reaction mixture (at flow rate of 2 L/min) to avoid contamination of oxygen. After completion of the

polymerization reaction, the total reaction mixture was dried in vacuum oven at 65°C for 15 h to remove water and unconverted monomer. To remove the surfactant present in the dried latex particles of PMMA/Fe_3O_4 nanocomposite, the particles were washed several times with water followed by filtration. The surfactants free PMMA/Fe_3O_4 nanocomposite particles were further dried under vacuum. The resulting PMMA/Fe_3O_4 latex were further dispersed in dichloromethane for casting of nanocomposite film. This film of the nanocomposite was used for characterization.

5.2.3 Characterization of Fe_3O_4 and PMMA/Fe_3O_4 nanocomposites

Fe_3O_4 nanoparticles and PMMA/Fe_3O_4 nanocomposites were characterized for composition and physical/structural morphology with following techniques: **(1) Particle size distribution:** Mean size and size distribution of Fe_3O_4 nanoparticles and PMMA/Fe_3O_4 latex was determined by dynamic light scattering (DLS) instrument (Beckman Coulter, Switzerland; Model Delsa Nano C). (**2) FE–SEM, TEM and EDX:** Structural morphology and elemental composition of Fe_3O_4 particles and PMMA/Fe_3O_4 nanocomposites were assessed using micrographs from Field Emission Scanning Electron Microscope (Zeiss, Model: Sigma), Transmission Electron Microscope (Jeol, Model: JEM 2100) and Energy Dispersive X–ray Spectroscopy (Zeiss, Model: Sigma). (**3) FTIR*:*** Infrared absorption spectroscopic analysis of the Fe_3O_4 nanoparticles and PMMA/Fe_3O_4 nanocomposites was carried out at room temperature using FTIR spectrophotometer (Shimadzu, Model: IRAffinity–1). **(4) XRD:** Crystalline structure of pristine Fe_3O_4 nanoparticles and PMMA/Fe_3O_4 nanocomposites was assessed using X–ray diffraction (Bruker D8 Advance) employing monochromatic Cu Kα radiation. **(5) Vibrating Sample Magnetometer:** magnetic properties of pristine Fe_3O_4 nanoparticles and PMMA/Fe_3O_4 nanocomposites were determined using vibrating sample magnetometry (Make: Lakeshore, Model: 7410 series). For measurement of magnetic properties, of Fe_3O_4 nanoparticles, 10 mg dried powdered The sample were loaded in Teflon tape and used for

further analysis. For measurement of magnetic properties, of rectangular thin films of PMMA/Fe_3O_4 nanocomposite (dimensions 8 mm × 4 mm × 2 mm) were prepared. These films were wrapped in Teflon tape prior to measurement of the magnetic properties. **(6) Thermogravimetric analysis:** Thermal stability of PMMA/Fe_3O_4 nanocomposites (in nitrogen environment) was determined by TGA instrument (NETZSCH TG 209F1 Libra) with heating rate of 10°C/min. **(7) Differential scanning calorimeter:** The glass transition temperature of PMMA/Fe_3O_4 nanocomposite was determined by DSC instrument (Metler Toledo–1 series) with heating rate of 10°C/min under nitrogen environment. **(8) Electrical properties:** Electrical conductivity of PMMA/Fe_3O_4 nanocomposites was determined using compression molded samples. A Keithley 6517A electrometer connected to a Keithley 8009 test fixture was employed. For samples with conductivity > 10^{-6} S cm^{-1}, a Loresta GP resistivity meter (MCP–T610 model, Mitsubishi Chemical Co., Japan) connected with an ESP four–pin probe was used. The electromagnetic interference (EMI) shielding effectiveness (SE) was determined with an Agilent Network Analyzer (Model E5071C) within the X–band frequency range (8.2–12.4 GHz). EMI SE of a material is a measure of the material's ability to attenuate the intensity of EM waves, defined as the logarithm of the ratio of incident power to transmitted power, and its unit is expressed in dB:

$$EMI\ SE = 10\log\left(\frac{P_i}{P_o}\right) \qquad (5.1)$$

where P_i is the incident power and P_o is the transmitted power.

(8) Tensile strength, Young's modulus and percentage elongation: The mechanical properties of the PMMA/Fe_3O_4 nanocomposites were determined with Universal Testing Machine (INSTRON 8801, UK). A nanocomposite specimen size 100 mm × 25 mm × 0.4 mm was used for the characterization tests based on ASTM D882 standard at a cross head speed of 0.5 mm/min. The gauge length of each film was maintained at 50 mm.

5.3 Results and Discussion

We present the results of our study such as characterization of sonochemically synthesized Fe_3O_4 nanoparticles and characterization of the PMMA/Fe_3O_4 nanocomposites.

5.3.1 Characterization of Fe_3O_4 nanoparticles and PMMA/Fe_3O_4 nanocomposites

***Energy dispersive X–ray* (EDX) *spectroscopy and particle size distribution*:** EDX spectra of Fe_3O_4 nanoparticles synthesized with two protocols, viz. co–precipitation with mechanical stirring and co–precipitation with sonication are depicted in Figs. 5.1A and B, respectively. EDX spectrum of the Fe_3O_4 synthesized with mechanical stirring (Fig. 5.1A) clearly shows presence of Fe and O as main elements with minor traces of impurities in the form of chlorides, sulfate etc. These impurities are attributed to presence of unreacted Fe^{2+} salt in the reaction mixture. Remarkably, the peaks corresponding to the impurities are absent in the EDX spectrum of the Fe_3O_4 synthesized with sonication. This result is essentially a corroboration of the hypothesis presented in preceding section reg. synergy between sonication and co–precipitation. In–situ generation of H_2O_2 through transient collapse of cavitation bubbles drives complete conversion of Fe^{2+} to Fe^{3+} through Fenton reactions.

The particle size distribution (PSD) analysis of Fe_3O_4 synthesized with both mechanical stirring and sonication are depicted in Fig. 5.1C. The PSD curves of Fe_3O_4particles synthesized using mechanical stirring and sonication show distinct differences. The mean (or average) particle size of Fe_3O_4 synthesized with sonication (75.1 nm) is significantly smaller than Fe_3O_4 synthesized with mechanical stirring (286.1 nm). Moreover, the size distribution of the Fe_3O_4 particles is also much narrower for sonication–assisted synthesis than mechanical stirring assisted synthesis. This feature is indicated the width or span of particle size distribution, which is determined as follows: $span = \frac{\left[d(0.9) - d(0.1)\right]}{d(0.5)}$. Using values of $d(0.9)$, $d(0.1)$ and $d(0.5)$

determined from the PSD measurements, the PSD span for Fe_3O_4 synthesized with the two protocols is calculated as: mechanical stirring = 0.65, sonication = 1.13. Reduction in mean particle size and widening of the span indicates narrowing of the particle size distribution. This result is attributed to generation of intense micro–convection and high shear rate during sonication, leading to particle fragmentation.

Table 5.2 also lists the mean particle sizes of the PMMA/Fe_3O_4 nanocomposites. It could be seen that the mean particle size of nanocomposites are in the range of 72.9 to 116.6 nm. Moreover, the mean particle size of nanocomposites is proportional to Fe_3O_4 loading. The highest mean particle size of 116.6 nm is obtained for Fe_3O_4 loading of 5 wt%, which essentially is an implication of greater encapsulation of the nanofiller in the polymer matrix. The polydispersity indices of the nanocomposites are in the range of 0.19 to 0.26, which indicate good homogeneity of the nanocomposite particles in aqueous medium.

Table 5.2: Mean particle size and zeta potential of Fe_3O_4 and PMMA/Fe_3O_4 Nanocomposites

Material	Zeta potential (mV)	Average diameter (nm)
Fe_3O_4 (pristine, MS)	–2.64	286
Fe_3O_4 (pristine, US)	–15.91	76
Fe_3O_4 (SDS treatment, MS)	–36.96	–
Fe_3O_4 (SDS treatment, US)	–47.74	–
Neat PMMA	–64.32	72.9
PMMA/Fe_3O_4 (1 wt%)	–57.36	78.5
PMMA/Fe_3O_4 (2 wt%)	–54.43	83.6
PMMA/Fe_3O_4 (5 wt%)	–48.34	116.6

Zeta potential analysis: The stability of the Fe_3O_4 nanoparticles in pristine form and after surfactant (SDS) treatment was analyzed using zeta potential measurement. Table 5.2 lists the zeta potential values of Fe_3O_4 particles in pristine form and post–surfactant treatment with either mechanical stirring or sonication. Fe_3O_4 nanoparticles synthesized under sonication (or ultrasound irradiation) have significantly higher zeta potential, which indicates greater stability against coagulation. Surfactant treatment was revealed to enhance the stability of the Fe_3O_4

particles with further increase in the zeta potential values. This is essentially attributed to adsorption of the surfactant molecules on the surface of the Fe_3O_4 particles. The surfactant treatment in presence of ultrasound (or sonication) resulted in greater augmentation of the zeta potential of pristine Fe_3O_4 (–47.74 mV), as compared to surfactant treatment with mechanical stirring (–36.96 mV). This essentially indicates better and greater adsorption of surfactant onto the surface of Fe_3O_4 in presence of sonication.

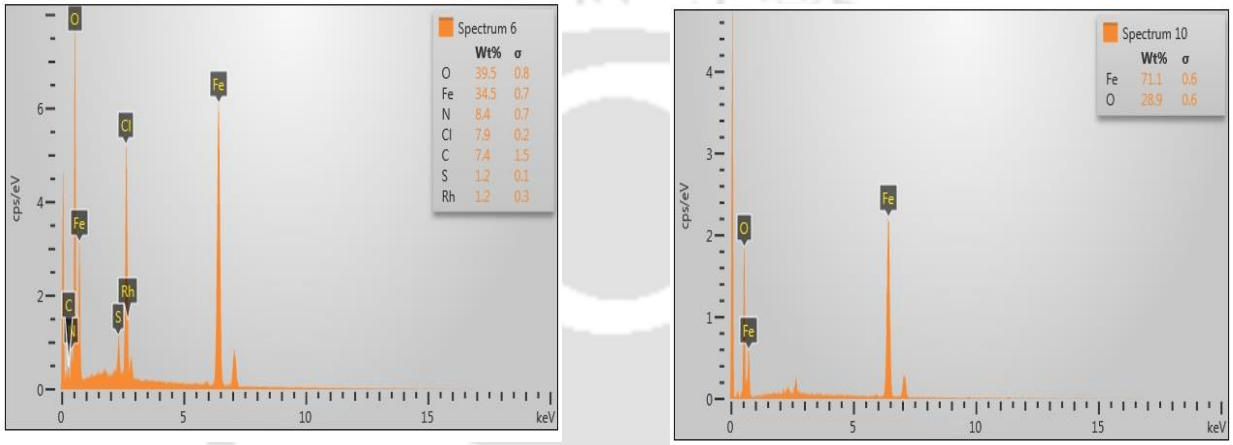

(A) (B)

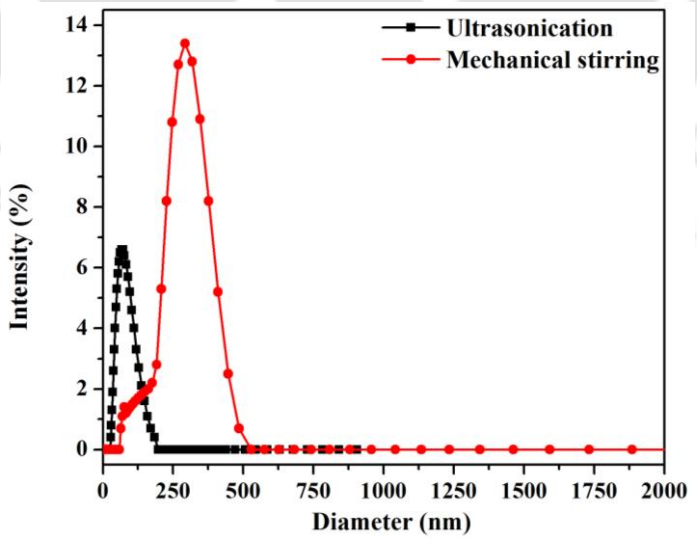

(C)

Figure 5.1: Characterization of Fe_3O_4 nanoparticles synthesized using different protocols. (A) EDX spectrum of Fe_3O_4 synthesized by co–precipitation with magnetic stirring. (B) EDX spectrum of Fe_3O_4 synthesized by co–precipitation with sonication. (C) Particle size distribution analysis of Fe_3O_4.

***FE–SEM and TEM analysis*:** The FE–SEM micrographs of the PMMA/Fe_3O_4 nanocomposites are shown in Figs. 5.2A–C. Figs. 5.2A and 5.2B show micrographs of PMMA/Fe_3O_4 nanocomposites synthesized with Fe_3O_4 loading of 1 and 2 wt%. These micrographs clearly illustrate uniform encapsulation and embedding of Fe_3O_4 particles in the polymer matrix. The micrograph in Fig. 5.2C, however, shows agglomeration of the Fe_3O_4 nanoparticles in PMMA matrix at the highest loading of 5 wt%. Agglomeration of the nanofiller in the polymer matrix at high concentrations essentially results in deterioration of the physical properties, as discussed subsequently.

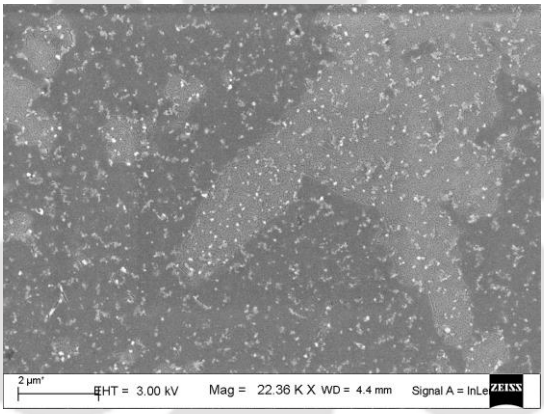

(A)

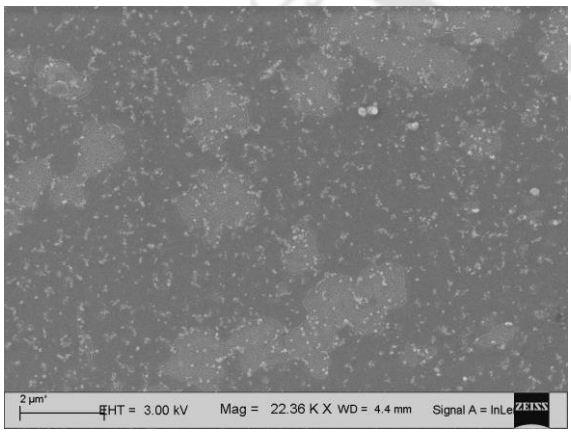

(B)

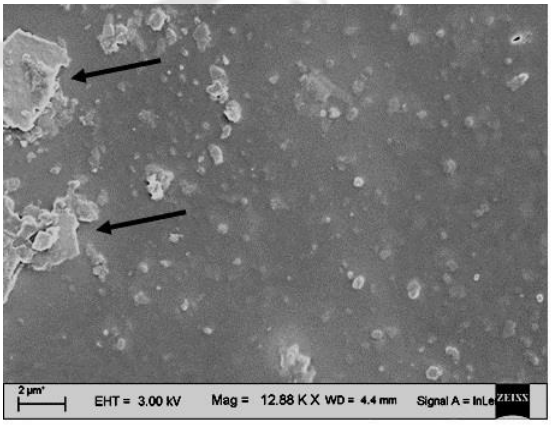

(C)

Figure 5.2: Field Emission Scanning Electron Microscope (FE–SEM) micrographs of PMMA/Fe_3O_4 nanocomposites synthesized with various loadings of Fe_3O_4. (A) 1 wt% loading. (B) 2 wt% loading. (C) 5

wt% loading.

TEM micrographs of Fe_3O_4 and PMMA/Fe_3O_4 nanocomposite synthesized with various Fe_3O_4 loadings are shown in Figs. 5.3A-B. Sphericity and monodispersity of Fe_3O_4 nanoparticles are clearly visible from the TEM micrographs. The bright spots observed in SAED pattern (in inset) depict crystalline nature of the synthesized nanoparticles (Cai et al., 2007; Wang et al., 2009).The translucent portion of the micrograph in Figs. 5.3B-D represents the polymer matrix, while the darker spots represent encapsulated Fe_3O_4 nanoparticles. Agglomeration of Fe_3O_4 nanoparticles in the PMMA matrix at the highest loading of 5 wt% is evident from micrograph in Fig. 5.3D.

FTIR analysis: FTIR spectra of Fe_3O_4 particles synthesized with sonication, neat PMMA and PMMA/Fe_3O_4 nanocomposites are shown in Fig. 5.4A. FTIR spectrum of Fe_3O_4 shows absorption bands at 580 cm^{-1} corresponding to stretching vibration of Fe–O bond in Fe_3O_4. The broad peak in the range of 3400–3650 cm^{-1} corresponds to O–H stretching vibration in water molecules adsorbed on Fe_3O_4 particles during sample preparation. The characteristic peak at 1730 cm^{-1} in the spectrum of neat PMMA is attributed to C=O stretching vibration of acrylate carboxyl group. Deformation vibration of $–CH_3$ and $–CH_2$ moieties in PMMA is represented by the peaks in the range of 1395–1450 cm^{-1}. Peaks in range of 1260–1040 cm^{-1} indicate C–O–C single bond stretching vibration. Encapsulation of Fe_3O_4 nanoparticles in PMMA matrix (or formation of PMMA/Fe_3O_4 nanocomposite) is confirmed by presence of absorption band at 580 cm^{-1} (characteristic of Fe–O stretching vibration in Fe_3O_4) in the spectrum of PMMA (Hong et al., 2009; Lan et al., 2011).

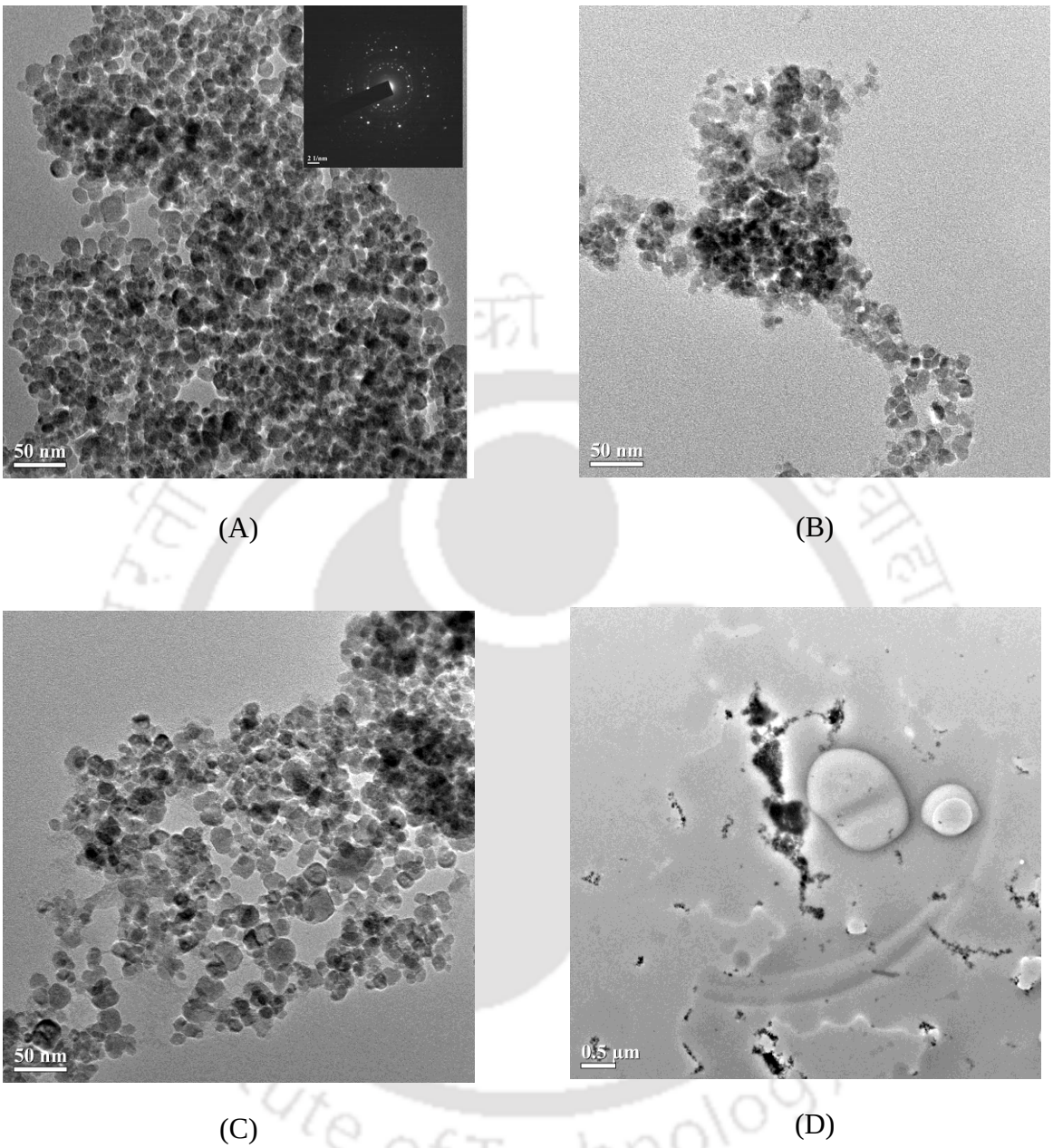

Figure 5.3: TEM analysis. (A) Micrographs of Fe_3O_4 nanoparticles (inset picture depicts corresponding SAED image). Micrographs of PMMA/Fe_3O_4 nanocomposites synthesized with various loadings of Fe_3O_4 nanoparticles. (B) 1 wt% loading, (C) 2 wt% loading, (D) 5 wt% loading.

XRD analysis: X–ray diffractograms of Fe_3O_4 nanoparticles and PMMA/Fe_3O_4 nanocomposites are illustrated in Fig. 5.4B. Diffractogram of Fe_3O_4 nanoparticles shows number of peaks corresponding to characteristic planes, viz. (220), (311), (400), (422), (511), (440) and (533). Diffractogram of neat PMMA shows a broad diffused peak at 2θ = 13° corresponding to

amorphous PMMA (from chapter 3). The peaks at various planes can be used to determine the crystallite size using Scherrer formula: $D = K\lambda/\beta\cos\theta$, where K is the shape factor (0.9), λ is the wavelength of X–ray (1.54 Å), and β = peak broadening at half maximum and θ = Braggs or diffraction angle. The sizes of the Fe_3O_4 nanoparticles calculated with Scherrer formula are in the range of 5.75 to 27.83 nm, and are listed in Table 5.3.

XRD patterns of PMMA/Fe_3O_4 nanocomposite for 1 wt% Fe_3O_4 loading exhibits very small and low intensity characteristic diffraction peaks corresponding to nanofiller in PMMA matrix. With increasing nanofiller loading, these diffraction peaks become sharp and intense, as observed from the X–ray diffractograms of nanocomposites for 2 and 5 wt% Fe_3O_4. Appearance of the characteristic peaks corresponding to Fe_3O_4 in the X–ray diffractogram of neat PMMA essentially confirms incorporation of Fe_3O_4 nanoparticles in PMMA matrix.

Table 5.3: Fe_3O_4 crystal size on the basis of Scherrer's formula

Plane ($h\ k\ l$)	Braggs angle 2θ (deg)	FWHM (deg)	Size (nm)
(2 2 0)	30.28	0.80	10.29
(3 1 1)	35.62	0.72	11.63
(4 0 0)	43.32	0.90	9.52
(4 2 2)	53.7	1.52	5.75
(5 1 1)	57.14	0.90	10.08
(4 4 0)	62.98	0.98	9.53
(5 3 3)	74.64	0.36	27.83

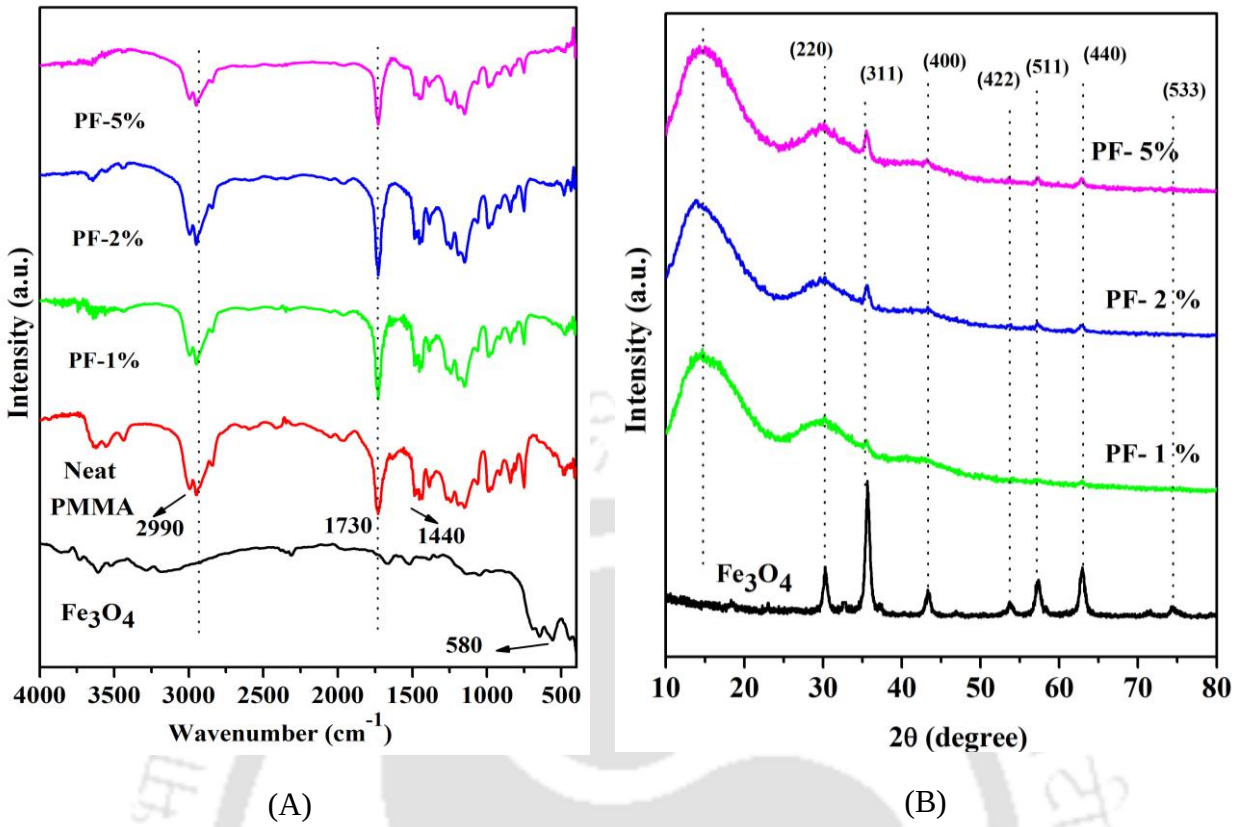

(A) (B)

Figure 5.4: Characterization of the PMMA/Fe_3O_4 nanocomposites synthesized with varying loading of Fe_3O_4. (A) FTIR spectra; (B) X-ray Diffractograms.

5.3.2 Physical properties of the PMMA/Fe_3O_4 nanocomposites

***Magnetic properties*:** Figs. 5.5C and 5.5D show the magnetic hysteresis loops (or the H–M curves) of the Fe_3O_4 nanoparticles and PMMA/Fe_3O_4 nanocomposites. The H–M loops essentially depict induced internal magnetization (B) as a function of externally applied magnetic field (H). The magnetic parameters, which can be obtained from the H–M curves, are as follows: (1) coercivity, (2) magnetic saturation, and (3) magnetic remanence. A brief description of these parameters can be given as follows: coercivity is the intensity of the applied magnetic field required to reduce the induced magnetization in a ferromagnetic material to zero after the magnetization of the material has been driven to saturation. Thus, coercivity represents demagnetization resistance of the ferromagnetic material. Materials with low coercivity are called magnetically soft material. Remanence or retentivity is the residual magnetism in a ferromagnetic material after removal of external magnetic field. Large residual magnetization is

not desirable property of materials to be used in transformers, electrical motors and generators as it is essentially tantamount to contamination. Saturation magnetization is the state reached when an increase in applied external magnetic field cannot further increase the induced magnetization of the material, and thus, the induced magnetic flux is more–or–less leveled off.

The magnetic parameters of Fe_3O_4 nanoparticles and the PMMA/Fe_3O_4 nanocomposites are summarized in Table 5.4. Fe_3O_4 nanoparticles synthesized with both mechanical stirring and sonication exhibit superparamagnetic behavior. Magnetic saturation (M_s) value of Fe_3O_4 synthesized with sonication (62.37 emu/g) is higher than M_s value for Fe_3O_4 synthesized with mechanical stirring (42.16 emu/g). Higher M_s value for the Fe_3O_4 synthesized with sonication is attributed smaller particle size, which also implies higher surface area of the particles. The magnetic properties of the Fe_3O_4 nanoparticles are strongly influenced by the surface effects, which could be due to lack of translational symmetry at outer boundaries of the particle, reduced condition number and broken magnetic exchange bonds of surface atoms. Reduction in the particle size essentially increases the ratio of surface spins to the total number of spins. Lower M_s value of Fe_3O_4 particles synthesized with mechanical stirring could also be consequence of impurities of unconverted divalent Fe^{2+} ions left in the cubic lattice of Fe_3O_4. The coercivity of the Fe_3O_4 synthesized with sonication is also higher than Fe_3O_4 synthesized with mechanical stirring. This facet can also be attributed to the finer size of the Fe_3O_4 particles synthesized with sonication. With reduction in size, the particles only support single domain within them that enhances the coercivity (Murali et al., 2016). Surface effects such as metal oxide exchange anisotropy also contribute to enhancement of coercivity. Internal defects in material structure that restrict magnetic domain movement also enhance the coercivity of Fe_3O_4 nanoparticles.

The coercivity of Fe_3O_4 particles shows marginal rise (~ 20%) after dispersion in polymer matrix. This essentially means that Fe_3O_4 particles become magnetically harder after incorporation into polymer matrix. Zhang et al. (2009) have attributed enhanced coercivity of

the Fe_3O_4 particles to reduction in inter–particle dipolar interactions, which is a possible sequence of increase in nanoparticle spacer distance for the single domain nanoparticles, as compared to the close contact of pure Fe_3O_4 nanoparticles. Zhang et al. (2009) have attributed coercivity enhancement to the interaction between the nanoparticles and the polymer matrix. The saturation magnetization of Fe_3O_4 shows sharp reduction after dispersion in polymer matrix. For nanocomposites with 1 wt% Fe_3O_4, M_s has a value of 0.67 emu/g, which is 2–orders of magnitude smaller than the M_s value of pristine Fe_3O_4. Secondly, M_s value of the nanocomposites shows proportionate increase with Fe_3O_4 loading. For the maximum loading of 5 wt%, the nanocomposites have saturation magnetization of 5.12 emu/g. Wilson et al. (2004) have reported M_s values of 0.091, 0.41 and 11.5 emu/g for PMMA/Fe_3O_4 nanocomposites for Fe_3O_4 concentrations of 0.5, 1 and 10 wt%. These nanocomposites were synthesized by melt blending. Comparing the results of Wilson et al. (2004) for 1 wt% Fe_3O_4 loading (M_s = 0.42 emu/g) with present study (M_s = 0.67 emu/g), the higher M_s value in present study is attributed to more uniform dispersion of the nanofiller in the polymer matrix in presence of sonication, as compared to melt blending.

Wilson et al. (2004) have observed that polymer nanocomposites are the system that exhibit mixture of single domain or multi–domain characteristics. The spin ordering at the surface of Fe_3O_4 particles dispersed in polymer matrix is different than in the bulk, which result in setting up of a magnetic core–shell configuration. Surface spin disorder and canting essentially contributes to lowering of the saturation magnetization. With increasing Fe_3O_4 loading, the interactions from other Fe_3O_4 may orient the canted spin.

The magnetic remanence (M_r) of the Fe_3O_4 particles synthesized with sonication (2.99 Oe) is >2× higher than that of the Fe_3O_4 synthesized with mechanical stirring (1.32 Oe). An explanation for this result can also be given along similarities. Similar to saturation magnetization, M_r value of Fe_3O_4 nanoparticles shows sharp reduction after dispersion in

polymer matrix, and explanation for the same can be given along similar lines as above. M_r values of the nanocomposites also show proportionate increase with Fe_3O_4 loading, which essentially points towards its strong dependence on the interaction among the nanofiller particles. In other words, the phenomenon of agglomeration of the Fe_3O_4 particles in polymer matrix at the highest Fe_3O_4 loading of 5 wt% helps in enhancing saturation (M_s) and remanent (M_r) magnetization. However, high Fe_3O_4 loading has adverse effect on thermal and mechanical properties of the nanocomposites, as explained in subsequent section.

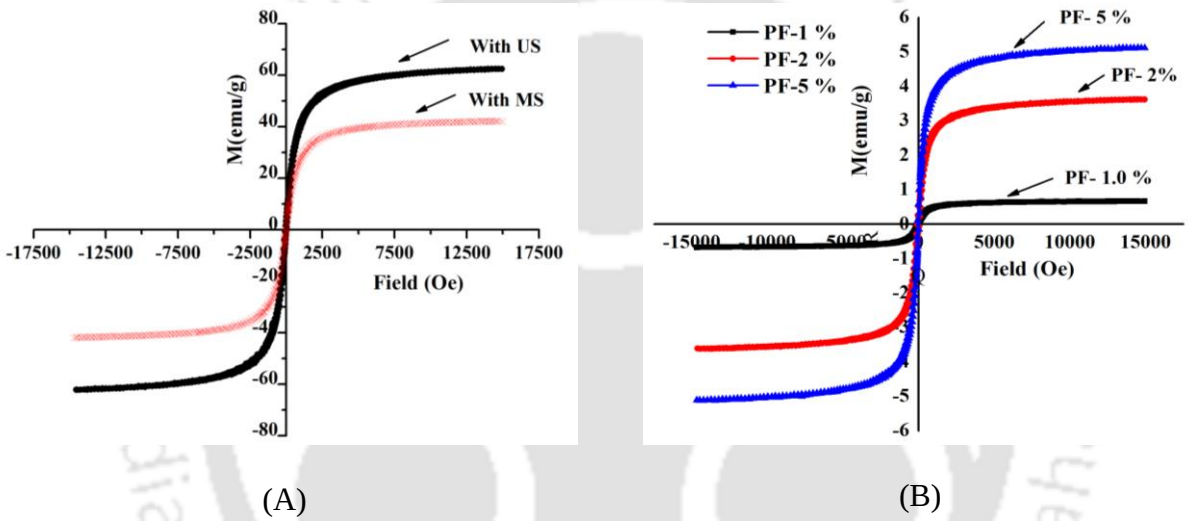

(A) (B)

Figure 5.5: Magnetization curves. (A) Fe_3O_4 nanoparticles synthesized with ultrasound and mechanical stirring, (B) PMMA/Fe_3O_4 nanocomposites synthesized with varying loading of Fe_3O_4. [Legends. PF–1% : PMMA/Fe_3O_4 (1 wt%), PF–2% : PMMA/Fe_3O_4 (2 wt%), PF–5% : PMMA/Fe_3O_4 (5 wt%), MS : with mechanical stirring, US : with ultrasonication.]

Table 5.4: Magnetic properties of Fe_3O_4 and PMMA/Fe_3O_4 Nanocomposites

Material	Coercivity (Oe)	Magnetic saturation, M_s (emu/g)	Magnetic remanence, M_r (emu/g)
Fe_3O_4 (pristine, MS)	31.18	42.16	1.32
Fe_3O_4 (pristine, US)	50.40	62.37	2.99
PMMA/Fe_3O_4 (1 wt%)	62.38	0.67	0.072
PMMA/Fe_3O_4 (2 wt%)	59.85	3.62	0.32
PMMA/Fe_3O_4 (5 wt%)	59.13	5.12	0.56

Abbreviations: MS – mechanical stirring, US – sonication (or ultrasound irradiation)

***Thermogravimetric (TGA) analysis*:** The TGA curve of the Fe_3O_4 nanoparticles (synthesized with sonication) and PMMA/Fe_3O_4 nanocomposites are shown Fig. 5.6A.1. The thermal heating of Fe_3O_4 curve essentially shows initial weight loss of ~4 % in the temperature range of 35–300 ^oC. This is attributed to removal of physically absorbed of residual moisture and traces of unreacted $FeCl_3$ present in the nanoparticles. With further increase in temperature till 600 ^oC, the Fe_3O_4 particles show an additional weight loss of only 5 wt%, which represents their thermal stability. The expanded view of the TGA curves of neat PMMA and PMMA/Fe_3O_4 nanocomposites in the temperature range of 250^o to 400^{o}C are shown in Fig. 5.6A.2. These curves clearly reveal enhanced thermal stability of the polymer matrix, as compared to the neat PMMA, after incorporation of Fe_3O_4 nanoparticles in the polymer matrix. The values of degradation temperatures for 5%, 25% and 50% weight loss (i.e. $T_{5\%}$, $T_{25\%}$, $T_{50\%}$) obtained from TGA curves are listed in Table 5.5. $T_{5\%}$ temperature for PMMA shows slight reduction with formation of nanocomposite. This reduction in thermal stability in low temperature range is essentially attributed to loss of impurities (such as unreacted $FeCl_3$) from the nanofiller material. Nonetheless, the degradation temperature for higher weight loss, viz. $T_{25\%}$ and $T_{50\%}$, shows significant rise with incorporation of nanofiller in polymer matrix indicating enhanced thermal stability of the nanocomposites. Maximum $T_{25\%}$ and $T_{50\%}$ temperatures are obtained for 2 wt% Fe_3O_4 loading. Increased thermal stability of nanocomposites could be attributed to hindrance offered by the nanofiller particles to diffusion of volatile products of thermal decomposition through the polymer matrix. The nanofiller particles also enhance the heat absorption capability of the nanocomposite. The rise $T_{50\%}$ temperature of the nanocomposite could be a consequence of resistance offered by Fe_3O_4 nanoparticles to homolytic scission of vinyl group in PMMA chain. The reduction in $T_{25\%}$ and $T_{50\%}$ temperature of the nanocomposites at 5 wt% Fe_3O_4 loading are attributed to the agglomeration of the Fe_3O_4 particles in PMMA matrix, which not only weakens the PMMA chain structure but also causes heat concentration in the polymer matrix that raises the local temperature that helps in initiation/propagation of degradation

reactions.

The Differential Thermogravimetric (DTG) curves (or the derivatives of the TGA curves) that depict thermal decomposition rates of the PMMA/ Fe_3O_4 nanocomposites at different temperatures are given in Fig. 5.6B. Peaks of the DTG curves (or the inflection points) essentially indicate the temperature at which rate of thermal degradation reaches maximum. As observed from Fig. 5.6B, the inflection point of neat PMMA occurs at 376^{o}C. The inflection points for PMMA/Fe_3O_4 nanocomposites for 1, 2 and 5 wt% Fe_3O_4 loading occur at 381^o, 383^o and 379^{o}C, respectively. This result is yet another corroboration of rise in thermal stability of the PMMA after formation of nanocomposite with Fe_3O_4. Rise in inflection points for PMMA/Fe_3O_4 nanocomposites (as compared to neat PMMA) is attributed to uniform dispersion of the Fe_3O_4 nanoparticles in PMMA matrix under intense microturbulence generated by sonication. Relatively small size of the Fe_3O_4 particles also results in high surface interaction between nanofiller and polymer matrix. The surface interaction between Fe_3O_4 and PMMA resists the thermal degradation of PMMA through random scission of PMMA chains. Similar to trends in $T_{25\%}$ and $T_{50\%}$ temperatures, the inflection points also show maxima at Fe_3O_4 loading of 2 wt%. Reduction in the inflection point for the highest Fe_3O_4 loading of 5 wt% is attributed to agglomeration of the nanofiller particles in polymer matrix that reduces and weakens the surface interaction between nanofiller surface and polymer. The agglomeration of Fe_3O_4 particles in PMMA matrix also creates points for concentration of thermal stress. Hong et al. (2009) have reported $T_{25\%}$ value of 330^{o}C and inflection point of 380^{o}C for Fe_3O_4 loading of 12 wt% for PMMA/Fe_3O_4 nanocomposites synthesized with mini-emulsion polymerization. Fe_3O_4 nanoparticles used by Hong et al. (2009) were surface modified with oleic acid prior to nanocomposite synthesis.

***DSC (Differential scanning calorimeter) analysis*:** As noted earlier, incorporation of Fe3O4 nanoparticles in PMMA matrix restricts the mobility of the polymer chains. A direct implication of this phenomenon is on the property of glass transition temperature of the PMMA. The glass transition temperature (T_g) of neat PMMA and PMMA/Fe_3O_4 nanocomposites was determined by the DSC curves, shown in Fig. 5.6C. T_g of neat PMMA was determined as 116 ^oC. Nanocomposite for 1 wt% Fe_3O_4 loading showed an enhanced T_g of 121.5 ^oC. The trend in T_g with Fe_3O_4 loading concurs with the trends in $T_{25\%}$, $T_{50\%}$ (determined using TGA analysis) or the inflection points (determined from DTG), in that maximum T_g = 122.5 ^oC of the nanocomposite is obtained for 2 wt% Fe_3O_4 loading. For the highest Fe_3O_4 loading of 5 wt%, T_g shows sharp reduction to 105 ^oC. This result can be explained along similar lines that agglomeration (or non–uniform dispersion) of nanofiller particles in polymer matrix at high loading creates weak spots for concentration of shear or thermal stress, which in turn, boosts the motion of polymer chains at relatively low temperature. Banert et al. (2006) have reported T_g value of 103 ^oC for PMMA/Fe_3O_4 nanocomposites synthesized by solvent blending with Fe_3O_4 loading of 22.8 wt%. Fe_3O_4 nanoparticles used by Banert et al. (2006) were surface-modified with oleic acid.

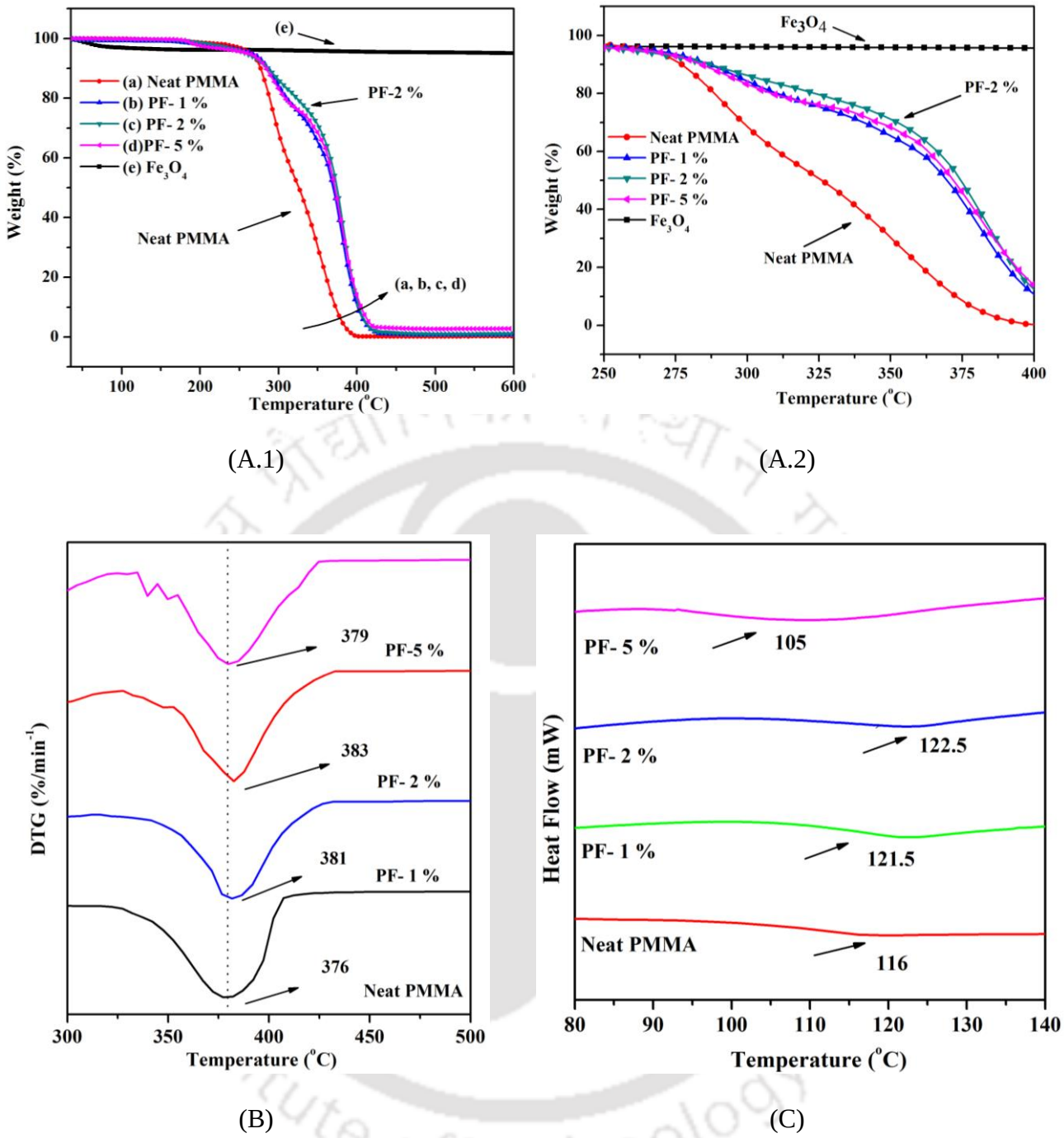

Figure 5.6: Characterization of PMMA/Fe_3O_4 nanocomposites synthesized with varying loading of Fe_3O_4. (A.1) Thermogravimetric (TGA) curves in full temperature range, (A.2) Expanded view of TGA curve in the temperature range of 300° to 500°C (B) Differential Thermogravimetric (DTG) curves. (C) Differential Scanning Calorimetric (DSC) curves.

Table 5.5: Results of thermogravimetric analysis of PMMA and PMMA/Fe_3O_4 nanocomposites

Material	$T_{5\%}$ (°C)	$T_{25\%}$ (°C)	$T_{50\%}$ (°C)	Δ $T_{25\%}$	Δ $T_{50\%}$
PMMA	267.40	293.22	326	_	_
PMMA/Fe_3O_4 (1 wt%)	264.11	327.11	367	33.89	41
PMMA/Fe_3O_4 (2 wt%)	259.11	335.93	373.22	42.71	47.22
PMMA/Fe_3O_4 (5 wt%)	257.25	329.84	371	36.62	45

***Electrical conductivity*:** Fig. 5.7 shows the electrical conductivity of the PMMA/Fe_3O_4 nanocomposites. With incorporation of Fe_3O_4 nanoparticles in the PMMA matrix, the electrical conductivity of nanocomposites showed proportionate rise of ~2 orders of magnitude for the maximum Fe_3O_4 loading of 5 wt%. As revealed by the trends in electrical conductivity shown in Fig. 5.7, the percolation threshold occurs at Fe_3O_4 loading of ~ 1 wt%, where the nanocomposite transformed from an insulative material into a conductive material. This transformation is due to the formation of conductive network of Fe_3O_4 nanofiller spanning the PMMA matrix. For maximum Fe_3O_4 loading of 5.0 wt%, the nanocomposites show electrical conductivity of 2.0×10^{-13} S/cm, whereas the conductivity of neat PMMA is 2.3×10^{-15} S/cm. Compared to other nanofillers (such as carbon nanotubes, metal nanowires or graphene), the increase in electrical conductivity of PMMA with incorporation of Fe_3O_4 nanoparticles (at loading of 5 wt%) is, thus, marginal. The probable cause leading to this effect is the spherical morphology (with very low aspect ratio) of the Fe_3O_4 nanoparticles, which restricts their surface area, and hence, the contact area with the polymer matrix. A possible solution to enhancement of electrical conductivity of the nanocomposite at low concentrations of Fe_3O_4 nanoparticles is to deposit these nanoparticles on the surface of high aspect ratio filler such as CNT or graphene, and use this hybrid material for synthesis of the nanocomposite. Such strategy essentially achieves synergy between the two fillers.

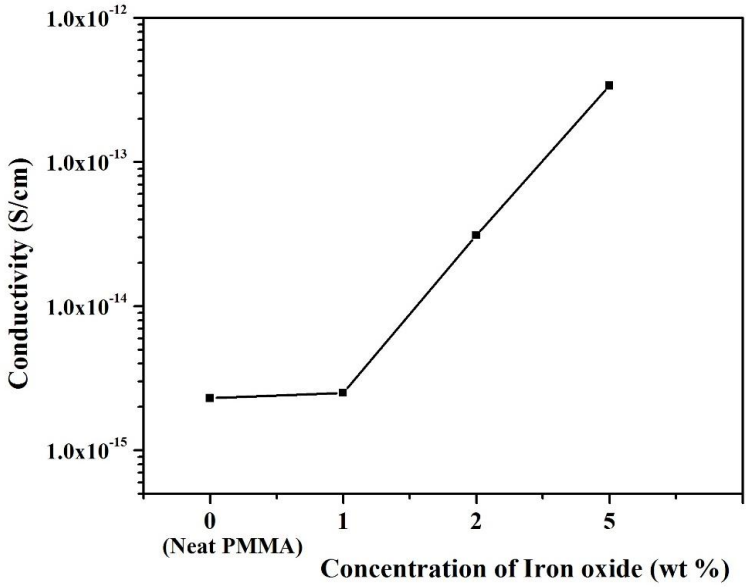

Figure 5.7: Electrical conductivity of neat PMMA and PMMA/Fe_3O_4 nanocomposites.

EMI Shielding: An electrical field and magnetic field oriented perpendicular to each other give rise to electromagnetic radiation. Thus, shielding of electromagnetic interference, which is a kind of electrical pollution, involves shielding of both electrical and magnetic field. Electrical charge on the surface of the metals that can offset the electrical field inside the metal can provide effective electrostatic field shielding. Magnetostatic field shielding could be provided by a ferromagnetic material with high magnetic permeability to provide low resistance path such that magnetic force line can be conducted through. The electromagnetic shielding thus has two components viz: attenuation of electrical field through reflection losses and attenuation of magnetic field through absorption losses. Higher reflection loss of electrical field is characterized by high electrical conductivity and low volume resistance. The attenuation of magnetic field through absorption loss is proportional to encapsulation surface of the hysteresis loop, which is determined by the saturation magnetization and coercivity. Thus, higher absorptive loss or attenuation of the magnetic field is characterized by high saturation magnetization and high coercivity of the shielding material. EMI SE of the PMMA/Fe_3O_4

nanocomposites has been calculated using equation 1 (in the unit of dB), stated earlier. Fig. 5.8A shows the overall SE (SE_o) of the generated nanocomposites as a function of frequency in the X–band frequency range for different Fe_3O_4 (1, 2 and 5 wt%) loadings. It can be inferred from Fig. 5.8A that SE_o of PMMA/Fe_3O_4 nanocomposites vary proportionately with Fe_3O_4 loading. Fig. 5.8B depicts the average shielding by reflection (SE_r), shielding by absorption (SE_a) and overall shielding effectiveness (SE_o) of the generated nanocomposites over the X–band. SE_o of PMMA/Fe_3O_4 nanocomposites is contributed by both absorption and reflection, although the contribution from absorption is higher than reflection for all loadings of the nanofiller. Moreover, SE_a shows a linear increase with the Fe_3O_4 loading. For the maximum nanofiller loading, PMMA/Fe_3O_4 nanocomposites demonstrated a combination of SE_r = 1.07 dB by reflection and SE_a = 1.45 dB by absorption. Analyzing the EMI SE of PMMA/Fe_3O_4 nanocomposites vis–à–vis their magnetic properties listed in Table 2C, one can perceive that EMI–SE of the nanocomposites at the highest Fe_3O_4 loading of 5 wt% is limited by low saturation magnetization despite high coercivity.

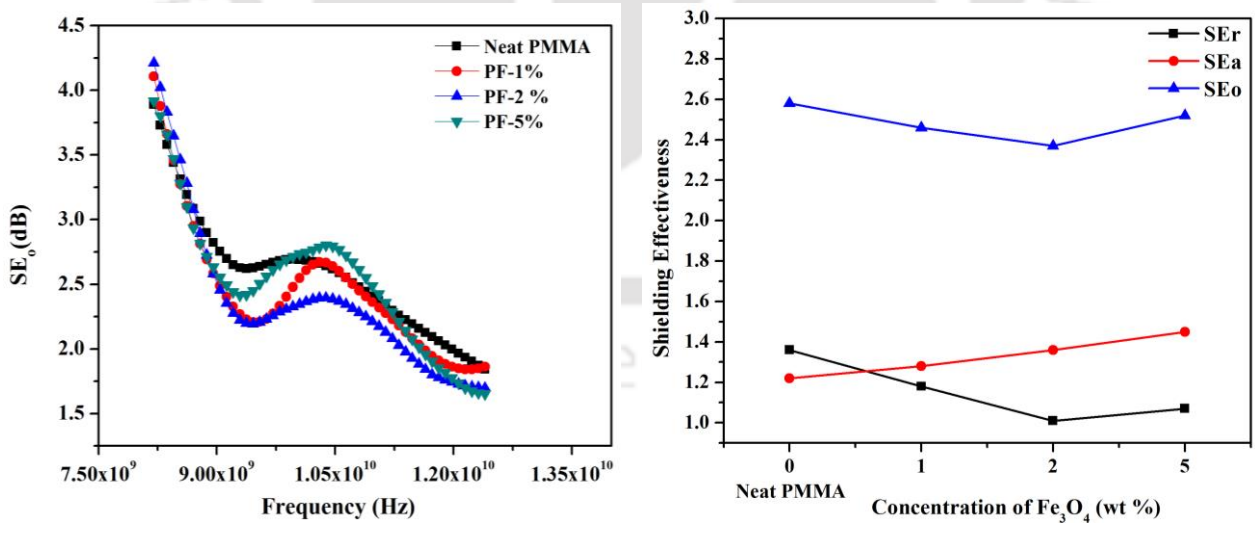

(A) (B)

Figure 5.8: Electromagnetic interference (EMI) shielding properties of PMMA/Fe_3O_4 nanocomposites. (A) Trends in overall shielding with frequency in the X-band (8.2–12.4 GHz). (B) Trends in EMI shielding efficiency with Fe_3O_4 loading (SE_a : shielding by absorption, SE_r : shielding by reflection, SE_o : overall shielding).

***Mechanical properties*:** Three mechanical properties of neat PMMA and PMMA/Fe_3O_4 nanocomposites, viz. tensile strength, Young's modulus and percentage elongation, were assessed using Universal Testing Machine, as noted earlier. Specimen films of neat PMMA and PMMA/Fe_3O_4 nanocomposite with dimensions 100 mm × 25 mm × 0.4 mm and gauge length of 50 mm have been used at a cross head speed of 0.5 mm/min (ASTM D882 standard test method). Results of this analysis are depicted in Fig. 5.9A. Trends in the mechanical properties of the nanocomposites with Fe_3O_4 loadings and possible justifications for the same are as follows.

Tensile strength: Tensile strengths of neat PMMA and PMMA/Fe_3O_4 nanocomposites are shown in Fig. 5.9 A. It could be seen that tensile strength of neat PMMA (32.74 MPa) increases with formation of nanocomposite with relatively low concentrations of Fe_3O_4. The PMMA/Fe_3O_4 nanocomposites with 1 and 2 wt% Fe_3O_4 loading have tensile strengths of 39.9 and 40.28 MPa, respectively. However, at 5 wt% Fe_3O_4 loading, the tensile strength of PMMA/Fe_3O_4 nanocomposite shows marked reduction to 25.13 MPa.

Rise in tensile strength of PMMA matrix at lower concentrations of the nanofiller is probable manifestation of uniform dispersion of Fe_3O_4 nanoparticles in the polymer matrix (due to intense microturbulence generated by ultrasound), strong interfacial interaction and adhesion between phases (possibly through H–bonds) and increase in the crystallinity. Presence of nanofiller in the polymer matrix also hinders the motion of polymer chains (Li et al., 2009). Tanniru et al. (2006) have also noted that dynamics of polymer chains in nanocomposite is affected due to confinement within host galleries of nanoparticles and polymer–surface interactions. Tanniru et al. have also noted that interphase polymer around the nanofiller (Fe_3O_4) particle gains crystalline nature due to surface interactions between nanofiller particle and polymer matrix. Reduction in tensile strength of nanocomposite at higher Fe_3O_4 loading is attributed to non–uniform distribution and agglomeration/segregation of Fe_3O_4 particles in

polymer matrix. These agglomerates could form "weak spots" in polymer matrix for concentration of stress field, which could result in rapid and easy propagation of cracks leading to premature failure. Esthappan (2012) has noted that increased concentration of nanofiller in polymer matrix can reduce interfacial contact area resulting in formation of defects and reduction in tensile strength.

Young's modulus: Trends in Young's moduli of the PMMA/Fe_3O_4 nanocomposites with nanofiller loading depicted in Fig. 5.9B are very similar to the trends in tensile strength. Young's modulus for 1 wt% Fe_3O_4 loading is 2.3 GPa, which is almost double that of neat PMMA (1.14 GPa). With further increase in Fe_3O_4 loading to 2 wt%, the Young's modulus increases marginally to 2.4 GPa. However, for the highest Fe_3O_4 loading of 5 wt%, Young's modulus shows slight reduction to 2.2 GPa. The trends in Young's modulus can essentially be explained along similar lines as the trends in tensile strength.

Percentage elongation: Fig. 5.9C depicts the trends in percentage elongation of the nanocomposites with nanofiller loading. This mechanical property shows marked reduction with incorporation of nanofiller in the PMMA matrix. Percentage elongation of neat PMMA was 3.92%, which showed marked reduction to 1.46% for 1 wt% Fe_3O_4 loading. For 2 wt% Fe_3O_4 loading, the percentage elongation increased to 2.24%; however, for 5 wt% Fe_3O_4 loading, the least percentage elongation of 1.12% was obtained. Reduction in percentage elongation with incorporation of Fe_3O_4 nanoparticles is essentially attributed to restricted mobility of the polymer chains in presence of nanofiller. Rise in percentage elongation for 2 wt% Fe_3O_4 loading could be a manifestation of improvement in ability of nanocomposite matrix to absorb energy of deformation due to increase in crystallinity of the polymer matrix with incorporation of nanofiller.

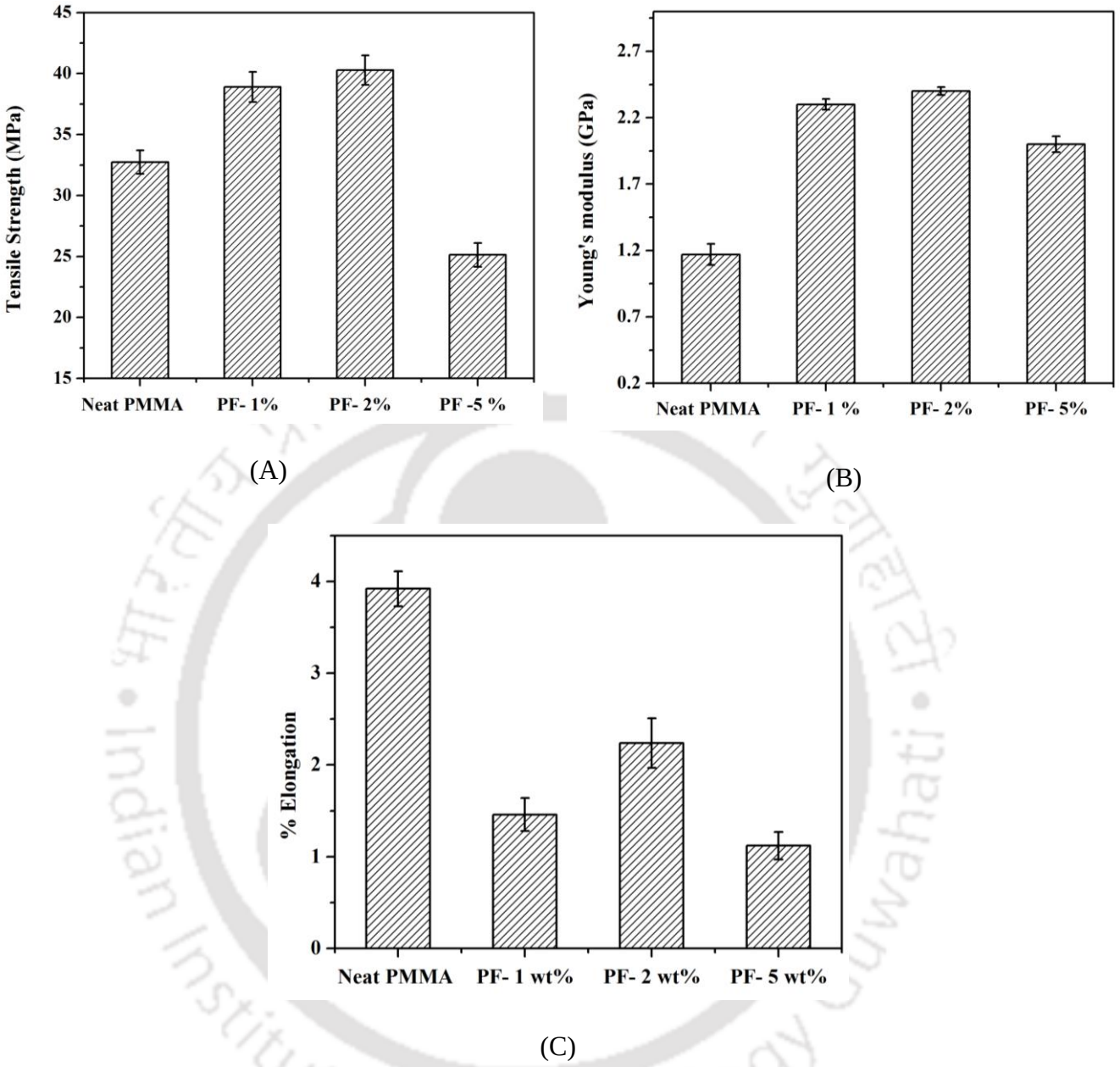

Figure 5.9: Mechanical properties of PMMA/Fe_3O_4 nanocomposites. (A) Tensile strength. (B) Young's modulus. (C) Percentage elongation. [Legends. PF–1% : PMMA/Fe_3O_4 (1 wt%), PF–2% : PMMA/Fe_3O_4 (2 wt%), PF–5% : PMMA/Fe_3O_4 (5 wt%)].

5.4 Conclusions

The present study has put forth a novel ultrasonic two–step method for synthesis of magnetic PMMA nanocomposites using nanoparticles of Fe_3O_4 as filler. Use of sonication during synthesis of both Fe_3O_4 particles and PMMA/Fe_3O_4 nanocomposites was revealed to have merit of imparting special properties the product. Sonochemical prepared Fe_3O_4 particles

had significantly smaller mean size and narrower size distribution as compared to particles synthesized mechanical stirring. The magnetic saturation and coercivity of these particles was also higher. Application of sonication during nanocomposite synthesis resulted in uniform encapsulation and dispersion of the Fe_3O_4 nanoparticles in polymer matrix at relatively low loading of ≤ 5 wt% due to intense micro–convection generated in the reaction medium. This facet of the nanocomposite synthesis was manifested in terms of excellent combination of mechanical, thermal, electrical, magnetic properties and EMI shielding efficiency of the PMMA/Fe_3O_4 nanocomposite. The thermal and mechanical properties of nanocomposite showed maxima for optimum Fe_3O_4 loading of 2 wt%. On the other hand, electrical conductivity, magnetic properties and EMI shielding efficiency of the nanocomposite varied proportionately with the Fe_3O_4 loading. In summary, ultrasonically synthesized PMMA/Fe_3O_4 nanocomposites in this study have demonstrated potential for applications in numerous areas due to their versatile properties.

References

Bach LG, Islam MD, Kim JT, Seo SY, Lim KT, Encapsulation of Fe_3O_4 magnetic nanoparticles with poly(methyl methacrylate) via surface functionalized thiol–lactam initiated radical polymerization, Appl. Surf. Sci.258 (2012) 2959–2266.

Banert T, Peuker UA, Preparation of highly filled super–paramagnetic PMMA–magnetite nano composites using the solution method, J. Mater. Sci. 41 (2006) 3051–3056.

Bansod AR, Chimankar OP, Turkar RK, Gandhe A, Synthesis, ultrasonic and other characterization of PMMA/Fe_2O_3, I.J.E.T.R. 2 (2014) 195–199.

Cai W, Wan J, Facile synthesis of superparamagnetic magnetite nanoparticles in liquid polyols, J. Colloid. Interf. Sci. 305 (2007) 366–370

Chakma S, Moholkar VS, Physical mechanism of sono–Fenton process, AIChE J. 59 (2013) 4303–4313.

Esthappan SK, Polypropylene/metal oxide nanocomposites: Fiber spinning and evaluation, Ph.D. Dissertation, Department of Polymer Science and Rubber Technology, Cochin University of Science and Technology, Kochi (Kerala), India, May 2012.

Gyergyek S, Makovec D, Mertelj A, Huskic M, Drofenik M, Superparamagnetic nanocomposite particles synthesized using the mini–emulsion technique, Colloids. Surfaces. A. Physicochem, Eng. Asp. 366 (2010) 113–119.

Hong RY, Feng B, Cai X, Liu G, Li HZ, Ding J, Zheng Y, Wei DG, Double–miniemulsion preparation of Fe_3O_4/Poly(methyl methacrylate) magnetic latex, J. App. Polym. Sci. 112 (2009) 89–98.

Fan X, Lin L, Messersmith PB, Surface–initiated polymerization fromTiO_2 nanoparticle surfaces through a biomimetic initiator: A new route toward polymer–matrix nanocomposites, Compos. Sci. and Technol. 66 (2006) 1195–1201.

Kaushik A, Khan R, Solanki PR, Pandey P, Alam J, Ahmad S, Malhotra BD, Iron oxide nanoparticles–chitosan composite based glucose biosensor, Biosens. Bioelectron. 24 (2008).676–683.

Kim J, Lee JE, Lee SH, Yu JH, Lee JH, Park, TG, Hyeon T, Designed fabrication of a multifunctional polymer nanomedical platform for simultaneous cancer–targeted Imaging and magnetically guided drug delivery, Adv. Mater. 20 (2008) 478–483.

Kirchberg S, Rudolph M, Ziegmann G, Peuker UA, Nanocomposites based on technical polymers and sterically functionalized soft magnetic magnetite nanoparticles: Synthesis, processing, and characterization, J. Nanomater. (2012) 1–8.

Lan F, Liu KX, Jiang W, Zeng XB, Wu Y, Gu, ZW, Facile synthesis of monodisperse superparamagnetic Fe_3O_4/PMMA composite nanospheres with high magnetization, Nanotechnology, 22 (2011), 225604.

Li JH, Hong RY, Li MY, Li HZ, Zheng Y, Ding J. Effects of Fe_3O_4 nanoparticles on the mechanical and antibacterial properties of polyurethane coatings, Prog. Org. Coat. 64 (2009) 504–509.

Mahdavian AR, Sehri Y, Mobarakeh HS, Nanocomposite particles with core–shell morphology II. An investigation into the affecting parameters on preparation of Fe_3O_4–poly(butyl acrylate–styrene) particles via miniemulsion polymerization, Eur. Polym. J. 44 (2008) 2482–2488.

Moser A, Takano K, Margulies DT, Albrecht M, Sonobe Y, Ikeda Y, Sun S, Fullerton EE, Magnetic recording: advancing into the future, J. Phys. D. Appl. Phys. 35 (2002) 157–167.

Murali KP, Sharma H, Raj, PM, Mishra D, Goyal M, Silver K, Shipton E, Tummala R, Structure magnetic property correlations in nickel- polymer nanocomposites, J. Matter. Sci. 27 (2016) 154–162.

Nsib F, Ayed N, Chevalier Y, Dispersion of hematite suspensions with sodium polymethacrylate dispersants in alkaline medium, Colloids Surf. A. 286 (2006) 17–26.

Ramirez LP, Landfester K, Magnetic polystyrene nanoparticles with a high magnetite content obtained by miniemulsion processes, Macromol. Chem. Phys. 204 (2003) 22–31.

Shen X, Gui S, Lin B, Surface organic modification of Fe_3O_4 nanoparticles by silane–coupling agents, Rare Metals, 25 (2006) 426–430.

Sivasankar T, Paunikar AW, Moholkar VS, Mechanistic approach to enhancement of the yield of a sonochemical reaction, AIChE J. 53 (2007) 1132–1143.

Tanniru M, Yuan Q, Misra KDK, On significant retention of impact strength in clay–reinforced high–density polyethylene (HDPE) nanocomposites, Polymer 47 (2006) 2133–2146.

Wang, X, Wang, L, He, X, Zhang, Y, Chen, L, A molecularly imprinted polymer-coated nanocomposite of magnetic nanoparticles for estrone recognition. Talanta 78 (2009) 327–332

Wilson JL, Poddar P, Frey NA, Srikanth H, Mohomed K, Harmon JP, Kotha S, Wachsmuth J, Synthesis and magnetic properties of polymer nanocomposites with embedded iron nanoparticles, J. Appl. Phys. 95 (2004) 1439–1443.

Zhang D, Karki AB, Rutman D, Young DP, Wang A, Cocke D, Electrospun polyacrylonitrile nanocomposites fibers reinforced with Fe_3O_4 nanoparticles: Fabrication and property analysis, Polymer, 50 (2009) 4189–4198.

CHAPTER 6

OVERVIEW AND SUGGESTIONS FOR FUTURE WORK

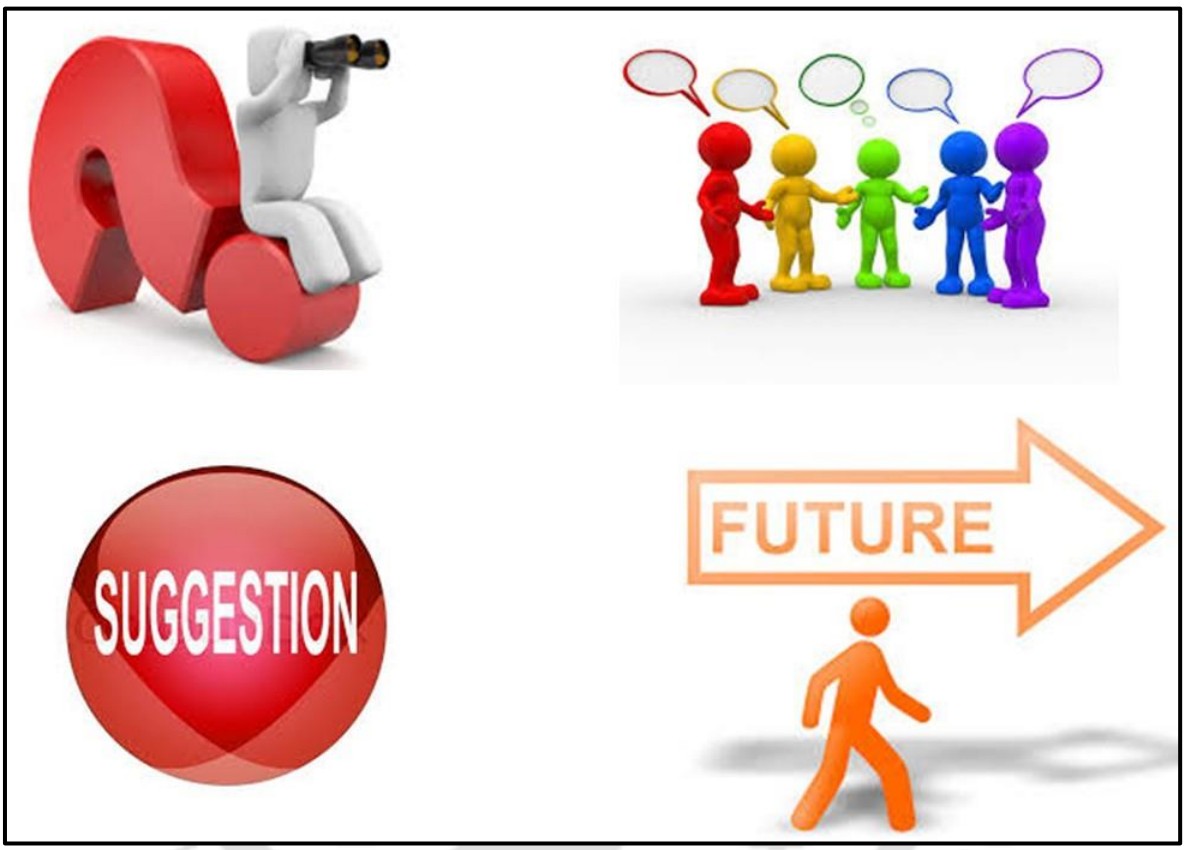

CHAPTER 6

Overview and Suggestions for Future work

Polymer nanocomposites have emerged as new generation of materials with remarkable mechanical, thermal, optical, electrical and magnetic properties, as compared to pristine polymers. By virtue of these properties, polymer nanocomposites have potential of use in numerous applications. Proper encapsulation and uniform dispersion of nanofiller material in polymer matrix is crucial to achieving enhancement of the physical properties. Among possible methods for synthesis of nanocomposites, in-situ emulsion polymerization has special merits, as outlined in chapter 1. Emulsion polymerization coupled with sonication has been widely investigated in recent years as potential technique for synthesis of variety of nanocomposites. Although significant literature has been published in this area, the basic physical mechanism of ultrasound-assisted in-situ emulsion polymerization has remained largely unexplored. Most of the published studies have rather black box approach, in which emphasis is put on results and characterization of the nanocomposites, rather than establishing the links between physical and chemical effects of ultrasound and cavitation and basic chemistry of polymerization in presence of nanofiller.

This thesis has attempted to present systematic mechanistic investigations in ultrasound-assisted emulsion polymerization. Methyl methacrylate (MMA) has been selected as base monomer due to its versatile properties. Polymerization and synthesis of

nanocomposites of MMA has been carried out in presence of 4 nanofillers, viz. Cloisite 30B clay, zinc oxide, reduced graphene oxide (with in-situ reduction) and iron oxide. In case of zinc oxide, reduced graphene oxide and iron oxide, the nanofiller particles have also been synthesized using sonochemical method. It has been revealed in this thesis research that the enhancement effect of ultrasound and cavitation on reaction system of nanocomposite synthesis is mostly of physical nature. Ultrasound and cavitation make energies available on extremely small spatial and temporal scale, which has several beneficial implications on nanocomposite synthesis. The intense micro-convection generated by ultrasound and cavitation not only causes fine emulsification of reaction mixture, but also effective encapsulation and uniform dispersion of the nanofiller in the polymer matrix. Enormous interfacial area generated due to emulsification also causes enhancement of the reaction kinetics and nanocomposite yield. The nanocomposites resulting from ultrasound-assisted in-situ emulsion polymerization have better thermal, mechanical, electrical, magnetic and optical properties than nanocomposites synthesized through conventional technique employing mechanical stirring. Intense micro-convection generated by ultrasound and cavitation obviates need for addition of surfactant in the reaction system. Moreover, micro-convection also achieves uniform dispersion of the nanofiller material in polymer matrix – without requiring the surface modification of the hydrophilic nanofiller to enhance its compatibility with the hydrophobic polymer matrix. Transient collapse of cavitation bubbles also creates sonochemical effect, which is in-situ generation of highly reactive radicals via thermal dissociation of the solvent vapor trapped inside the bubble – as the temperature/pressure in the bubble reach extreme during transient collapse. However, role of these in-situ generated radicals in the polymerization in presence of nanofiller has been revealed to be negligible. No polymerization was seen to occur without addition of the external initiator.

Given below is the overall summary of all chapters. These result, when viewed and analyzed at a glance, present a cogent and coherent physical picture of synthesis and intensive characterization of PMMA based various nanocomposites.

- Chapter 2 reported the ultrasound-assisted synthesis of PMMA/Cloisite 30B nanocomposites with optimization using statistical design of experiment. Polymerization of MMA to PMMA was strongly dependent on free radicals generated by inorganic initiator, and not on the in-situ generated radicals through transient cavitation due to highly sporadic nature of transient cavitation (in time and spatial domain). However, the micro-convection generated by ultrasound and cavitation (through microstreaming and shock waves) had beneficial influence on synthesis of nanocomposites. It was revealed that micro-convection generated by sonication increases the interlayer *d*-spacing among the clay layers which assists effective exfoliation of the nanofiller. The shock waves generated by the transient cavitation also assist de–agglomeration and uniform dispersion of clay particles in the reaction mixture. Micro–streaming (or oscillatory motion of fluid elements) generated by ultrasound causes uniform intercalation of the monomer in the layers of the clay particles or entrapment of monomer swollen micelles between the silicate layers of clay. Overall kinetics of polymerization was revealed to be third order with respect to monomer. Although thermal and mechanical properties such as Young ’s modulus of PMMA/Cloisite 30 B nanocomposite have been enhanced as compared to neat PMMA, there is no direct proportionality between the property enhancement and loading of clay during the reaction. Thermal and mechanical properties of the nanocomposites were increased with the clay loading.
- Chapter 3 reported ultrasound-assisted synthesis of PMMA/ZnO nanocomposites. For this synthesis, ZnO particles were used in pristine form without surface modification. Experimental results showed that use of ultrasound during synthesis resulted in uniform dispersion of ZnO in polymer matrix. This lead to strong interfacial interaction and adhesion

between nanoparticles and polymer matrix. PMMA/ZnO nanocomposites synthesized with this technique possessed enhanced thermal, mechanical and optical properties as compared to neat PMMA. However, this enhancement was strongly dependent on the ZnO loading in reaction mixture during synthesis. All physical properties of nanocomposites showed an optimum with ZnO loading. Maximum properties were obtained only up to 2 wt% loading of ZnO. With further increase in ZnO loading (> 2 wt%), the physical properties of the nanocomposites showed reduction. This essentially is manifestation of the formation of agglomerates of the nanofiller in polymer matrix at higher loading of ZnO during synthesis.

- Chapter 4 reported further research on ultrasound–assisted synthesis of polymethyl methacrylate (PMMA)/reduced graphene oxide (RGO) nanocomposites by in–situ emulsion polymerization coupled with in–situ reduction of graphene oxide. Addition of RGO significantly enhanced the physical properties of resulting nanocomposites even at very low filler loading (1.0 wt %). Use of ultrasound during in-situ emulsion polymerization improves the intermolecular interaction between PMMA and graphene sheets. This essentially is attributed to the exfoliation of the graphene sheet in the PMMA matrix under influence of strong microconvection generated by ultrasound and cavitation.Relatively low concentration of nanofiller (≤ 1.0 wt%) employed during nanocomposite synthesis was aimed at achieving good balance between thermal/mechanical and electrical properties of the nanocomposites. The highest thermal and mechanical properties (viz. maximum thermal degradation temperature, glass transition temperature, tensile strength, Young's modulus, percentage elongation) were obtained for RGO loading of 0.4 wt%, while the highest electrical properties (viz. conductivity and electromagnetic interference shielding efficiency) were seen for RGO loading of 1.0 wt%.
- Chapter 5 treated ultrasound assisted synthesis of PMMA/iron oxide nanocomposites.Fe_3O_4 nanoparticles were synthesized using coprecipitation technique

coupled with sonication. Use of sonication during co-precipitation resulted in low particle size higher yield of Fe_3O_4 due to in-situ generated H_2O_2.Addition of iron oxide nanoparticles in polymer matrix increases its magnetic, thermal and mechanical properties. Sonication of solution of nanoparticles in presence of surfactant achieves higher adsorption of the surfactant on the particles, which not only enhances their stability against agglomeration, but also improves interaction with polymer matrix. This results in uniform distribution of iron oxide particles in polymer matrix under influence of strong microconvection generated by ultrasound and cavitation.

The physical properties of all nanocomposites synthesized in this thesis (as listed in Tables 6.1 A-D, Tables 6.2 A-D, Figs. 6.1A-D and Figs. 6.2 A-D), when viewed together, give an insight into the effect of incorporation of nanofillers with different intrinsic properties on the physical properties of the resulting nanocomposite – as compared to pristine polymer. Since all nanofillers used in this study were oxides, they rendered excellent effect on thermal and mechanical properties of the polymer. All nanofillers increased the thermal stability and glass transition temperature due to hindrance of diffusion of volatile products of thermal degradation out of polymer matrix and restriction of the relative motion of polymer chains. ZnO being a semiconductor oxide had high absorbance in the UV range, and thus the PMMA/ZnO nanocomposite also showed absorbance peak in UV range. Fe_3O_4 nanoparticle possessed high magnetic saturation, and thus, the PMMA/magnetite nanocomposites also showed good magnetic properties – although the saturation magnetization was reduced due to protection of the Fe_3O_4 particles by surrounding polymer. Among all nanofillers used in this study, the reduced graphene oxide showed highest enhancement in the physical properties of polymer with formation of nanocomposite. The addition of RGO nanofiller in PMMA matrix significantly increased the thermal, mechanical and electrical properties of resulting nanocomposites with minimum loading (1 wt%). In addition, RGO incorporation in PMMA

matrix also resulted in marked increase in the electrical conductivity of nanocomposite. This was manifested in terms of good EMI shielding properties. Most notably, the concentration of RGO required to achieve highest physical properties of the PMMA/RGO nanocomposite was least among all nanofillers. These results are attributed to exceptional intrinsic physical properties of graphene, and also to its highest aspect ratio due to which renders maximum interaction between nanofiller and the polymer matrix. Fig. 6.3 presents a comprehensive picture of the suitability of different nanofiller for enhancing certain physical properties of the PMMA through formation of nanocomposites.

The results of this thesis, as summarized above, also inspire further research in the area of ultrasound-assisted nanocomposite synthesis. Some suggestions for future work in this area are given as follows:

1. All of the work carried out in this thesis is on laboratory scale. It would be worthwhile to conduct bench or pilot scale studies on synthesis of polymer nanocomposites using the results obtained at laboratory scale.

2. All studies in the present thesis have used constant frequency and power of ultrasound. It would be worthwhile to conduct the same experiment at different frequency and power so as to ascertain the individual effect of ultrasound and cavitation to the system.

3. In chapter 3 and 5 we have synthesized PMMA/ZnO and PMMA/Fe_3O_4 nanocomposites without surface modification of ZnO and Fe_3O_4 nanofillers. The synthesis of these nanocomposites can be further carried out using surface modification of these nanofillers under the effect of ultrasound.

4. Combination of various nanofillers like CNT/Fe_3O_4, copper nanowires/RGO, Fe_3O_4/RGO, silver nanowires/$Fe_3O_4$and many others can be incorporated into different polymer matrix for the enhancement in electrical conductivity and EMI shielding of resulting nanocomposites.

5. PMMA can be copolymerized with other monomers like butyl acrylate in order to overcome the limitation of low ductility or brittleness of PMMA at high shear loading.

Table 6.1: Comparison of thermal properties of all nanocomposites

(A) PMMA/Cloisite 30B clay nanocomposite

Name of Sample	$T_{5\%}$ (°C)	$T_{50\%}$(°C)	T_{max} (°C)	T_g (°C)
PMMA	267.4	326	376	116
Clay (1 wt%)	274.7	340.1	380	121
Clay (2 wt%)	**276.6**	356.7	385	122
Clay (4 wt%)	267.3	369.3	388	125
Clay (5 wt%)	240.4	**381.9**	**393**	113

(B) PMMA/ZnO nanocomposite

Name of Sample	$T_{5\%}$ (°C)	$T_{50\%}$(°C)	T_{max} (°C)	T_g (°C)
PMMA	267.4	326	376	116
ZnO (1 wt%)	271.3	366	385	122
ZnO (2 wt%)	279.3	367.5	386.1	**122.5**
ZnO (4 wt%)	**279.9**	**368.1**	**386.4**	121
ZnO (5 wt%)	278.6	367.2	**386.4**	119

(C) PMMA/RGO nanocomposite

Name of Sample	$T_{5\%}$ (°C)	$T_{50\%}$(°C)	T_{max} (°C)	T_g (°C)
PMMA	267.4	326	376	116
RGO (0.2 wt%)	283.2	373.0	380	123.5
RGO (0.4 wt%)	288.2	375.2	391	124.5
RGO (0.4 wt%)	**291.3**	**375.8**	**393**	117.3

(D) PMMA/Magnetite (Fe_3O_4) nanocomposite

Name of Sample	$T_{5\%}$ (°C)	$T_{50\%}$(°C)	T_{max} (°C)	T_g (°C)
PMMA	267.40	326	376	116
Fe_3O_4 (1 wt%)	264.1	367	381	121.5
Fe_3O_4 (2wt%)	259.1	**373.2**	**383**	**122.5**
Fe_3O_4 (5 wt%)	257.3	371	379	105

Table 6.2: Comparison of mechanical properties of all nanocomposites

(A) PMMA/Cloisite 30B clay nanocomposite

Name of Sample	Tensile Strength(MPa)	Youngs Modulus(GPa)	Percentage Elongation (%)
PMMA	32.74	1.17	3.92
Clay (1 wt%)	28.51	1.40	2.6
Clay (2 wt%)	25.3	1.67	1.99
Clay (4 wt%)	25.11	**2.16**	1.58
Clay (5 wt%)	21.71	1.74	1.2

(B) PMMA/ZnO nanocomposite

Name of Sample	Tensile Strength (MPa)	Young's Modulus (GPa)	Percentage Elongation (%)
PMMA	32.74	1.17	3.92
ZnO 1 wt%)	**36.57**	**1.47**	**17.56**
ZnO (2 wt%)	27.77	1.21	13.1
ZnO (4 wt%)	26.10	1.14	11.8
ZnO (5 wt%)	25.92	1.09	10.98

(C) PMMA/RGO nanocomposite

Name of Sample	**Tensile Strength (MPa)**	**Young's Modulus (GPa)**	**Percentage Elongation (%)**
PMMA	32.74	1.17	3.92
RGO 0.2 wt%)	34.1	2.1	5.94
RGO (0.4 wt%)	**40.37**	**2.6**	**9.28**
RGO (1 wt%)	18.57	1.18	1.82

(D) PMMA/Magnetite (Fe_3O_4) nanocomposite

Name of Sample	**Tensile Strength (MPa)**	**Young's Modulus (GPa)**	**Percentage Elongation (%)**
PMMA	32.74	1.17	3.92
Fe_3O_4 (1 wt%)	38.90	2.3	1.46
Fe_3O_4 (2wt%)	**40.28**	**2.4**	**2.24**
Fe_3O_4 (5 wt%)	25.13	2.0	1.12

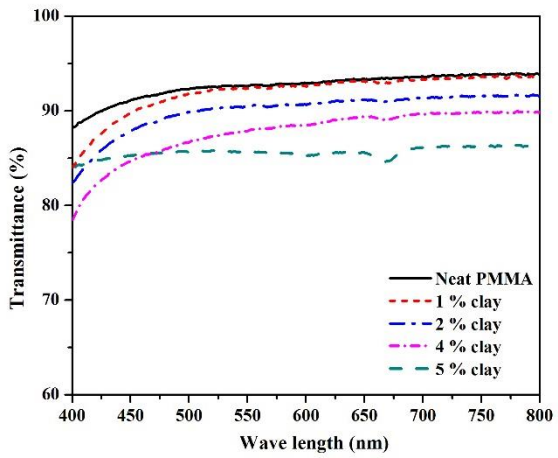

(A) PMMA/Cloisite 30B

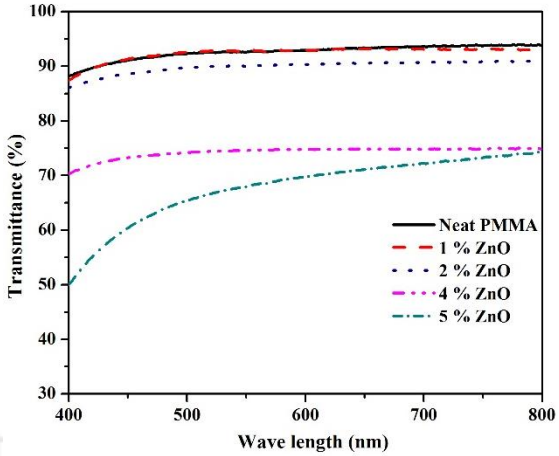

(B) PMMA/ZnO

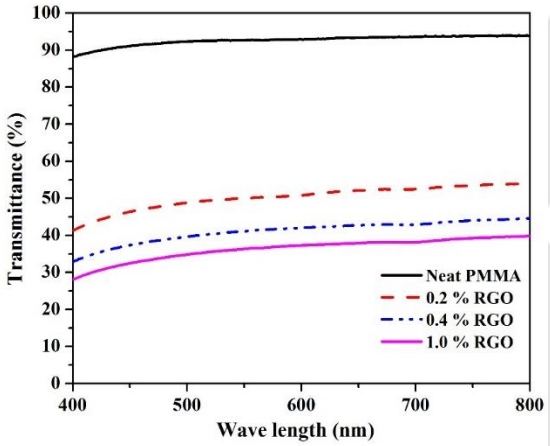

(C) PMMA/RGO

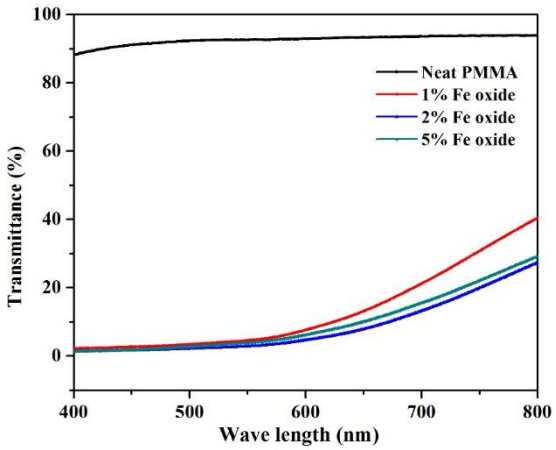

(D) PMMA/Fe_3O_4

Figure 6.1: Comparison of optical properties of (A) PMMA/Cloisite 30B (B) PMMA/ZnO (C) PMMA/RGO (D) PMMA/IO nanocomposites

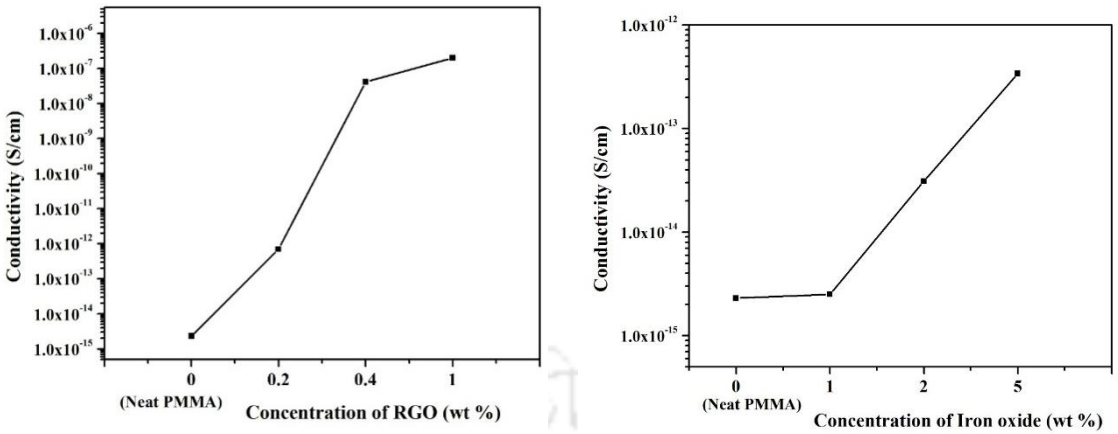

(A) PMMA/RGO (B) PMMA/IO

Figure 6.2: Comparison of electrical conductivities of (A) PMMA/RGO (B) PMMA/IO nanocomposites.

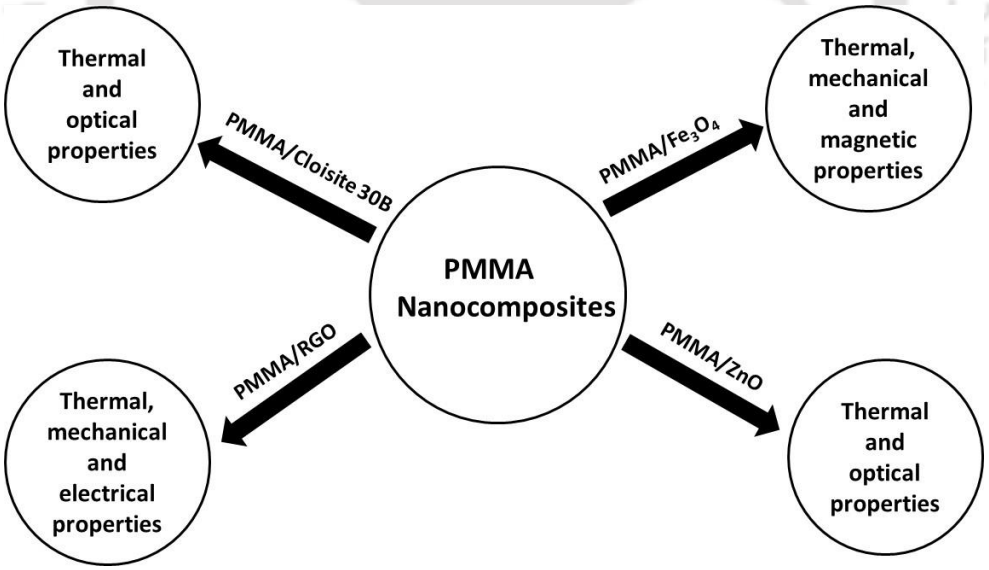

Figure 6.3: Overall conclusion for choice of properties of PMMA nanocomposites.

ACKNOWLEDGEMENTS

I express my sincere and deep gratitude to each and everyone for helping me directly and indirectly towards the completion of my research work and made this thesis possible. I owe my deepest respect to everyone.

The first and foremost gratitude goes to my supervisor **Prof. V. S. Moholkar** for their valuable and productive guidance throughout my entire research work. I thank him for his encouragement, valuable support and his immense trust in me which enabled me to develop a better understanding of the subject leading to present this thesis. I would like to thank him for spending his precious time to discuss thoroughly on the topic and make me somehow expert in the field of polymer nanocomposites. I would also like to acknowledge my sincere gratitude to my doctoral committee members, **Prof. G. Pugazhenthi, Prof. P. Ghosh** and **Prof. P. K. Iyer,** for their valuable comments and suggestions throughout my research period. I also express my sincere gratitude to all faculty members of Department of Chemical Engineering, I. I. T. Guwahati, for their continuous suggestions and motivations. I also like to express my thanks to all staff members for their support during analytical facilities.

I would also like to acknowledge Prof D. Pamu, S. Pattipaka (Department of Physics) for analysis of electrical conductivity test and Mr. Sanjib Sarma (Department of Mech. Engg.) I. I. T. Guwahati for analysis of mechanical properties test. I also express my sincere thanks to North Eastern Hill University (NEHU), Shillong for providing TEM facilities.

I would also like to thank Prof. Uttandaraman Sundararaj and Dr. Mohammad Arjamand (Department of Chemical and Petroleum Engg University of Calgary, Canada) for analysis of electrical conductivity and EMI shielding facilities.

I am grateful to all my seniors, my Friends, colleague members and Lab mates from our group Hanif Chaudhary, Shuchi Singh, Sankar Chakma, Jay Bhasarkar, Binota Thokchom, Pritam Dikshit, Arup Jyoti Borah, Shyamali Sarma, Amit Batghare, Neha Singh, Kuldeep, Niharika Kashyap, Ritesh Malani, Belachew Zegale, Philip Saynik, Debarshi Mullick, Sumitha Banu, Udhangshree Boro, Kajal Ingtipi, Sachin Sharma, Mayank Agarwal, Sushobhan Pradhan, Avinash Anand and Saiprasad Pati. I must thank to my friend Shailesh, Venkatanarasimha Rao and Debashis Kundu for helping various characterization techniques.

Finally, I express my gratitude to my beloved family members for supporting and encouraging me throughout my life. I extend my gratefulness to my parents and my brother who have been the motivation behind my hard work, patience and character.

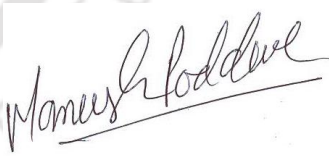

Maneesh Kumar Poddar

March, 2017

RESEARCH OUTPUT FROM THE THESIS

1. Poddar MK, Sharma S, Moholkar VS, Sonochemical synthesis of PMMA/Cloisite 30B nanocomposites: A mechanistic investigation, Macromol. Symp. 361(2016) 82–100.

2. Poddar MK, Sharma S, Moholkar VS, Investigations in two-step ultrasonic synthesis of PMMA/ZnO nanocomposites by in–situ emulsion polymerization, Polymer,99 (2016) 453–469.

3. Poddar MK**,** Arjmand M, Sundararaj U, Moholkar VS, Thermal, electrical and mechanical properties of PMMA/RGO nanocomposites synthesized via ultrasound–assisted in–situ emulsion polymerization. AIChE J. (Under Review)

4. Poddar MK, Arjmand M, Sundararaj U, Moholkar VS, Ultrasound-Assisted Synthesis and Characterization of Magnetite Nanoparticles and Polymethyl Methacrylate/Magnetite Nanocomposites. Polymer (Under Review)

5. Poddar MK, Moholkar vs, Studies of thermal kinetic degradation and mechanical properties of PMMA/Cloisite 30B nanocomposites by ultrasound assisted in situ emulsion polymerization method, (To be communicated)

OTHERS PUBLICATIONS

1. Poddar MK, S Sharma S, Moholkar VS, Enhancement of thermal and mechanical properties of poly (MMA–co–BA)/Cloisite 30B Nanocomposites by ultrasound–assisted in–situ emulsion polymerization, Ultrason Sonochem. 36: (2017), 212–225.

2. Poddar MK, Sharma S, Pattipaka S, Pamu D, Thermal, electrical and optical properties of poly(MMA–co–BA)/ZnO nanocomposites synthesized via Ultrasound–assisted In–situ emulsion polymerization. Polymer. Composite. (Under Review)

3. Pradhan S, Poddar MK, Borah AJ, Dikshit PK, Rohidas L, Moholkar VS, Microbial production, ultrasound-assisted extraction and characterization of biopolymer polyhydroxybutyrate (PHB) from Terrestrial and Aquatic Invasive Weeds, Bioresource Technology. (Under Review)